Study of Directional Ocean Wavefield Evolution and Rogue Wave Occurrence Using Large-Scale Phase-Resolved Nonlinear Simulations

by

Wenting Xiao

Submitted to the Department of Mechanical Engineering
in partial fulfillment of the requirements for the degree of

Doctor of Philosophy in Mechanical Engineering

at the

MASSACHUSETTS INSTITUTE OF TECHNOLOGY

February 2013

Author .....
Department of Mechanical Engineering
January 10, 2013

Certified by .....
Dick K. P. Yue
Philip J. Solondz Professor of Engineering
Professor of Mechanical and Ocean Engineering
Thesis Supervisor

Accepted by .....
David E. Hardt
Chairman, Department Committee on Graduate Students

Study of Directional Ocean Wavefield Evolution and Rogue Wave Occurrence Using Large-Scale Phase-Resolved Nonlinear Simulations

by

Wenting Xiao

Submitted to the Department of Mechanical Engineering
on January 10, 2013, in partial fulfillment of the
requirements for the degree of
Doctor of Philosophy in Mechanical Engineering

Abstract

It is challenging to obtain accurate predictions of ocean surface wavefield evolutions due to several complex dynamic processes involved, including nonlinear wave interaction, wave breaking and wind forcing, and also wave interactions with currents and bottom bathymetry. With fast computational algorithms for nonlinear phase-resolved wave simulations and modern computational capabilities, we now develop and apply a direct large-scale nonlinear phase-resolved wavefield simulation tool, which we call SNOW (Simulation of Nonlinear Ocean Wavefields), to study the evolution of directional ocean waves and occurrence of rogue waves (extremely large waves).

Using SNOW, we obtain an ensemble of nonlinear deep-water wavefield simulations, initialized by JONSWAP spectrum with a broad range of spectral parameters, over large space-time scales. Spectral evolutions, nonlinear wave statistics and rogue wave occurrence are investigated based on the simulated wavefields. The SNOW results are compared to available wave basin experiments and predictions from linear theory and approximate nonlinear-Schrödinger-equation (NLS) type models. SNOW predictions give an overall better comparison with wave-basin experiments than NLS-type model predictions. For initially narrow-banded and narrow-directional-spreading wavefields, we find modulational instability develops over short time, resulting in considerable spectral broadening, strongly non-Gaussian statistics and probability of rogue wave occurrence an order of magnitude higher than linear theory prediction. For longer time, the wave spectrum in SNOW simulations reaches a non-Gaussian quasi-stationary state, and this is not predicted by NLS-type models, where a continuous spectral broadening is observed. When waves spread broadly in frequency and direction, the modulational-instability effect is reduced and the wave statistics and rogue wave probability are close to linear theory prediction. Number and area-based probabilities are introduced to measure the likelihood of rogue wave occurrence. To effectively predict rogue wave occurrence in directional seas, we propose a new modified Benjamin-Feir index (MBFI), which accounts for the effects of wave directionality.

It is shown that the occurrence probabilities of rogue waves are well correlated with MBFI over a broad range of spectral parameters. Based on a large catalogue of rogue waves found from SNOW simulations, the geometric shapes of rogue waves are analyzed using proper orthogonal decomposition (POD). It is found that rogue wave profiles can generally be described by a small number of POD modes.

SNOW simulations are also used to investigate the influence of finite depth on the evolution of nonlinear wavefields. As water depth decreases, the modulational instability decreases and finally diminishes. It is found that the occurrence probability of rogue waves and wave kurtosis decrease as water depth decreases. The wave statistics and rogue wave occurrence in bimodal wavefields are also studied. The influence of swell on the wave statistics of single-modal wind sea is not monotonic. The occurrence probability of rogue waves can either increase or decrease depending on the bimodal spectrum shape. We find the rogue wave probability and wave kurtosis are minimized when the propagation directions of swell and wind sea are orthogonal.

By assimilating wave measurements from in-situ buoy and/or remote sensing into SNOW, we develop and demonstrate the capability of phase-resolved reconstruction and forecasting of wavefield evolution and rogue wave occurrence. Such capability could significantly enhance marine design and operation.

This research paves the way for a new-generation wave forecasting model that is capable of providing heretofore unavailable large-scale phase-resolved information on the ocean wave evolution. Such capability is critically useful such as in the understanding of rogue wave dynamics and in the practical marine operations and safety.

Thesis Supervisor: Dick K. P. Yue
Title: Professor of Mechanical Engineering

Acknowledgments

I owe my gratitude to all the people who have made this thesis possible and because of whom my graduate experience has been one that I will cherish forever.

First and foremost, I offer my sincerest gratitude to my supervisor, Professor Dick K. P. Yue, who is the most influential person during my graduate career. His passion, guidance, and discipline have been indispensable to my growth as a scientist and as a person over the past six years. I am especially grateful to Professor Yue for his devotion to my education and success. When I look back at the struggles I had gone through during my Ph.D. study, I am so grateful for the confidence he always had in me that encouraged me to take up all challenges and his countless hours of support to make this work to a new level of excellence. I am also thankful for the inspiring role model he has provided through his wide-ranging activities in education, his tremendous productivity and contributions in research, and his incredible ability to manage different demands. I consider myself very fortunate for being able to work with him.

I am specially indebted to Dr. Yuming Liu, for his scientific advice and knowledge and many insightful comments and discussions at different stages of this research. He is also my great source of learning and getting my scientific questions answered. I am also thankful to him for holding me to a high research standard.

I have been greatly blessed with a friendly and cheerful group of fellow students and many of them have become my extended family over the last several years. The members of the VFRL group have contributed immensely to my professional and personal time at MIT. I am specially grateful to Grgur Tokic, Sankha Banerjee, Yulin Pan and Meng Shen, who have provided invaluable friendships as well as good advice and collaboration. Also, I thank Yulin for proofreading two chapters of this thesis.

I thank two of my best friends especially, Tea Zakula and Sarah Druecke, for making my life at MIT such a joyful experience. I have had the great fortune of having developed such great friends during my graduate life. The encouragement

and fun times they have provided have meant a lot to me.

Lastly, I would like to thank my family for all their love and encouragement. I thank my parents for their unconditional love and support, for raising me and providing me the best education they could afford. Most of all, I give my heartfelt thanks to my husband, Jinhui Zhao, for his unfailing love, care, support, and encouragement during my good and bad times. These past several years were not easy for us as we stayed in two different cities. He traveled every two weeks from Pittsburgh to Boston to visit me and never complained about my busy schedule. I truly thank Jinhui for always being there for me. Besides all these, he also helped to proofread all the chapters of this thesis. Words are just not enough here to express my appreciation.

Contents

Chapter 1

Introduction

This thesis is devoted to the study of the directional ocean surface wave evolutions with a primary focus on the extremely large wave events, *rogue waves*, using a direct numerical simulation approach. In this chapter, the key physical processes in ocean wave dynamics are briefly described and a short introduction to rogue waves is given. We then review various types of numerical wave forecasting models developed at different stages in the literature and discuss the model capabilities and limitations. In the end, we state the objectives, problem statement, and contributions of present thesis.

1.1 Historical note on ocean waves

Ocean surface gravity waves are one of the most familiar natural phenomena that are both fascinating and intimidating to human. Man's relationship with ocean and ocean waves has started since the invention of oceangoing vessels and large ships. The stories of ancient marine explorers can be traced back to six centuries ago. The great Chinese mariner and explorer, Zheng He, led seven expeditions to the Indian Ocean, historically referred to as the "the voyages of Zheng He", during 1405 to 1433. Despite the long experiences of human with ocean waves, significant attempts for understanding water waves started only 200 years ago. The celebrity mathematicians in eighteenth and nineteenth century, including Laplace, Lagrange, Poisson, Cauchy, Green, Airy,

Stokes, Boussinesq and many others, who found the mathematical problems associated with water waves both fascinating and challenging, made solid contributions to the development of water wave theory. Sophisticated mathematical techniques were developed and applied to describe the propagation of small-amplitude monochromatic sinusoidal waves, the wave pattern generated by dropping a pebble in the water, and the shape of solitary waves generated by the stopping of a barge in a canal. Since eighteenth century the water wave theory has triggered significant advances in mathematic techniques and state of knowledge of fluid mechanics. Interesting reviews on the regular deterministic water wave theories in a historic perspective can be found in Craik (2004, 2005); Darrigol (2003). A number of textbooks are devoted to the beautiful mathematics and rich fluid dynamics in water wave theories, including Mei et al. (2005a,b), Whitham (2011), and Kundu and Cohen (2004).

The subject of random ocean waves is more complex than that of regular deterministic water waves. The major challenges in the ocean waves are their randomness and the complex dynamic processes involved. When looking at the ocean, the motion of waves appears to be totally random in space and time and the ocean surface appears to be composed of waves with various lengths and periods. In addition to the complicity of wave randomness, several complicated physical dynamics evidently involved in the ocean wave motion, including wind blowing, wave profile steepening, and wave breaking (figure 1-1).

Substantial progresses in the ocean wave theories started during World War II for the landing operations of Normandy in 1945 (Sverdrup and Munk, 1947) . In the pioneer work of Sverdrup and Munk (1947), statistical quantities were introduced to characterize quantitatively the properties of irregular random waves. Two wave statistics of practical importance are significant wave height and significant wave period, which are the average height and period of the highest one-third of the waves. In Sverdrup and Munk (1947), an *energy balance equation* was introduced to describe the evolution of the waves. In this equation, the wave evolution was determined by a source function which is a sum of energy input and decay due to wind forcing and wave breaking. Although empirical formula were used for the wind input and

breaking and effect of nonlinear wave interactions were completely ignored in Sverdrup and Munk (1947), Sverdrup and Munk's work set up the basic framework for ocean wave forecasting which is still adopted today. In particular, the idea of the evolution of ocean waves being controlled by a sum of key physical processes allows the study on each physical process to be separated. Once a dynamic process is understood, the forecasting model can be advanced by adding or updating the corresponding term in the source of the energy balance equation. Since then, enormous progresses have been made to expand our knowledge of ocean wave dynamics, including the mechanisms of wave generation by wind (Phillips, 1957; Miles, 1957), the energy transfer of nonlinear waves (Phillips, 1960; Hasselmann, 1962, 1966), wave breaking and energy dissipation (Duncan, 1981; Rapp and Melville, 1990), and equally importantly, the stochastic aspects of ocean waves (Longuet-Higgins, 1952, 1975; Pierson et al., 1955; Ochi, 2005). A number of extensive field measurements has also made considerable contribution to clarify and advance our understanding of ocean waves (Mitsuyasu, 1968, 1969; Hasselmann et al., 1973; Snyder et al., 1981). Elaborate literature review on process in ocean wave forecasting can be found in Mitsuyasu (2002); Janssen (2008); Komen et al. (1984)

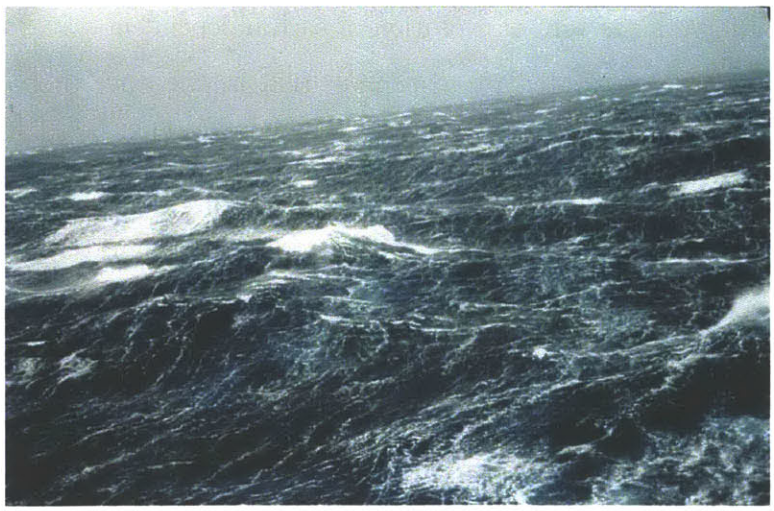

Figure 1-1: North Pacific storm waves, *NOAA*.

1.2 Basic dynamic processes in ocean waves

There are several complex physical processes involved in the ocean wave evolutions. For deep water wavefield, the essential dynamic processes include energy input from wind forcing, energy transfer due to nonlinear wave interactions, and energy dissipation due to wave breaking. In the context of coastal environment, other effects including wave-current interaction, refractions from varying bathymetry and coastal zone boundaries should also be considered.

1.2.1 Linear waves

The ocean waves appear to be composed of waves of various lengths and directions, therefore we may assume that the wave surface is made up of a large number of simple sinusoidal waves with different frequencies and propagation directions. This idea is supported by the mathematical concept of Fourier series for period functions, any surface being represented as an infinite series of sine and cosine functions oriented in all possible directions. In linear wave theory, each wave mode is assumed to be independent. There is no energy transfer among different wave modes and individual wave with random phase propagates with its own speed. The evolution of linear wavefield, therefore, is the sum of evolution of each independent wave.

Surface waves in deep water are *dispersive*, that is, the wave propagation speed depends on the wavelength. Waves with longer wavelength propagate faster than the ones with shorter wavelength. As waves of different lengths propagate away from their origin, eventually, they are sorted according to the wavelengths with long waves being in front of short waves. While the short waves are dissipated over a long journal, the long waves are able to survive as the dissipation associated with them is much less significant. This situation occurs when the waves are generated from a powerful storm thousands of miles away and have propagated several days to reach their present location. These waves are called *swell*. The swell waves usually have a narrow range of wavelengths (typically $\sim$100 m) and directions. Figure 1-2 shows a swell at Lyttelton harbor in New Zealand and the waves are found to have

an appearance close to regular monochromatic sinusoidal waves. The evolution of swell with small amplitude in deep open sea can be captured by the linear theory reasonably well (Snodgrass et al., 1966). Linear wave theory is the foundation of ocean waves and it is discussed extensively in many textbooks including Mei et al. (2005a), Whitham (2011) (part II), and Kundu and Cohen (2004) (Chapter 7).

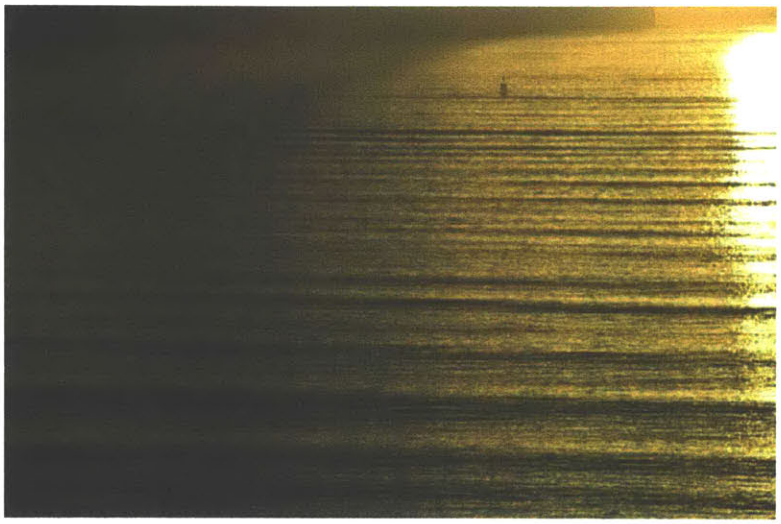

Figure 1-2: Swell at Lyttelton Harbour, New Zealand, 2008.

1.2.2 Nonlinear waves

For monochromatic periodic surface waves with finite amplitude, their profiles are no longer sinusoidal. In 1847, Stokes generalized the linear wave theory for constant water depth by including high-order bound-wave effects to the sinusoidal waves (Stokes, 1847). These period nonlinear waves are named as *Stokes waves*. Stokes waves have sharper crests and flatter troughs comparing to sinusoidal waves (figure 1-3). For many years even until today, Stokes waves have been used as the model waves in many practical marine design applications where the information of wave kinematics is required (Patel, 1989).

Benjamin and Feir (1967) find initially periodic Stokes wave train is unstable to side-band modulations. This Benjamin-Feir (modulational) instability causes the wave train to disintegrate into wave groups within which large waves could form. Lake

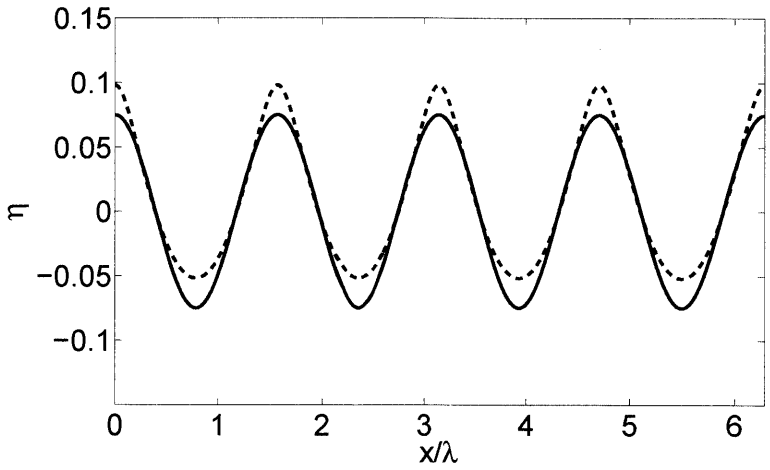

Figure 1-3: Regular sinusoidal wave (—) and ninth-order Stokes wave with steepness $ak = 0.3$ (- - -).

et al. (1977) find the unstable modulations grow to a maximum and then decreases. Over a long evolution time, the wave train actually return to its initial profile. In the absence of energy dissipation, the long time evolution of modulational instability becomes a series of focusing and de-focusing cycles, known as the Fermi-Pasta-Ulam recurrence phenomenon. The related time scale of Benjamin-Feir type modulational instability for nonlinear wave energy transfer is $\mathcal{T} = O(T_p\varepsilon^{-2})$, where $\varepsilon = ak$ is the wave steepness, with a and k being the wave amplitude and wavenumber of the dominant wave, and T_p is the wave period. The Fermi-Pasta-Ulam recurrence phenomenon occurs on the time scale $O(T_p\varepsilon^{-3})$. In other words, without energy dissipation, the energy transfer caused by modulational instability is reversible over time scale $\mathcal{T} = O(T_p\varepsilon^{-3})$. A good review on nonlinear wave interactions for deep water waves can be found in Yuen and Lake (1980).

In random wavefields, the randomness of the wavefields reduces the growth rate of the modulational instability (Alber, 1978). For wavefield which are sufficiently random, characterized by a broad range of wave frequencies and directions, the modulational instability could be eliminated. For wavefields in which the waves have a narrow range in frequencies and directions, the modulational instability could still occur. Recently, modulational instability is studied theoretically, experimentally, and numerically as possible generation mechanism for extraordinarily large waves (see

§1.4).

Benjamin-Feir instability is only one special example of four-wave (quartet) interactions (Phillips, 1960; McLean et al., 1981; Mei et al., 2005b). For deep water waves, the resonant interactions of lowest order occur among four waves. The resonant interaction theory plays an important role in understanding the wavefield evolution and nonlinear wave phenomena. The energy transfer caused by four-wave resonant interactions occurs on a much longer time scale $\mathcal{T} = O(T_p\varepsilon^{-4})$. The evolution of the random wavefield consists of a relatively fast energy transfer process (over time scale $O(T_p\varepsilon^{-2})$ caused by Benjamin-Feir instability and a much slower energy transfer process (over time scale $O(T_p\varepsilon^{-4})$ caused by four-wave resonant interactions. It is believed that the former process is reversible similar to the Fermi-Pasta-Ulam recurrence phenomenon and it is the later process that is responsible for the net energy transfer among waves because it is irreversible Yuen and Lake (1980). In fact, the energy transfer due to quartet resonant interactions is believed to be one of the major driving sources that leads to the change of the wavefield (Hasselmann, 1962, 1966) However, the Fermi-Pasta-Ulam recurrence has not been discovered in realistic random wavefields because of the presence of many unstable side bands (Caponi et al., 1982) and non-ignorable wave breaking (Tulin and Waseda, 1999). Recent research finds, for unidirectional random ocean wavefields composed of waves with a narrow range of frequencies, modulational instability can lead irreversible redistribution of the wave energy over the short modulational-instability time scale $\mathcal{T} = O(T_p\varepsilon^{-2})$ (Janssen, 2003).

For wave evolutions over even longer time, the higher wave nonlinearity such as quintet (five) wave interactions may also be relevant. It is found, for steep stokes wave train, the three-dimensional modulational instability caused by resonant quintet interactions develops leading to a "horseshoe" pattern of the waves (McLean et al., 1981; Su, 1982b). The instability of Stokes wave train caused by the quintet interactions and the coupled resonant quartet and quintet interactions are studied in Stiassnie and Shemer (1984, 1987). Review on wave resonant interactions can be found in Hammack and Henderson (1993). Although a few attempts have been made

(Dyachenko et al., 1995; Mori and Yasuda, 2001; Kalmykov, 1998), the study on the role of high-order wave nonlinearity on the random wavefield evolution is very limited and the conclusion is far from complete.

The space and time scales of the nonlinear wave interactions involved in ocean wave evolutions are summarized in Table 1.1. In this thesis, we focus on the effect of the Benjamin-Feir type modulational instability on the wavefield evolution, therefore, the spatial-temporal scales with $\mathcal{L} = O(\lambda\ \varepsilon^{-2})$ and $\mathcal{T} = O(T\ \varepsilon^{-2})$ are considered.

1.2.3 Wind input

Although the understanding on the generation mechanism of ocean waves has not be conclusive, it is generally accepted that wind forcing is the dominant generation mechanism for surface waves. When wind blows the ocean surface, it generates small ripples and the small ripples grow to larger waves as the wind continues blowing. As the larger waves evolve, waves with even longer wave length are generated as result of nonlinear wave interactions. Two fundamental papers, Phillips (1957) and Miles (1957), contribute greatly to the understanding of wave generation and evolution due to wind and they still provide the basic formulation in today's wave forecasting models. The energy input from wind forcing may be estimated using the empirical fetch and duration law described in Donelan et al. (1985):

$$E = 8.4 \times 10^{-7} X^{0.76}; \tag{1.1a}$$

$$E = 7 \times 10^{-9} \tau^{1.13}; \tag{1.1b}$$

where E is the non-dimensional variance, X and τ are the non-dimensional fetch and duration defined as

$$E = \frac{g^2\sigma^2}{U_{10}^4}; \quad X = \frac{gx}{U_{10}^2}; \quad \tau = \frac{gt}{U_{10}}. \tag{1.2}$$

Here σ is the standard deviation of the surface elevation. U_{10} is the wind speed at height 10 m and $U_{10}/c_p = 50\tau^{-0.34}$, where c_p is the phase velocity of the peak wave.

Space and time scales	Nonlinear wavefield evolution
$\mathcal{L} = O(\lambda_p\, \varepsilon^{-2})$ $\mathcal{T} = O(T_p\, \varepsilon^{-2})$	• Wavefields change significantly due to quartet resonance interactions including Benjamin-Feir instabilities. • The energy distribution over different wave modes changes due to quartet resonance interactions for wavefields with a narrow range in frequencies and directions. • There is no significant change in the energy distribution over different wave modes for wavefields with a broad range in frequencies and directions.
$\mathcal{L} = O(\lambda_p\, \varepsilon^{-3})$ $\mathcal{T} = O(T_p\, \varepsilon^{-3})$	• Wavefield changes significantly due to quintet resonance interactions. • There is no significant change in the energy distribution over different wave modes for wavefields with a broad range in frequencies and directions.
$\mathcal{L} = O(\lambda_p\, \varepsilon^{-4})$ $\mathcal{T} = O(T_p\, \varepsilon^{-4})$	• The energy distribution over different wave modes changes due to quartet resonance interactions for wavefields with a broad range in frequencies and directions.
$\mathcal{L} = O(\lambda_p\, \varepsilon^{-6})$ $\mathcal{T} = O(T_p\, \varepsilon^{-6})$	• The energy distribution over different wave modes changes due to quintet resonance interaction for wavefields with a broad range in frequencies and directions.

Table 1.1: Space and time scales of nonlinear wave interactions involved in the nonlinear wavefield evolution. λ_p and T_p are wave length and period of the peak wave in the wavefield and ε is the wavefield steepness.

Figure 1-4 shows the growth of significant wave height H_s, calculated as four times of the standard deviation of the surface elevation, as a function of time for wind speed U_{10}=10 m/s blowing over a sea with H_s=4 m and T_p=8 sec, where T_p is the peak period. After one hour, the increase of significant wave height is $\Delta H_s \approx 0.1$ m. For the time scale we considered in this thesis $\mathcal{T} = O(T_p \varepsilon^{-2})$, it reasonable to assume wind input is negligible for size of the problem. At greater scales, effects from wind (at even moderate speeds) could also play appreciable roles (Abdalla and Cavaleri, 2002; Lavrenov, 1998; Dysthe et al., 2003; Kharif et al., 2007).

Based on the field measurements done by Snyder and Cox (1966) and Barnett and Wilkerson (1967), the measured growth rate of the waves are one order of magnitude greater than the theoretical predictions by Miles (1957). The overestimation on the growth rate from field observations could be due to the effect of nonlinear transfer (Mitsuyasu, 2002). To clarify this discussion, accurate measurements using advanced measuring techniques are, therefore, strongly needed to provide insights to the understanding of wind input.

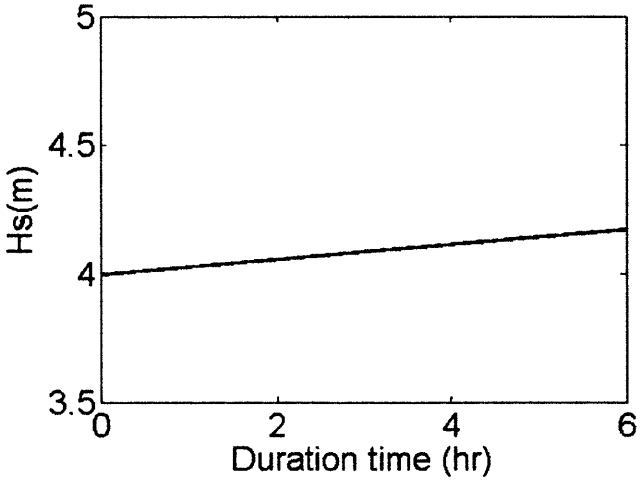

Figure 1-4: Growth of significant wave height as a function of duration time.

1.2.4 Viscous dissipation and wave breaking

Two sources can cause the dissipation of waves in the open sea. One is due to viscous damping over long time and distance and the other is breaking of waves as they

become locally steep.

The decay time scale due to viscosity for an infinitesimal wave with wavenumber k is $\mathcal{T}_v$=$O(1/2\nu k^2)$ (Kinsman, 1965), where ν is kinematic viscosity of the water and typically $\nu = 10^{-6}\,\mathrm{m}^2/\mathrm{s}$. For ocean waves, the typical wave length ranges from 1 m to 200 m and the corresponding decay time scales are ranging from a few hours to a few years. Based on this scaling argument, it is reasonable to assume the viscous decay is important only for very short capillary waves; for non-capillary ocean waves, the effect of viscous decay is insignificant.

Besides attenuating wave amplitude, viscosity could have two effects on (resonance) wave-wave interactions (Hammack and Henderson, 1993): it detunes resonances and it imposes a minimum steepness in order for the growth of inviscid instabilities to occur. It is found recently by Segur et al. (2005) that a modulated Stokes wave train can be stabilized with presence of viscosity and the growth of modulational perturbations that are initially small enough can be stopped by viscous damping before the nonlinearity becomes important. The effective time scale is about 0.01 per wave length based on the wave tank experiments (Benjamin and Feir, 1967; Segur et al., 2005). The possible influence of viscosity on the modulational instability of random waves are investigated in Segur et al. (2008); Kharif et al. (2010). In particular, Segur et al. (2008) speculated that an inclusion of viscosity may affect the early development of large waves. When wind input is not present, for the modulational instability to grow, the nonlinear growth rate has to be greater than the viscous decay rate. In real ocean, the dissipation due to viscosity is very weak compared to the nonlinear interactions Kharif and Pelinovsky (2003), therefore, the dissipation due to viscosity may not play a role for the time scale we consider.

Energy dissipation due to wave breaking is a non-ignorable process in the ocean wave dynamics. To obtain accurate information on the wavefield evolution, it is very important to account for energy loss associated with wave breaking. However, our understanding on wave breaking dynamics is very limited and the knowledge has been focused on breaking of single deterministic wave (group). The deep water breaking waves have been studied in the laboratory for one single breaking wave (Duncan,

1981) and a dispersive wave packet (Rapp and Melville, 1990). For different types of spilling or plunging breaking waves in the laboratory and field, it is observed that the energy dissipation is generally confined in the high frequency or wavenumber range of the wave spectrum (Gemmrich and Farmer, 1999; Rapp and Melville, 1990). In existing wave models, wave breaking is modelled by several different approximate theories of the energy dissipation via breaking (Komen et al., 1994).

1.2.5 Coexistence of wind sea and swell

In many situations the ocean waves are combinations of wind sea and swell and they are generally referred as bimodal seas. *Wind sea* is generated by local wind and it has a relatively broader range of frequencies and directions. *Swell* it is generated from a storm far distance away and has relatively narrow and low frequency range and long crested. Based on the data collected from the open North Sea, it is reported that the percentage of spectra with bimodal structure is about $20 \sim 25\%$ (Guedes Soares, 1991). Comparing to single component wind wave system, the bimodal seas receive much less attention. It is found that the dynamic processes of the ocean waves in the near surface region could be affected due to the presence of swell (Mitsuyasu and Yoshida, 1991; Dobson et al., 1994; Donelan et al., 1997). Moreover, the nonlinear wave interactions in bimodal sea system are more complex than the single wave system. Energy can be transferred from wind-sea to swell due to resonance interactions (Masson, 1993). Onorato et al. (2006) find for directional bimodal seas with close periods, a second system with small oblique angle can result in an increase of the instability growth rates and enlargement of the instability region. The enhanced instability region could lead to greater occurrence probability of large waves.

1.3 Wave measurements

Ocean wave theories are developed with guidance of measurements. The field and laboratory measurements contribute significantly to the discovery of new phenomena, verification of theoretical predications, and clarification of dynamic processes involved

in wind waves (Mitsuyasu, 2002). One example is the recognition of the role of nonlinear wave interactions. The important role of nonlinear wave interactions in the wave evolution was ignored in the 1960s. The connection between energy transfer among nonlinear waves and wavefield evolution was established after the extensive field experiments by Mitsuyasu (1968, 1969); Hasselmann et al. (1973). Another example is the quantification of the wind input. The wind input to waves were carefully measured by pressure fluctuations on the moving wave surface by Snyder et al. (1981) and this measurement have shed light on the understanding of wind input and motivated people to reconsider Phillips' theory in 1970s (Mitsuyasu, 2002).

Recent advanced remote sensing technology provide an enormous amount of data on wind and waves over a global scale. These measurements can also be used in advanced numerical wave prediction models (see, for example Chapter 9). However, the capability of using satellite to measure waves globally is still debatable. Because the synthetic aperture radar (SAR) imaging mechanism is in general strongly nonlinear, the SAR image of the ocean waves is highly distorted which bears little resemblance with the actual ocean waves (Janssen and Alpers, 2006). Further validation and study on the fundamental imaging mechanism is required.

1.4 Rogue waves

This section is devoted to a short introduction to an interesting ocean wave phenomenon, called *rogue wave*, which is addressed considerably in the remaining thesis.

1.4.1 Observations

Rogue waves, also called freak waves, killer waves, or sea monsters, are extremely large water waves that suddenly appear on the ocean surface. Some of these giant waves are reported to be more than 90 feet high, a size comparable to a 10-floor building. Rogue waves are very catastrophic and they crash large oil tankers into pieces within seconds. Ship accident reports show that more than 520 people were killed and 22 super carriers were lost because of freak waves between 1969 and 1994 (Kharif and

Pelinovsky, 2003).

Based on linear ocean wave theory, the probability of rogue waves is so small that their occurrence is regarded to be impossible. Only until decades ago, people started realizing that rogue waves could occur much more often than they thought when solid evidence became available. On January 1, 1995, a wave of more than 20 m was recorded at the Draupner Platform in the North Sea, and this extreme wave is named as "New Year's wave" due to the date of its occurrence. Another famous case of rogue waves, encountered by the oil tanker Esso Languedoc, occurred in 1980 off the east coast of South Africa. "*We were struck by a monstrous wall of water that rose out of nowhere and slammed onto the deck like the gist of God*" Philippe Lijour, first mate of Esso Languedoc recalled (Lawton, 2001). He and his shipmates were the lucky ones to survive. The wave they encountered has an estimation height of 30 meters or more. The Bay of Biscay near the 100-fathom curve in France is a notorious place for rogue waves. Figure 1-5 is a picture of rogue wave taken in that area and it looks like a "*wall of water*".

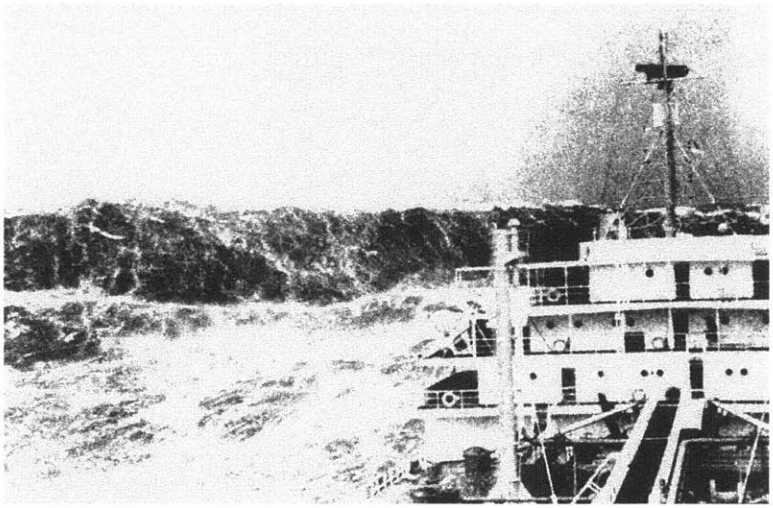

Figure 1-5: Rogue wave in the Bay of Biscay, France, in 1940. Picture from National Oceanic and Atmospheric Administration (NOAA).

Rogue waves are sometimes confused with Tsunami, but rogue waves are not tsunami. Tsunami is formed due to the movement of the sea floor. It propagates thousands of miles across the ocean and becomes noticeable and hazardous only

when it arrives to the shore. Rogue waves can appear suddenly in the open sea, often having a tremendous high crest, and live only for a short period, typically as short as a few minutes.

1.4.2 Dynamic mechanisms of rogue waves

There are several mechanisms that could be responsible for the formation of rogue waves. The mechanisms that, to the leading order, do not involve nonlinear wave-wave interactions, commonly referred as *linear mechanisms*, include (Kharif and Pelinovsky, 2003):

1. *Focusing due to wave dispersion*

   Large waves can form when a large number of waves are superposed at one location with proper phases and directions due to wave dispersion. For unidirectional wavefields, this can happen when long waves overtake short waves.

2. *Wave-current interactions*

   The formation of freak waves in the area where the current is strong, such as Gulf stream and Agulhas current, could be due to the "blocking" effect of the current (Lavrenov, 1998). When waves propagate into a current with different directions, the waves are stopped by the current at the locations where the wave group velocity in the inertial frame is zero. This causes a localized energy accumulation at such locations leading to formation of large waves in that area.

3. *Geometrical focusing due to bathymetry*

   When waves propagate into varying bathymetry, they are refracted due to the change of bottom topography, leading to the focusing of wave energy in particular places. This might be responsible for the formation of large waves in the areas along irregular coastlines.

The linear mechanisms might be responsible for occurrences of rogue waves in certain locations, however, they can not explain a large number of freak wave events reported from the open sea where the current and bathymetry play a minimal role.

Nonlinear mechanism (modulational instability) is expected to be the most promising one responsible for the rogue waves generation in the open sea. As we mentioned

in §1.2.2 the type of Benjamin-Feir modulational instability also obtains in irregular wavefields under certain conditions (Alber, 1978). The occurrence probability of rogue waves could be enhanced in wavefields suffering the modulational instability. The relevance of modulational instability to rogue wave formation are supported by wave tank experiments and numerical simulations of unidirectional wavefields (Onorato et al., 2001, 2005). Recent reviews of the rogue wave problem may be found in Kharif and Pelinovsky (2003); Kharif et al. (2009); Dysthe et al. (2008); Slunyaev et al. (2011). The rogue wave occurrence in directional wavefields is one big subject of present thesis and is discussed in great detail in Chapter 5, 6, and 7. for rogue wave occurrence in deep water, finite water depth, and bimodal seas. The typical rogue wave shapes are studied in Chapter 8.

1.5 Numerical ocean wave forecasting models

The accurate prediction of ocean surface wavefield evolutions is a very challenging task. First, it requires the good knowledge on *all* the complex dynamic processes described in §1.2. Second, advanced wave models, including accurate mathematical formulations/modelling of the involved physical processes, need to be developed. Third, reliable field measurements need to be taken to provide initial input and validations for the forecasting models. Fourth, depending the type of forecasting models and desired resolutions, modern high-performance computing technologies may be essential. In this section, we describe various types of wave forecasting models which are developed at different stages in the literature.

1.5.1 Spectral models for broad-band waves

The ocean wave forecasting starts with the development of spectral models Sverdrup and Munk (1947) . In the classic linear wave theory, the ocean wavefield can be assumed as a superposition of a large number of sinusoidal waves with different frequencies and directions of propagation. Concept of wave spectral density function, sometimes also called wave (energy) *spectrum*, is introduced to describe the mean

potential and kinematic energy of each wave mode (Pierson et al., 1955). The spectral wave forecasting models are then developed to describe the evolution of the wave spectrum. These models are sometimes referred as *phase-averaged* models because they only describe the evolution of the energy (spectrum) of each wave (wave energy is proportional to the square of wave amplitude) and the phase information of each wave is ignored.

The phase-averaged wave forecasting models are based on the spectral transport equation that states the energy balance in the dynamical system. The key physic processes described in §1.2 are expressed in source-sink terms for energy balance equation. The spectral prediction models based on the energy balance equation are classified as first generation, second-generation, and third-generation models. In the first generation models, each wave mode is modelled independently. The nonlinear energy transfer among different wave components is ignored. Energy dissipation due to wave breaking is modelled by putting a limit form of saturation spectrum. The field measurements provided useful information leading to new constructions of the forecasting model. In second generation model, the nonlinear interactions among waves are modelled using simplified parameterizations.

Great advances have been made in the development of the third generation models. In the third generation wave models, the source functions of the transport equation has the form:

$$S = S_{in} + S_{nl} + S_{ds}, \tag{1.3}$$

where S_{in}, S_{nl} and S_{ds} represent wind input, nonlinear wave-wave transfer, and energy dissipation by whitecapping. The terms in (1.3) are formulated based on the understanding of wave generation due to wind input by Phillips (1957) and Miles (1957), resonant four-wave nonlinear transfer by Hasselmann (1962), and energy dissipation due to whitecapping by Komen et al. (1984) and Hasselmann (1974). A number of field experiments contribute greatly to the wave spectral formulations including Hasselmann et al. (1973) and Mitsuyasu (1968, 1969). The typical third-generation models include WAM for deep water (Group, 1988), WAVEWATCH for regions with

varying bathymetry and current (Tolman, 1991), and SWAN for coastal regions (Booij et al., 1999; Ris et al., 1999). Due to their simplified formulations and parameterizations, the spectral models are very computational efficient and are suitable for global wave predictions and large-scale regional operations.

While much progress has been made using phase-averaged models for ocean wave forecasting over the past decades, the success has not been uniform, with predictions often falling outside the error band of the observations (Komen et al., 1994). In the frame work of phase-averaged models, it is difficult to make major advances due to their inherent assumptions and necessary simplifications. Equally important, the phase-averaged models do not deliver the detailed space-time information of the wave surface, which are critically important in the study of extreme wave dynamics as well as in practical operational guidance.

The nonlinear interaction term in the source of (1.3) is a parametrization of resonance four wave-wave interactions (Hasselmann, 1962) and quasi-resonance and non-resonance wave-wave interactions are not included. According to (1.3), the significant spectral change due to nonlinear interactions occurs over a long time scale associated with four-wave interactions; therefore, the spectral change over relatively short time due to quasi-resonant trio wave interactions including the modulational (Benjamin-Feir type) instability is not captured in third-generation spectral models (Janssen, 2003). Consequently, rogue waves caused by modulational instability may not be predicted using third-generation spectral models.

1.5.2 Wave envelop models for narrow-banded waves

The phase-averaged spectral models do not describe the detailed spatial-temporal information of the surface elevation. To obtain a phase-resolved description of the wave evolution, one may simulate the full Euler equations describing the ocean surface in a large domain. This is generally very computationally expensive and considered impossible before the recent advances in high-performance computing technologies. For wavefields with narrow-band spectra, the wavefield elevation can be approximated as a dominant fast oscillating wave train with central frequency modulated by a slowly

varying wave envelope. For computational efficiency, many existing studies use model equations that describe the slowly evolutions of the wave envelope. The envelope models include the nonlinear Schrödinger (NLS) equation and its modifications forms such as the modified nonlinear Schrödinger equations and its various extended forms (Dysthe, 1979; Trulsen and Dysthe, 1996; Trulsen et al., 2000). Kharif et al. (2010) considered wind forcing and viscous dissipation within the framework of a forced and damped nonlinear Schrodinger equation. Mathematical formulations and numerical implementations of NLS-type models are described in Chapter 2.

Using NLS-type simulations for unidirectional wavefields, the relevance of modulational instability to the significant wave spectral change and enhanced occurrence of rogue waves is confirmed Onorato et al. (2001). For directional wavefields, Gramstad and Trulsen (2007) find that the importance of BF-type modulational instability is reduced with decreasing crest length which is confirmed by wave basin experiments (Waseda et al., 2009; Onorato et al., 2009). However, the applicability of NLS-type models in realistic ocean waves could be limited by their inherent assumptions and simplifications. First, the assumption of narrow-banded spectrum may not obtain in realistic wavefields, since it is known that even initially narrow-band spectrum may become broad-banded due to nonlinear evolution (Dysthe et al., 2003). Secondly, it is also debatable whether the assumption of slowly-varying modulation is applicable for rogue waves which are expected to be very steep. Thirdly, the inherent limited valid spatial-temporal scales in NLS-type models are not easily to be further extended.

1.5.3 Direct phase-resolved nonlinear simulations

With the development of modern computational capability and advanced numerical wave modeling algorithms, it is now possible to obtain phase-resolved prediction of the wavefields using direct simulation approach. To obtain a more reliable prediction of ocean wavefield evolution, we develop a direct deterministic wave simulation tool, called SNOW (**S**imulation of **N**onlinear **O**cean **W**avefields), which is based on a high-order spectrum method described in Dommermuth and Yue (1987) and West et al. (1987). SNOW is fundamentally different from the existing phase-averaged models.

It predicts the nonlinear wavefield evolution by direct simulation of the wave dynamics including nonlinear wave-wave, wave-current, and wave-bottom interactions, wind input, and wave-breaking dissipation. The physical processes are either directly accounted for or modeled in physical space-time domain. Since phase information and wave profile are inherent in the simulation, the model can be further calibrated and advanced with better understanding on key physical process. In addition, nonlinear spectral and statistical wave information obtained from SNOW simulations could provide valuable guidance to develop new models or to improve parameterizations in existing phase-averaged models. Unlike NLS-type models described in 1.5.2, SNOW does not have any restriction on the spectral bandwidth, thus it can be applied for studying the realistic ocean wave evolution. For practical applications, the detailed space-time information of the free surface from SNOW simulations can be used as the necessary wave environmental condition for the design of Navy advanced ships, as well as to improve the operational safety of Navy ships. The mathematical formulations, numerical implementations, and computational parallelization strategy of SNOW are the subjects of Chapter 2. A few attempts have also been made to obtain fully nonlinear simulations for the evolution of ocean waves, but the simulations generally are applied over limited dimensions (Zakharov et al., 2002; Chalikov, 2009; Slunyaev and Sergeeva, 2011; Bateman et al., 2001; Ruban, 2011).

In this thesis, SNOW simulations are applied over space-time scales responsible for modulational instability to study its relevance to the spectral change and formation of rogue waves. According to Table 1.1, the space and time scales are $\mathcal{L}/\lambda_p, \mathcal{T}/T_p = O(\varepsilon^{-2})$. These length and time scales are also roughly the spatial resolution and time step in a (phase-averaged) WAM regional model, which assumes a quasi-stationary and quasi-homogeneous state over such scales. In order to capture higher order nonlinear effects or the spatial-temporal spectrum evolution, simulations of wavefield in a much larger length and time scales are theoretically needed (see Table 1.1), but probably will not be attainable in the near future mainly due to the limitations in computational capabilities (Liu and Yue, 2009).

1.6 Problem statement, objective and scope

This thesis is devoted to the study of the evolution of ocean waves with primary focus on the occurrence of rogue waves using direct phase-resolved numerical simulations. In particular, we would like to understand (a) the essential generation mechanisms of rogue waves; (b) the exact occurrence probability of rogue waves; (c) the typical shapes of rogue waves for given sea state.

These are addressed through the following points of interest:

(1) Developing and applying a direct numerical simulation tool, SNOW, for the study of ocean wave evolutions and rogue wave occurrence;

(2) Elucidating the importance of modulational instability in the ocean wave evolution and its relevance to the rogue wave occurrence;

(3) Investigating the nonlinear wave-wave interactions as fundamental mechanisms for generation of rogue waves;

(4) Quantifying the occurrence probability of rogue waves for given sea state and identification of the key effective spectral parameter(s) for rogue wave prediction;

(5) Identifying the accuracy, reliability, and validity range of existing linear theories and simplified wave models in predicting ocean waves and rogue wave occurrence;

(6) Investigating the effects of environmental factors, including wave directionality, finite water depth, and bimodal seas, on ocean wave evolutions;

(7) Characterizing the kinematic and geometric features of rogue waves for given sea state;

(8) Developing a capability for deterministically reconstructing and forecasting the wavefields over intermediate space-time scales by assimilating high-resolution wave measurements.

To achieve these, we perform a significant number of large-scale nonlinear three-dimensional SNOW simulations covering broad range of spectral parameters. The spatial and temporal scales of the simulations are commensurate with those of quartet

wave-wave interactions, including BF-type instabilities, that is, $\mathcal{L}/\lambda_p, \mathcal{T}/T_p \sim O(\varepsilon^{-2})$. To account for natural dissipation due to wave breaking, we implement a robust phenomenological-based model in SNOW which obtains satisfactory wave breaking dissipation for 2D and 3D breaking waves compared to laboratory measurements. For the spatial-temporal scales considered in this study, the growth of waves due to wind input is practically insignificant (Dysthe et al., 2003; Janssen, 2003). We thus ignore the wind effect. In this study, we consider deep water as well as finite water depth, single wind sea as well as bimodal seas. For comparison, we also implement NLS-type models and compare SNOW and NLS-type-model predictions over the large-scale space-time domains we consider.

1.7 Thesis contributions

This thesis is a first attempt to use large-scale direct phase-resolved nonlinear simulations to study the ocean wave evolutions and understand the essential generation mechanisms of rogue waves for a broad range of sea states

The major contributions of this thesis are summarized below:

- Development and application of direct large-scale nonlinear wavefield simulations to study ocean wave evolution and rogue wave occurrence
- Identification of the validity range of existing theories and simplified models (NLS-type) in predicting rogue waves
- Understanding of nonlinear rogue wave generation mechanisms
- Understanding of the effects of environmental conditions including wave directionality, finite water depth and bimodal seas on the wave evolution
- Quantification of rogue wave occurrence probability and nonlinear wave statistics as functions of wave spectral parameters
- Prediction of rogue wave occurrence probability and kinematics

- Identification of canonical rogue wave profiles as functions of wave spectral parameters

1.8 Thesis content

The remainder of this thesis is organized as follows.

In Chapter 2, the mathematical formulations and numerical implementations of two types of numerical wave predicting models, NLS-type models and direct phase-resolved simulations (SNOW), are described.

Chapter 3 presents the wave spectral evolution over modulational-instability time scale obtained from NLS-type models and SNOWsimulations. The spectral characteristics including omnidirectional spectrum, high-frequency spectral tail, and directional spectral spreading obtained from the two kinds of models are also discussed.

Chapter 4 gives the evolution of nonlinear wave statistics and their dependence on initial spectral parameters, including skewness, kurtosis, and exceeding probability, obtained from simulations based on NLS-type models and SNOW.

In Chapter 5, we study the generation mechanisms and occurrence probabilities of rogue waves in deep water using SNOW simulations. We provide the occurrence probability of rogue waves as a function of the initial spectral parameters.

Chapter 6 and Chapter 7 discuss two environmental factors, finite water depth and bimodal seas, that could affect the wave evolutions. The spectral evolutions, nonlinear wave statistics, and rogue wave occurrences in finite water depth and in bimodal seas are discussed.

Chapter 8 presents the geometric characteristics of rogue waves by analyzing the rogue waves identified from SNOW simulated wavefields.

Chapter 9 describes one practical application, in which a capability of phase-resolved reconstructing and forecasting of nonlinear wavefields using high-resolution wave measurement is developed. Based on the reconstructed and forecasted wavefield, the nonlinear wave statistics and occurrence probability of rogue waves are investigated.

Finally, in Chapter 10 we summarize the conclusions of this thesis and discuss several worthy possibilities for extending current work in the future.

1.9 Summary

In this chapter, we give a brief review on the ocean wave theory and key dynamical processes involved in the ocean wave evolution, including nonlinear wave-wave interactions, wind input, energy dissipation due to viscosity and wave breaking. The relevant spatial-temporal scales related to these processes are discussed. In this thesis we study the generation mechanisms and occurrence probability of extreme wave events, rogue waves. Reviews on rogue wave observations and possible generation mechanisms are given. Different types of numerical wave forecasting models developed at different stages, including spectral models, wave envelope models, and direct large-scale phase-resolved simulations (SNOW) are reviewed and their validity and limitations in the study of ocean waves are discussed. In the end, the objectives, problem statement, and outline of this thesis are described.

Chapter 2

Simulations of nonlinear three-dimensional wavefield evolution

2.1 Introduction

we develop and apply a phase-resolved numerical simulation tool, named as SNOW (**S**imulation of **N**onlinear **O**cean **W**avefields) to study the ocean wave evolution and occurrence of rogue waves. In particular, the spectral evolution, nonlinear wave statistics, and occurrence of rogue waves are calculated from SNOW simulated large-scale nonlinear directional wavefields. SNOW directly solves the primitive Euler equation based on a high-order spectral method developed in Dommermuth and Yue (1987) and West et al. (1987). In this chapter, we describe the mathematical formulations and numerical implementations of SNOW. To capture the energy dissipation due to wave breaking, a phenomenological-based filter is implemented in SNOW. To assess the validity of the existing results obtained from simplified Nonlinear shrödinger (NLS) type equations, in this thesis we compare and contract the results obtained from NLS-type models and SNOW simulations. In this chapter, the NLS-type models derived in Dysthe (1979) and Trulsen and Dysthe (1996) and their computational

implementations are also described.

2.2 Direct Simulation of Nonlinear Ocean Wavefields (SNOW)

2.2.1 High-order spectrum method

The fluid is assumed to be homogeneous, incompressible, inviscid, and the surface wave motion is irrotational. We perform phase-resolved simulations of large-scale nonlinear wavefields based on a high-order spectrum method (HOS) (Dommermuth and Yue, 1987; West et al., 1987). The formulation is briefly described here. HOS directly solves the field equation:

$$\nabla_{\mathbf{x}}^2\Phi + \Phi_{zz} = 0, \quad \text{for } z \leq \eta(\mathbf{x},t); \tag{2.1}$$

with the kinematic and dynamic boundary conditions on the free surface in the Zakharov form:

$$\eta_t - \Phi_z = -\nabla_{\mathbf{x}}\eta\cdot\nabla_{\mathbf{x}}\Phi^S + (\nabla_{\mathbf{x}}\eta\cdot\nabla_{\mathbf{x}}\eta)\Phi_z\,, \quad \text{at} \quad z=\eta(\mathbf{x},t); \tag{2.2a}$$

$$\Phi_t^S + g\eta = -\frac{1}{2}(\nabla_{\mathbf{x}}\Phi^S\cdot\nabla_{\mathbf{x}}\Phi^S) - \frac{1}{2}(1+\nabla_{\mathbf{x}}\eta\cdot\nabla_{\mathbf{x}}\eta)\Phi_z^2\,, \quad \text{at} \quad z=\eta(\mathbf{x},t); \tag{2.2b}$$

where $\mathbf{x}=(x,y)$ and z are the horizontal and vertical coordinates; $\nabla_x = (\partial/\partial_x, \partial/\partial_y)$ is the horizontal gradient; $\Phi(\mathbf{x},z,t)$ is the velocity potential; and $\Phi^S(\mathbf{x},t)\equiv\Phi(\mathbf{x},z=\eta(\mathbf{x},t),t)$ is the value of the potential on the free surface $\eta(\mathbf{x},t)$.

The velocity potential $\Phi(\mathbf{x},z,t)$ is written in a perturbation series up to a given order M in wave steepness, denoted by ε, assuming that Φ and η are $O(\varepsilon)$:

$$\Phi(\mathbf{x},z,t) = \sum_{m=1}^{M}\phi^{(m)}(\mathbf{x},z,t), \tag{2.3}$$

where $\phi^{(m)}=O(\varepsilon^m)$. The surface potential is evaluated using the Taylor expansion

around z=0:

$$\Phi^s(\mathbf{x},t) = \Phi(\mathbf{x},\eta,t) = \sum_{m=1}^{M}\sum_{k=0}^{M-m}\frac{\eta^k}{k!}\frac{\partial^k}{\partial z^k}\phi^{(m)}(\mathbf{x},z,t)\big|_{z=0}. \tag{2.4}$$

By comparing the terms with same order in (2.4) we obtain the sequence of boundary values for $\phi^{(m)}$, m=1$\cdots$M, at z=0. $\phi^{(m)}$ can be obtained from the *boundary-value problem*:

$$\nabla^2\phi^{(m)}(\mathbf{x},z,t) = 0, \tag{2.5a}$$

$$\phi^{(m)}(\mathbf{x},0,t) = f^{(m)}, \qquad m = 1,2,\cdots,M, \tag{2.5b}$$

$$\nabla\phi^{(m)} \to 0, \qquad \text{as } z \to -\infty,\ m = 1,2,\cdots,M, \tag{2.5c}$$

where

$$\begin{cases} f^{(1)} = \Phi^S \\ f^{(m)} = -\sum_{l=1}^{m-1}\frac{\eta^l}{l!}\frac{\partial\phi^{(m-l)}}{\partial z^l}|_{z=0} \end{cases}, \quad m = 2,3,\cdots,M. \tag{2.6}$$

The boundary-value problem (2.5) is solved with mode-coupling approach by representing $\phi^{(m)}$ as truncated eigenfunction expansion of free modes

$$\phi^{(m)}(\mathbf{x},z,t) = \sum_{n=1}^{N}\phi_n^{(m)}\Psi_n(\mathbf{x},z), \quad z \leqslant 0, \tag{2.7}$$

where the free modes Ψ_n satisfy all but the free-surface condition (2.6). After $\phi_n^{(m)}(t)$ is obtained, the vertical velocity at free surface is

$$\Phi_z(\mathbf{x},\eta,t) = \sum_{m=1}^{M}\sum_{k=0}^{M-m}\frac{\eta^k}{k!}\sum_{n=1}^{N}\phi_n^{(m)}\frac{\partial^{k+1}}{\partial z^{k+1}}\Psi_n(\mathbf{x},z)\Big|_{z=0}. \tag{2.8}$$

The final evolution equations for η and Φ^S are

$$\eta_t + \nabla_{\mathbf{x}}\Phi^S \cdot \nabla_{\mathbf{x}}\eta - (1 + \nabla_{\mathbf{x}}\eta \cdot \nabla_{\mathbf{x}}\eta)[\sum_{m=1}^{M}\sum_{k=0}^{M-m}\frac{\eta^k}{k!}\sum_{n=1}^{N}\Phi_n^{(m)}(t)\frac{\partial^{k+1}}{\partial z^{k+1}}\Psi_n(x,0)] = 0, \tag{2.9a}$$

$$\Phi_t^S + \eta + \frac{1}{2}\nabla_{\mathbf{x}}\Phi^S \cdot \nabla_{\mathbf{x}}\Phi^s - \frac{1}{2}(1 + \Delta_{\vec{x}}\eta \cdot \Delta_{\vec{x}}\eta) \times \left[\sum_{m=1}^{M}\sum_{k=0}^{M-m}\frac{\eta^k}{k!}\sum_{n=1}^{N}\phi_n^{(m)}(t)\frac{\partial^{k+1}}{\partial z^{k+1}}\Psi_n(x,z)\Big|_{z=0}\right]^2 = -P_a. \tag{2.9b}$$

For rectangular domain $-L_x/2 \leqslant x \leqslant L_x/2$ and $-L_y/2 \leqslant y \leqslant L_y/2$ with double period boundary conditions, the free modes $\Psi_n(\mathbf{x}, z)$ have simple forms in deep water:

$$\Psi_n(\mathbf{x}, z) = \exp(i\mathbf{k}_n \cdot \mathbf{x} + k_n z) \tag{2.10}$$

and in constant finite water depth:

$$\Psi_n(\mathbf{x}, z) = \frac{\cosh[k_n(z+h)]}{\cosh k_n h}\exp(i\mathbf{k}_n \cdot \mathbf{x}) \tag{2.11}$$

where $\mathbf{k}_n$=(k_{xn}, k_{yn})=$(2\pi m_1/L_x, 2\pi m_2/L_y)$, m_1=0, $\pm$1, $\cdots$, $\pm(N_x - 1)$, m_2=0, $\pm$1, $\cdots$, $\pm(N_y - 1)$; N_x, N_y are the maximum Fourier modes in x and y directions; and $k_n = |\mathbf{k}_n|$ and h is the constant water depth.

In HOS simulations, nonlinear interactions among a large number of wave components, N=$N_x \times N_y$, are accounted for up to arbitrary order M in wave steepness. The computational effort is approximately linear in N, M, with exponential convergence with M and N for waves up to ~80% of Stokes limiting steepness (Dommermuth and Yue, 1987). The validity and efficacy of this method has been demonstrated extensively for nonlinear wave-wave interactions (Dommermuth and Yue, 1987), and the method has been extended to include atmospheric forcing (Dommermuth and Yue, 1988), variable finite depth (Liu and Yue, 1998), and effects of energy dissipation (Wu

et al., 2006). For the spatial-temporal scales considered in this study, the growth of waves due to wind input is practically insignificant (see discussions in Dysthe et al. (2003); Janssen (2003) and also §10.2 in Chapter 10). We thus ignore the wind effect. To account for energy dissipation due to wave breaking, a robust phenomenological-based model is implemented in HOS (§2.2.2). Computational convergence tests of SNOW regarding the grid size N_x and N_y, order of nonlinearity M, and number of realizations for one given initial spectrum can be found in appendix A.

2.2.2 Modeling energy dissipation due to wave breaking

A phenomenological-based filter

For the large-scale long-time simulations we consider, it is important to account for energy loss associated with wave breaking dissipation in the evolution. The study on the detailed mechanism and dynamics of different types of (2D and 3D) breaking events is beyond the scope of present thesis. It is however possible to capture the effect of wave breaking dissipation on the overall wavefield evolution using relatively simple phenomenological models in HOS.

For different types of spilling or plunging breaking waves in the laboratory and field, it is observed that the energy dissipation is generally confined in the high frequency or wavenumber range of the wave spectrum (Gemmrich and Farmer, 1999; Rapp and Melville, 1990). Based on this, we propose an energy dissipation model in HOS, where a low-pass filter in the wavenumber space is applied at every time step on the free surface elevation and velocity potential. An example of such a filter is

$$\Lambda(\mathbf{k} \,|\, k_p, \beta_1, \beta_2) = \exp\Big\{ - |\frac{k}{\beta_1 k_p}|^{\beta_2} \Big\}, \tag{2.12}$$

where $k = |\mathbf{k}|$ with $\mathbf{k} = (k_x, k_y)$ and β_1, β_2 are filter parameters.

The model (2.12) is found to be robust for a variety of 2D and 3D wavefields in that the estimate of energy dissipation is found to be somewhat insensitive to the choice of parameter values β_1, β_2. This is confirmed by repeated simulations varying (the parameters of) (2.12). Figure 2-1 shows the energy dissipation using filter (2.12)

with a range of β_1 and β_2 values. The energy dissipation is measured as $\Delta E/E$, where E is the total potential energy, $\Delta E = E_2 - E_1$ with E_1, E_2 being the potential energy of the surface elevations before and after wave breaking.

We find there exists a range for β_1 and β_2 where the estimation is not sensitive to their values. The non-sensitive estimations are close to lab measurements on the energy dissipation (indicated by color horizontal lines in the figure). For large-scale simulations considered in this thesis, varying β_1=7$\sim$8 and β_2=20$\sim$35, the total energy variation is within 2% at evolution time t=150T_p.

Two-dimensional breaking dispersive wave packets

The efficacy of this modeling is confirmed by direct comparisons with two-dimensional laboratory breaking waves (Rapp and Melville, 1990). Figure 2-2 shows the energy loss, defined as $\Delta E/E_0$, measured from laboratory breaking dispersive wave packets as a function of wave packet steepness (Rapp and Melville, 1990) compared with HOS predictions. An acceptable quantitative agreement is found over a broad range of steepnesses (and corresponding breaking types).

HOS model with the filter (2.12) provides not only a satisfactory estimation on the energy loss due to wave breaking, but also reasonable descriptions on the wave profile both before and after breaking. In the experiment, a plunging breaking wave was generated near $x = 0$ by focusing multiple wave components with different frequencies and designed phase combination. Figure 2-3 shows the evolution of surface elevation at different locations along the wave tank. Comparing to the experimental records, HOS simulations with the breaking model implemented capture the profiles of breaking waves reasonably well not only before and but also after the wave breaking. From both experiment and HOS simulations, we observe the wave envelope of the dispersive wave packet becomes narrower as approaching the linear theoretical focal point x=0. At location close to the focal point, a large breaking wave with significantly higher and narrower crest and flatter trough occurs. As the wave packet propagates away from the focal point, the wave profile de-focused quickly due to dispersion over a time scale $\sim O(5\lambda_c)$, leading to a longer wave packet.

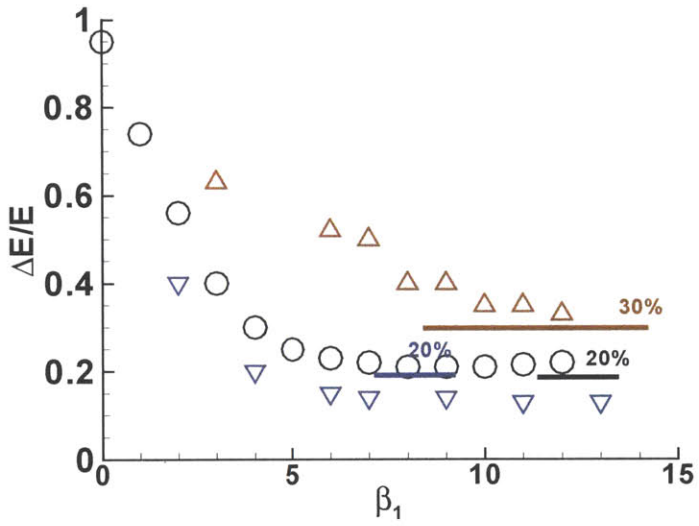

(a)

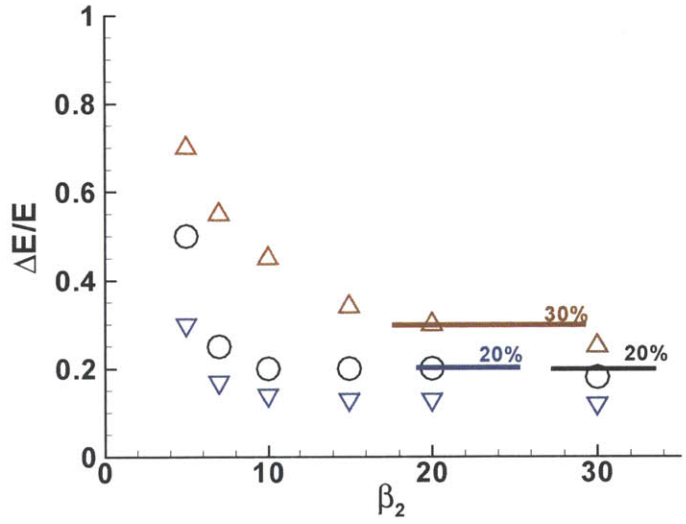

(b)

Figure 2-1: Dependence of energy dissipation on the parameter values of (a) β_1 (with β_2=30), (b) β_2 (with β_1=8) in breaking model (2.12). Initial setups used are identical to laboratory breaking waves: dispersive wave packet (Rapp and Melville, 1990) (△, 30%), square wave packet (Su, 1982a) (◯, 20%), bimodal stokes wave group (Banner and Peirson, 2007) (▽, 20%).

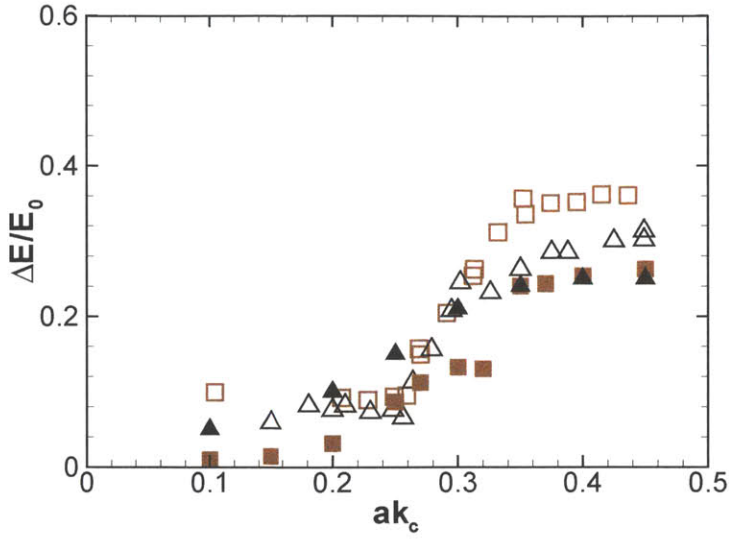

Figure 2-2: Loss of energy due to wave breaking as a function of steepness of the dispersive wave packet ak_c. Experiments (Rapp and Melville, 1990): $f_c = 0.88$ (□) and 1.08 (△); HOS: $f_c = 0.88$ (■) and 1.08 (▲). f_c and k_c are the central frequency and wavenumber of a dispersive wave packet. Results are obtained using HOS with (2.12) with β_1=8, β_2=30. HOS simulations: N=2048, M=5, N_T=40.

More interestingly, we find HOS simulations with breaking model also provides the information on the location of the energy dissipation. Figure 2-4 shows the $x-t$ plot of the location of energy dissipation for the plunging breaking wave shown in figure 2-3. The energy dissipation is measured as $\Delta P(x,t)/P$, where P is the total potential energy, $\Delta P(x,t) = \eta^2(x,t) - \eta_f^2(x,t)$, and $\eta(x,t)$, $\eta_f(x,t)$ are the surface elevations before and after the filter is applied. We observe that the energy dissipation associated with breaking waves is very localized. The energy is mainly lost at the steep peak of the wave packet. Note that locally $\Delta P(x,t)$ can be positive or negative, but the net energy dissipation is always positive.

Three-dimensional steep breaking crescent waves

For a 2D plane stokes wave with large steepness $\varepsilon = ak \geqslant 0.3$, transverse (three-dimensional) instability, having larger growth rate, becomes more important than two-dimensional instability (Benjamin-Feir instability) (McLean, 1982). The transverse instability leads to crescent waves in a *horseshoe* pattern (McLean, 1982; Su,

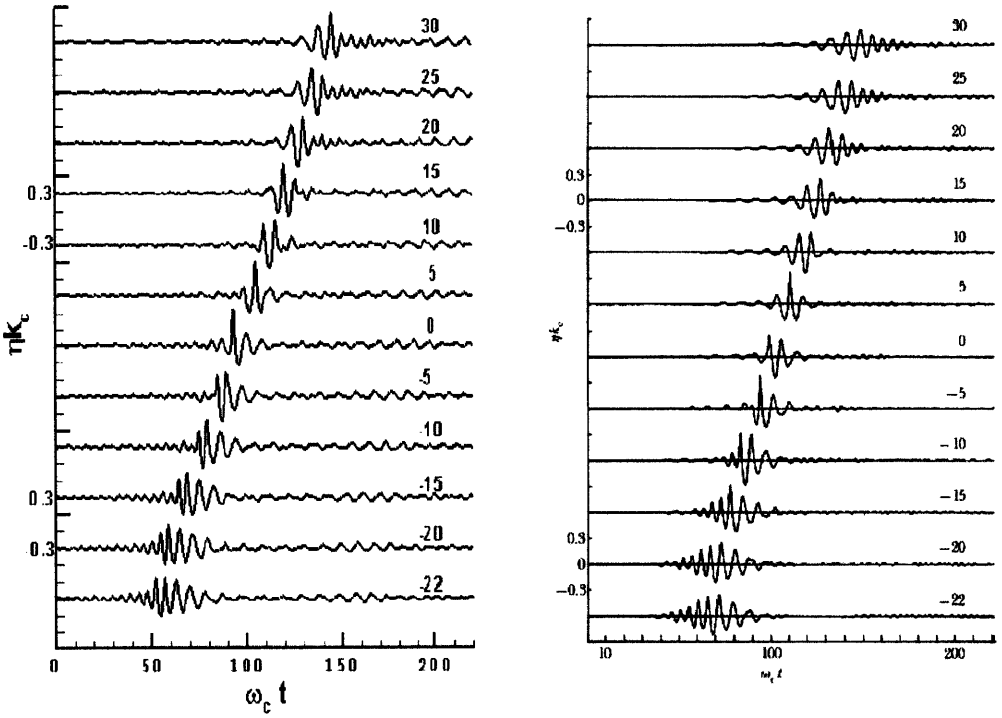

(a) (b)

Figure 2-3: Comparison of surface evolution of a dispersive packet between (a) experimental measurements and (b) HOS simulations. The center frequency f_c=0.88 Hz, steepness ka=0.352, bandwidth $\Delta f/f_c$=0.73. The numbers on the plots indicate the non-dimensional locations (normalized by center wave length λ_c) relative to the designed wave focusing point $x = 0$.

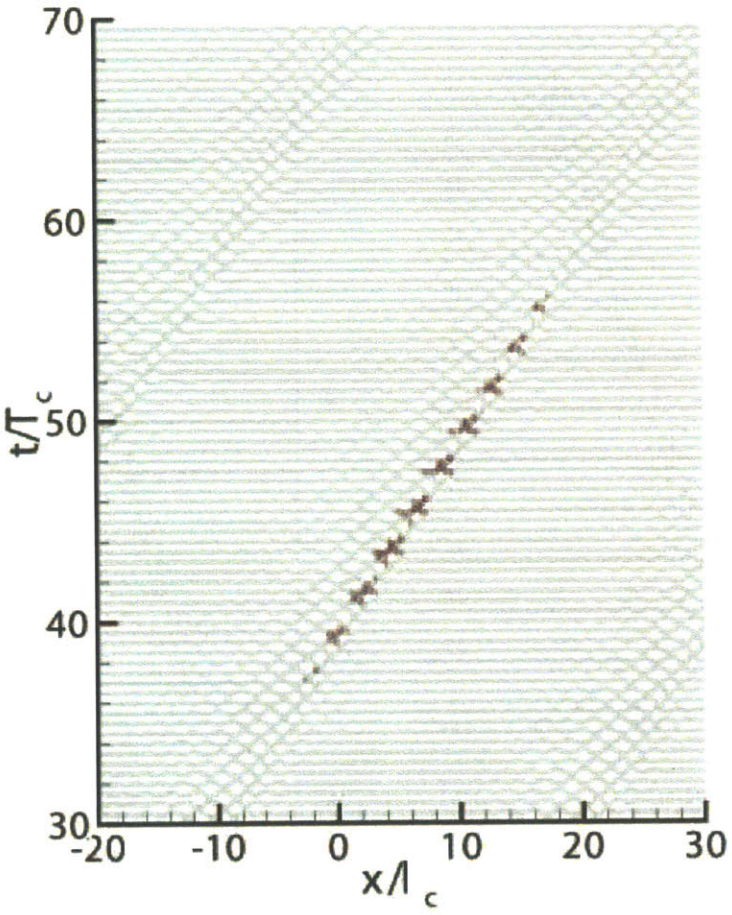

Figure 2-4: The location of energy dissipation for a dispersive wave packet. The center frequency f_c=0.88 Hz, steepness ka=0.352, bandwidth $\Delta f/f_c$=0.73. Contour of local energy dissipation scaled by the total $\Delta P/P \geqslant$0.04 (●); $\Delta P/P \leqslant$-0.04 (●)

1982b). For 2D plane stokes wave with steepness ak=0.33, the most unstable instability for the fundamental wavenumber k=1 occurs when the 3D disturbance wavenumber satisfies $(k_x, k_y) = (p+k, q) = (1.5, 1.23)$, where p and q are the longitudinal and transverse perturbation wavenumber. We use Stokes wave $[\varepsilon, k] = [0.33, 4]$, where ε and k are steepness and central wavenumber of the stokes wave, with three-dimensional perturbation in the form of Xue et al. (2001)

$$\eta' = \epsilon A \sin(k_x x + \beta)\cos(k_y y) \tag{2.13a}$$

$$\phi' = -\frac{\epsilon A}{(k_x^2 + k_y^2)^{1/4}} \cos(k_x x + \beta)\cos(k_y y)\exp[(k_x^2 + k_y^2)^{1/2}\eta] \tag{2.13b}$$

where $\epsilon = 0.16$, (k_x, k_y) are chosen as $(6, 4.92)$; A is the amplitude of the Stokes wave and η is the undisturbed Stokes wave. The phase of the Stokes waves is chosen to make the maximum elevation at $x = 0$ and $t = 0$,and we choose $\beta = 0$. The typical resolution we used is $M = 4$, $N = 256$ and $\Delta t = T/100$. The evolution of the steep Stokes plane wave is shown in figure 2-5. We see as the three-dimensional instability develops, the two-dimensional wave train of large steepness evolves into three-dimensional horseshoe pattern. The energy dissipation $\Delta P/P$ due to wave breaking is shown as the color contour. We find the energy loss occurs on the shoulders of the steep wave front. This is observed in Su (1982b), where static spilling breaking was observed on the crescent wave shoulders.

Figure 2-6 shows the comparison of the longitudinal profile between HOS simulations and a fully nonlinear simulation using mixed Euler-Lagrangian method (MEL) (Xue et al., 2001).The profile of MEL is obtained by digitalizing figure 16 in Xue et al. (2001). We observe HOS results agree with MEL results remarkably well. To be more quantitative, Table 2.1 shows comparisons of the geometric parameters of crescent waves (denoted in figure 2-6) in the quasi-steady breaking state from experiments (Su, 1982b), HOS and MEL simulations. We again see the HOS simulations agree with the experimental data and MEL simulations.

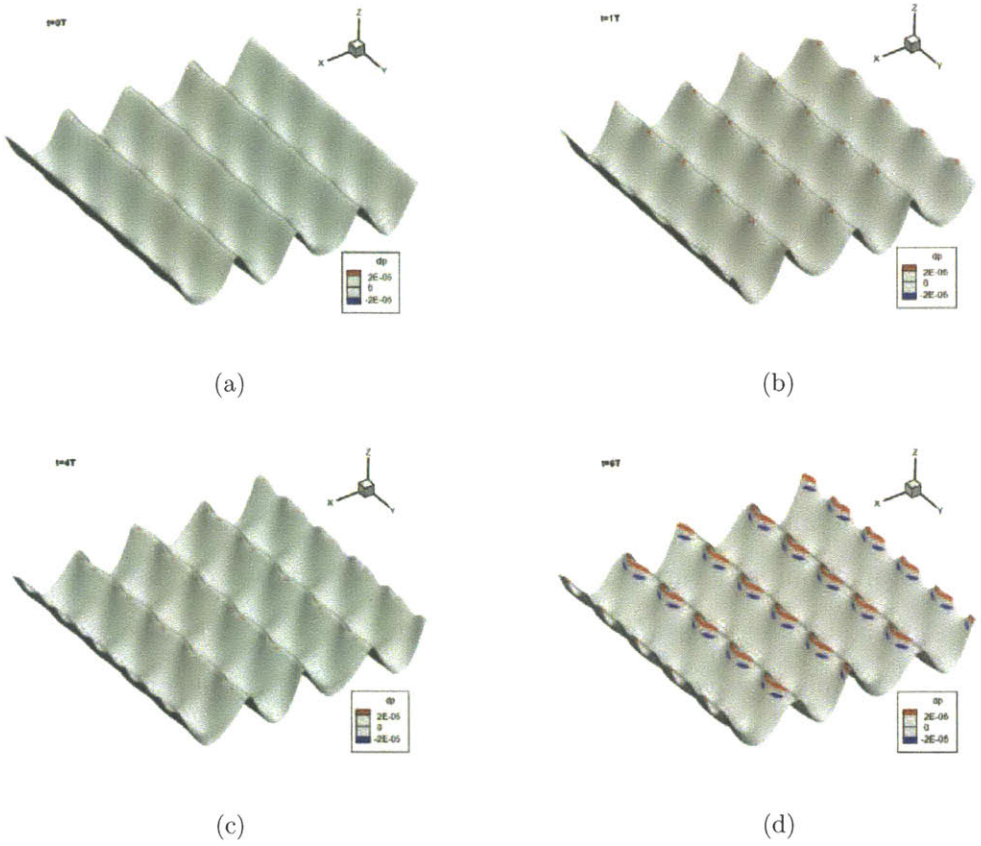

(a) (b)

(c) (d)

Figure 2-5: Evolution of a plane Stokes wave of steepness ε=0.33 with three-dimensional initial disturbance (2.13) ϵ=0.16, β=0 and $(k_x, k_y) = (1.5, 1.23)$. (a) t/T=0; (b) t/T=1; (c) t/T=4; (d) t/T=6. Color contour $\Delta P/P \geqslant 2\times10^{-5}$ (●), $\Delta P/P \leqslant$-2×10^{-5} (●).

	Su (1982)	HOS (t=4.5T)	HOS (t=6T)	MEL (t=4.338T)
λ_2/λ_1	1.28	1.02	1.06	1.07
h_{11}/h_{12}	1.10	1.08	1.12	1.09
h_{21}/h_{22}	0.88	0.86	0.76	0.88
h_{11}/h_{21}	1.66	1.52	1.63	1.64

Table 2.1: Comparisons among experimental data by Su (1982a), MEL (Xue et al., 2001) and HOS.

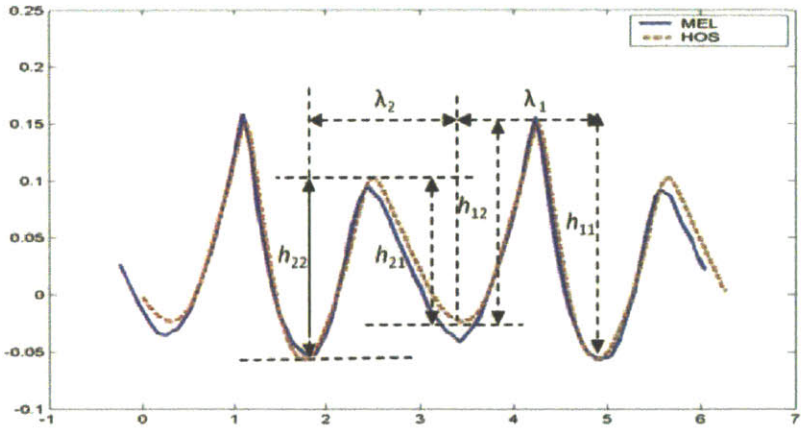

Figure 2-6: The Longitudinal profile of the crescent wave at $y = -L_y/4$. kA=0.33, ϵ=0.16, β=0 and $(k_x, k_y) = (1.5, 1.23)$. MEL (Xue et al., 2001) $t = 4.338T$ (—); HOS $t = 4.5T$ (- - -).

2.2.3 Computational performance on high performance computing platforms

For the present study involving very large scale (N=$O(10^{7-8})$) simulations, we develop a parallelized version of HOS optimized for modern massively-parallel high-performance computing (HPC) platforms, using Message Passing Interface (MPI) functions (Wu, 2004). This parallel version of HOS hereafter is referred as SNOW (**s**imulation of **n**onlinear **o**cean **w**avefields). Parallel implementation of SNOW is achieved by decomposing the spectral domain across processors using MPI. SNOW utilizes transposes and on processor fast Fourier transforms to move between the physical and spectral domains. Our experience with SNOW using up to $\mathcal{P}$=$O(10^3)$ processors indicates near linear scaling of HPC time with $\mathcal{P}^{-1}$ on Cray systems at the U.S. Army Engineer Research and Development Center (ERDC). Figure 2-7 shows the typical performance of SNOW as a function of processors and problem size on the Cray XT3, XT4, XT5 and XE6 platforms. The performance is measured as the number of time steps achieved in five wall-clock minutes. In general, the near linear scalability is achieved on all Cray systems tested.

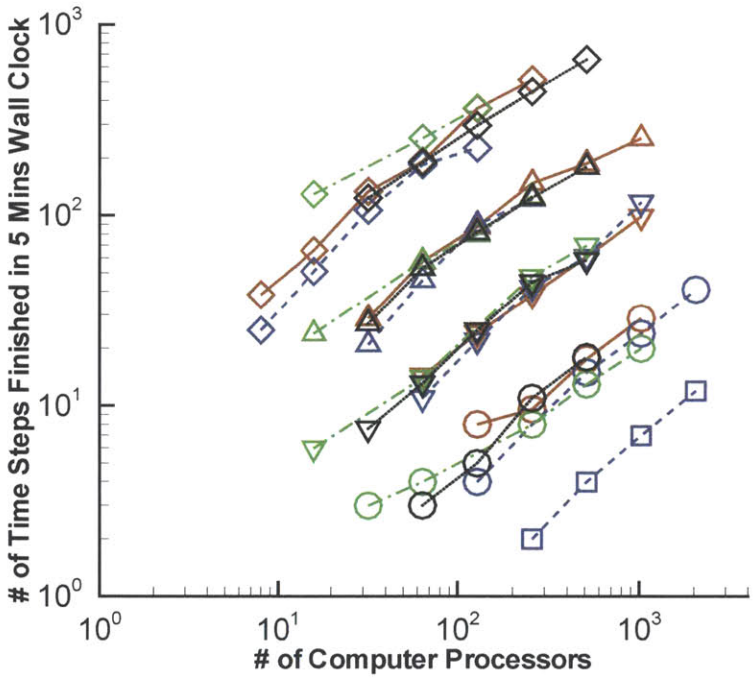

Figure 2-7: Scalability of typical SNOW simulations on Cray XT3 (blue), Cray XT4 (red), Cray XT5 (green) and Cray XE6 (black). Plotted is the number of time steps of computations completed within 5 minutes of wall clock time versus the number of processors used in the simulation for different problem scales $N_x \times N_y$. $N_x \times N_y$=1024×1024 (◊), 2048×2048 (△), 4096×4096 (▽), 8192×8192 (◯), 16384×16384 (□).

2.3 Nonlinear shrödinger (NLS) type equations

2.3.1 Mathematical formulations

We implement the modified nonlinear shröndinger equations (MNLS) derived in Dysthe (1979) and the broader bandwidth MNLS equations (BMNLS) described in (Trulsen and Dysthe, 1996) to assess the range of validity of NLS-type models in describing nonlinear wave statistics and rogue wave probability over the large-scale spatial domains $\mathcal{L}\times\mathcal{L}$ and evolution times $\mathcal{T}$, where $\mathcal{L}/\lambda_p$, $\mathcal{T}/T_p \sim O(\varepsilon^{-2})$ (λ_p, T_p are peak wavelength and period, ε is the steepness of the wavefield).

The MNLS and BMNLS models (to fourth order in wave steepness) describe the evolution of the wave envelope $B(\mathbf{x},t)$ which is slowly varying with space and time. The temporal version of BMNLS equations, after applying the length and time scaling $\omega t \to t$, $k(\mathbf{x},z) \to (\mathbf{x},z)$, are

$$\begin{aligned} B_t + \frac{1}{2}B_x \;+\; & \frac{i}{8}B_{xx} - \frac{i}{4}B_{yy} - \frac{1}{16}B_{xxx} + \frac{3}{8}B_{xyy} \\ & = -\frac{i}{2}|B|^2 B - \frac{3}{2}|B|^2 B_x - \frac{1}{4}B^2 B_x^* - iB\overline{\phi}_x \\ & + \frac{5i}{128}B_{xxxx} - \frac{15i}{32}B_{xxyy} + \frac{3i}{32}B_{yyyy} - \frac{7}{256}B_{xxxxx} \\ & + \frac{35}{64}B_{xxxyy} - \frac{21}{64}B_{xyyyy}, \quad z=0, \end{aligned} \tag{2.14}$$

where $\overline{\phi}$ is solved through the boundary value problem:

$$\begin{aligned} & \overline{\phi}_{xx} + \overline{\phi}_{yy} + \overline{\phi}_{zz} = 0 \quad -h < z < 0, \\ & \overline{\phi}_z = \frac{1}{2}(|B|_x^2), \quad z=0, \\ & \overline{\phi}_z = 0, \quad z=-h, \end{aligned} \tag{2.15}$$

The BMNLS model is an improved form of MNLS model (Dysthe, 1979) with the additional terms in the last two lines in (2.14) to relax the bandwidth limit of MNLS model from $O(\varepsilon)$ to $O(\varepsilon^{1/2})$, where ε is the wave steepness. After $B(\mathbf{x},t)$ is solved,

the surface elevation is reconstructed as

$$\eta(x,t) = \overline{\eta} + \frac{1}{2}(Be^{i\theta} + B_2 e^{2i\theta} + B_3 e^{3i\theta} + \cdots + c.c.), \tag{2.16}$$

where B_2, B_3, and $\overline{\eta}$, obtained from B, represent corrections of second and third harmonics and the mean surface elevation associated with the radiation stress. $\theta = \mathbf{k}_p \cdot \mathbf{x} - \omega_p t$ is the phase of the peak wave. In MNLS model B_2, B_3 and $\overline{\eta}$ are calculated as (Dysthe, 1979):

$$\begin{aligned} \overline{\eta} &= \frac{1}{2}\overline{\phi}_x, \\ B_2 &= \frac{1}{2}B^2 - \frac{i}{2}BB_x, \\ B_3 &= \frac{3}{8}B^3 \end{aligned} \tag{2.17}$$

and in BMNLS model, they are calculated as (Trulsen and Dysthe, 1996; Toffoli et al., 2010):

$$\begin{aligned} \overline{\eta} &= \frac{1}{2}\overline{\phi}_x - \frac{1}{16}(|B|^2)_{xx} - \frac{1}{8}(|B|^2)_{yy}, \\ B_2 &= \frac{1}{2}B^2 - \frac{i}{2}B_x + \frac{1}{2}BB_{yy} - \frac{3}{4}B_y^2, \\ B_3 &= \frac{3}{8}B^3 \end{aligned} \tag{2.18}$$

Wave breaking is generally not considered in NLS-type models (Dysthe et al., 2003; Socquet-Juglard et al., 2005), although the effect of dissipation can be included (see, e.g. Segur et al., 2005).

2.3.2 Split-step fourier method

The MNLS and BMNLS models are solved numerically using the split-step Fourier method described in Lo and Mei (1985), which is briefly repeated here. Both MNLS and BMNLS has the form

$$\frac{\partial B}{\partial t} = -(\mathcal{L} + \mathcal{N})B, \tag{2.19}$$

where $\mathcal{L}$ and $\mathcal{N}$ are linear and nonlinear operators of B, and for MNLS model

$$\begin{aligned}\mathcal{L}(B) &= \frac{1}{2}B_x + \frac{i}{8}B_{xx} - \frac{i}{4}B_{yy} - \frac{1}{16}B_{xxx} + \frac{3}{8}B_{xyy} \\ \mathcal{N}(B) &= \frac{i}{2}|B|^2B + \frac{3}{2}|B|^2B_x + \frac{1}{4}B^2B_x^* + iB\overline{\phi}_x\end{aligned} \tag{2.20}$$

The computations are performed in a double period domain:

$$B(0,y,t) = B(L_x,y,t) \quad \text{and} \quad B(x,0,t) = B(x,L_y,t). \tag{2.21}$$

The solution of (2.19) is approximated as

$$B_{(t+\Delta t)} \approx \exp\left[-(\mathcal{L}+\mathcal{N})\right] B_{(t)} = \exp\left[-\Delta t\mathcal{L}\right] \exp\left[-\Delta t\mathcal{N}\right] B_{(t)}. \tag{2.22}$$

The linear and nonlinear terms are separately treated at each time step. The nonlinear part is evolved in time by finite difference:

$$\begin{aligned}B_{t+1/2\Delta t} &= B_t + \Delta t\mathcal{N}(B_t)/2 \\ \hat{B}_{t+\Delta t} &= B_t - \Delta t\mathcal{N}(B_{t+1/2\Delta t}).\end{aligned} \tag{2.23}$$

The linear evolution is taken exactly in the wavenumber space. For MNLS model, it is

$$B_{t+\Delta t} = \mathcal{F}^{-1}\left\{\mathcal{F}(\hat{B}_{t+\Delta t}\exp\left[-i\left(k_x/2 - k_x^2/8 + k_y^2/4 + k_x^3/16 - 3k_xk_y^2/8\right)\Delta t\right])\right\}, \tag{2.24}$$

where $\mathcal{F}$ and $\mathcal{F}^{-1}$ are the Fourier and inverse Fourier Transform.

For all the NLS-type simulations, the energy is verified to conserve to within $\sim 0.5\%$. The solvers for NLS-type models have been systematically validated through convergence tests (see figure 2-8) and direct comparisons with various existing results in the literature (Lo and Mei, 1985; Dysthe et al., 2003; Socquet-Juglard et al., 2005; Toffoli et al., 2011) and the HOS simulations.

The applicability of NLS-type simulations in simulating evolution of nonlinear

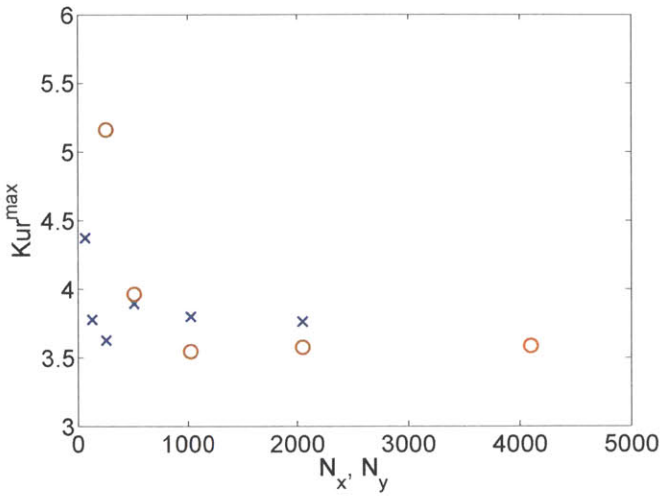

(a)

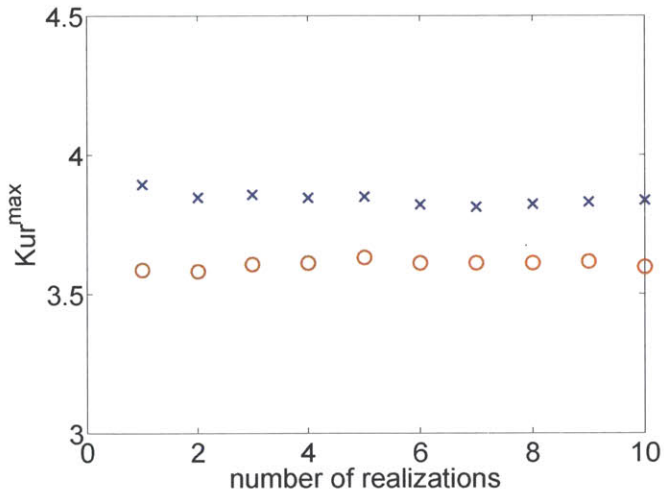

(b)

Figure 2-8: Convergence tests of maximum kurtosis by BMNLS (×) and SNOW (◯) as a function of (a) grid size and (b) number of realizations. The initial wavefield is specified by a JONSWAP wave spectrum with H_s=0.08 m, T_p=1 sec, γ=6, and Θ=12°. For the results in (b), N_x=N_y=512 and 4096 in BMNLS and HOS, respectively.

ocean wavefields is questionable due to the inherent assumptions of narrow-band spectrum and slowly-varying spatial and temporal modulations. One of the objectives of this thesis is to assess the range of validity of NLS-type models for predicting nonlinear wave statistics and rogue wave occurrence.

2.4 Summary

In this chapter, the mathematical formulations and numerical implementations of two types of numerical wave forecasting models, direct phase-resolved nonlinear simulations (SNOW) and NLS-type models are described. In particular, for modelling energy dissipation due to wave breaking, a phenomenological-based filter is developed and applied in SNOW. The reliability and accuracy of this filter is validated by directly comparing the numerical results with measurements from laboratory breaking waves. Moreover, the good computational performance of SNOW on high performance computing platforms is demonstrated. Unlike NLS-type models, SNOW does not have spectral bandwidth limitation and thus are more suitable for simulations of realistic directional ocean waves.

Chapter 3

Spectral evolution of nonlinear directional wavefields

3.1 Introduction

The prediction of ocean wavefield evolution has been largely based on phase-average spectral models, such as WAM and SWAN. To the leading order, the wavefield is assumed to be Gaussian, quasi-stationary and quasi-homogeneous. The slow variation of wave energy spectrum over time and space is described through the action balance equation. In deep water, neglecting current, the change of energy spectrum is controlled by wind input, nonlinear wave interactions and energy dissipation due to wave breaking. Based on phase-average model, considerable spectral change occurs at a very large time scale $\mathcal{T}/T_p \sim O(\varepsilon^{-4})$, where T_p is the peak period of the spectrum and ε is a measure of wave steepness. Recently, it is found from wave tank experiments and NLS-type numerical simulations that spectrum can change on a much shorter time scale $\mathcal{T}/T_p \sim O(\varepsilon^{-2})$ due to modulational instability described in Alber (1978) (Onorato et al., 2004; Dysthe et al., 2003).

In this chapter, we study the nonlinear spectral evolutions using SNOW simulations. Our focus is the spectral change due to modulational instability over space and time scale $\mathcal{L}/\lambda_p$, $\mathcal{T}/T_p \sim O(\varepsilon^{-2})$, where λ_p is the peak wave length of the spectrum (see Table 1.1). To assess the range of validity of NLS-type models, we also

perform MNLS and BMNLS models described in Dysthe (1979); Trulsen and Dysthe (1996), and compare their predictions with SNOW. In Chapter 4, and 5, we discuss the influence of the spectral change on the nonlinear wave statistics and rogue wave occurrence.

The short waves, which have wavenumber or frequency greater than about three times the values at the peaks in the spectra, are of inherent scientific interest because data show that, when scaled properly, the spectrum of short waves collapse onto universal curves. The spectral slope of short waves is a reflection of the crucial dynamical balance among wind input, nonlinear interaction and energy dissipation. Phillips (1985) has concluded for one dimensional spectrum, the spectral density in the equilibrium range is proportional to the power law of $k^{-2.5}$. The saturation range they discuss occur at time scale $\mathcal{T}/T_p \sim O(\varepsilon^{-4})$.

The directional spreading of ocean wavefields is classically assumed to be unimodal, that is, for any given frequency or wavenumber, the wave energy is focused in the main propagating direction and decreases monotonically when deviating from this direction. Unimodal directional spreading functions such as the COS-square function are commonly assumed in wave simulation models (Hughes, 1985; GODA, 1999). However, recent field measurements indicate that the wave energy for short waves can demonstrate a bi-modal feature. For the directional distribution of short waves, the wave energy are focused in two directions nearly symmetric about the main propagating direction (Ewans, 1998; Hwang et al., 2000). The determination of the directional distribution of wind waves is important to understand the dominant mechanisms of wave dynamics.

In this chapter, we study the spectral change and spectral characteristics including spectral slope and directional spreading of short waves to understand the key dynamics that govern the wave motion.

3.2 Initial wavefield

3.2.1 Initial wave spectrum

The initial linear wavefield is generated from a given directional wave spectrum. In this study, we investigate nonlinear evolutions of two kinds of spectra. One is very narrow-banded Gaussian spectrum and the other is JONSWAP ocean wave spectrum. The Gaussian spectrum is used in the theoretical study by Alber (1978) and BMNLS numerical simulations in Gramstad and Trulsen (2007). The JONSWAP spectrum is a more realistic description of the random wavefields (Hasselmann et al., 1973).

The directional JONSWAP spectrum is described as:

$$S(\omega,\theta) = \frac{\alpha g^2}{\omega^5}\exp\left[-\frac{5}{4}(\frac{\omega}{\omega_p})^{-4}\right]\gamma^{\exp\left[-\frac{(\omega-\omega_p)^2}{2\sigma^2\omega_p^2}\right]}D(\theta), \tag{3.1}$$

where ω is the wave frequency, ω_p the peak wave frequency, α the Phillips parameter, γ the peak enhancement factor specifying the spectral bandwidth, and σ=0.07 for $\omega \leq \omega_p$; σ=0.09 for $\omega > \omega_p$.

The direction spreading is given by cosine-square function:

$$D(\theta) = \begin{cases} \frac{2}{\Theta}\cos^2\left(\frac{\pi\theta}{\Theta}\right), & \text{for } |\theta| \leq \Theta/2 \\ 0, & \text{for } |\theta| > \Theta/2, \end{cases} \tag{3.2}$$

where θ is propagating direction and Θ is the directional spreading width. The corresponding directional wavenumber spectrum is given by

$$\Psi(\mathbf{k}) = g^2/(2\omega^3)S(\omega)D(\theta), \tag{3.3}$$

where $\mathbf{k} = (k_x, k_y)$ is the wavenumber vector.

To elucidate the case of a very narrow-banded Gaussian spectrum considered by Alber (1978) and Dysthe et al. (2003), we also perform HOS and BMNLS simulations

for wavefields specified by a Gaussian wavenumber spectrum:

$$\Psi(\mathbf{k}) = \frac{\sigma^2}{2\pi\delta_k^2} \exp\left[-\frac{1}{2k_p^2}\left(\frac{(k_x - k_p)^2}{\delta_k^2} + \frac{k_y^2}{\delta_k^2}\right)\right], \tag{3.4}$$

where $\sigma=(\int \Psi(\mathbf{k})\ d\mathbf{k})^{1/2}$ is the standard deviation of the surface elevation, k_p is the peak wavenumber, and δ_k is the spectral bandwidth in the x and y directions.

The initial wavefield surface elevation and the linear velocity potential are expressed as

$$\eta(\mathbf{x}) = \mathcal{R}\left[\sum_{m=0}^{N_x/4} \sum_{n=-N_y/4}^{N_y/4} A_{mn} \exp^{i\mathbf{k}_{mn}\cdot\mathbf{x}}\right]; \tag{3.5}$$

$$\Phi^S(\mathbf{x}) = \mathcal{R}\left[\sum_{m=0}^{N_x/4} \sum_{n=-N_y/4}^{N_y/4} -\frac{igA_{mn}}{\omega_{mn}} \exp^{i\mathbf{k}_{mn}\cdot\mathbf{x}}\right]; \tag{3.6}$$

where ω_{mn}, A_{mn}, and α_{mn} are the frequency, complex amplitude and phase of the wave component with wavenumber vector $\mathbf{k}_{mn}=(m\Delta k_x, n\Delta k_y)$ respectively. For each $\mathbf{k}_{mn}$, ω_{mn} and $\mathbf{k}_{mn}$ is related by linear dispersion relation. The complex amplitude $A_{mn} = \sqrt{2S(\mathbf{k}_{mn})\Delta k_x \Delta k_y}\exp(i\alpha_{mn})$, and the phase α_{mn} is a random variable uniformly distributed on the range $[0, 2\pi]$. At the initial stage of SNOW simulations of nonlinear wave-field evolution, the free-surface boundary conditions are smoothly transitioned in time from linear to nonlinear conditions to minimize any standing wave effect that results from using linear initial conditions (Dommermuth, 2000).

3.2.2 Physical and numerical parameters

Table 3.1 shows the definitions of physical parameters and numerical parameters used in typical SNOW simulations of large-scale directional wavefields. In this thesis, a uniform grid with size of $N_x \times N_y$ is applied on a wavefield with a domain size $L_x \times L_y$. Without loss of generality, we consider wave components propagating in both positive and negative y direction but only in positive x direction. The wave modes, considered in the wavefield evolution, are $0 \leq k_x/\Delta k_x \leq N_x/4$ and $-N_y/4 \leq k_y/\Delta k_y \leq N_y/4$

after complete de-aliasing is applied. To include the nonlinear wave-wave interaction up to third order, the typical domain size used in this paper is $L_x \times L_y = 128\lambda_p \times 128\lambda_p$, with λ_p being the wave length of the dominant wave component. The grid size is $N_x = N_y = 4096$ unless stated otherwise. This leads to a spatial resolution of $\Delta x = \Delta y = \lambda_p/32$ and spectral resolution of $\Delta k_x = \Delta k_y = k_p/128$. The maximum wavenumber resolved in the simulation after a complete aliasing is $k_{x,\max} = k_{y,\max} = N_x/4 = 1024 = 8k_p$. The typical evolution time considered is $0 \leqslant t/T_p \leqslant 150$ to allow the development of modulational instability. Although for the purpose of study it is sufficient to use $M = 3$ to include the effect of modulational instability, we choose to use $M = 4$ to achieve better accuracy for locally steep waves. No considerable difference is noticed between the results using $M = 3$ and $M = 4$ over the evolution time $0 \leqslant t/T_p \leqslant 150$. Computational convergence tests of SNOW regarding the grid size N_x and N_y, order of nonlinearity M, and number of realizations for one given initial spectrum can be found in appendix A. We find the statistics are invariant for higher resolution and nonlinear order for the space and time scale considered.

Table 3.1: Physical and numerical input parameters for SNOW simulations.

Spectral parameters (JONSWAP)	
H_s	significant wave height
k_p	wavenumber of the dominant wave
λ_p	wavelength of the dominant wave
ε	$\varepsilon = \varepsilon H_s/2$ representative steepness
Θ	spreading angle
α	Phillips parameter
γ	peak enhancement factor
Numerical parameters	
N_x	grid number in x-coordinate
N_y	grid number in y-coordinate
M	order of nonlinearity used in HOS
N_T	number time steps per period

In MNLS and BMNLS simulations, the envelope function $B(\mathbf{x}, t)$ is solved in the modulational wavenumber space $\mathbf{K} = (\mathbf{k} - \mathbf{k_p})/k_p$ and only the modes within $|K_x| \leqslant 1$ and $|K_y| \leqslant 1$ are used. This is slightly different from (Socquet-Juglard et al., 2005) where wave modes within $|\mathbf{K}| \leqslant 1$ are used. The computational domain

is $128\lambda_p \times 128\lambda_p$, over which a uniform grid size $N_x = N_y = 512$ is applied. To resolve the fast oscillating surface elevation, $\eta(\mathbf{x}, t)$, uniform grid size of 4096×4096 is used. These computational parameter values lead identical spatial and spectral discretization with HOS simulations. For all the BMNLS simulations, the energy is verified to conserve within 0.5% in all simulations.

3.3 Nonlinear evolution of very narrow-banded Gaussian spectrum

In this section, we study the nonlinear evolutions of very narrow-banded Gaussian spectrum, described by (3.4), using MNLS, BMNLS, and SNOW simulations.

3.3.1 Evolution of directional spectrum

We consider the very narrow-banded Gaussian spectrum (3.4), which is theoretically unstable if $\delta_k < 2\varepsilon$, where $\varepsilon = \sqrt{2}\sigma k_p$ according to Alber (1978). The stability of this Gaussian spectrum is assessed by Dysthe et al. (2003) using BMNLS simulations, where they find a spectral broadening during wavefield evolution regardless of the initial spectral bandwidth for three-dimensional wavefields. We investigate the evolution of the same very narrow-banded Gaussian spectrum using SNOW simulations and compare the results with those from MNLS and BMNLS predictions. The initial spectra are chosen to be identical to those used in Dysthe et al. (2003). The spectra have same steepness ε=0.1 but two different bandwidths: δ_k=0.1 and 0.2. The initial spectra are shown in figure 3-1.

Figure 3-2 shows the spectral evolution of the case ε=0.1 and δ_k=0.1 from the MNLS, BMNLS, and SNOW simulations. The spectrum contours are obtained by ensemble averaging over five realizations and smoothed. In this case, $\delta_k < 2\varepsilon$ and the spectrum is unstable due to modulational instability according to Alber (1978). All MNLS, BMNLS and SNOW models give similar predictions for the features of spectral change, including significant spectral widening and spectral peak downshift-

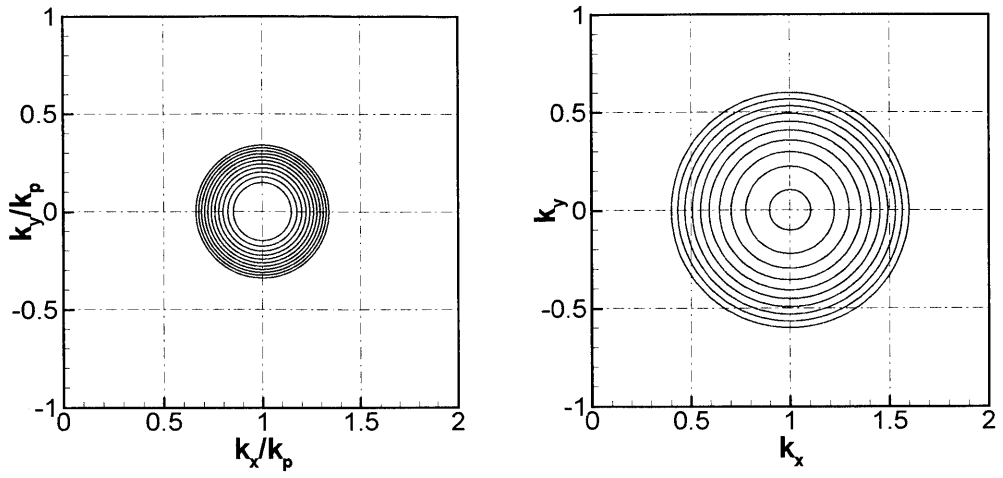

Figure 3-1: Initial very narrow-banded Gaussian shape spectrum $\Psi(\mathbf{k})$. (a) $\varepsilon = 0.1$, $\delta_k = 0.1$; (b) $\varepsilon = 0.1$, $\delta_k = 0.2$.

ing. Comparing MNLS and BMNLS simulations (figure 3-2(a)$\sim$ (f)), for evolutions within a short time $t \leqslant 50T_p$, the two models give comparable predictions on the spectral change; however, for large evolution time, MNLS predicts more significant energy spreading over short waves in comparison with BMNLS. Comparing MNLS and BMNLS with SNOW simulations, the BMNLS model, with extensions to allow broader spectral bandwidth, in general gives an overall better comparisons with SNOW simulations, although in BMNLS simulations noticeable overestimation of energy spreading over short waves at large evolution time ($t > 100T_p$) is still observed relative to SNOW simulations. Moreover, we observe a continuous energy spreading towards short waves in the NLS-type (MNLS and BMNLS) models, while in SNOW simulations, at large time, the spectrum changes much slower and eventually reaches a nearly quasi-stationary state after the initial rapid change over a relatively short time.

Figure 3-3 shows the spectral evolution for the case ε=0.1 and δ_k=0.2. This spectrum, with $\delta_k \geqslant 2\varepsilon$, is stable based on Alber (1978). For all MNLS, BMNLS and SNOW models, considerable modifications on the spectral shape, including spectral

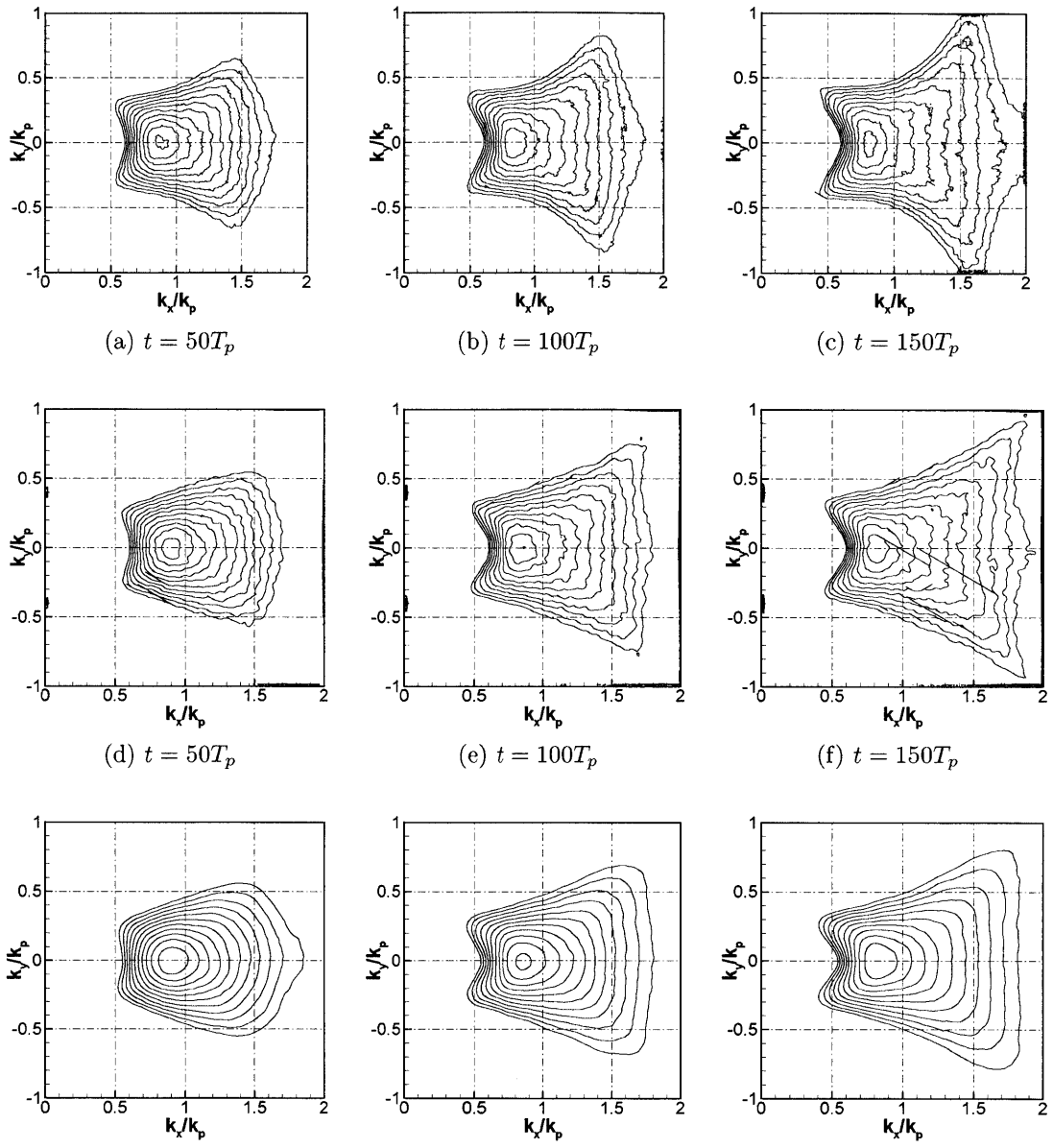

(a) $t = 50T_p$ (b) $t = 100T_p$ (c) $t = 150T_p$

(d) $t = 50T_p$ (e) $t = 100T_p$ (f) $t = 150T_p$

(g) $t = 50T_p$ (h) $t = 100T_p$ (i) $t = 150T_p$

Figure 3-2: Spectra evolution of narrow-band Gaussian-shape spectrum $\Psi(\mathbf{k})$ (Equation 3.4) with steepness $\varepsilon = 0.1$ and spectral bandwidth δ_k=0.1. MNLS: (a), (b), (c); BMNLS: (d), (e), (f); SNOW: (g), (h), (i). The contour values are logarithmic ranging 1×10^{-6} to 1×10^{-4}.

peak downshifting and spectral widening, are present. NLS-type models (MNLS and BMNLS) predict more significant spectral broadening in comparison with SNOW and the overestimation of spectral broadening is more serious in MNLS simulations. Similar to figure 3-2, in NLS-type models the spectrum broadens continuously, while in SNOW simulations, the spectrum is nearly invariant with time at large time scale ($t \gtrsim 100T_p$).

In both simulations, Gaussian spectrum changes in three-dimensional wavefield and more significantly so when the instability condition $\delta_k < 2\varepsilon$ is satisfied. These are reasonably well predicted by both HOS and NLS-type simulations (specially BMNLS simulations), with minor quantitative differences.

3.3.2 Omnidirectional spectrum

The one dimensional omnidirectional spectrum is defined as

$$S(k) = \int_\theta k\Psi(k,\theta)\, d\theta, \tag{3.7}$$

where $\Psi(k_x, k_y) = \Psi(k,\theta)$ is obtained by mapping the wavenumber spectrum in (k_x, k_y) to (k,θ), $k = \sqrt{k_x^2 + k_y^2}$ is the magnitude of the wavenumber vector and θ is the wave direction.

Figure 3-4 shows the evolution of omnidirectional spectrum of the Gaussian spectra with same steepness but different spectral bandwidths from MNLS and SNOW simulations. For the cases considered, a clear spectral peak downshifting and bandwidth broadening are observed from both models. For the spectrum with narrower bandwidth (figure 3-4(a), (b), (c)), MNLS and SNOW give qualitatively similar predictions on the omnidirectional spectrum, although at large evolution time noticeable differences are still found over the large wavenumber range. In both MNLS and SNOW simulations, the spectral around peak wave evolves to the power law of $k^{-2.5}$, although the power law of spectral tail is derived for large wave number in the saturation range over time scale $\mathcal{T}/T_p = O(\varepsilon^{-4})$. For large evolution time, comparing to SNOW simulations, MNLS model overestimates the wave energy over short waves.

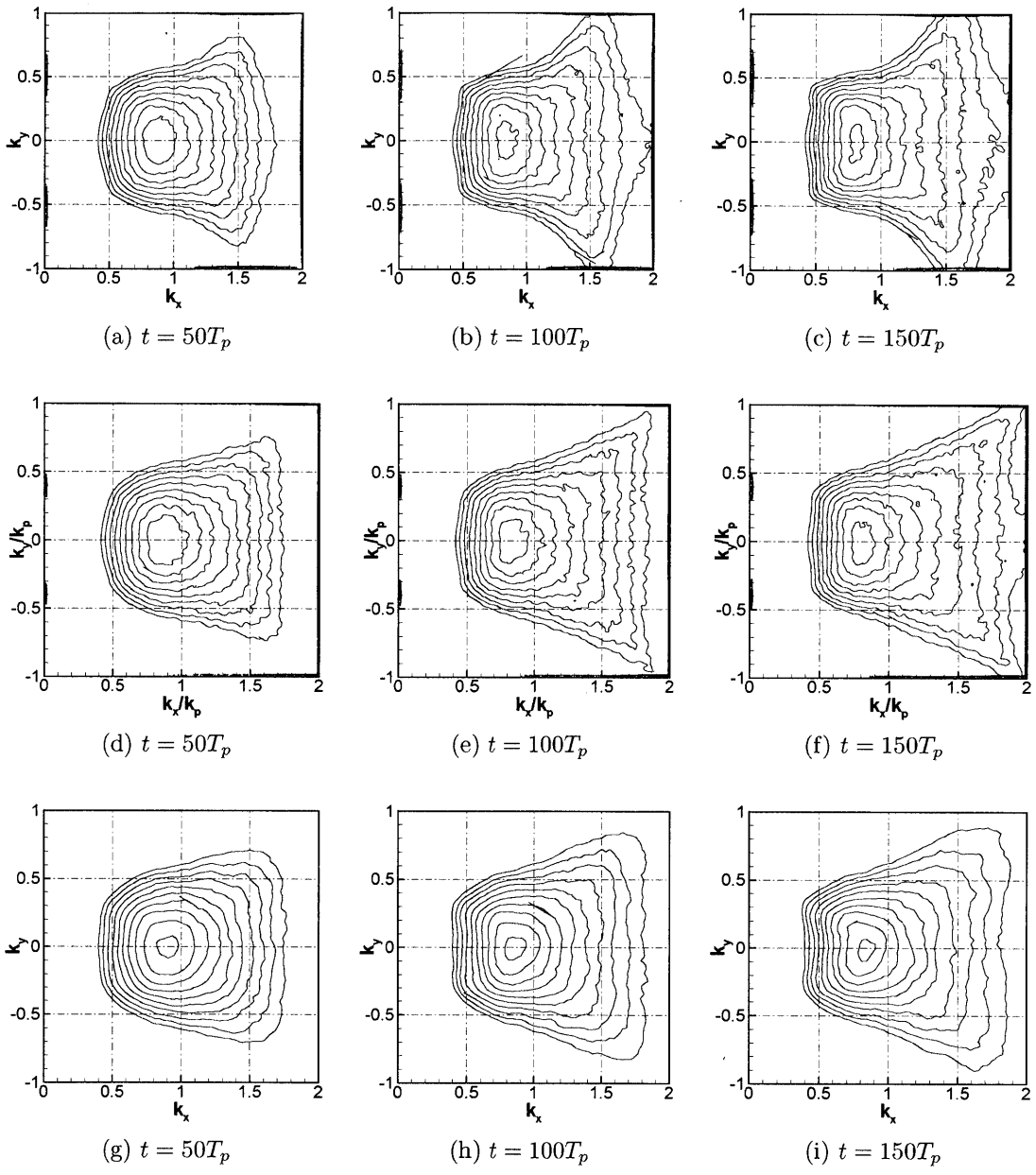

(a) $t = 50T_p$ (b) $t = 100T_p$ (c) $t = 150T_p$

(d) $t = 50T_p$ (e) $t = 100T_p$ (f) $t = 150T_p$

(g) $t = 50T_p$ (h) $t = 100T_p$ (i) $t = 150T_p$

Figure 3-3: Spectra evolution of narrow-band Gaussian-shape spectrum $\Psi(\mathbf{k})$ (Equation 3.4) with steepness $\varepsilon = 0.1$ and spectral bandwidth $\sigma = 0.2$. MNLS: (a), (b), (c); BMNLS: (d), (e), (f); SNOW: (g), (h), (i). The contour values are logarithmic ranging 1×10^{-6} to 1×10^{-4}.

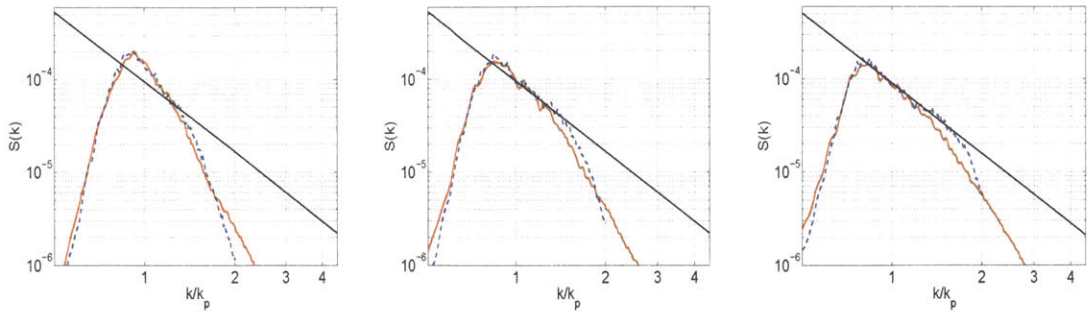

(a) $\sigma = 0.1, t = 50T_p$ (b) $\sigma = 0.1, t = 100T_p$ (c) $\sigma = 0.1, t = 150T_p$

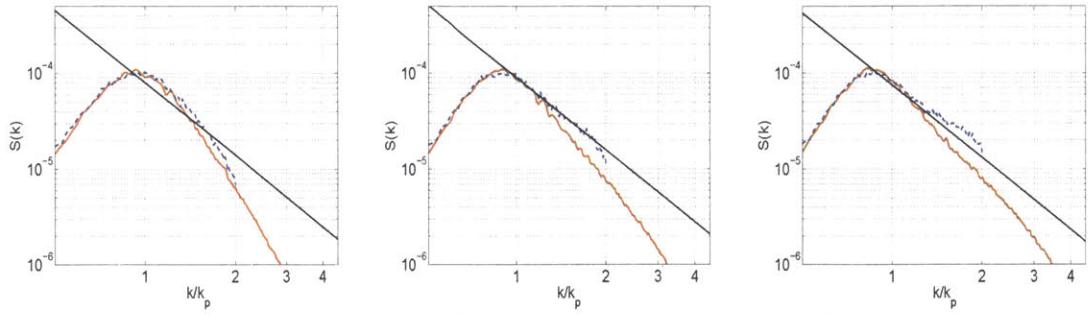

(d) $\sigma = 0.3, t = 50T_p$ (e) $\sigma = 0.3, t = 100T_p$ (f) $\sigma = 0.3, t = 150T_p$

Figure 3-4: Log-log plots of one-dimensional omnidirectional spectrum $S(k)$ of the wavefields for Gaussian spectrum ε=0.1, δ_k=0.1 and δ_k=0.3. SNOW (—); MNLS (- - -); Power law $k^{-2.5}$ (—).

For the case with broader bandwidth (δ_k=0.3), MNLS agrees with SNOW simulations over a relatively short time $t \leqslant 50T_p$. For large time, considerable energy accumulation at the edge of spectrum is observed in MNLS simulations (figure 3-4(e), (f)). Comparing with SNOW simulations, at $t = 100T_p$, the spectral range agrees with the $k^{-2.5}$ power law is broader in MNLS simulations. This is mainly caused by the energy cumulation at the edge of spectrum in MNLS model. This is confirmed at later time $t = 150T_p$, where a continuous energy cumulation is observed in MNLS model and the tail of spectral has a smaller slope than $k^{-2.5}$. In SNOW simulations, the spectrum is nearly quasi-stationary at large time.

3.4 Nonlinear evolution of directional JONSWAP ocean wave spectrum

We here investigate the evolutions of JONSWAP spectra using MNLS, BMNLS, and SNOW simulations. The initial JONSWAP spectra are chosen to have same steepness $\varepsilon=H_s k_p/2=0.16$ and spectral bandwidth which is controlled by the peakness enhancement parameter $\gamma=6$, but a range of spreading angles.

3.4.1 Evolution of directional spectrum

Figure 3-5 shows the evolution of wavenumber spectrum for the wavefield with small initial spreading angle $\Theta = 12°$ from MNLS, BMNLS and SNOW simulations. A significant spectral broadening and peak frequency downshift as result of nonlinear wave interactions are observed from all the simulations. In comparison with BMNLS, MNLS predicts a much broader spectral spreading, specially over short waves. Comparing NLS-type models (MNLS and MNLS) with SNOW, BMNLS in general gives better comparisons with SNOW relative to MNLS. Both of MNLS and BMNLS models overpredict the energy spreading over short waves over large evolution time. In NLS-type simulations, wave energy spreads towards short waves continuously. In SNOW simulations, however, the directional spectrum reaches a quasi-stationary state and the spectrum is nearly invariant with time after a large time $t \geqslant 100T_p$. The similar features are observed for the case with slightly broader spreading angle $\Theta = 21°$ shown in figure 3-6.

Figure 3-7 shows the spectral evolution for the wavefield with broad spreading angle $\Theta = 62°$ from MNLS, BMNLS and SNOW simulations. The spectral change including spectral peak downshifting and spread broadening are again observed in all three models. Similar to previous cases, NLS-type models give a broader prediction on the spectral spreading angle, in comparison with SNOW simulations. Contrasting figure 3-7 with figure 3-5, we find the spectral change is much slower in this case where the initial spectral spreading angle is large, which suggests the importance of

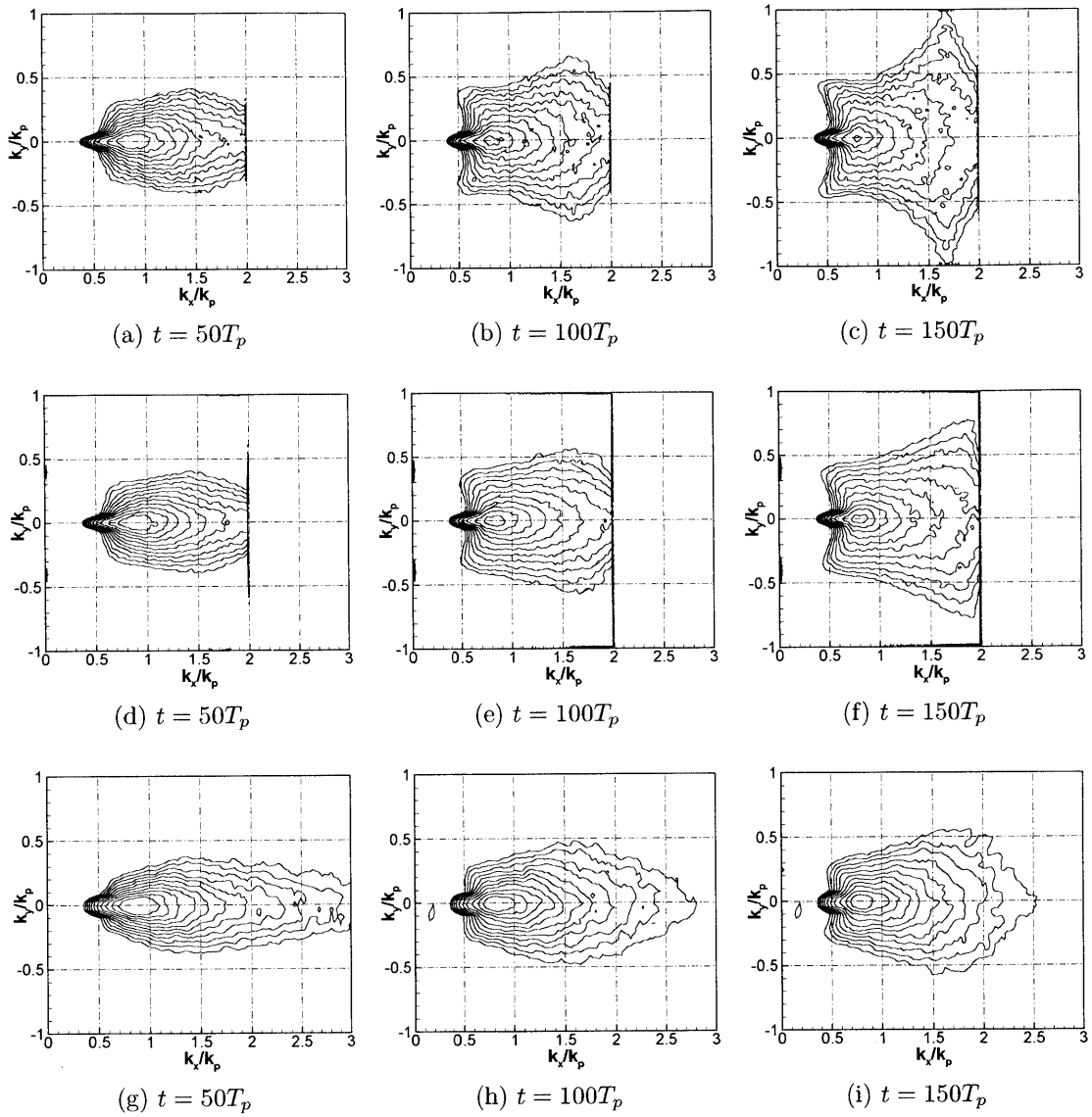

(a) $t = 50T_p$ (b) $t = 100T_p$ (c) $t = 150T_p$

(d) $t = 50T_p$ (e) $t = 100T_p$ (f) $t = 150T_p$

(g) $t = 50T_p$ (h) $t = 100T_p$ (i) $t = 150T_p$

Figure 3-5: Spectra evolution of JONSWAP spectrum $\Psi(\mathbf{k})$ with H_s= 0.08 m, T_p=1 sec, γ=6 and $\Theta = 12°$. MNLS ((a), (b), (c)); BMNLS: (d), (e), (f); SNOW: (g), (g), (h), (i). The contour values are logarithmic ranging 1×10^{-6} to 1×10^{-4}.

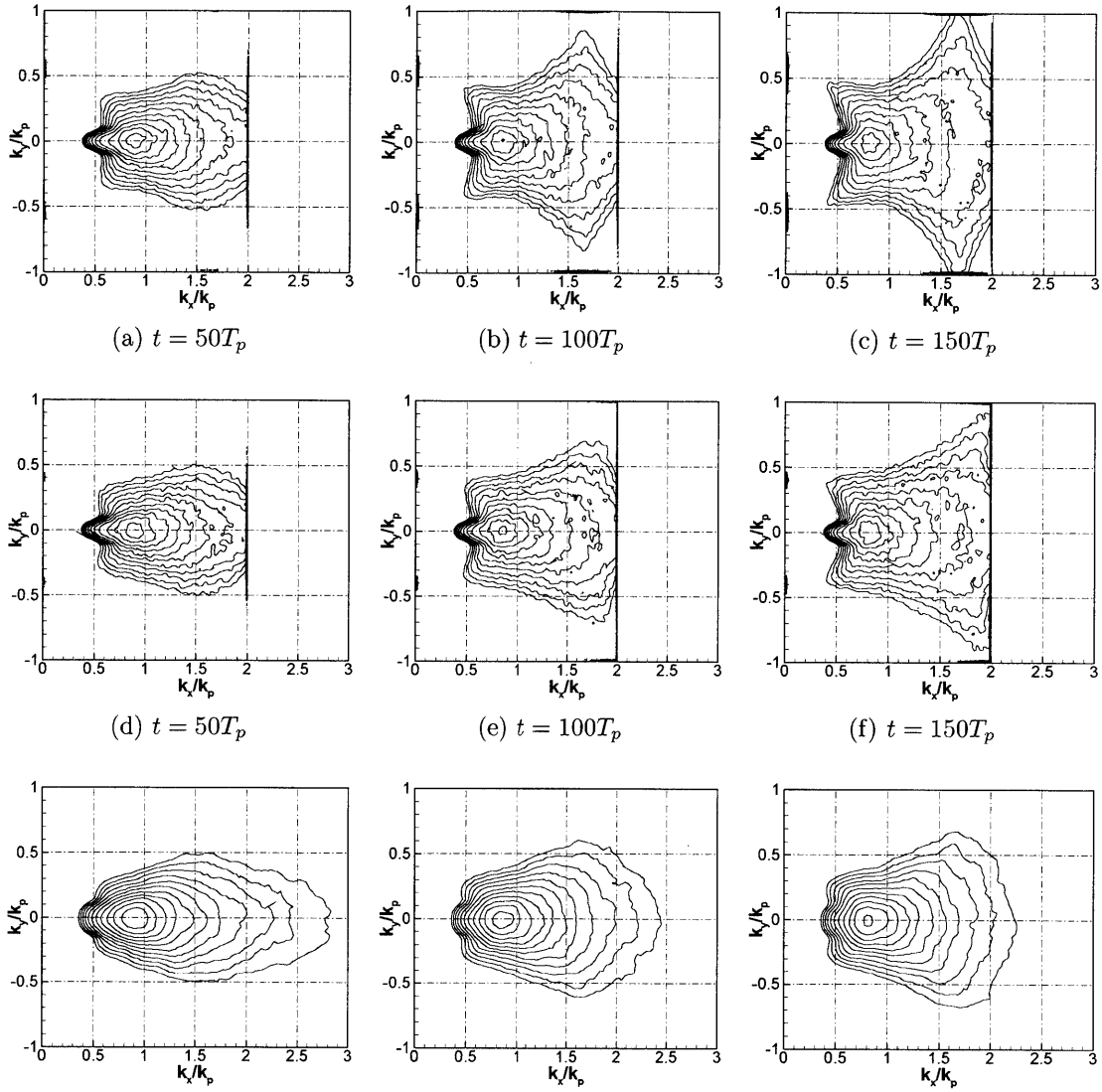

(a) $t = 50T_p$ (b) $t = 100T_p$ (c) $t = 150T_p$

(d) $t = 50T_p$ (e) $t = 100T_p$ (f) $t = 150T_p$

(g) $t = 50T_p$ (h) $t = 100T_p$ (i) $t = 150T_p$

Figure 3-6: Spectra evolution of JONSWAP spectrum $\Psi(\mathbf{k})$ with $H_s = 0.08\,\mathrm{m}$, T_p=1 sec, γ=6 and $\Theta = 21°$. MNLS: (a), (b), (c); BMNLS: (d), (e), (f); SNOW: (g), (h), (i). The contour values are logarithmic ranging 1×10^{-6} to 1×10^{-4}.

modulational instability is reduced when the spreading angle becomes large.

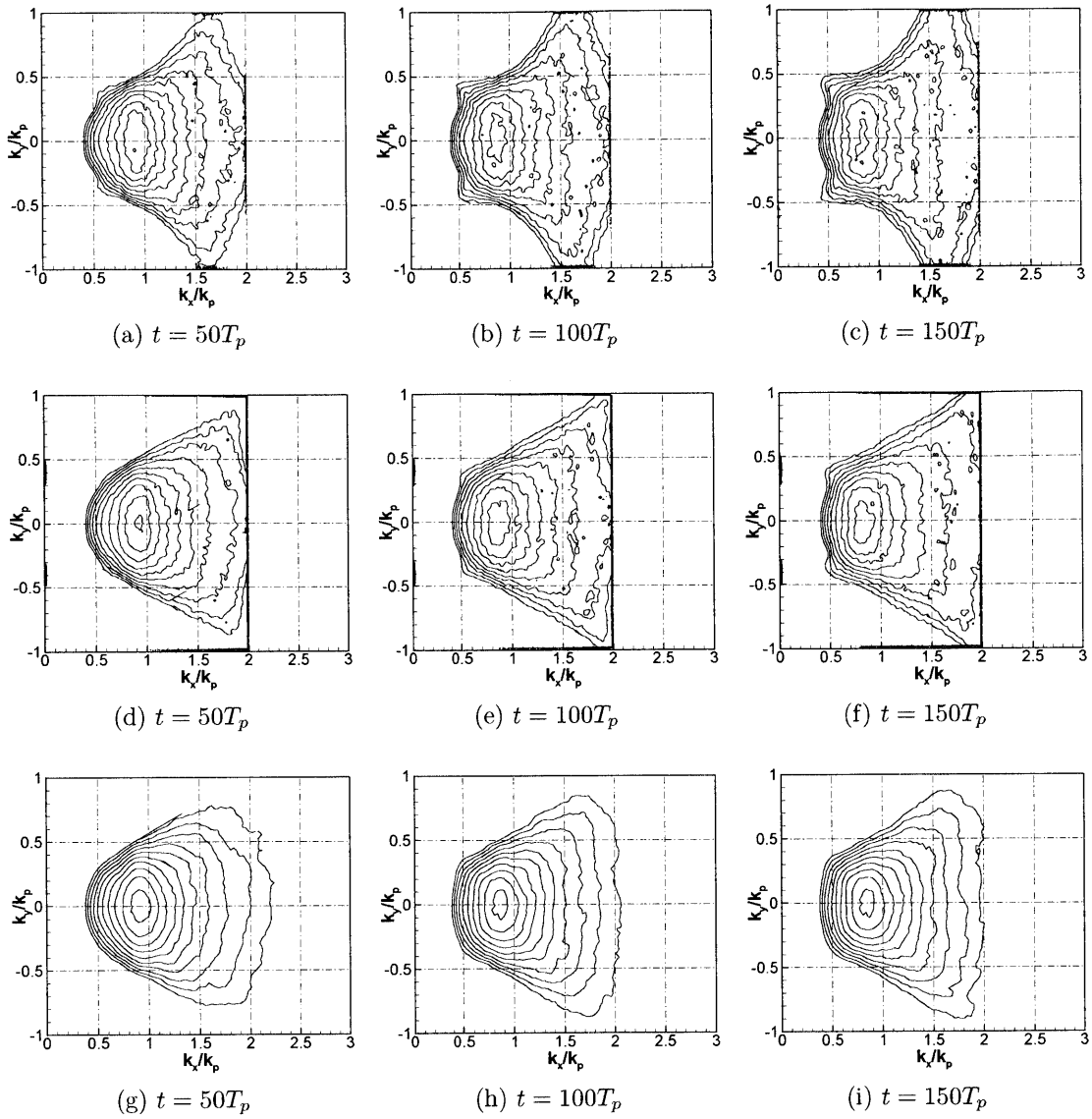

(a) $t = 50T_p$ (b) $t = 100T_p$ (c) $t = 150T_p$

(d) $t = 50T_p$ (e) $t = 100T_p$ (f) $t = 150T_p$

(g) $t = 50T_p$ (h) $t = 100T_p$ (i) $t = 150T_p$

Figure 3-7: Spectra evolution of JONSWAP spectrum $\Psi(\mathbf{k})$ with H_s=0.08 m, T_p=1 sec, γ=6 and $\Theta = 62°$. MNLS: (a), (b), (c); BMNLS: (d), (e), (f); SNOW: (g), (h), (i). The contour values are logarithmic ranging 1×10^{-6} to 1×10^{-4}.

3.4.2 Omnidirectional spectrum

Evolution of the omnidirectional spectra $S(k)$ for the directional JONSWAP spectra is shown in figure 3-8. Both BMNLS and SNOW predict the spectral peak downshift.

The two models, however, differ qualitatively in the spectral tail. In the SNOW predictions, the tail of $S(k)$ is nearly time-invariant and remains very close to the $k^{-2.5}$ power law for large k, for both the narrow and broad spreading cases. This is not predicted by BMNLS predictions which shows continuous energy accumulation in time for short waves. The overestimation of the energy spreading is more significant in the case with broader initial spreading angles. For SNOW simulations, we observe the slope of spectral tail approaches to the power law of $k^{-2.5}$ from its initial value, while for BMNLS simulations, a continuous broadening of spectrum is observed.

It is important to point out that the feature of the spectral slope depends on the balance among wind input, nonlinear wave interaction and wave breaking. In our simulation, the wind input is not considered and the wave breaking occurs mainly on the very short waves $|\mathbf{k}| \geqslant 5k_p$. The feature of spectral slope discussed here is contributed dominantly by nonlinear wave interaction.

3.4.3 Integral directional spreading function

The integral directional distribution function, $D(\theta)$, is defined as

$$D(\theta) = \int_k k\Psi(k,\theta)dk. \tag{3.8}$$

Figure 3-9 shows the evolution of $D(\theta)$ for the JONSWAP spectra with different spreading angles. Both BMNLS and SNOW show a broadening in the angle spreading. For relatively short time, BMNLS and SNOW give very close prediction on $D(\theta)$. For larger time, BMNLS simulations give a slightly broader profile on $D(\theta)$. Comparing the profiles of $D(\theta)$ obtained from two initial spreading angles, $\Theta = 12°$ and $\Theta = 62°$, the spectral directional spreading changes much more significantly in the wavefield with small initial spreading angle ($\Theta = 12°$).

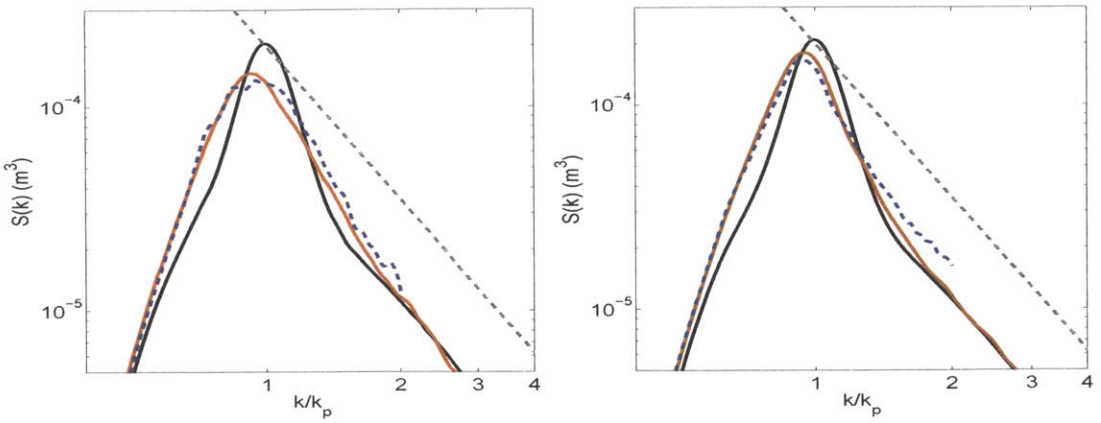

(a) $\Theta = 12°, t = 50T_p$

(b) $\Theta = 62°, t = 50T_p$

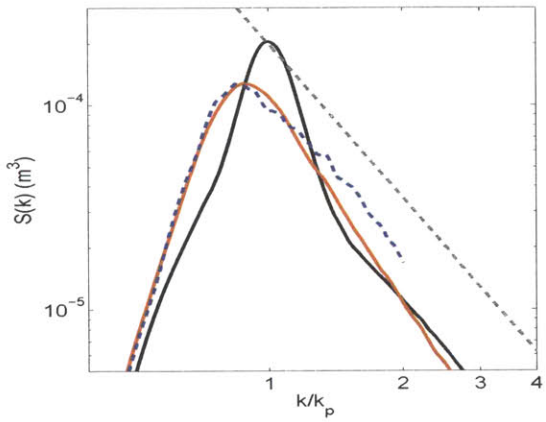

(c) $\Theta = 12°, t = 100T_p$

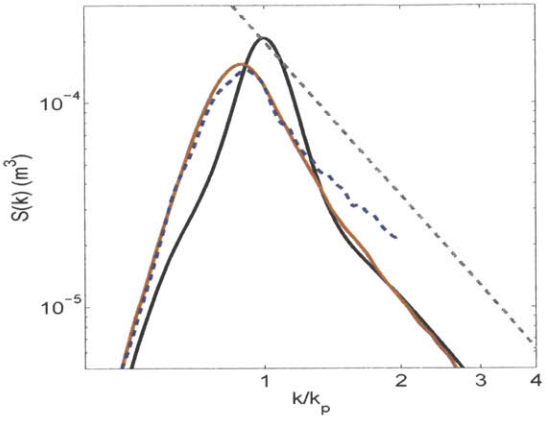

(d) $\Theta = 62°, t = 100T_p$

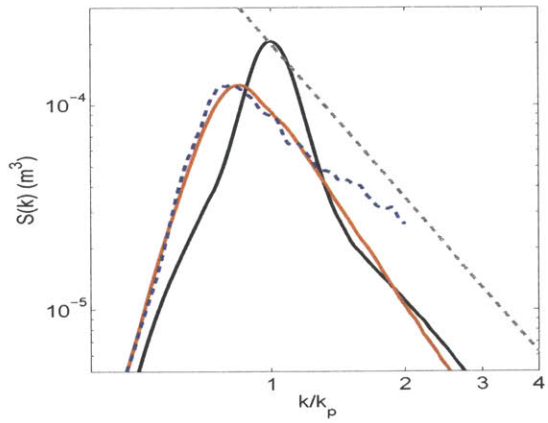

(e) $\Theta = 12°, t = 150T_p$

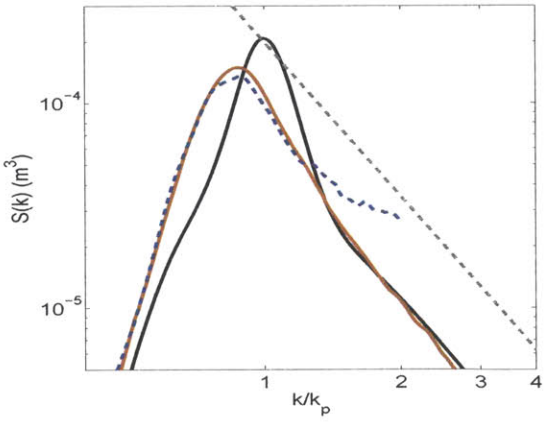

(f) $\Theta = 62°, t = 150T_p$

Figure 3-8: Log-log plots of one-dimensional omnidirectional spectrum $S(\mathbf{k})$ of JONSWAP spectrum H_s=12 m, T_p=13 s, ($\varepsilon = 0.16$), γ=6 and spreading angles $\Theta = 12°$ ((a), (c), (e)) and 62° ((b), (d), (f)). SNOW (—); BMNLS (- - -); Initial spectrum (—); Power law $k^{-2.5}$ (- - -).

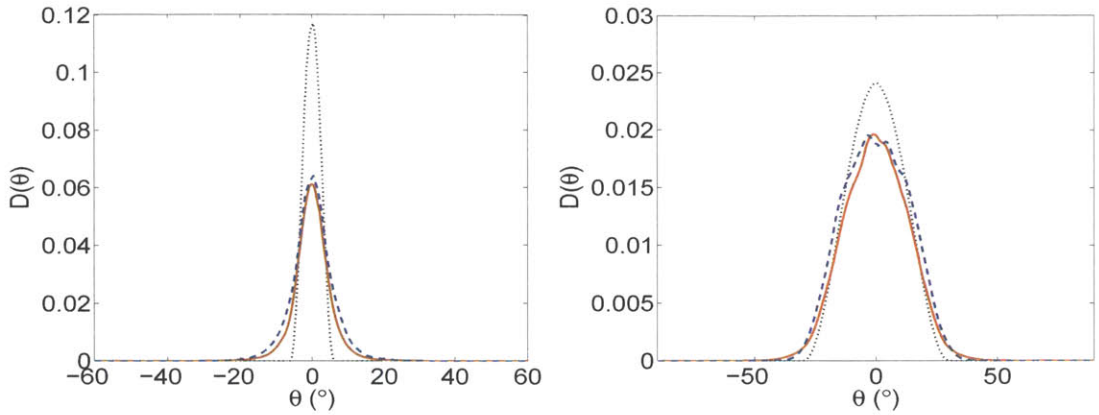

(a) $\Theta = 12°, t = 50T_p$

(b) $\Theta = 62°, t = 50T_p$

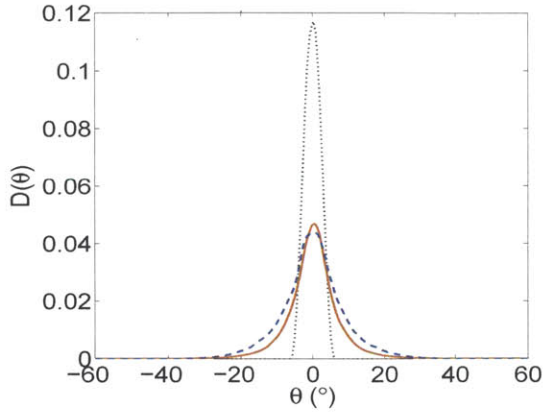

(c) $\Theta = 12°, t = 100T_p$

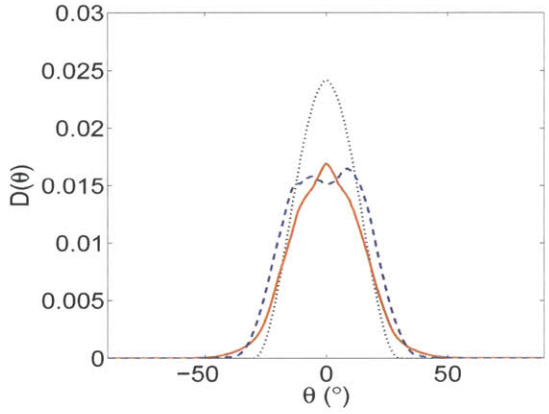

(d) $\Theta = 62°, t = 100T_p$

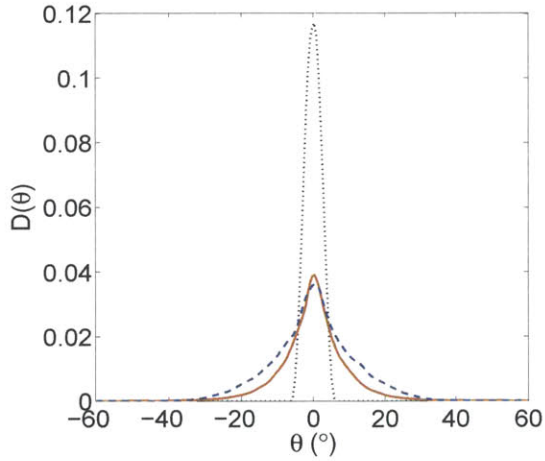

(e) $\Theta = 12°, t = 150T_p$

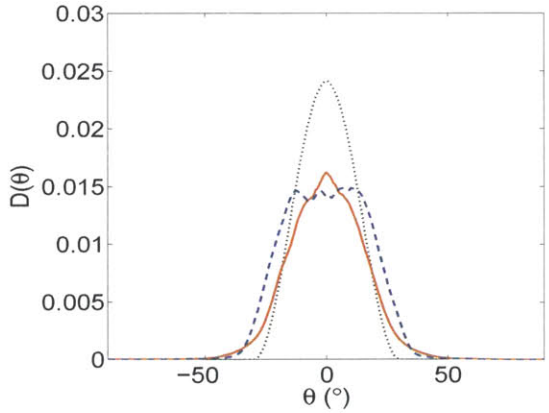

(f) $\Theta = 62°, t = 150T_p$

Figure 3-9: Integral directional function $D(\theta)$ of the JONSWAP spectrum H_s=0.08 m, T_p=1 s, ($\varepsilon = 0.16$), $\gamma = 6$ and spreading angles $\Theta = 12°$ ((a), (c), (e)) and 62° ((b), (d), (f)). SNOW (—); BMNLS (- - -); initial profile ($\cdots$).

3.4.4 Directional spreading function

The directional distribution function is defined by (Hwang et al., 2000):

$$D(k,\theta) = \frac{k\Psi(k,\theta)}{S(k)}, \tag{3.9}$$

with $D(k,\theta) \geqslant 0$ and $\int_{-\pi/2}^{\pi/2} D(k,\theta)\, d\theta = 1$. The normalized directional distribution function $D_k(\theta)$ is defined as

$$D_k(\theta) = \Psi(k,\theta)/\max(\Psi(k,\theta)). \tag{3.10}$$

The moments of directional distributions are

$$\theta_m(k) = \frac{\int_0^{\pi/2} \theta^m D_k(\theta)\, d\theta}{\int_0^{\pi/2} D_k(\theta)\, d\theta}. \tag{3.11}$$

The integration of the directional distribution function is

$$I_D(k) = \int_{-\pi/2}^{\pi/2} D_k(\theta)\, d\theta. \tag{3.12}$$

Apparently,

$$D(k,\theta) = D_k(\theta)/I_D(k). \tag{3.13}$$

The directional resolution of SNOW simulations can be estimated by $dk_x dk_y = k dk d\theta$, which gives $d\theta = dk_x dk_y/(kdk) \approx dk/k$ (if $dk = dk_x = dk_y$). For $k = k_p/2$, $d\theta < 1°$.

The mean directional spread $\delta\theta$=$\overline{\theta_2(k)}$ is defined as the average of the second-order moment of the directional distribution function. Figure 3-10 shows the temporal variation of $\delta\theta$ for wavefields with different initial spreading angles from BMNLS and SNOW simulations. For the initially narrow spread case, $\Theta = 12°$, SNOW and BMNLS predict a similar increasing $\delta\theta$ with evolution time up to $t/T_p \approx 50$. For large time, BMNLS overpredicts $\delta\theta$ significantly in comparison with SNOW. For the initially broader spreading case, BMNLS overpredicts $\delta\theta$ relative to SNOW over the

entire evolution. Comparing the two spreading cases, we see that the rate of change in $\delta\theta$ is greater for smaller Θ as observed in figure 3-6.

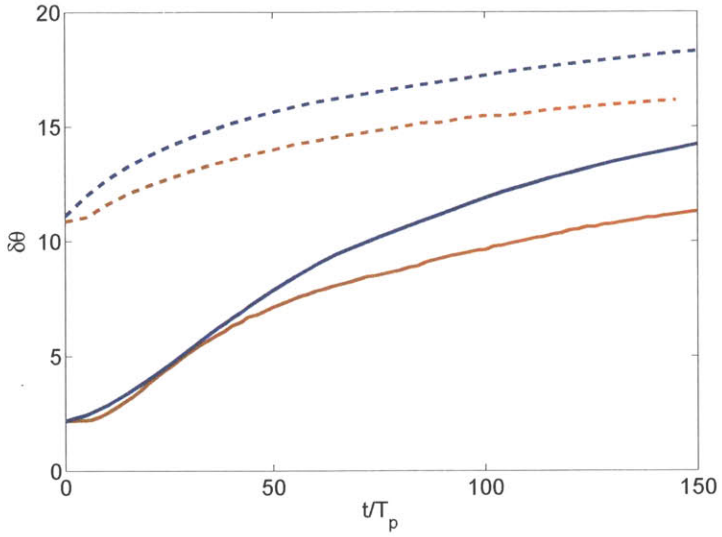

Figure 3-10: Temporal variation of mean directional spread $\delta\theta$. SNOW: Θ=12° (—), 62° (- - -); BMNLS: Θ=12° (—), 62° (- - -).

The directional spreading functions for the wavefields with different initial spreading angles have been studied in Wu et al. (2012) and are reproduced in figure 3-11. An interesting phenomenon observed is that the directional spreading function may not remain its original unimodal COS-square shape and an obvious bi-modal shape is developed for the wavefield with broad initial spreading angle. For all three cases, it shows that the directional spreading function for a wavenumber near the peak wavenumber stays as a unimodal function and does not deviate significantly from its initial shape. However, in wavefields with broad spreading angle, the directional spreading function of short waves ($k > 3k_p$) deforms from its initial shape significantly and develops into a bi-modal function. The bi-modal feature of short waves becomes less significant as the initial spreading angle decreases. Therefore, we conclude that the bi-modal distribution of spreading angle of short waves is a unique feature of short-crested wavefields.

To study the dependence of bimodal feature on wavenumber, in figure 3-12 we plot the first-moment of directional distribution function as function of wavenumber

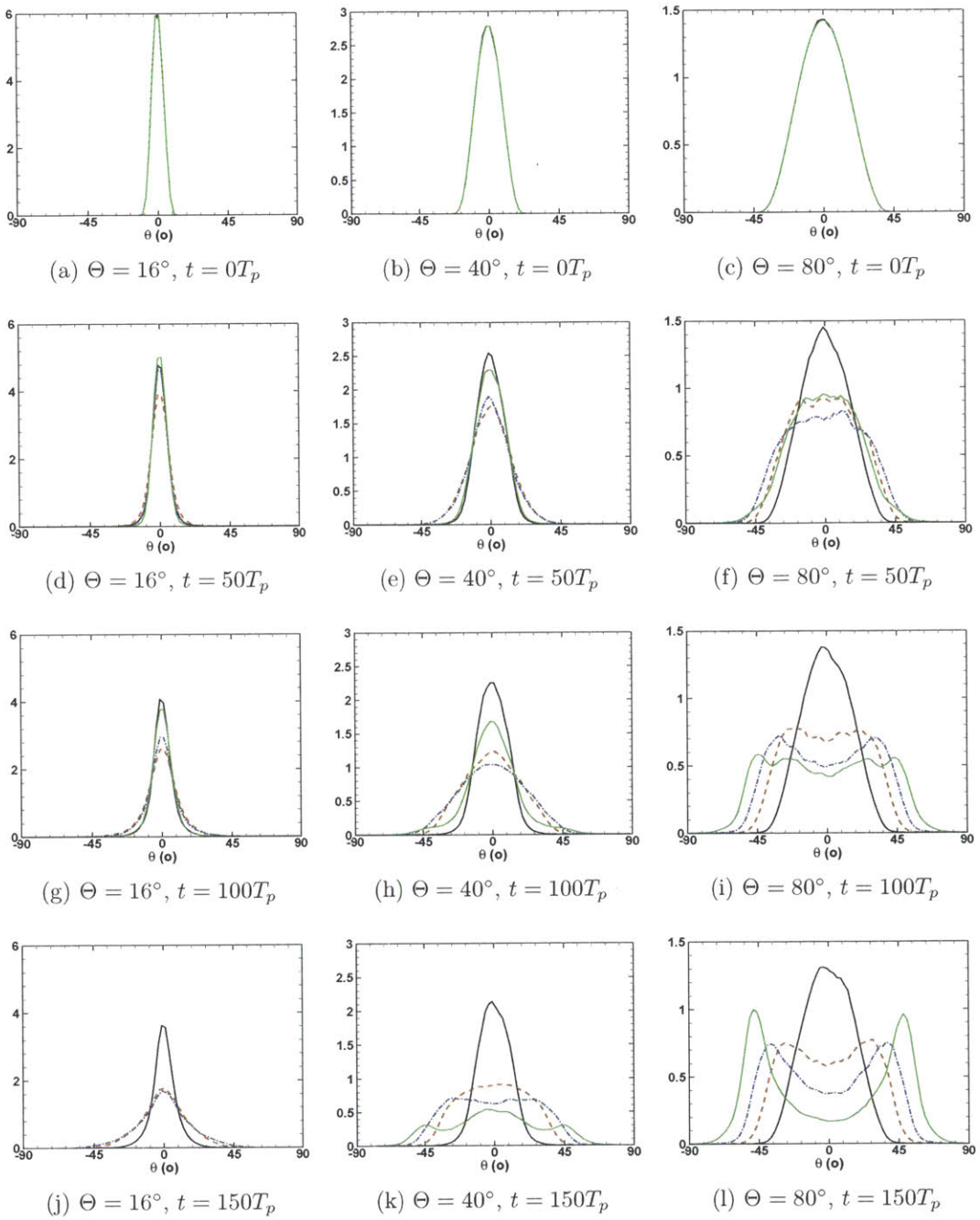

(a) $\Theta = 16°$, $t = 0T_p$ (b) $\Theta = 40°$, $t = 0T_p$ (c) $\Theta = 80°$, $t = 0T_p$

(d) $\Theta = 16°$, $t = 50T_p$ (e) $\Theta = 40°$, $t = 50T_p$ (f) $\Theta = 80°$, $t = 50T_p$

(g) $\Theta = 16°$, $t = 100T_p$ (h) $\Theta = 40°$, $t = 100T_p$ (i) $\Theta = 80°$, $t = 100T_p$

(j) $\Theta = 16°$, $t = 150T_p$ (k) $\Theta = 40°$, $t = 150T_p$ (l) $\Theta = 80°$, $t = 150T_p$

Figure 3-11: Directional spreading functions $D(k, \theta)$ for the JONSWAP spectrum $H_s = 12\,\text{m}$, $T_p = 13\,\text{s}$, $\gamma = 5$, and $\Theta = 16°$ ((a), (d), (g), (j)); $\Theta = 40°$ ((b), (e), (h), (k)); $\Theta = 80°$ ((c), (f), (i), (l)). $k = k_p$ (—), $k = 3k_p$ (- - -), $k = 5k_p$ (– · –), and $k = 7k_p$ (· · ·).

obtained from SNOW simulations with Θ=80° and field measurement (Hwang et al., 2000). We find SNOW agrees with field measurement reasonably well, although the wave conditions used in SNOW is not the same as the sea state of the measurements.

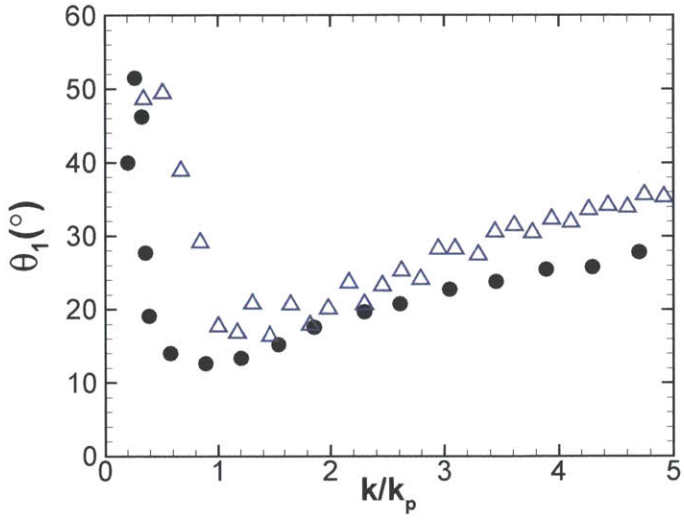

Figure 3-12: The comparison of the first moment of the angle spreading function between field measurements (△) (Hwang et al., 2000) and SNOWsimulations (•) ($H_s = 12\,\mathrm{m}$, $T_p = 13\,\mathrm{s}$, $\gamma = 5$ and $\Theta = 80°$).

The bimodal properties of the spreading function can be described more quantitatively by the spreading angle width $\theta_w(k)$, which is the angle where maximum $D_k(\theta)$ is obtained, and the scaled spreading amplitude, $r_w(k)$, which is the ratio between maximum $D_k(\theta)$ and $D_k(\theta_p)$, its value at the dominant direction. The comparison of the spreading angle width and the amplitude between the field measurement and SNOW simulations is shown in figure 3-13. It is observed the comparison is reasonably well for spreading width. For the amplitude of the spreading angles, comparing with field measurements SNOW simulations generally overpredict $r_w(k)$, specially for short waves.

The dependence of the first-moment of spreading angle $\theta_1(k)$ and the spreading width $\theta_w(k)$ on the initial spreading angle are summarized in figure 3-14. We observe that for small spreading angle ($\Theta = 16°$), the bi-modal feature is almost absent. As the initial spreading angle increases, the bi-modal feature starts to develop from

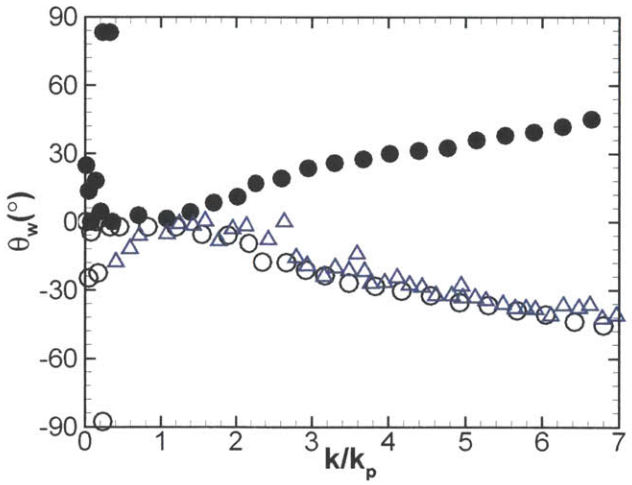

(a)

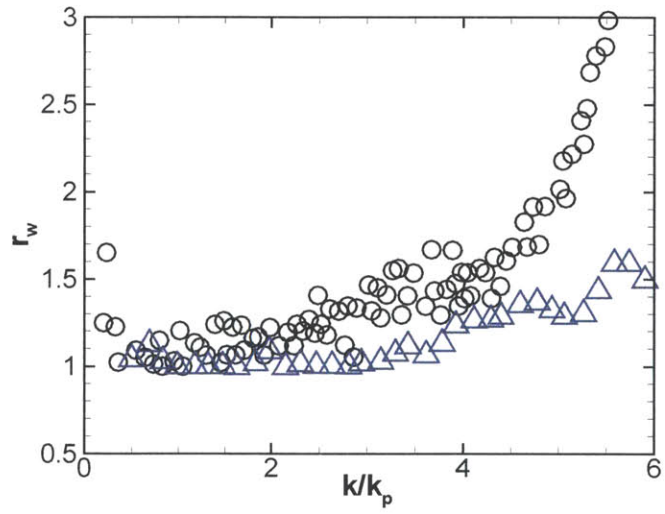

(b)

Figure 3-13: The comparison of (a) the spreading angle width and (b) spreading angle amplitude between the field measurements (△) and SNOW simulations (◯/●) ($H_s = 12$m, $T_p = 13$s, $\gamma = 5$ and $\Theta = 80°$).

large wavenumber. The angle width θ_w increases with wavenumber. Moreover, the dependence of angle width θ_w on the wavenumber becomes nearly independent of initial spreading angle for wavefields with broad initial spreading angle $\Theta \geqslant 60°$. The spreading angle θ_w becomes nearly constant for large wavenumber $\theta_w \approx 40°$ for large initial spreading angles. Since the wind-input are not considered and wave breaking are mainly preformed over waves with wavenumber $|\mathbf{k}|/k_p > 7$, we conclude the bimodal feature of directional spreading is dominantly contributed by nonlinear wave interactions.

3.5 Summary and conclusions

We study the spectral evolution of three-dimensional nonlinear deep water wavefields using direct simulations based on a high-order spectral method (SNOW). Consistent with modulational instability of nonlinear waves, which is our main focus, we consider spatial domains $\mathcal{L} \times \mathcal{L}$ and evolution times $\mathcal{T}$, where $\mathcal{L}/\lambda_p$, $\mathcal{T}/T_p \sim O(\varepsilon^{-2})$, for our simulations.

To assess range of validity of NLS-type models in describing spectral change, we obtain results using MNLS and BMNLS models, and compare and contrast these with SNOW. In general, NLS-type models and SNOW obtain qualitatively similar results for initial time. For $\mathcal{L}/\lambda_p$, $\mathcal{T}/T_p \sim O(\varepsilon^{-2})$ and initially narrow frequency and directional spread wavefields, however, SNOW obtains quasi-stationary states after the broadening of the spectra. This is not predicted by NLS-type models which in general obtain monotonic spreading of energy to shorter and more directionally-spreading waves.

We elucidate the importance of modulational instability in the evolution of directional wavefields. Spectral change over the modulational instability scales is examined using both NLS-type and SNOW simulations. BMNLS obtains in general a better comparison with SNOW results than MNLS predictions. For very narrow-banded Gaussian spectrum, NLS-type models and SNOW give very similar predictions on the spectral peak downshift and spectral broadening, although NLS-type models give

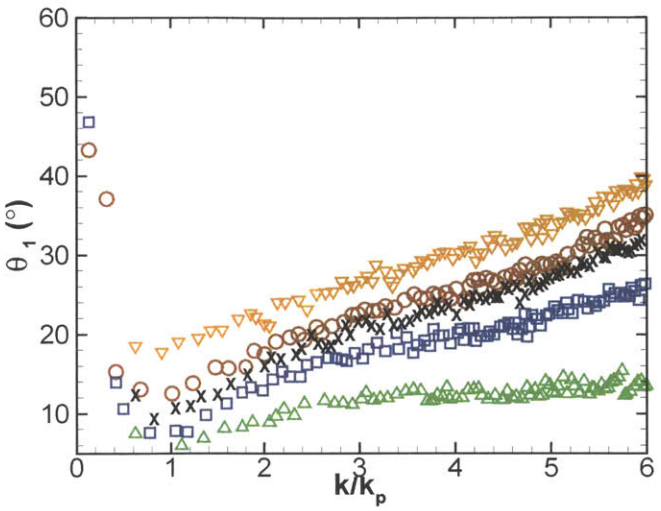

(a)

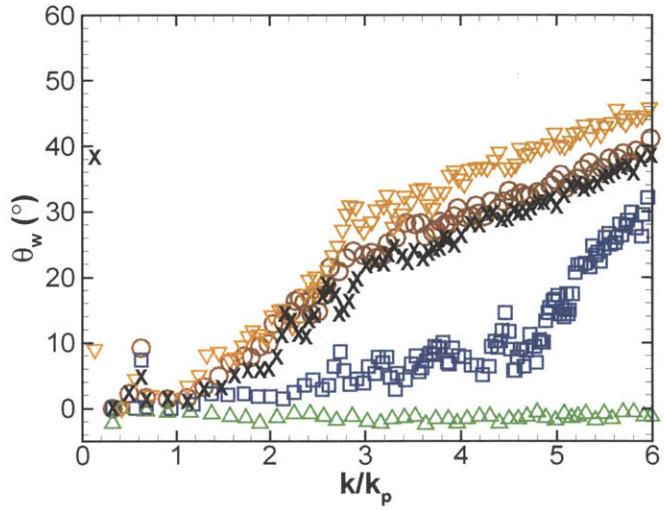

(b)

Figure 3-14: (a) The first moment of the angle spreading $\theta_1(k)$; (b) the spreading angle width as function of wavenumber $\theta_w(k)$. $\Theta = 16°$ (△); $\Theta = 40°$ (□); $\Theta = 60^o$ (×); $\Theta = 80°$ (○); $\Theta = 120°$. (▽).

a slightly broader energy spreading over short waves. For initial spectrum theoretically unstable to the modulational instability, a considerable spectral broadening over a relatively short time scale is observed in all the simulations. For initial spectrum theoretically stable, the spectrum still broadens, however, the spectral broadening process is much slower, which suggests a larger time scale is relevant for evolution of broad-spreading seas. For JONSWAP wavefields with small spreading angles, modulational instability leads to significant spectral broadening. For wavefields with large spreading angles, the importance of modulational instability becomes less significant.

We find the directional spreading function may not remain its original COS-square shape. An obvious bi-modal shape is developed for the directional distribution function of short waves in the wavefields with large initial spreading angles. For the wavefields with small initial spreading angles, the bimodal features of directional distribution function are absent.

Chapter 4

Nonlinear wave statistics of ocean wavefield in deep water

4.1 Introduction

Reliable descriptions of the probability distributions of ocean waves are critically important to many marine engineering applications. In linear random wave theory, the wavefield is considered as a superposition of sinusoidal wave components with different frequencies and directions of propagation. Based on the central limit theory, the surface is therefore described by Gaussian distribution. For unidirectional waves which are narrow-banded in frequency, Longuet-Higgins (1952) show that the wave heights follow a Rayleigh distribution. This linear theory is extended to include second-order bound-wave effects (Tayfun, 1980; Forristall, 2000). The inclusion of second-order nonlinearity leads to sharper crests and flatter troughs with improved statistical comparison to field measurements. The crest-to-trough wave heights, however, remain the same. The deviations of the nonlinear wave statistics from Gaussian distribution can be quantified by the non-Gaussian values of skewness and kurtosis, where skewness and kurtosis are the second and third moment of the surface elevation. For unidirectional wavefields with narrow-banded spectrum, using second-order theory, the skewness and kurtosis are Skew=$3k_p\sigma$ and Kur=$3+24(k_p\sigma)^2$, where k_p and σ are peak wavenumber and standard deviation of the surface elevation (Longuet-

Higgins, 1963; Onorato et al., 2009). Observations from wave tank experiments indicate that the classical linear and second-order theories do not describe the nonlinear statistics accurately for the wavefields which are steep and narrow-banded (Onorato et al., 2004, 2009).

For general directional wave spectra which have finite or broad band, it is challenging to derive nonlinear wave statistics theoretically because the governing equations of the wave dynamics are highly nonlinear. The numerical approaches, therefore, are quite useful in this context. For the wavefields with narrow-band spectra and small spreading angle, considerable non-Gaussian statistics are observed in NLS-type simulations (Socquet-Juglard et al., 2005). As the spectral spreading angle becomes large, numerical simulations of NLS-type models indicate that the statistics are close to linear or second-order theoretical predictions (Gramstad and Trulsen, 2007).

The NLS-type models are derived assuming the wavefield is narrow-banded and the wave envelope is slowly varying with space and time. How applicable of these assumptions on the realistic wavefields is questionable. In this chapter, we study the nonlinear statistics of directional random wavefields, including significant wave height, wave skewness and kurtosis, and distribution of wave crests, using direct simulation approach (SNOW). The reliability of using SNOW simulation in describing nonlinear wave statics are verified by direct comparisons with wave basin experiment (Onorato et al., 2009). To assess the validity of using NLS-type models in describing the nonlinear statistics of ocean waves, the predictions from BMNLS simulations are compared with SNOW simulations.

4.2 Significant wave height

The significant wave height H_s introduced by Sverdrup and Munk (1947) during World War II, defined originally as the average of the one-third highest wave heights, was used to describe the severity of the wavefield. However, it is rarely calculated using its original definition. Now the significant wave height is more commonly defined as four times of the standard deviation of the surface elevation. For narrow-banded

wavefield with Rayleigh-distributed wave height, H_s=4.01σ, where σ is standard deviation of the surface elevation (Ochi, 2005). In this thesis, the later definition is used, that is, $H_s \equiv 4\sigma$.

Figure 4-1 shows the evolution of the significant wave height from experiments (Onorato et al., 2009) and SNOW simulations. The wavefields have same steepness and spectral bandwidth but different initial spreading angles. For a range of spreading angles considered, SNOW predictions agree qualitatively well with experiments. We find the reduction of H_s, as a measure of the energy dissipation due to wave breaking, is more significant in wavefields with small spreading angles. The reduction of H_s decreases as the spreading angle increases. This is consistent with the experimental observations where the wave breaking is found more frequent in the wavefields with small spreading angles (Onorato et al., 2009). When comparing temporal variational results from SNOW simulations with spatial records from experiments, x=$c_g t$ is used to transfer from temporal variations to spatial variations, where c_g is the group velocity of the dominant wave, . A discussion on the validity of this transformation can be found in Toffoli et al. (2010). Figure 4-2 shows the influence of the spreading angle and spectral bandwidth on the change of H_s due to wave breaking, measured as $H_s/H_{s,0}$, where H_s is the value of significant wave height at time $t = 150T_p$ and $H_{s,0}$ is the initial value. We find the energy dissipation reduces with the spreading angle increases. For small spreading angles, the change of H_s is nearly independent of spectral bandwidth. For large spreading angles, the reduction of H_s is more significant for wavefield with broader spectral bandwidth. Because wave breaking is a nonlinear wave phenomenon, the reduction of wave breaking in wavefields with broad spreading angle suggests the deduction of nonlinearity in short-crested wavefields.

4.3 Skewness of surface elevation

Skewness, the third moment of surface elevation, is defined as

$$\text{Skewness} = \langle \eta^3 \rangle / \langle \eta^2 \rangle^{3/2}, \tag{4.1}$$

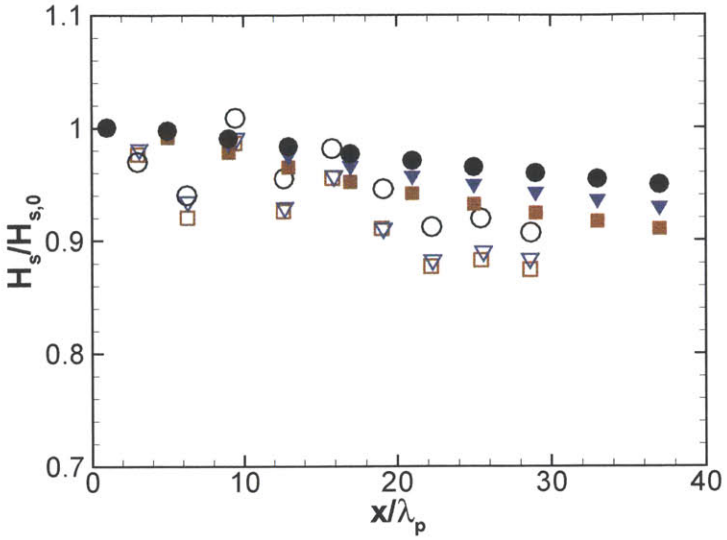

Figure 4-1: Spatial variation of significant wave height H_s scaled by its initial value for wavefields initially given by the JONSWAP spectra with ε=0.16, γ=6, with a range of spreading angles. Experiment (Onorato et al., 2009): $\Theta = 12°$ (□), 21° (▽) and 62° (○). HOS: $\Theta = 12°$ (■), 21° (▼); and 62° (●). Results are obtained using SNOW with breaking model (2.12) described in Chapter 2 §2.2.2 with β_1=8, β_2=30.

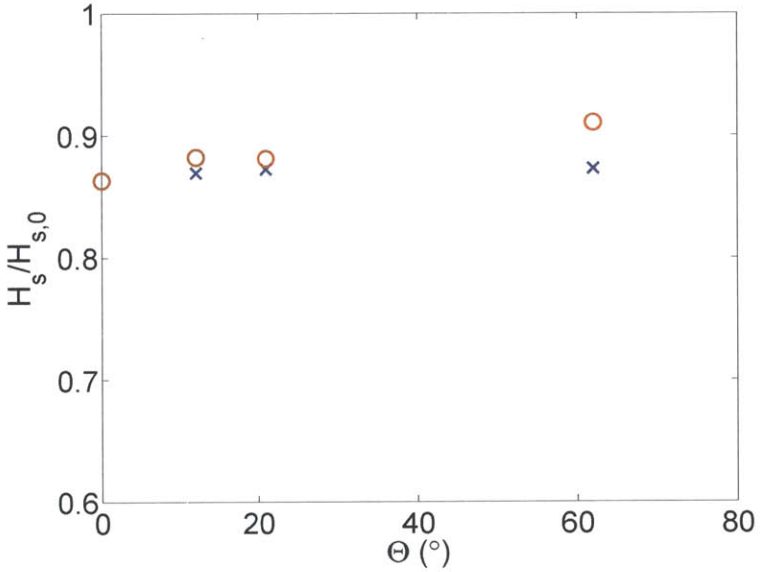

Figure 4-2: Significant wave height at time $t = 150T_p$ scaled by its initial value, $H_s/H_{s,0}$, as a function of the initial spreading angle Θ for wavefields H_s=0.08 m T_p=1 sec ($\varepsilon = 0.16$), and γ=3 (×), 6 (○).

where $\langle\cdot\rangle$ denotes an ensemble average, and $\langle\eta^2\rangle$ and $\langle\eta^3\rangle$ are second and third-order moment of the surface elevation. It measures the asymmetry of the free surface elevations and larger value of skewness suggest more skewed/assymetric wave profile. The value of skewness vanishes for linear Gaussian wavefields. The second-order theory for unidirectional narrow-banded spectrum gives (Longuet-Higgins, 1963; Onorato et al., 2009):

$$\text{Skewness} = 3k_p\sigma. \tag{4.2}$$

4.3.1 Evolution of skewness

Figure 4-3 shows the evolution of skewness from experiments (Onorato et al., 2009), BMNLS and SNOW simulations for wavefields with a range of spectral bandwidth and spreading angle. The BMNLS and SNOW models give similar predictions on the skewness, close to the second-order theoretical prediction $3k_p\sigma \approx 0.24$, although, comparing with experiments, both of the numerical models overestimate the skewness, specially at the locations away from the wavemaker. For all the wavefields, from the SNOW simulations, skewness quickly deviates from its initial Gaussian value over a very short time scale and stays rather stationary over the time because skewness is mainly contributed by the second-order wave nonlinearity and are not sensitive to higher order wave nonlinearities. Moreover, the variations of skewness have a similar pattern for all cases considered and are not sensitive to the spreading angle of the wavefields.

4.3.2 Effect of spectral directional spreading on skewness

Figure 4-4 shows the effect of initial spreading angle on the average value of skewness ($\langle$Skewness$\rangle$) over evolution time $0 \leqslant t/T_p \leqslant 150$. We observe that a directional spreading in general leads to a reduction in the average value of skewness, and $\langle$Skewness$\rangle$ decreases as spreading angle increases. These results indicate the second-order nonlinearity is in general weaker in directional wavefields.

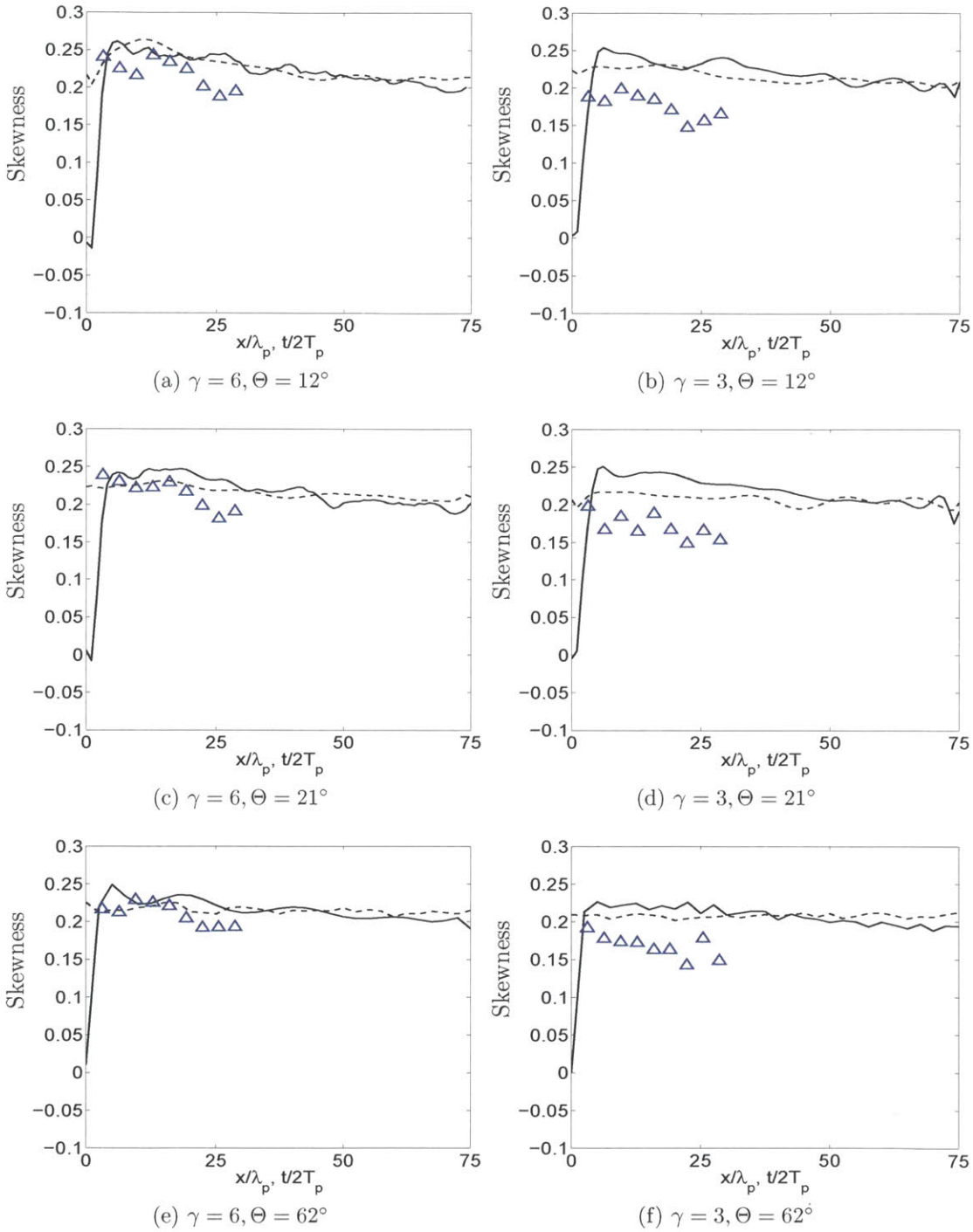

(a) $\gamma = 6, \Theta = 12°$ (b) $\gamma = 3, \Theta = 12°$

(c) $\gamma = 6, \Theta = 21°$ (d) $\gamma = 3, \Theta = 21°$

(e) $\gamma = 6, \Theta = 62°$ (f) $\gamma = 3, \Theta = 62°$

Figure 4-3: Evolution of skewness for directional JONSWAP wavefields H_s=0.08 m and T_p=1 sec ($\varepsilon = 0.16$), γ=6 ((a), (d), (e)), γ=3 ((b), (c), (f)). Experiment (Onorato et al., 2009) ($\triangle$) (for γ=3, ε=0.13 and for γ=6, ε=0.16); SNOW (—); BMNLS (- - -).

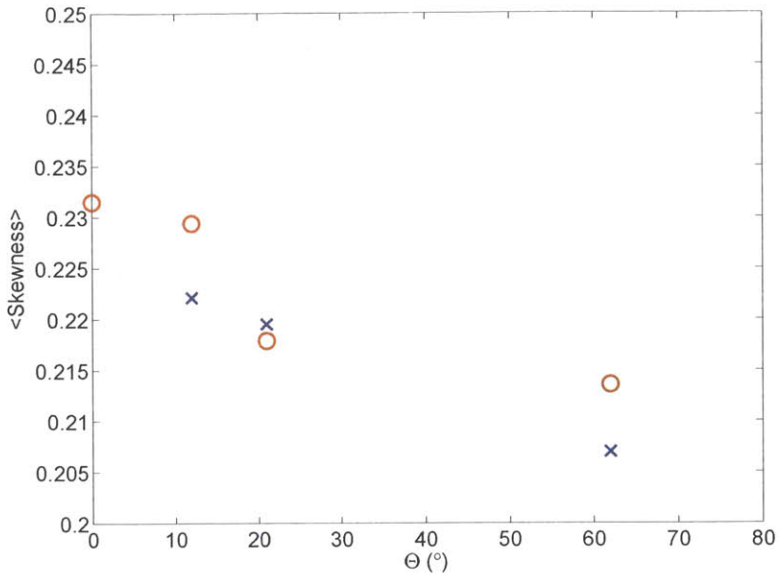

Figure 4-4: Dependence of the average skewness ⟨Skewness⟩ on the initial spreading angle Θ for wavefields H_s=0.08 m T_p=1 sec ($\varepsilon = 0.16$), and γ=3 (×), 6 (◯).

4.4 Kurtosis of surface elevation

Kurtosis, which is the fourth moment of the wave elevation, is defined as

$$\text{Kur} = \langle \eta^4 \rangle / \langle \eta^2 \rangle^2, \tag{4.3}$$

where $\langle \cdot \rangle$ denotes an ensemble average, and $\langle \eta^2 \rangle$ and $\langle \eta^4 \rangle$ are second and fourth-order moment of the surface elevation. Kurtosis denotes the peakness of one distribution. Greater value of kurtosis suggests a longer tail of the distribution. For a linear Gaussian wavefield Kur=3. The second-order approximation is (Longuet-Higgins, 1963; Onorato et al., 2009)

$$\text{Kur} = 3 + 24(k_p\sigma)^2. \tag{4.4}$$

Kurtosis strongly depends on third-order wave nonlinearity and it is regarded as an important indicator of the probability of rogue wave occurrence and greater the value of kurtosis higher occurrence probability of rogue waves (Mori and Janssen, 2006).

4.4.1 Evolution of kurtosis

Figure 4-5 shows comparisons of the evolution of kurtosis for wavefields with a range of γ and Θ, obtained from experiments (Onorato et al., 2009), SNOW and BMNLS simulations. For both BMNLS and SNOW models, for wavefields with small spreading angles, we find that kurtosis increases from initial value of Kur$\approx$3, coinciding with the initial rapid spectral broadening observed in figures 3-5 (Chapter 3) due to modulational instability. BMNLS overestimates kurtosis during this time. At large time, in BMNLS simulations, kurtosis reduces to the Gaussian value. In SNOW simulations, however, kurtosis decreases slowly to a quasi-stationary value, which is nearly invariant over time $100 \leqslant t/T_p (= 2x/\lambda_p) \leqslant 150$ (and beyond). The quasi-stationary kurtosis obtained from SNOW is considerably non-Gaussian. For wavefields with large spreading angles (e.g., θ=62°), both BMNLS and SNOW predict slower variations of kurtosis over the time, consistent with the slower spectral change observed in figure 3-7 (Chapter 3). Overall, SNOW consistently obtains greater values of kurtosis for longer time. SNOW also appears to obtain better comparisons to measurements over the different wavefields considered.

We define the maximum kurtosis $\mathrm{Kur}^{\max}$ as the maximum value of kurtosis during the evolution time $0 \leqslant t/T_p \leqslant 150$, and the average value of kurtosis Kur^{+} during the stationary phase of the wavefield $100 \leqslant t/T_p \leqslant 150$. Figure 4-6 shows the dependence of $\mathrm{Kur}^{\max}$ on the initial spreading angle from experiments (Waseda et al., 2009) and SNOW simulations. For wavefields with small spreading angles, $\mathrm{Kur}^{\max}$ decreases quickly with Θ increases. For wavefields with spreading angle $\Theta \geqslant 40°$, $\mathrm{Kur}^{\max}$ decreases to a value close to Gaussian Kur=3 and $\mathrm{Kur}^{\max}$ is nearly independent of Θ.

The spatial homogeneity of kurtosis may be in the regional-dependence of the value of maximum kurtosis

Figure 4-7 shows the dependence of $\mathrm{Kur}^{\max}$ on the domain size from BMNLS and SNOW simulations. We find that kurtosis is not homogeneous locally. For small size domains, the value of $\mathrm{Kur}^{\max}$ varies considerably in both of the simulations. For large

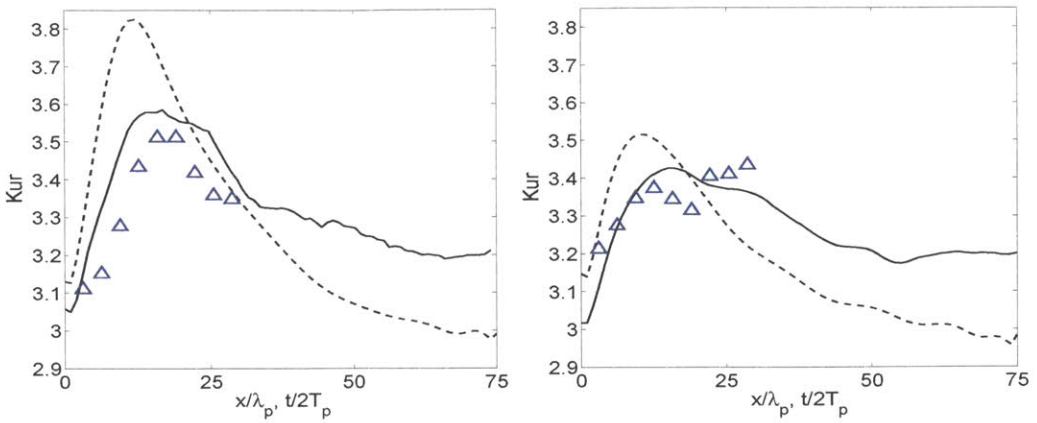

(a) $\gamma = 6$, $\Theta = 12°$ (b) $\gamma = 3$, $\Theta = 12°$

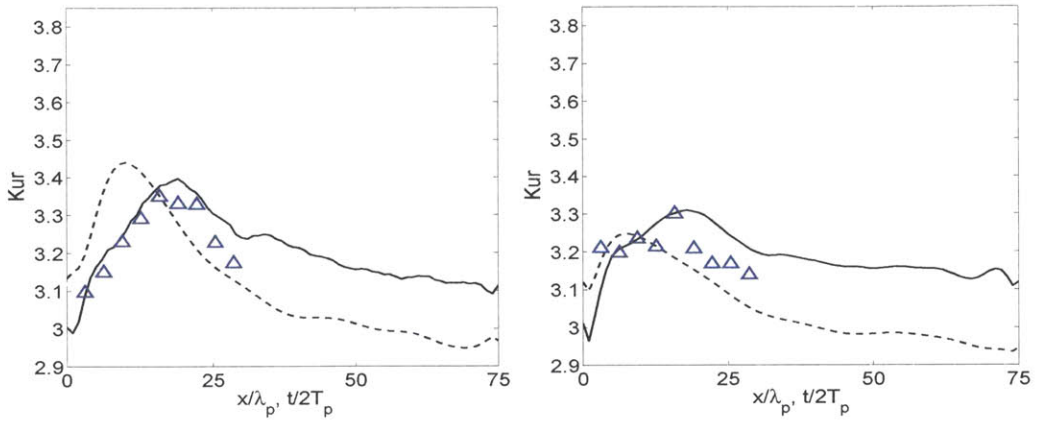

(c) $\gamma = 6$, $\Theta = 21°$ (d) $\gamma = 3$, $\Theta = 21°$

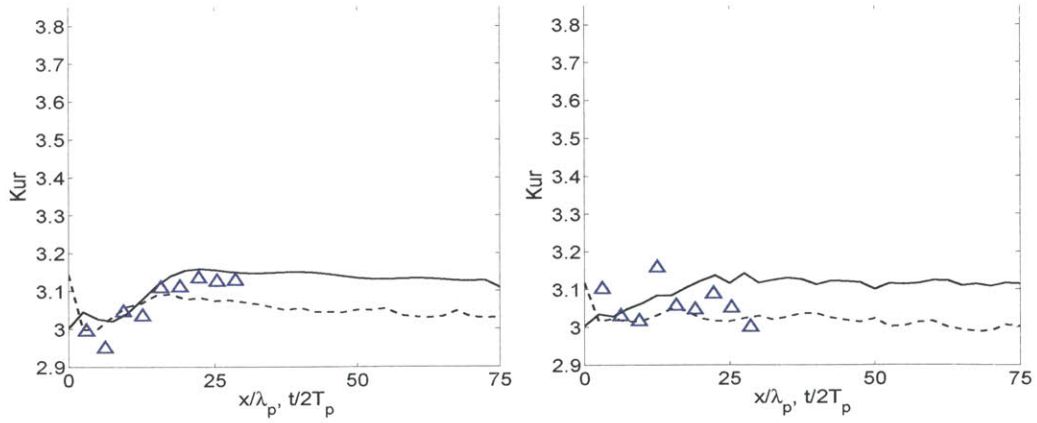

(e) $\gamma = 6, \Theta = 62°$ (f) $\gamma = 3, \Theta = 62°$

Figure 4-5: Spatial variation of kurtosis for directional wavefields H_s=0.08 m and T_p=1 sec ($\varepsilon = 0.16$), γ=6 ((a), (c), (e)), γ=3 ((b), (d), (f)). Experiment (Onorato et al., 2009) ($\triangle$) (for γ=3, ε=0.13 and for γ=6, ε=0.16); SNOW (—); BMNLS(- - -).

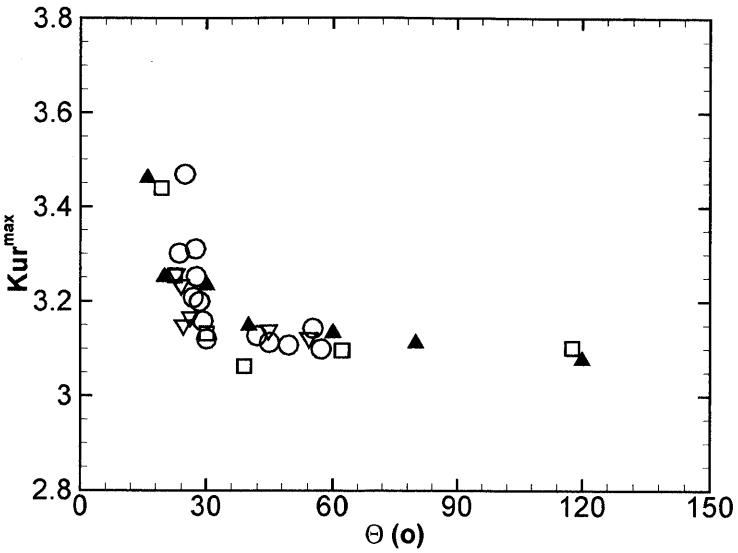

Figure 4-6: The dependence of maximum kurtosis $\mathrm{Kur}^{\max}$ on the initial directional spreading Θ for directional wavefields H_s=0.0415 m, T_p=0.7626 s and γ=3.0. Experiments (Waseda et al., 2009) □ (H_s=3.50 cm), ○ (H_s=4.15 cm), ▽ (H_s=5.00 cm); SNOW▲ (H_s = 4.15 cm). The SNOW simulation results are obtained based on an ensemble average of 5 realizations

size domains, the value of $\mathrm{Kur}^{\max}$ no longer depend on the domain size. This suggests the value of wave kurtosis is statistically useful only for wavefields with large domain sizes.

4.4.2 Quasi-stationary value of kurtosis Kur^{+}

Aggregating $O(200)$ SNOW simulations for wavefields with a broad range of initial spectral parameters, figure 4-8 plots the predicted values of $(\mathrm{Kur}^{\max}, \mathrm{Kur}^{+})$ for these cases. We see a clear relationship between Kur^{+} and $\mathrm{Kur}^{\max}$. For smaller $\mathrm{Kur}^{\max}(\leqslant 3.2)$, $\mathrm{Kur}^{+} \approx \mathrm{Kur}^{\max}$; while for greater $\mathrm{Kur}^{\max}$, Kur^{+} remains almost constant ($\approx$3.2) with increasing values $\mathrm{Kur}^{\max}$. These suggest that for evolutions with $\mathrm{Kur}^{\max} \lesssim \mathrm{Kur}^{a}$, $\mathrm{Kur}^{\max}$ is reached in the asymptotic quasi-steady state; while evolutions with values of $\mathrm{Kur}^{\max} \gtrsim 3.2$ are reached at an early phase of the evolution which then decrease towards the longer-time average value Kur^{+}. The former case is indicative of significant modulational instability resulting in rapid change of the (initial)

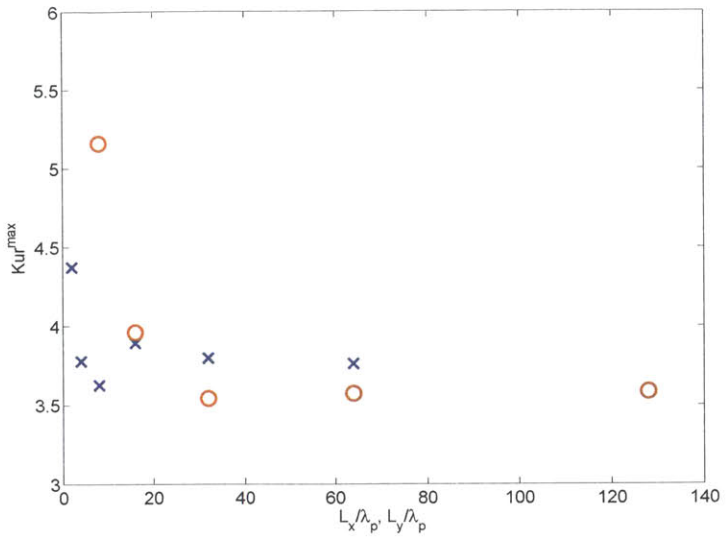

Figure 4-7: The dependence of maximum kurtosis $\mathrm{Kur}^{\max}$ on the domain size for JONSWAP directional wavefields H_s=0.08 m and T_p=1 sec ($\varepsilon = 0.16$), γ=6. BMNLS ($\times$) and SNOW ($\bigcirc$).

spectra and strongly nonlinear/non-Gaussian wave statistics, while the latter case corresponds to the absence of significant modulational instability resulting in a slowly varying wavefield and slowly developing non-Gaussian statistics. An estimation of kurtosis using second-order theory for narrow-banded waves gives $\mathrm{Kur}_2 = 3+24(k_p\sigma)^2$ (Longuet-Higgins, 1963; Onorato et al., 2009). For the wavefields in figure 4-8, the largest (initial) steepness is $\varepsilon = 0.14$, which obtains Kur_2=3.12. This value is considerably smaller than 3.2. This suggests the second-order approximation is not accurate for general broad-band wavefields or the higher-order nonlinearities are required to obtain an accurate description.

4.4.3 Dependence of kurtosis on initial BFI and spreading angle

For unidirectional wavefields described by very narrow-banded Gaussian spectra, Mori et al. (2007) find kurtosis only depends on the so-called Benjamin-Feir index (BFI):

$$\mathrm{Kur} = 3 + 2\pi \mathrm{BFI}^2/\sqrt{3}. \tag{4.5}$$

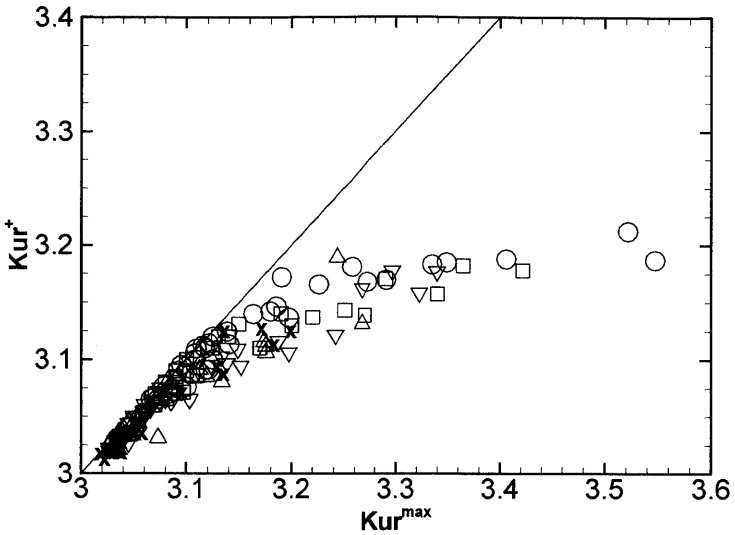

Figure 4-8: $\mathrm{Kur}^{\mathrm{max}}$ vs. Kur^{+} for ~ 200 wavefields with a range of spectral parameters ε, γ and Θ. ε=0.06 ($\times$); 0.08 (Δ); 0.1 (∇); 0.12 ($\square$); 0.14 ($\bigcirc$).

BFI is introduced in Janssen (2003) as a measurement of the importance of modulational instability, and it is defined as

$$\mathrm{BFI} = \varepsilon/(\Delta k/k_p), \tag{4.6}$$

where Δk is the spectral bandwidth. The direct dependence of kurtosis on BFI for unidirectional seas with more general sea conditions is also observed in wave flume experiment (Onorato et al., 2004). However, For short-crested wavefields, it is found from experiments and NLS-type simulations that the dependence of kurtosis on BFI is greatly reduced (Onorato et al., 2009; Waseda et al., 2009; Gramstad and Trulsen, 2007).

Figure 4-9 plots $\mathrm{Kur}^{\mathrm{max}}$ versus (initial) BFI-square for wavefields with a range of Θ, ε and γ. The effect of direction spreading on the correlation between kurtosis and BFI-square is clearly seen, especially for large BFI. For the very narrow spreading case(s), $\mathrm{Kur}^{\mathrm{max}}$ has a clear linear correlation with BFI^2. For large Θ, a linear (trend) correlation between Kur and BFI is still seen; however, the slope with which $\mathrm{Kur}_{\mathrm{max}}$ depends on BFI decreases with Θ increases, so that for very broad spread case,

$\mathrm{Kur}_{\mathrm{max}}$ is almost independent of BFI. Although for a given Θ, we observe linear-like correlation between kurtosis and BFI. For given BFI, the value of kurtosis is still unknown if the influence of spreading angle is not considered. Using just BFI without Θ information creates huge scatter because of different rate of dependencies on BFI.

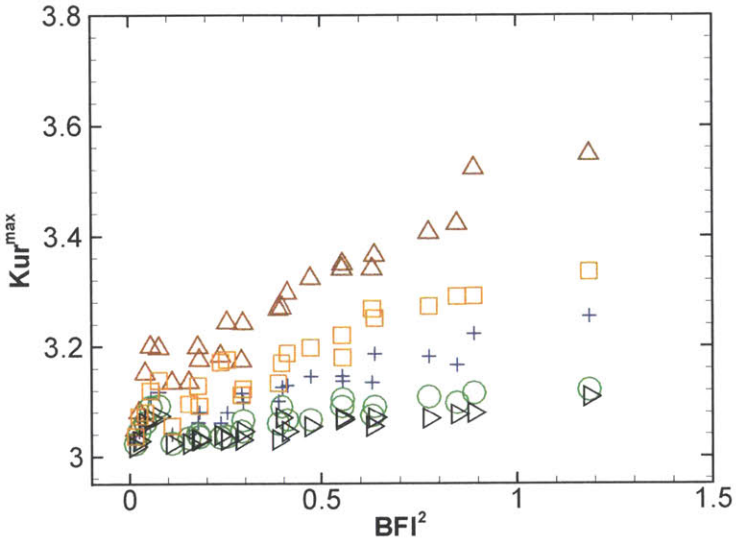

Figure 4-9: Dependence of maximum kurtosis $\mathrm{Kur}^{\mathrm{max}}$ on the initial BFI^2 for wavefields with a range of ε, γ and Θ in MIT-Wave. Θ=20° (△); Θ=30° (□); 40° (+); 80° (○); 120° (▷).

Figure 4-10 shows the overall dependence of $\mathrm{Kur}^{\mathrm{max}}$ on BFI and spreading angle of the initial spectrum. For given BFI, $\mathrm{Kur}^{\mathrm{max}}$ decreases as Θ increases. For wavefields with relatively small spreading angle $\Theta \lesssim 40°$, there is a clear dependence of $\mathrm{Kur}^{\mathrm{max}}$ on BFI. Strong non-Gaussian statistics are observed for wavefields with small spreading angles. For wavefields with relatively large spreading angle $\Theta \gtrsim 60°$, $\mathrm{Kur}^{\mathrm{max}}$ is close to Kur=3 and becomes nearly independent of BFI.

4.5 Exceeding probability of wave crests

In SNOW simulations the wave crests are defined as the local maxima of the wave surface. In BMNLS simulations the wave crests are estimated as the third-order upper

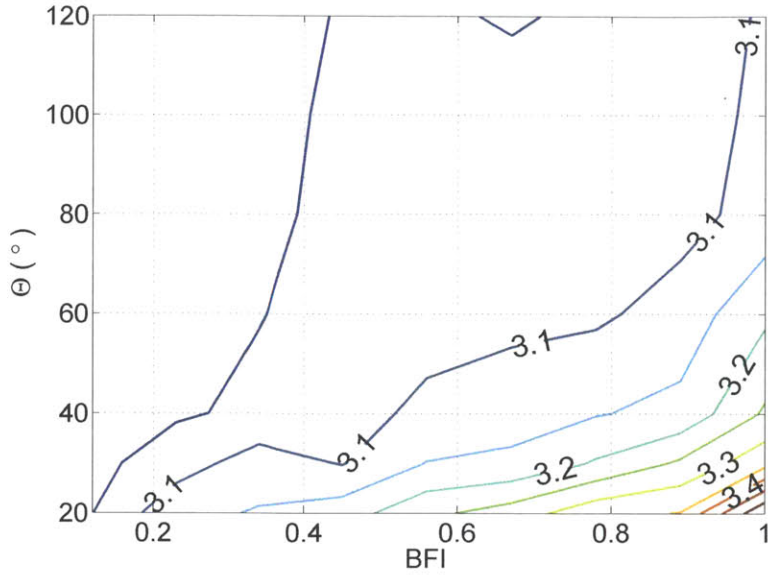

Figure 4-10: The contour plots of $\mathrm{Kur}^{\mathrm{max}}$ as a function of initial BFI and spreading angle Θ.

surface envelope

$$\eta_c = \overline{\eta} + |B_1| + |B_2| + |B_3|, \tag{4.7}$$

where B_1, B_2 and B_3, defined as (2.18) (Chapter 2), are slowly varying in space and time, and have magnitudes of first, second and third order in wave steepness; $\overline{\eta}$, also slowly varying in space and time, is the mean surface elevation and is third order in wave steepness.

4.5.1 Evolution of crest distribution

Figure 4-11 shows the exceeding probability of crests for unidirectional wavefields from experiments (Onorato et al., 2009), BMNLS and SNOW simulations. Predictions from linearized (Rayleigh) and second-order theories (Tayfun, 1980) are also shown as references. For all the locations considered, Rayleigh theory underestimates the probability of crests considerably, especially for large crests. At the location close to the wavemaker, $x/\lambda_p(= t/2T_p)$=3.1, probability of crests obtained from experiments, BMNLS, and SNOW simulations all are close to the second-order theory. At location $x/\lambda_p(= t/2T_p)$=15.9, where kurtosis reaches its maximum in the experi-

ment, significant deviations of probability of large crests from linear (Rayleigh) and second-order predictions are observed in both BMNLS and SNOW simulations. Similar features are observed for the comparison at location $x/\lambda_p(= t/2T_p)$=28.7, the farthest location from the wavemaker in the experiment (figure 4-11(c)), although the exceeding probability is reduced somewhat relative to x/λ_p=15.9. Figure 4-11(d) shows the results for $t/2T_p$=x/λ_p=50, where the wavefield statistics have reached the quasi-steady state (t/T_p=$2x/\lambda_p \gtrsim O(100)$) predicted by SNOW (see §4.4). In this case, BMNLS predictions are close to second-order theory, while SNOW predicts considerably larger probability of large crests.

Figure 4-12 to figure 4-14 show the exceeding probability of crests for directional wavefields with spreading angle Θ =12°, 21° and 62° from experiments (Onorato et al., 2009), BMNLS and SNOW simulations. Predictions from linearized (Rayleigh) and second-order theories (Tayfun, 1980) are also shown as references. Comparing figure 4-12 and figure 4-11, the evolutional trend of exceeding probability of crests with small spreading angle is very similar to the unidirectional case. For the wavefield with slightly broader spreading angle (Θ = 21°), the evolution of crests is similar to the case Θ = 12°, except that the deviation of large crest probability from the Rayleigh and second-order theory is somewhat decreased comparing the case Θ = 12°. Figure 4-14 shows the crest distribution for initially broadly spread sea, Θ=62°, BMNLS and SNOW simulations give similar predictions and agree well with experiments. In this case, second-order theory provides a good prediction on the crest distribution.

In all cases, SNOW appears to obtain a better overall comparison to measured values.

4.5.2 Effect of initial spreading angle on crest probability

Figure 4-15 shows summary plots of the exceeding probability of wave crests at location x/λ_p=28.7 for wavefields with different spreading angles. The occurrence of large crests is greatly enhanced in wavefields with small spreading angles. The probability of large crests decreases as the initial spreading angle increases. Referring the spectral change observed in §3.4 (Chapter 3), the large crest occurrence is significantly

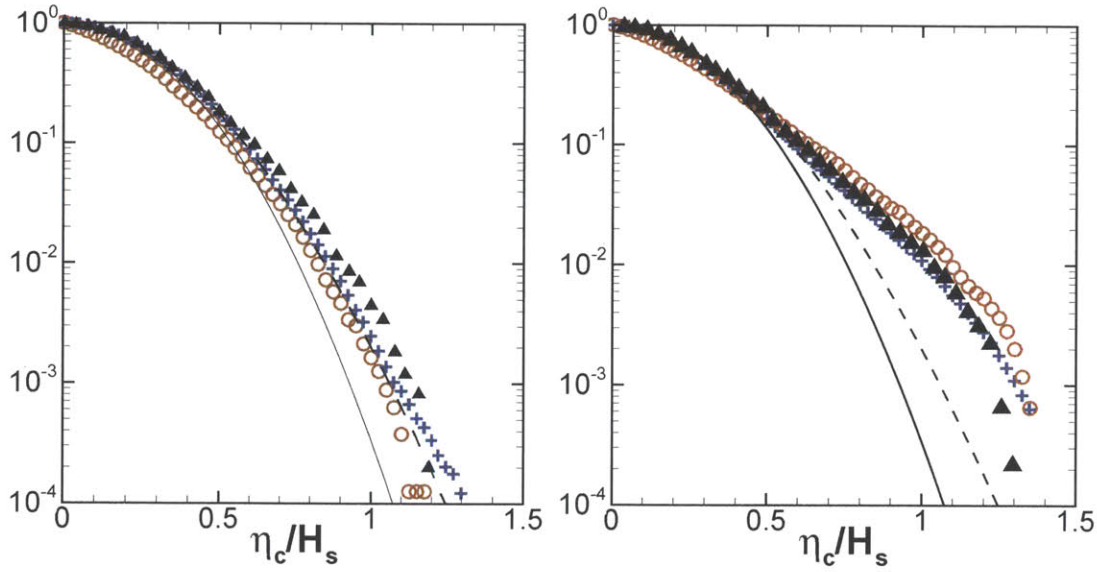

(a) $x/\lambda_p = 3.1$

(b) $x/\lambda_p = 15.9$

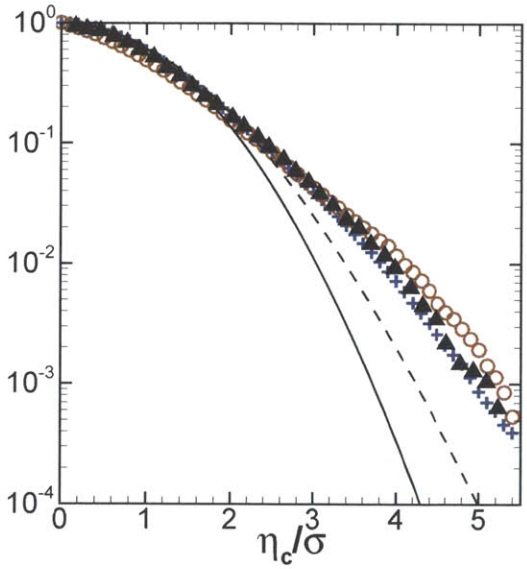

(c) $x/\lambda_p = 28.7$

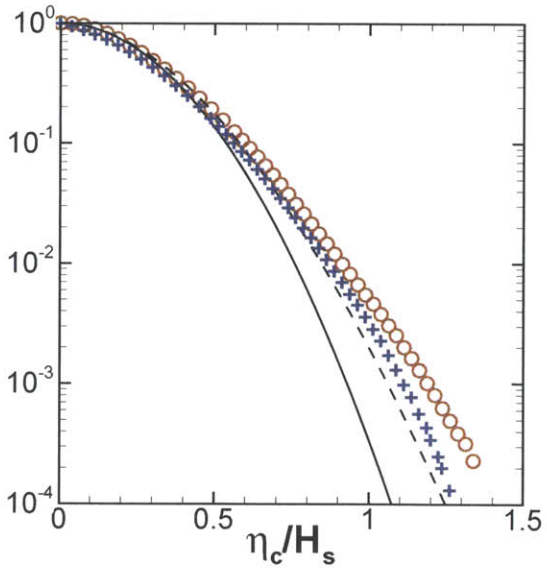

(d) $x/\lambda_p = 50$

Figure 4-11: Exceeding probability of wave crests for unidirectional JONSWAP wavefields with H_s=0.08 m, T_p=1 sec, $\gamma = 6$. SNOW (○); BMNLS (+); Rayleigh distribution (—); second-order theory (Tayfun, 1980) (- - -); experiment (Onorato et al., 2009) (▲). SNOW and BMNLS results are averaged over five realizations.

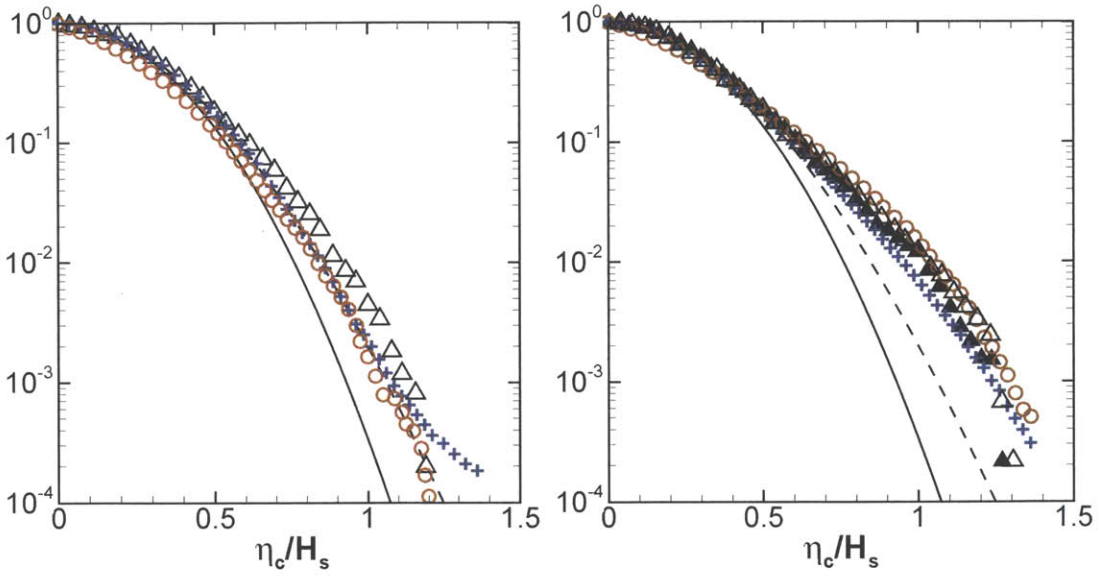

(a) $x/\lambda_p = 3.1$ (b) $x/\lambda_p = 15.9$

(c) $x/\lambda_p = 28.7$ (d) $x/\lambda_p = 50$

Figure 4-12: Exceeding probability of wave crests for JONSWAP wavefields with H_s=0.08 m, T_p=1 sec, $\gamma = 6$ and Θ=12° (corresponding to exponents $s = 840$ in Mitsuyasu spreading function $\cos^s\theta$). SNOW (○); BMNLS (+); Rayleigh distribution (—); second-order theory (Tayfun, 1980) (- - -); compared to experiment (Onorato et al., 2009, 2008) for △: unidirectional; and ▲: s=840. (experimental values for $\Theta = 12°$ at x/λ_p=28.7 are not published). SNOW and BMNLS results are averaged over five realizations.

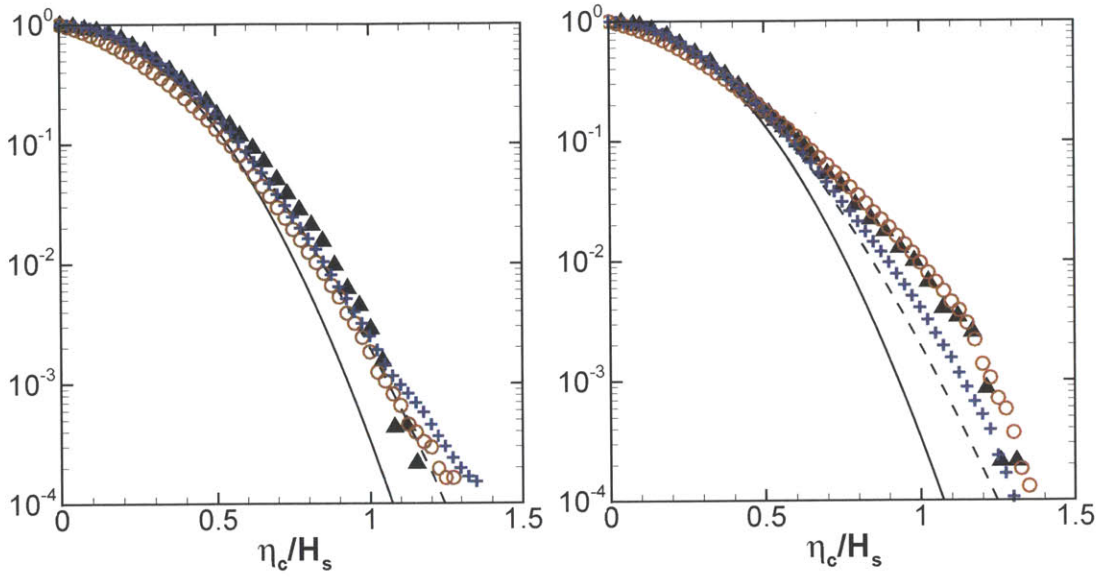

(a) $x/\lambda_p = 3.1$ (b) $x/\lambda_p = 15.9$

(c) $x/\lambda_p = 28.7$ (d) $x/\lambda_p = 50$

Figure 4-13: Exceeding probability of wave crests for JONSWAP wavefields with H_s=0.08 m, T_p=1 sec, $\gamma = 6$ and Θ=21° (corresponding to exponents $s = 200$ in Mitsuyasu spreading function $\cos^s\theta$). SNOW (○); BMNLS (+); Rayleigh distribution (—); second-order theory (Tayfun, 1980) (- - -); experiment (Onorato et al., 2009) (▲). SNOW and BMNLS results are averaged over five realizations.

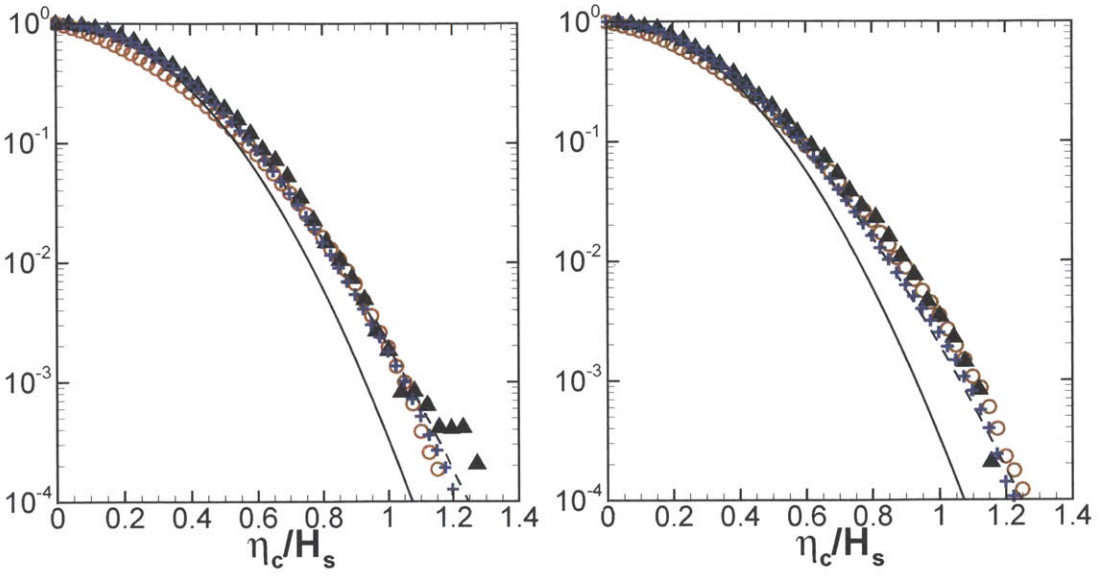

(a) $x/\lambda_p = 3.1$

(b) $x/\lambda_p = 15.9$

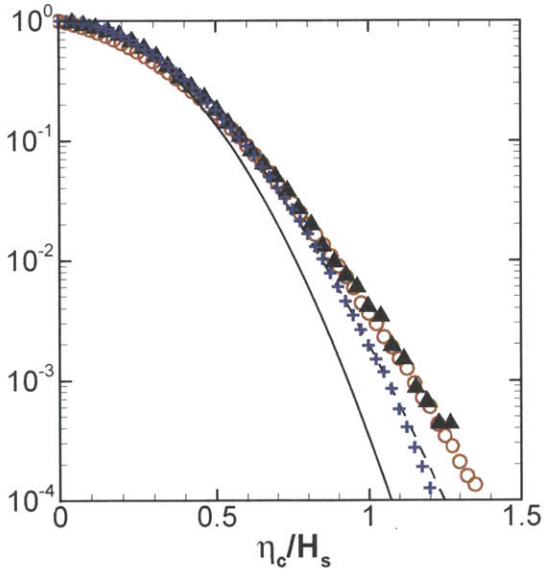

(c) $x/\lambda_p = 28.7$

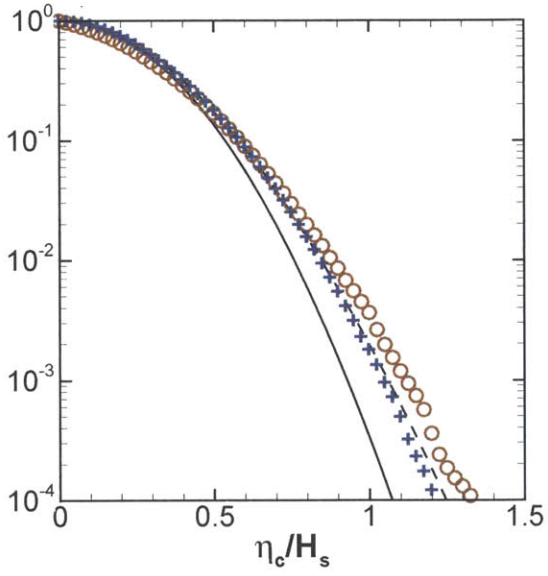

(d) $x/\lambda_p = 50$

Figure 4-14: exceeding probability of wave crests for JONSWAP wavefields H_s=0.08 m, T_p=1 sec, $\gamma = 6$ and Θ=62° (corresponding to exponents $s = 24$ in Mitsuyasu spreading function $\cos^s\theta$). SNOW (○); BMNLS (+); Rayleigh distribution (—); second-order theory (Tayfun, 1980) (- - -); experiment (Onorato et al., 2009) (▲). SNOW and BMNLS results are averaged over five realizations.

increased in the wavefields where the modulational instability plays an important role in the spectral evolution.

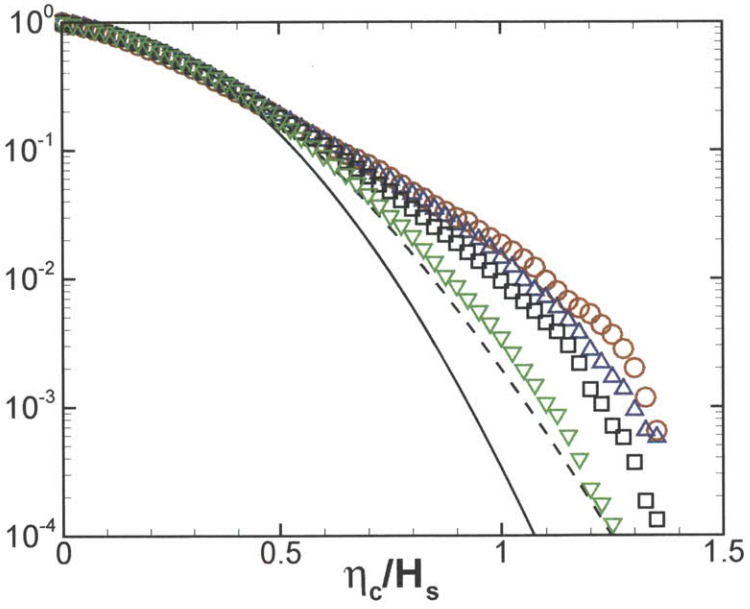

Figure 4-15: Exceeding probability of wave crests at x/λ_p=28.7 for wavefields H_s=0.08 m, T_p=1 sec, $\gamma = 6$. Unidirectional (◯), Θ=12° (△), 21° (□), 62° (▽).

4.6 Summary and conclusions

In this chapter, we study the nonlinear wave statistics and their dependence on the spectral parameters. The reliability of SNOW simulations in describing nonlinear wave statistics is confirmed by direct comparisons with wave basin experiments (Onorato et al., 2009). The linear and second order theory of wave statistics are examined by direct comparisons with SNOW simulations. We find for the wavefields with small spreading angles, the wave statistics are considerably non-Gaussian and the occurrence of the large crests are greatly enhanced relative to first and second-order theory. The non-Gaussian statistics are closely related to the spectral change due to modulational instability. In next chapter (Chapter 5), we show modulational instability also plays a crucial role in the generation of rogue waves.

The validity of using NLS-type models (BMNLS) in describing the nonlinear s-

tatistics is investigated by comparing with SNOW simulations. Up to short evolution time $t/T_p \lesssim 100$, we find BMNLS predictions agree with SNOW reasonably well. For large time, however, BMNLS simulations underestimate the non-Gaussian statistics in comparison with SNOW simulations. SNOW overall obtains a better comparison with wave basin experiments.

Chapter 5

Rogue wave occurrence in deep water

5.1 Introduction

Rogue waves are extraordinarily large surface waves that appear infrequently in the ocean. A common definition of rogue waves is waves whose heights exceed twice the significant wave height. Occurrences of such large waves have been reported worldwide from ships, offshore platforms and radars (Lawton, 2001; Kharif and Pelinovsky, 2003; Forristall, 2005). Collisions with such waves have caused catastrophic damages to ship and offshore structures (Kharif and Pelinovsky, 2003; Toffoli et al., 2005). The picture of rogue wave approaching a merchant ship shown in §1.4 (Chapter 1), reproduced here in figure 5-1, shows the wave has crest height much higher than the ambient waves and it also has a long crest length leading to a shape similar to "wall of water". Moreover, it has an extremely steep front indicating its strong nonlinearity.

The prediction of occurrence probability of rogue waves is of central interest. In linear random wave theory, for unidirectional wavefield that is narrow-banded in frequency, Longuet-Higgins (1952) shows that wave height and thus rogue wave occurrence follow a Rayleigh distribution. The inclusion of second-order nonlinearity leads to sharper crests and flatter troughs with improved statistical comparison to field measurements (Tayfun, 1980; Forristall, 2000), although the crest to trough wave

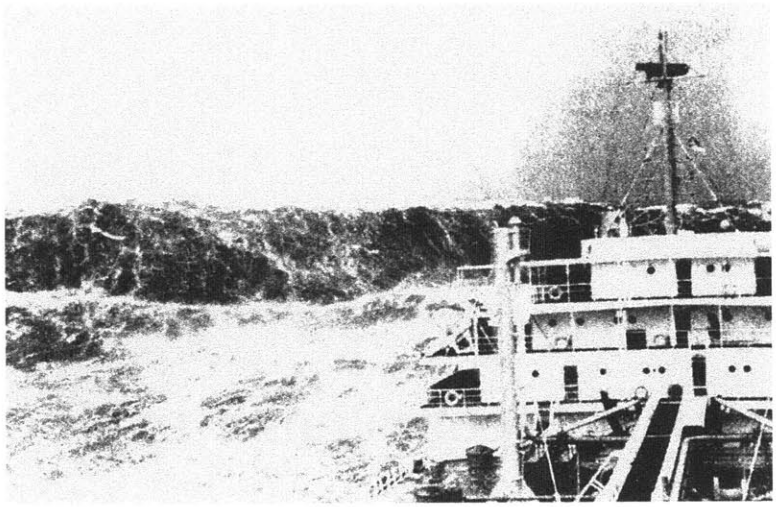

Figure 5-1: Rogue wave in the Bay of Biscay, France, in 1940. Picture from National Oceanic and Atmospheric Administration (NOAA).

height remains the same. Significantly, observations indicate that the classical linear and second-order theories do not properly describe the occurrence of large waves with heights greater than twice the significant wave height (Skourup et al., 1997; Stansell, 2005).

There are several mechanisms that could be responsible for the formation of rogue waves. The mechanisms that, to the leading order, do not involve nonlinear wave-wave interactions, commonly referred as *linear mechanisms*, are summarized below. Recent reviews of the rogue wave problem may be found in Kharif and Pelinovsky (2003); Kharif et al. (2009); Dysthe et al. (2008); Slunyaev et al. (2011).

1. *Focusing due to wave dispersion*

   Gravity surface waves are dispersive and their phase (and group) velocity is proportional to the square root of the wave length and inversely proportional to the wave frequency. Large waves can form when a large number of waves are superposed at one location with proper phases and directions due to wave dispersion. For unidirectional wavefields, this can happen when long waves overtake short waves.

2. *Wave-current interactions*

   The formation of freak waves in the area where the current is strong, such as

Gulf stream and Agulhas current, could be due to the "blocking" effect of the current (Lavrenov, 1998). When waves propagate into a current with different directions, the waves are stopped by the current at the locations where the wave group velocity in the inertial frame is zero. This causes a localized energy accumulation at such locations leading to formation of large waves in that area.

3. *Geometrical focusing due to bathymetry*

   When waves propagate into varying bathymetry, they are refracted due to the change of bottom topography, leading to the focusing of wave energy in particular places. This might be responsible for the formation of large waves in the areas along irregular coastlines.

The linear mechanisms might be responsible for occurrences of rogue waves in certain locations, however, they cannot explain a large number of freak wave events reported from the open sea where the current and bathymetry play a minimal role.

Nonlinear mechanism is fundamentally different from linear mechanism. In linear wave theory, the waves with different frequencies are independent and they do not interact with each other. However, in nonlinear mechanism, one unstable wave mode may absorb energy from other waves. When nonlinearity is present, significant interactions occur at the third order and it is postulated that nonlinear focusing due to modulational instability is an important generation mechanism of rogue waves. It is known that an initially periodic Stokes wave train is unstable to side-band modulations (Benjamin and Feir, 1967) which causes the wave train to disintegrate into wave groups within which large waves could form. This type of Benjamin-Feir modulational instability also obtains in narrow-band irregular wavefields (Alber, 1978), and its relationship to rogue wave formation has been studied theoretically, experimentally and numerically.

For unidirectional narrow-banded seas, Janssen (2003) shows theoretically that the modulational instability can cause an exponential growth of the central wave mode leading to the formation of large waves, and the importance of modulational instability can be measured by the Benjamin-Feir index (BFI) which is a ratio of the wavefield steepness to the spectral bandwidth. By including the third-order nonlin-

earity of modulational instability, the wave height follows the modified Edgeworth-Rayleigh (MER) distribution, which involves the fourth-order moment or kurtosis of the surface elevation (Mori and Yasuda, 2002a; Mori and Janssen, 2006). MER distribution deviates from Rayleigh distribution and predicts increasing probability of rogue waves with increasing kurtosis. In the special case when the wavefield is described by very-narrow-band Gaussian spectrum, kurtosis is specified by the value of BFI (Mori and Janssen, 2006). The strong dependence of rogue wave occurrence on BFI in unidirectional wavefields is supported by wave flume experiments (Onorato et al., 2004) and numerical simulations based on nonlinear Schrödinger equation (NLS) (Onorato et al., 2001).

For general 3D wavefields with broad directional spreading, statistical theories on rogue wave occurrence accounting for nonlinearity are difficult to obtain, and much of the investigation is based on numerical simulations. For computational efficiency, many existing studies use model equations based on the wave envelope approximation (assuming narrow-band waves) such as nonlinear Schrödinger (NLS) or modified nonlinear Schrödinger equations (BMNLS) (Dysthe, 1979; Trulsen and Dysthe, 1996). Using BMNLS simulations, Gramstad and Trulsen (2007) study the effect of crest length on the rogue wave occurrence and find that the importance of modulational instability is reduced with decreasing crest length. For broad directional wavefields, the probability of rogue wave occurrence is found to be close to Gaussian statistics and nearly independent of BFI. The similarity between nonlinear and linear statistics for broad directional wavefield has also been found in wave basin experiments (Waseda et al., 2009; Onorato et al., 2009).

NLS-type simulations are potentially limited by the inherent assumptions of narrow-band spectrum and slowly-varying spatial and temporal modulations. These assumptions may not obtain in general, since it is known that even initially narrow-band spectrum may become broad-banded due to nonlinear evolution (Dysthe et al., 2003). For steep waves (which might be expected in rogue wave events), the assumption of slowly-varying modulation may also be invalid locally. One of the objectives of present work is to assess the range of validity of wave envelope models for rogue wave pre-

dictions. This is addressed in the recent study of Toffoli et al. (2010) where BMNLS is compared with direct simulation using a high-order spectral method (Dommermuth and Yue, 1987; West et al., 1987). Toffoli et al. (2010) show that BMNLS and HOS obtain qualitatively similar results which compare reasonably with wave tank experiments of Onorato et al. (2009). The simulations are however limited to relatively short evolution time (suggested by the scale of the tank experiments) and small computational domains.

A few attempts have been made to study extreme waves using fully nonlinear simulations, but most of simulations are performed for unidirectional wavefields or directional wavefields over limited domain size. Using a higher-order spectrum method, Mori and Yasuda (2002b) find high-order nonlinearities play an important role in the formation of extreme waves for unidirectional wavefields with narrow-banded spectra. Zakharov et al. (2002) develop a numerical method for fully nonlinear wavefield evolution. Bateman et al. (2001) simulate evolution of a realistic wavefield of limited size, using a spectral wave model allowing fully nonlinear simulations of broad-band broad spreading wavefield. In this thesis, we apply the direct simulations, SNOW, to study the generation mechanisms, occurrence probability and kinematics of rogue waves.

In this chapter, we apply direct numerical simulations to study the generation mechanisms and occurrence probability of rogue waves in three-dimensional wavefields using SNOW. We focus on the importance of modulational instability as a generation mechanism of rogue waves over space and time scales $\mathcal{L} \times \mathcal{L}$ and $\mathcal{T}$ with $\mathcal{L}/\lambda_p, \mathcal{T}/T_p \sim O(\varepsilon^{-2})$, where λ_p and T_p are the peak wavelength and period of the (initial) spectrum. $\varepsilon = H_s k_p/2$ is the steepness of the wavefield, where H_s is the significant wave height and k_p is the peak wavenumber. Our objectives are to obtain the occurrence probability, mechanisms and geometry of rogue wave events and their quantification in terms of statistical and spectral parameters. To achieve this, we perform a significant number of large-scale nonlinear 3D SNOW simulations covering broad range of spectral parameters. The spatial and temporal scales of the simulations are commensurate with those of quartet resonance interactions, including BF-type

instabilities. The simulations are performed on massively-parallel high-performance computing (HPC) platforms. For comparison, we also implement BMNLS and compare SNOW and BMNLS model predictions on rogue wave occurrence over the large-scale space-time domains we consider.

5.2 Statistical models

In linear random wave theory, the wavefield is considered as a superposition of sinusoidal wave components with different frequencies and directions of propagation. Using large number theory, the surface elevation is described by Gaussian distribution. Under this assumption, Longuet-Higgins (1952) shows that, for unidirectional waves that is narrow-banded in frequency, wave height and thus rogue wave occurrence follow a Rayleigh distribution. The exceeding probability of wave heights with a Rayleigh distribution is

$$P_R(h) = Pr[H > h] = \exp\left(-\frac{h^2}{8\sigma^2}\right), \tag{5.1}$$

where H is the wave height and σ is the standard deviation of the surface elevation. The crest height in linear theory is half of the wave height, and the exceeding probability of wave crests is

$$P_A(a) = Pr[A > a] = \exp\left(-\frac{a^2}{2\sigma^2}\right). \tag{5.2}$$

This linear theory is extended to include second-order bound-wave effects (Tayfun, 1980; Forristall, 2000). The exceeding probability of wave crests based on the second order theory, according to Tayfun (1980), is:

$$P_A^T(a) = \exp\left[-\frac{1}{\sigma^2}(a + 1 - \sqrt{2a+1})\right]. \tag{5.3}$$

where A=$H/2$ is the crest height. The inclusion of second-order nonlinearity leads to sharper crests and flatter troughs with improved statistical comparison to field

measurements, although the crest to trough wave height remains the same. Field observations indicate that the classical linear and second-order theories do not properly describe the occurrence of large waves with heights greater than twice the significant wave height (Skourup et al., 1997; Stansell, 2005).

5.3 Collections of large-scale SNOW wavefields: MIT-Wave database

To study the occurrence probability of rogue waves in directional random wavefields, we simulate a large number of nonlinear directional ocean wavefields using a broad range of spectral parameters, including representative steepness ε, spectral bandwidth controlled by the peakness enhancement factor γ, and spreading angle Θ. The representative steepness, $\varepsilon \equiv H_s k_p/2$ (H_s, k_p are the significant wave height and peak wavenumber), ranges from 0.06 to 0.14 with increment 0.2. The peakness enhancement parameter, γ, varies over 1, 3.3, 5, 6 and 10. The spreading angle Θ = 20°, 30°, 40°, 60°, 80°, 100°, and 120°. The input parameter values for MIT-Wave dataset are summarized in Table 5.1. For unidirectional wavefields, a measure of the importance of modulational instability is BFI$\equiv\varepsilon/(\Delta k/k_p)$ and the modulational instability is important if BFI$> 1/\sqrt{2}$ (Janssen, 2003). The corresponding value of BFI for the MIT-Wave dataset ranges from 0.1 to 1.1 (the spectral bandwidth Δk is calculated as the half width at half maximum of the wavenumber spectrum). We hereafter refer this database as MIT-Wave. Number of $O(10)$ realizations are performed where needed to achieve convergent statistics.

Table 5.1: Input parameters for MIT-Wave database.

ε	0.06, 0.08, 0.1, 0.12, 0.14
γ	1, 3.3, 5, 6, 10
Θ (°)	20, 30, 40, 60, 80, 100, 120

5.4 Identification of rogue waves

For the purpose of identifying a large *rogue wave* (group), we use the criterion that the crest-to-trough wave height H exceeds $H/H_s \geq \alpha$. In this study, we use α=2.0. In the context of long-crested waves, the identification of a wave (or wave group), and hence its crest-to-trough height, obtains readily in terms of, say, zero crossings. For short-crested seas, this is problematic. Nevertheless, for the identification of rogue waves, large wave events are generally isolated from the ambient small waves, which allows us to obtain a meaningful identification and definition.

The precise definition of the extent of the rogue wave event (within which $H \geq \alpha H_s$ obtains) is not unique. For the present study, we use the following procedure (the results below are unaffected if "crest" and "trough" are interchanged). At any given time, for every local maxima ("crest") located at, say, $\mathbf{x}_c$=(x_c, y_c), in the wavefield, we define a rectangular region $\mathcal{R}$ centered on $\mathbf{x}_c$, given by

$$\mathcal{R} = \{(x,y) || x - x_c| \leqslant \lambda_p, |y - y_c| \leqslant C_y\}, \tag{5.4}$$

where C_y=$\lambda_y/2$ is the average crest length and λ_y is the average wave length in y direction, defined as

$$\lambda_y = 2\pi/\langle k_y^2 \rangle^{1/2}, \ \langle k_y^2 \rangle = \frac{\int k_y^2 \Psi(\mathbf{k}) \, d\mathbf{k}}{\int \Psi(\mathbf{k}) \, d\mathbf{k}}. \tag{5.5}$$

Within each $\mathcal{R}$ we search for all the minima ("trough") points to evaluate the corresponding H. If the maximum H thus obtained satisfies $H/H_s \geqslant \alpha$, a rogue wave is identified associated with the corresponding crest-tough pair $\mathbf{x}_c$ and $\mathbf{x}_t$. In the case where a $\mathbf{x}_t$ is shared by two or more $\mathbf{x}_c$ (centered on different $\mathcal{R}$), only the ($\mathbf{x}_c$, $\mathbf{x}_t$) pair that obtains the maximum H among these (and the corresponding $\mathcal{R}$) is counted. The influence of using a different $\mathcal{R}$ and a different value of threshold α on the resulting identified rogue waves is discussed in appendix B.

Figure 5-2(a) shows an example of the locations of the large waves identified in a directional wavefield using the approach described above and Figure 5-2(b) shows

one example of identified rogue wave with $H/H_s \approx 2.43$.

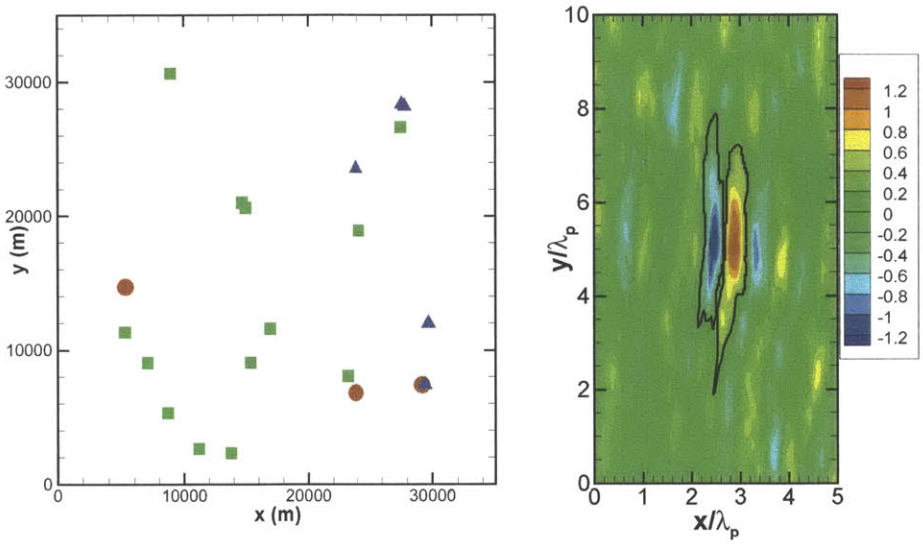

(a) (b)

Figure 5-2: (a) The locations of large waves found in a directional wavefield H_s=12 m, T_p=13 s γ=5 and Θ=60°. $1.9 \leqslant H/H_s < 2.0$ (■), $2.0 \leqslant H/H_s < 2.1$ (▲), $H/H_s \geqslant 2.2$ (●). (b) One example of identified rogue wave with $H/H_s \approx 2.43$. Zero contours around the crest and trough points of the rogue wave (—).

5.5 Number probability of rogue waves

The number probability of rogue waves at given time, denoted as P_N, can be defined as:

$$P_N = N_{\text{rogue}}/N_w, \tag{5.6}$$

where N_{rogue} is the number of rogue waves identified, and N_w the total number of waves in the wavefield. For general short-crested wavefield, precise value of N_w can be difficult to obtain (or define). For specificity, we set

$$N_w = L_x L_y/\bar{a}, \tag{5.7}$$

where $\bar{a}$ is the average area of a wave, estimated by (Piterbarg, 1996; Socquet-Juglard et al., 2005):

$$\bar{a} = \lambda_x \lambda_y / \sqrt{2\pi}, \tag{5.8}$$

and

$$\lambda_x = 2\pi / \langle k_x^2 \rangle^{1/2}, \quad \text{and} \quad \lambda_y = 2\pi / \langle k_y^2 \rangle^{1/2} \tag{5.9}$$

where

$$\langle k_x^2 \rangle = \int k_x^2 \Psi(\mathbf{k}) \, d\mathbf{k} / \int \Psi(\mathbf{k}) \, d\mathbf{k}, \tag{5.10a}$$

$$\langle k_y^2 \rangle = \int k_y^2 \Psi(\mathbf{k}) \, d\mathbf{k} / \int \Psi(\mathbf{k}) \, d\mathbf{k}. \tag{5.10b}$$

Note that with this definition, N_w varies in time as the spectrum changes, and generally increases with directional spreading.

5.5.1 Evolution of number probability of rogue waves

Figure 5-3 shows the evolution of P_N from SNOW and BMNLS simulations. The convergence of the P_N statistic, estimated by the standard deviation $P_N/\sqrt{N_{\text{rogue}}}$ is indicated as error bars. For small (initial) spreading angles (Figure 5-3(a), (b)), from both BMNLS and SNOW simulations, P_N increases initially over a time scale corresponding to the rapid spectral change (see Figure 3-5 in Chapter 3), reaching values of $P_N^{\max}$ that are an order of magnitude greater than the linear prediction. During this time, BMNLS overestimates P_N. At larger time, P_N decreases, with BMNLS predictions approaching the Rayleigh prediction P_R, where for SNOW, P_N approaches a quasi-stationary non-Gaussian value which is multiple times greater than P_R and BMNLS predictions. Contrasting Figures 5-3(a) and (b), it is clear that the magnitude of P_N is greater for narrower (initial) frequency bandwidth (larger γ) corresponding to stronger modulational instability.

For greater spreading angles, the qualitative trends remain, although the amplification of P_N relative to P_R is progressively less significant. For the very broadly-spreading case Θ=62°, P_N in SNOW generally increases slowly with time (towards

quasi-stationary value); while in BMNLS, P_N monotonically decreases with time, eventually becomes smaller than P_R.

In summary, we see that P_N generally increases with decreasing Θ and increasing γ, with $P_N^{\max}$ many times greater than P_R for narrow spreading wavefields, and generally reached over a relatively small time scale corresponding to the initial strong modulational instability of the wavefield. In all cases, SNOW obtains a nonlinear quasi-static state after long time, with P_N^+ still multiple times greater than P_R (and BMNLS predictions).

Comparing Figure 5-3 and the evolution of kurtosis shown in Figure 4-5 (Chapter 4, §4.4.1) corresponding to the same (initial) spectral parameters, the qualitative resemblance between P_N and kurtosis is quite apparent, suggesting that the latter is a good indicator/predictor of the likelihood of rogue waves.

5.5.2 Number probability of rogue waves in the quasi-stationary state

To better understand the quasi-stationary probability of rouge waves in large time predicted by SNOW, we plot P_N^+ versus $P_N^{\max}$ for $\sim$ 200 wavefields in MIT-Wave dataset. Similar to figure 4-8, the ensemble of wave cases fall into two relatively distinct categories. For cases with relatively small $P_N^{\max}(\lesssim 4P_R)$, $P_N^+ \approx P_N^{\max}$, indicating that $P_N^{\max}$ is obtained in the quasi-stationary state. For greater $P_N^{\max}$, P_N^+ shows some scatter but is aggregated around $P_N^+/P_R \sim 4$. These latter cases correspond to situations where $P_N^{\max}$ is achieved due to strong initial modulational instability before the quasi-stationary state.

We want to point out that the calculation of P_N could be problematic. First, N is estimated statistically and how relevant of the estimated N to the precise total number of waves in the wavefield is not known to the author. Second, the value of N could vary significantly due to the spreading angle broadening as wavefields evolve. Figure 5-5 shows the variation of N for directional wavefields with different spreading angles. It shows, for the wavefield with narrow-banded spectrum and narrow spreading angle,

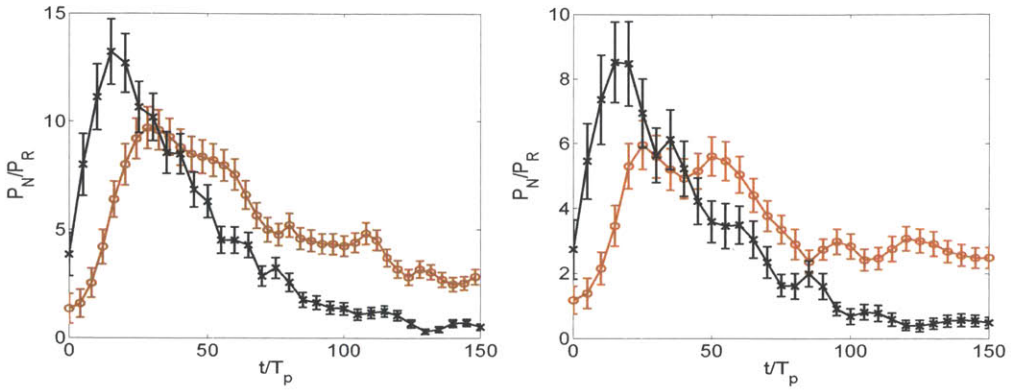

(a) $\gamma = 6, \Theta = 12°$ (b) $\gamma = 3, \Theta = 12°$

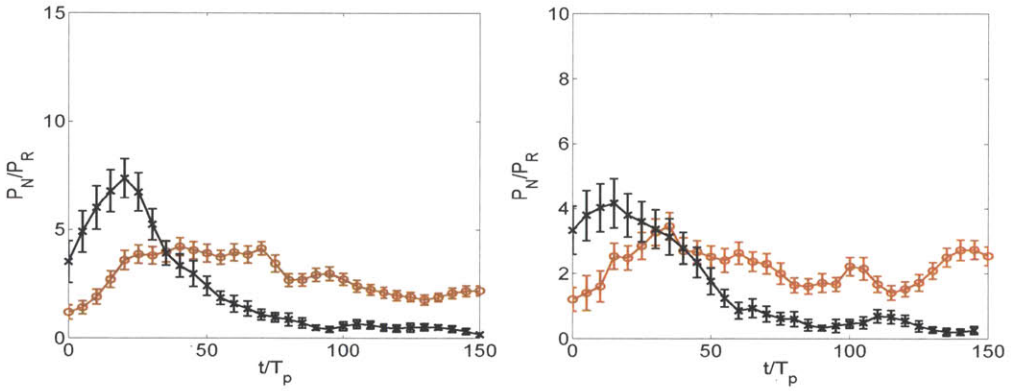

(c) $\gamma = 6, \Theta = 21°$ (d) $\gamma = 3, \Theta = 21°$

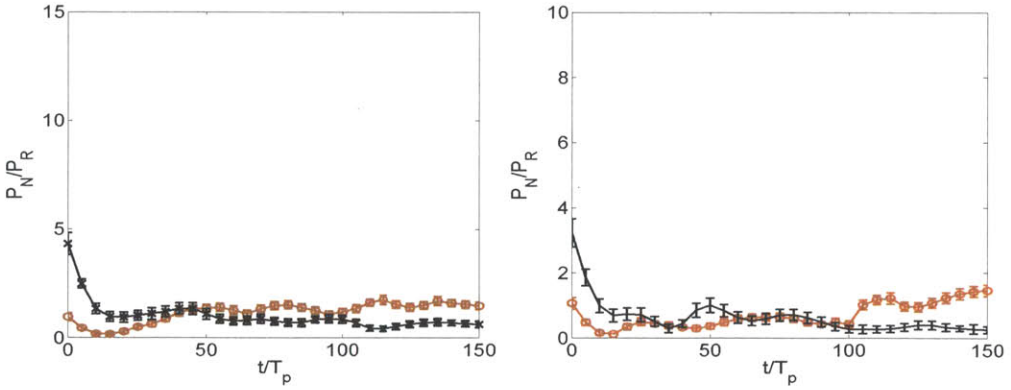

(e) $\gamma = 6, \Theta = 62°$ (f) $\gamma = 3, \Theta = 62°$

Figure 5-3: Evolution of the number probability of rogue waves P_N for JONSWAP wavefields H_s=0.08 m, T_p=1 sec, γ =3 and 6, and spreading angles Θ=12°, 21° and 62°. SNOW (○); BMNLS (×). The standard deviations of the statistic, $\pm P_N/\sqrt{N_{\text{rogue}}}$ are indicated as error bars. Results are scaled by the Rayleigh distribution P_R=3.35×10^{-4} for $H/H_s \geqslant \alpha$, α=2. SNOW and BMNLS results are averaged over five realizations.

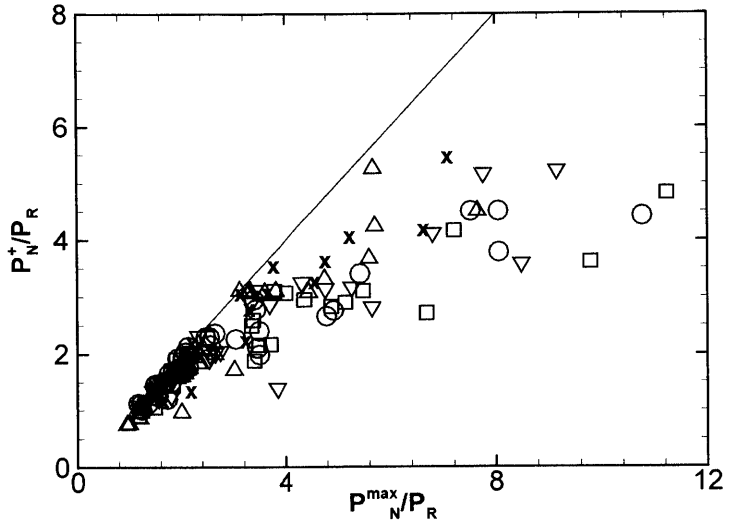

Figure 5-4: $P_N^{\max}$ vs. P_N^+ for $\sim$ 200 wavefields with a range of ε, γ and Θ from MIT-Wave. ε=0.06 ($\times$); 0.08 (Δ); 0.1 (∇); 0.12 ($\square$); 0.14 ($\bigcirc$).

N can increase to four times of its initial value. To overcome the difficulties related to the calculation of P_N, we here introduce a new quantity to measure the rogue wave occurrence based on the area they occupy. We define the rogue wave area probability, P_A, as

$$P_A = A_{\text{rogue}}/A, \tag{5.11}$$

where S_R is the coverage area of rogue waves and S is the area of the entire wavefield. A detailed study on rogue wave area statistics are demonstrated in section 5.6.

5.6 Area probability of rogue waves

5.6.1 Definition of area probability of rogue waves

As we pointed out earlier, the number probability of rogue waves in terms of relative frequency of *number* of (rogue) waves is problematic for (very) broad directional spreading waves. For short-crested seas, N_{rogue} does not distinguish between events of different sizes, while the validity of (5.7) for estimating the total number of waves N_w may be questioned. The problem is exacerbated by the fact that even initially

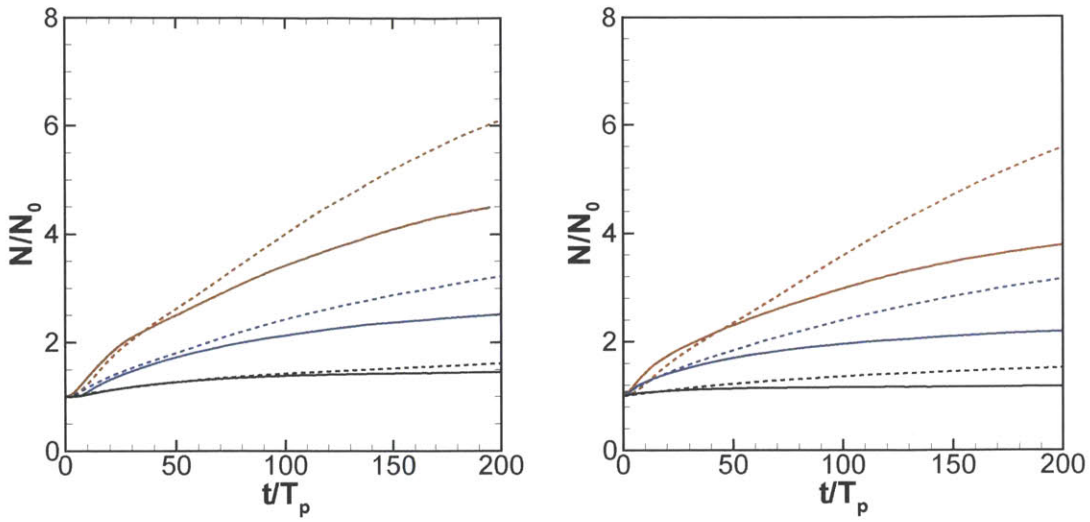

Figure 5-5: Variation of estimated total number of waves N_w using (5.7) in the wavefields H_s=0.08 m, T_p=1 s with (a) γ=6 and (b) γ=3. $\Theta = 15°$: SNOW (—); BMNLS (- - -). $\Theta = 31°$: SNOW (—); BMNLS (- - -). $\Theta = 72°$: SNOW (—); BMNLS (- - -).

narrow spreading spectra tend to evolve toward broader spreading and furthermore, as the spectrum evolves, N_w is a time varying (but a priori unknown) function. For instance, for the case of figure 5-3(a), N_w at $t = 150T_p$ is over 4 times its initial value shown in figure 5-5.

To overcome these problems, we introduce a general and robust area probability of rogue waves, denoted by P_A, as a useful measure of the likelihood of rogue waves for general directional spread wavefields. P_A is defined as

$$P_A = A_{\text{rogue}}/A_w, \tag{5.12}$$

where A_{rogue} is the total area of rogue waves, and A_w=$L_x L_y$ is the total area of the wavefield under consideration (which, unlike N_w, is invariant). After a rogue wave event is identified, its area a_{rogue} is defined as the sum of the zero elevation contours enclosing the crest point $\mathbf{x}_c$ and trough point $\mathbf{x}_t$ associated with the rogue wave (figure 5-2b). Clearly P_A is applicable for any general directional spreading sea.

Note that while both P_N, $P_A \in [0,1]$ are well defined as probability, their quantitative values can differ substantially for short-crested wavefields. In general, P_A and P_N are related by:

$$P_A/P_N = \bar{a}_{\text{rogue}}/\bar{a}, \tag{5.13}$$

where

$$\bar{a}_{\text{rogue}} = A_{\text{rogue}}/N_{\text{rogue}} \tag{5.14}$$

is the average area of a rogue wave. In Chapter 8, §8.2, we find $\lambda_{\text{rogue}} \approx \lambda_p$, so that $P_A/P_N = \bar{\lambda}_{\text{rogue}}/\lambda_x >\sim 1$ (since $\lambda_p > \lambda_x$ for JONSWAP spectrum). For short-crested wavefields, the value of $\bar{a}_{\text{rogue}}/\bar{a}$ is not generally known. In Chapter 8, §8.2, we find that $\bar{a}_{\text{rogue}}/\bar{a} \approx O(5)$ (depending on wavefield parameters, see figure 8-6).

5.6.2 Evolution of area probability of rogue waves

Figure 5-6 shows the evolution of P_A for the same cases considered in §5.5. Comparing figures 5-6 and 5-3, we observe that the qualitative trends of P_N and P_A are somewhat similar, except that the magnitude of P_A is several times (~ 5) greater than P_N, indicative of $\bar{a}_{\text{rogue}}$ much greater than $\bar{a}$, characteristic of short-crested seas. The notable difference between P_A and P_N are seen in the initially narrow spread cases (Θ=12° and 21°), where BMNLS now consistently under estimates P_A throughout the evolutions. As observed earlier, P_A predicted by HOS again displays the quasi-stationary state after $t/T_P \gtrsim O(100)$; while the BMNLS predicted P_A diminishes monotonically with increasing time.

5.6.3 Area probability of rogue waves in the quasi-stationary state

Figure 5-7 shows the relation between P_A^+ and $P_A^{\max}$ for the ~200 wavefields we used in the MIT-Wave dataset. We observe very similar pattern relative to those

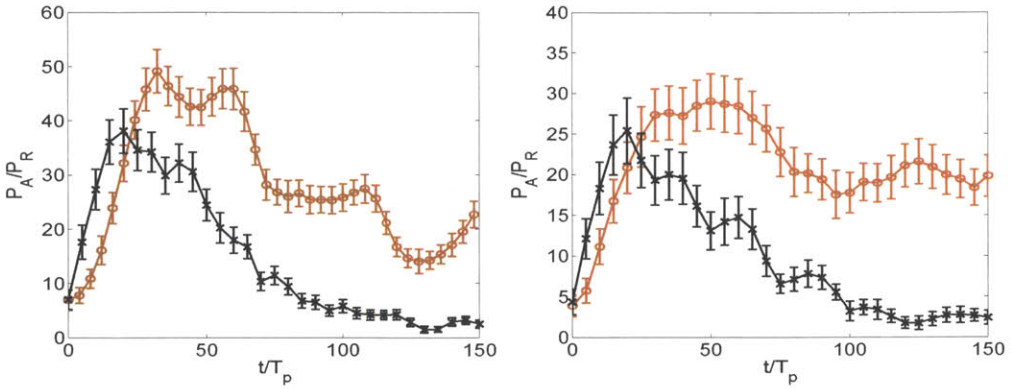

(a) $\gamma = 6, \Theta = 12°$ (b) $\gamma = 3, \Theta = 12°$

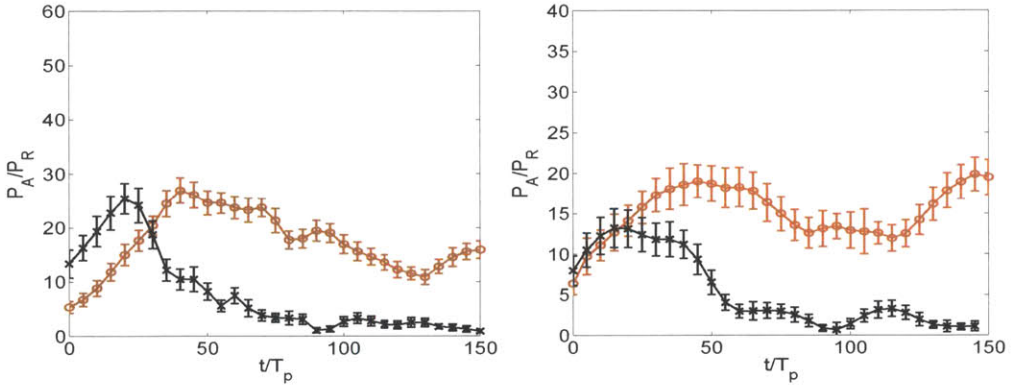

(c) $\gamma = 6, \Theta = 21°$ (d) $\gamma = 3, \Theta = 21°$

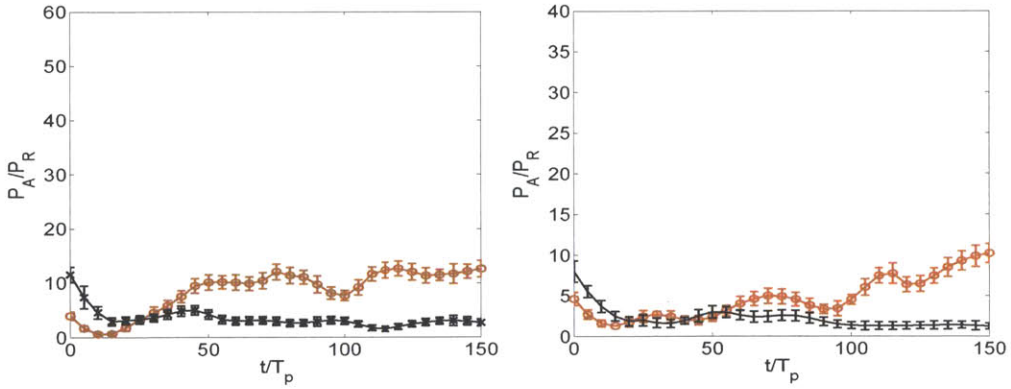

(e) $\gamma = 6, \Theta = 62°$ (f) $\gamma = 3, \Theta = 62°$

Figure 5-6: Evolution of the number probability of rogue waves P_A for JONSWAP wavefields H_s=0.08 m, T_p=1 sec, γ =3 and 6, and spreading angles Θ=12°, 21° and 62°. SNOW (○); BMNLS (×). The standard deviations of the statistic, $\pm P_A/\sqrt{N_{\text{rogue}}}$ are indicated as error bars. Results are scaled by the Rayleigh distribution P_R=3.35 × 10^{-4} for $H/H_s \geqslant \alpha$, α=2.0. SNOW and BMNLS results are averaged over five realizations.

for kurtosis and P_N. In this case, the threshold value beyond which P_A^+ departs from $P_A^{\max}$, and modulational instability is significant in the (initial) evolution, is $P_A^+/P_R \approx 20$. With the more valid definition of rogue wave occurrence in terms of area, the scatter in $P_A^+/P_R \approx 20$ obtained in the quasi-stationary state is substantially reduced. Despite the range of $P_N^{\max}/P_R$ spanning over an order of magnitude, the quasi-stationary value of $P_A^+/P_R \approx 20$ has a remarkably narrow range, suggesting that this might be a somewhat (more) common value of probability of occurrence of rogue waves ($H/H_s \geqslant \alpha$=2) under a broad range of ocean wavefield conditions for which modulational instability is relevant. For greater/smaller values of α, this threshold/quasi-stationary value of P_A^+/P_R is expected to increase/decrease, which we verify in Appendix B, §B.2.

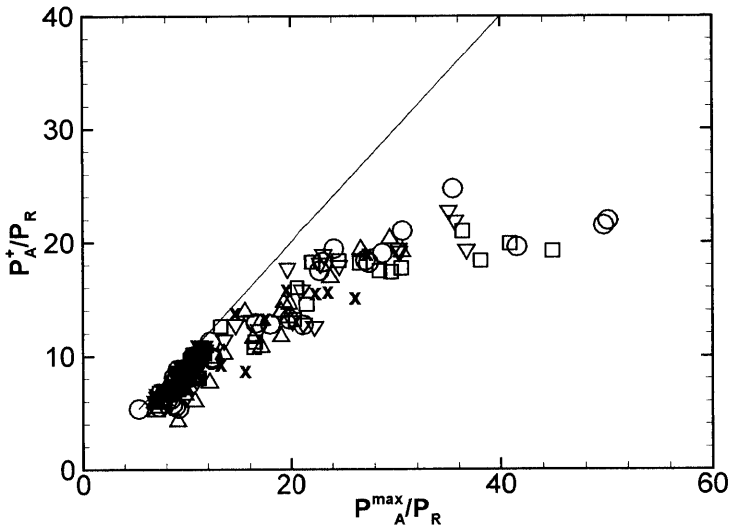

Figure 5-7: $P_A^{\max}$ vs. P_A^+ for $\sim$ 200 wavefields with a range of ε, γ and Θ from MIT-Wave. ε=0.06 ($\times$); 0.08 (Δ); 0.1 (∇); 0.12 ($\square$); 0.14 ($\bigcirc$).

5.7 Occurrence probability of rogue waves vs. kurtosis

The enhanced occurrence of rogue waves is related to the modulational instability of nonlinear waves, which is a third-order nonlinear effect. Including the effects of

third order nonlinearity, the distribution of wave heights in a uni-directional, narrow-banded wavefield follows the modified Edgeworth Rayleigh (MER) distribution (Mori and Janssen, 2006; Gramstad and Trulsen, 2007):

$$P_H(H/\sigma) = e^{-1/8(H/\sigma)^2}[1 + (\mathrm{Kur} - 3)B_H(H/\sigma)], \tag{5.15}$$

where σ is the standard deviation of the surface elevation and Kur is the kurtosis of the wave elevation, and

$$B_H(H/\sigma) = 1/384(H/\sigma)^2[(H/\sigma)^2 - 16]. \tag{5.16}$$

The MER distribution states that the probability of rogue wave occurrence increases as the kurtosis increases.

5.7.1 Number probability of rogue waves vs. kurtosis

The probability of rogue wave occurrence has been found to be closely related to the kurtosis of the wavefield at a given time. Figure 5-8 plots $P_N^{\max}$ as a function of $\mathrm{Kur}^{\max}$ for the $\sim$ 200 wavefields from MIT-Wave dataset. For comparison, we also include the modified Edgeworth Rayleigh (MER) distribution (5.15) for the "number" exceeding probability of wave heights, wherein the third-order wave nonlinearity effects related to modulational instability are included (Mori and Yasuda, 2002a; Mori and Janssen, 2006). We see that $P_N^{\max}$ has almost linear correlations with $\mathrm{Kur}^{\max}$ for the full range of $\mathrm{Kur}^{\max}$ that we obtained from broad ranges of (initial) spectral parameters in the MIT-Wave cases considered. For $P_N^{\max}$, MER substantially underestimates the occurrence probability and appears to be relevant only for small Kur values (above Kur=3).

5.7.2 Area probability of rogue waves vs. kurtosis

Figure 5-9 plots $P_N^{\max}$ as a function of $\mathrm{Kur}^{\max}$ for the $\sim$ 200 wavefields from MIT-Wave dataset. Comparing figure 5-8 and figure 5-9, it is evident that $P_A^{\max}$ has a better linear

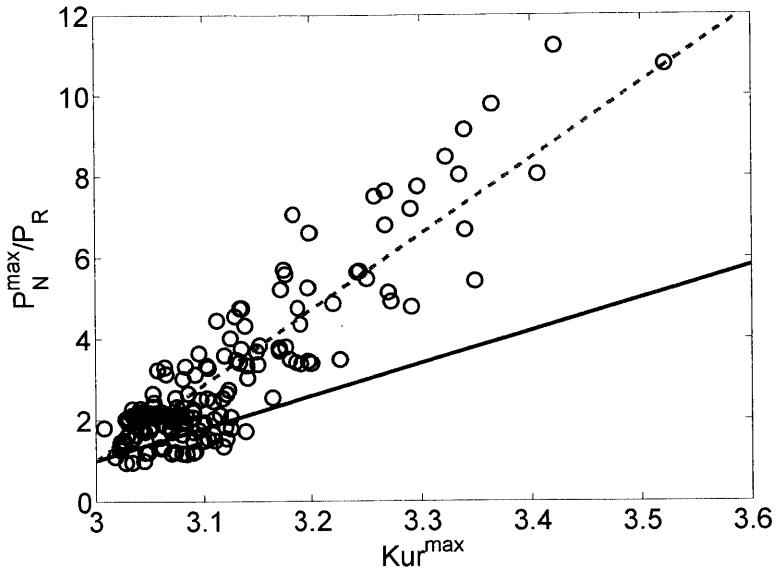

Figure 5-8: $P_N^{\max}$ vs. $\mathrm{Kur}^{\max}$ for ~200 directional wavefields from MIT-Wave. SNOW (○); MER (Mori and Janssen (2006)) (—). Linear regression line (- - -): $P_N^{\max}/P_R$=1+18.64($\mathrm{Kur}^{\max}-3$) (coefficient of determination $R^2 = 0.82$).

correlation (with higher R^2 value) relative to $P_N^{\max}$ (especially for greater $\mathrm{Kur}^{\max}$). This is not surprising since many of the MIT-Wave wavefields are (eventually) broadly spread. Clearly, P_A is a preferred measure of rogue wave probability for general wavefield conditions.

Overall, we find that both $P_N^{\max}$ and $P_A^{\max}$ have almost linear correlations with $\mathrm{Kur}^{\max}$ for the full range of $\mathrm{Kur}^{\max}$ that we obtained from broad ranges of (initial) spectral parameters in the MIT-Wave cases considered.

5.8 Number and area probability of rogue waves vs. Benjamin-Feir Index (BFI)

The dependence of the number and area probability of rogue waves on the initial value of BFI and spreading angle is shown in figure 5-10. Similar to kurtosis, For the very narrow spreading cases, both $P_N^{\max}$ and $P_A^{\max}$ have a strong dependence on BFI^2, especially for large probabilities. For large Θ, the slope with which $P_N^{\max}$ and $P_A^{\max}$ depends on BFI^2 decreases with Θ increases, so that for very broad spread cases,

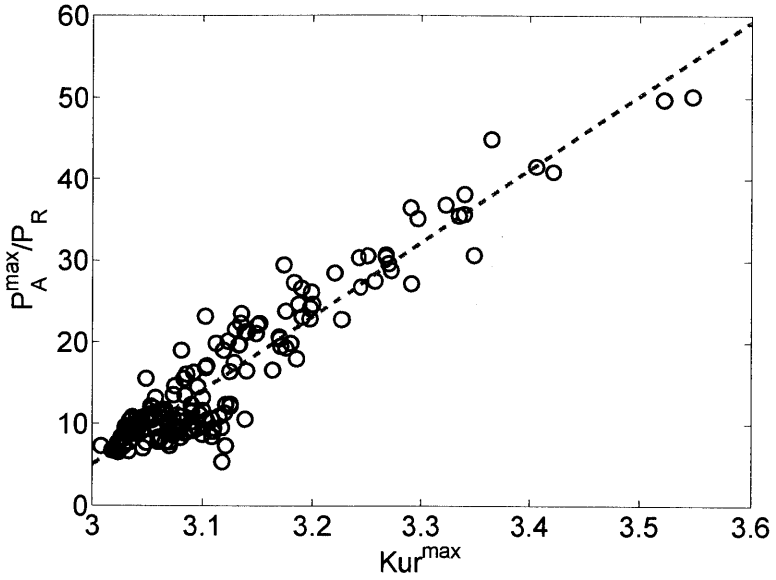

Figure 5-9: P_A^{max} vs. Kur^{max} for ~200 directional wavefields from MIT-Wave. SNOW (○); MER (Mori and Janssen, 2006) (—). Linear regression line (- - -): P_A^{max}/P_R=5.06+90.30(Kur^{max} − 3) (R^2 = 0.89).

the number and area probability of rogue wave occurrence are almost independent of BFI.

Although for a given Θ, we observe linear-like correlation between kurtosis, P_N^{max}, P_A^{max}, and BFI^2. For given BFI, the value of kurtosis and rogue wave probability are still unknown if the influence of spreading angle is not considered. Using just BFI without Θ information creates huge scatter because of different rate of dependencies on BFI.

5.9 Modified Benjamin-Feir Index (MBFI): a spectral parameter for rogue wave prediction

5.9.1 Definition of MBFI

The above findings suggest the need for a more general spectral parameter, applicable to wavefields with arbitrary directional spreading, that measures the probability of extreme waves. Different forms of modified BFI have been proposed by Waseda et al.

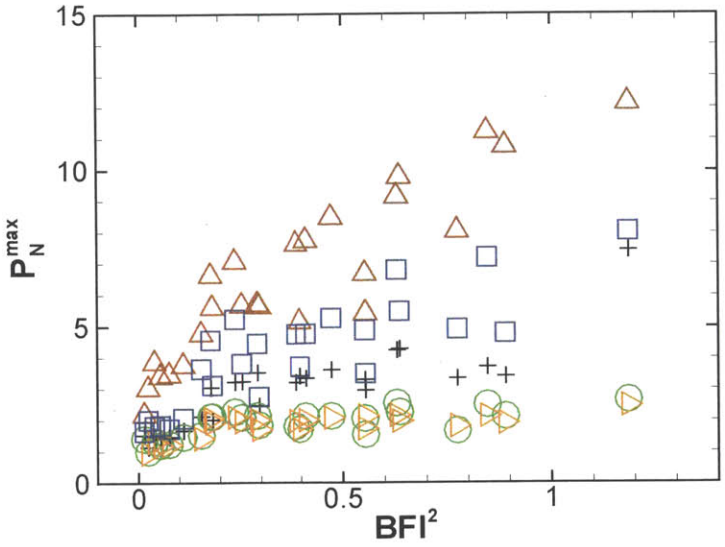

(a)

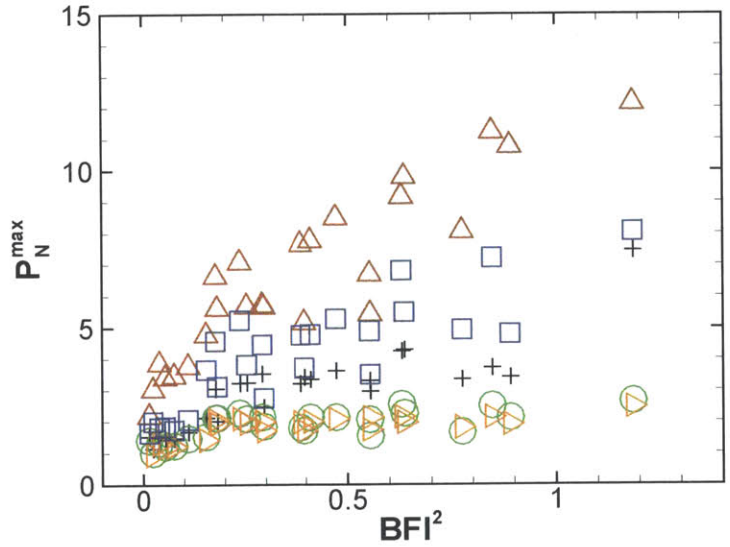

(b)

Figure 5-10: Dependence of (a) $P_N^{\max}$ and (b) $P_A^{\max}$ on the initial BFI^2 for wavefields with a range of ε, γ and Θ in MIT-Wave. Θ=20° (△); Θ=30° (□); 40° (+); 80° (◯); 120° (▷).

(2009) and Mori et al. (2011). The parameterization in Waseda et al. (2009), which is obtained based on limited number of wave basin experiments, does not reflect the general feature of monotonic reduction of kurtosis with increasing spreading angle. The modified BFI in Mori et al. (2011) is obtained by fitting to the results from NLS simulations and is thus applicable to wavefields with narrow-band wave spectra only. We here introduce a new modified Benjamin-Feir index (MBFI) defined as:

$$\text{MBFI} = \left[\frac{1+\tan^2(\Theta/2)}{1+4\tan^2(\Theta/2)}\right]\frac{\varepsilon}{\Delta k/k_p}, \tag{5.17}$$

i.e., MBFI=$F(\Theta)$·BFI, where $F(\Theta)$ is the quantity in the square brackets in (5.17). For uni-directional wavefields $F(0)$=1 and MBFI=BFI, while for very broadly directional spread seas, MBFI/BFI=$F(180°)$=0.25.

This definition of MBFI (5.17) is derived based on a generalization of the result of Alber (1978) who considered the effect of three-dimensional disturbance on the stability of the very narrow-band Gaussian spectrum (3.4). In this case, the wavefield is unstable for:

$$\frac{2\sqrt{2}k_p\sigma}{\Delta k/k_p}G(K_x,K_y) > 1, \quad G(K_x,K_y) = \left[\frac{1-2(K_y/K_x)^2}{1+(2K_y/K_x)^2}\right]^{1/2}, \tag{5.18}$$

where K_x and K_y are the modulation wavenumber in the x and y directions, and Δk is the spectral bandwidth in the x direction. The effect of the presence of transverse disturbance $G(K_x,K_y)$ can be related to the directional spreading Θ by taking, say, Θ=$2\tan^{-1}(K_y/K_x)$ and writing:

$$G(K_x,K_y) = \left[\frac{1-2(K_y/K_x)^2}{1+(2K_y/K_x)^2}\right]^{1/2} \simeq \left[\frac{1-2\tan^2(\Theta/2)}{1+4\tan^2(\Theta/2)}\right]^{1/2} \approx \frac{1+\tan^2(\Theta/2)}{1+4\tan^2(\Theta/2)} \equiv F(\Theta), \tag{5.19}$$

where the last approximation, valid for small Θ, is used to make $F(\Theta)$ defined for general value of $\Theta \in [0, 180°]$. The profile of $F(\Theta)$ is shown in figure 5-11.

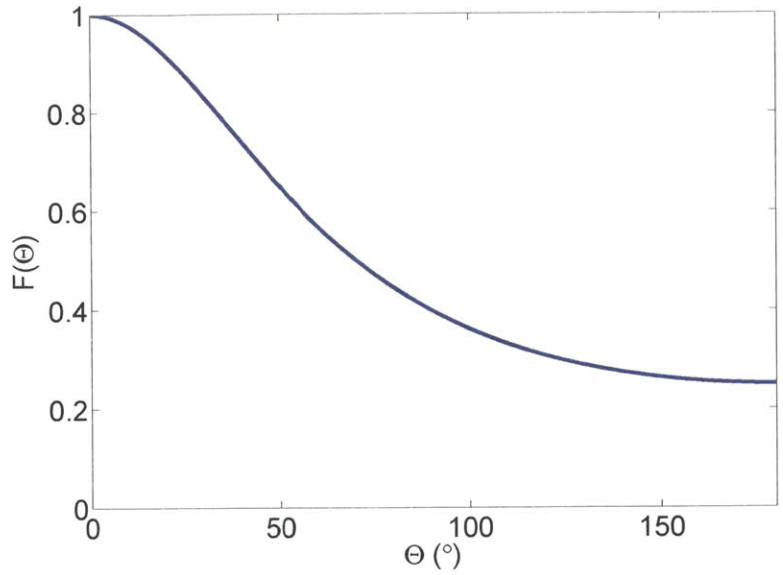

Figure 5-11: The spreading angle factor function $F(\Theta)$

5.9.2 Kurtosis vs. MBFI

Figure 5-12 shows the dependence of Kur^{max} on MBFI and BFI for the MIT-Wave data. With MBFI, the scatter in the data is greatly reduced, resulting in a clear and almost linear parametrization of Kur^{max} and MBFI^2 over the broad range of initial spectral parameters we considered, especially in the range $\text{Kur}^{\text{max}} \gtrsim 3.2$. This indicates that $F(\Theta)$ (5.19) is a reasonable description of the influence of the spreading angle on maximum value of kurtosis.

Figure 5-13 shows the color contours of Kur^{max} as functions of $F^2(\Theta)$ and BFI^2, using the $O(200)$ large-scale simulations in MIT-Wave. The hyperbolic contour lines corresponding to $\text{MBFI}^2 = \text{BFI}^2 F^2(\Theta) = \text{constant}$ are also plotted. We see a strong dependence of Kur^{max} on Θ, especially for large value of BFI. The general dependence of Kur^{max} on both BFI and Θ is generally captured by MBFI, clearly shown in the comparison between the value contours of Kur^{max} and the MBFI^2 contours.

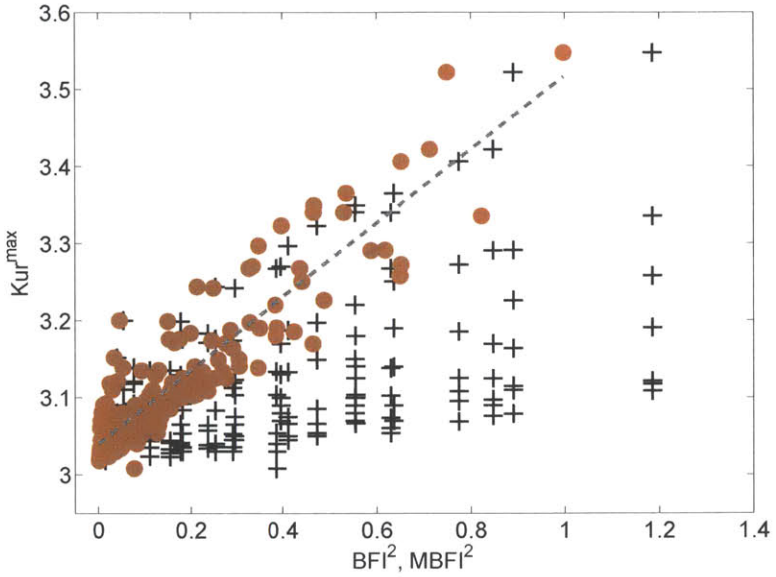

Figure 5-12: Dependence of Kur^{max} on BFI^2 and MBFI^2 for ~ 200 wavefields from MIT-Wave. BFI (+); MBFI (●); linear regression line (- - -): $\text{Kur}^{\text{max}} = 0.48\text{MBFI}^2 + 3.04$ ($R^2 = 0.82$).

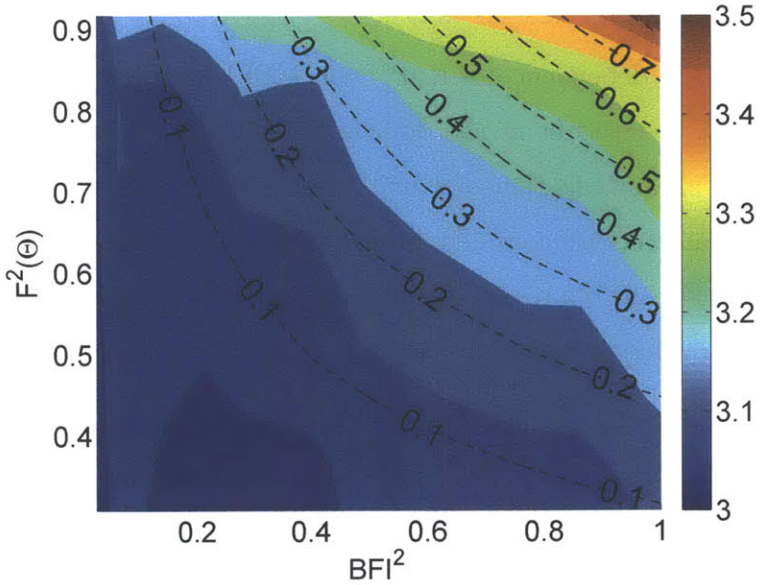

Figure 5-13: Contour plots of Kur^{max} as function of BFI^2 and $F^2(\Theta)$. Contours of MBFI^2 (- - -).

5.9.3 Number and area probabilities of rogue waves vs. MBFI

Given the known dependence of rogue wave occurrence on kurtosis, it is expected that MBFI would also be the (single) metric for the occurrence probability. This is shown in figure 5-14, where we see a remarkable correlation between occurrence probability and MBFI especially for P_A. Indeed, a linear fit obtains:

$$P_A/P_R \approx b_1 \times \text{MBFI}^2 + b_0, \tag{5.20}$$

where, over a broad range of spectral parameters, b_0 and b_1 are functions of the rogue wave criterion $H/H_s \geqslant \alpha$ only. For figure 5-14, α=2, and we obtain b_0=8.60 and b_1=43.88 with R^2=0.76. A similar fit obtains for P_N/P_R with a somewhat smaller R^2=0.67. Considering the broad range of wavefield conditions represented in figure 5-14, the surprisingly simple result (5.20) is noteworthy.

Figure 5-15 shows the color contours of the number and area probabilities of rogue wave occurrence, as functions of $F^2(\Theta)$ and BFI^2, compiled from the $O(200)$ large-scale simulations in MIT-Wave. Also included in the figures are the hyperbolic contour lines corresponding to $\text{MBFI}^2=\text{BFI}^2F^2(\Theta)$=constant. We see a strong dependence on Θ suggesting that prediction of the occurrence using BFI alone is inadequate (except for the special case of very small Θ, i.e., large $F(\Theta)$). The general dependence on both BFI and Θ is generally captured by MBFI, with the suggested fit (5.20) clearly shown in the comparison between the computed probabilities and the MBFI^2 contours. Comparing P_N/P_R and P_A/P_R, it appears that P_A/P_R is better parameterized by MBFI, especially for greater values of directional spreading Θ (smaller values of $F(\Theta)$ and MBFI), as expected.

5.10 Summary and conclusions

We study the occurrence probability of rogue waves and their dependence on the spectral parameters over a broad range. Our interest is the importance of modulational

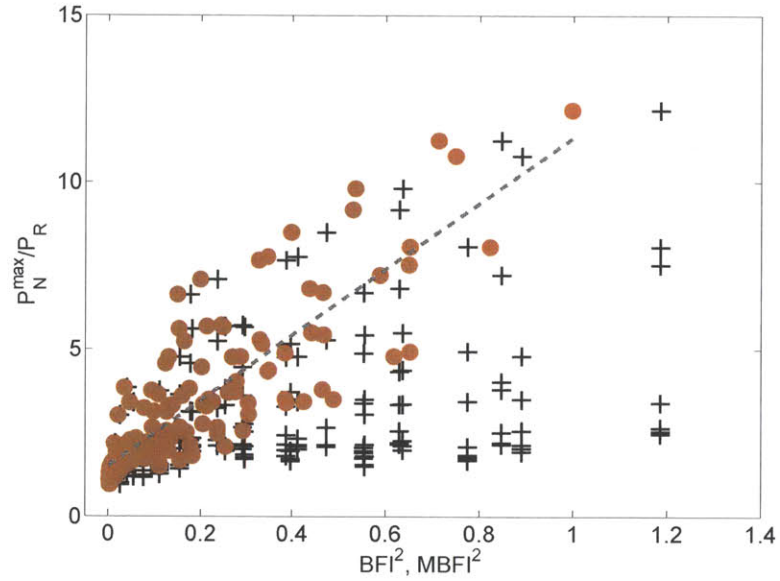

(a)

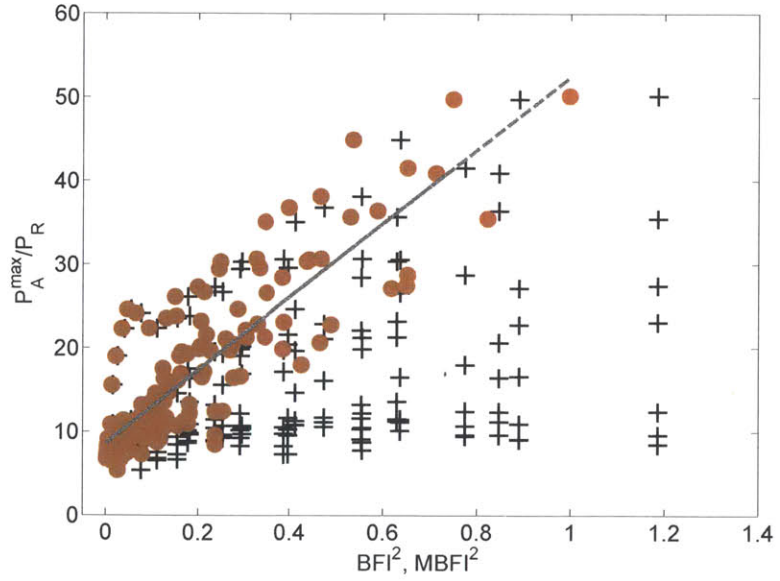

(b)

Figure 5-14: Dependence of (a) $P_N^{\max}/P_R$, (b) $P_A^{\max}/P_R$ on BFI^2 and MBFI^2 for ~ 200 wavefields from MIT-Wave for α=2: BFI (+); MBFI (●); linear regression line (5.20) with b_0=8.60, b_1=43.88 ($R^2 = 0.76$) for P_A/P_R; and b_0=1.51, b_1=9.80 ($R^2 = 0.67$) for P_N/P_R.

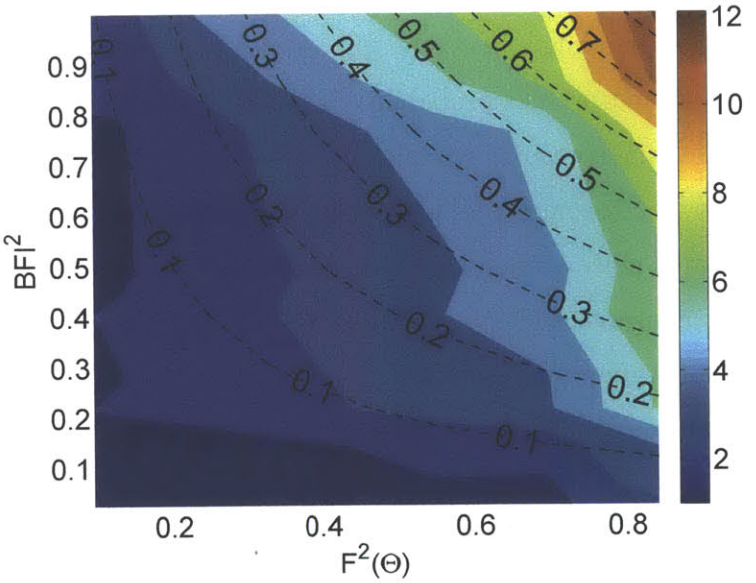

(a)

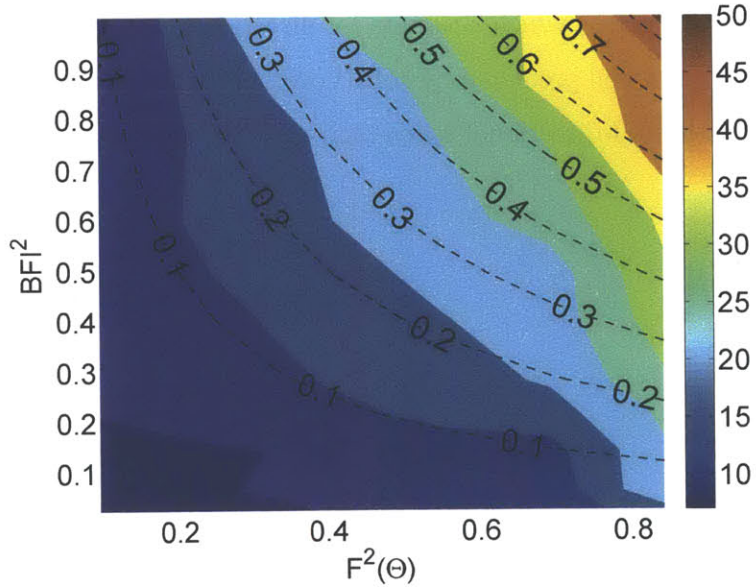

(b)

Figure 5-15: Contour plots of (a) $P_N^{\max}/P_R$; (b) $P_A^{\max}/P_R$ as function of BFI^2 and $F^2(\Theta)$. Contours of MBFI^2 (- - -).

instability as a generation mechanisms of rogue waves. The simulations are performed over spatial-temporal scale $\mathcal{L}/\lambda_p$, $\mathcal{T}/T_p$=$O(\varepsilon^{-2})$. For wavefields with small spreading angles, modulational instability leads to enhanced probability of rogue waves. For wavefields with large spreading angles, the importance of modulational instability is less significant and the occurrence probability is closer to Rayleigh distribution.

For general directional spreading wavefields, occurrence probability based on number of rogue waves P_N becomes problematic as crest lengths become short. The problem is exacerbated since even initially narrowly spread seas become directionally broadened in the nonlinear evolution. To overcome this, we introduce the definition of *area* probability of rogue wave occurrence P_A, which is well-defined and convergent for arbitrary 3D wavefields. We confirm the general correlation between both P_N, P_A, and kurtosis.

For relatively narrow spreading wavefields, kurtosis, and hence occurrence probability, can be reasonably well predicted by the (initial) BFI of the wavefield. This is no longer true for broad directionally-spreading wavefields. We propose a modified Benjamin-Feir index (MBFI) which accounts for directional spreading and show that kurtosis, P_N and P_A are well predicted by MBFI over a broad range of wave steepness, frequency bandwidth, and directional spreading.

Chapter 6

Nonlinear wave statistics and rogue wave occurrence in finite water depth

6.1 Introduction

The understanding and prediction of nearshore wave environment, specially a reliable forecast of occurrence probability of rogue waves, is of fundamental importance to the design and safe operation of naval ships and marine structures. Moreover, an appropriate description of nearshore wave statistics is a necessary input in the motion analysis of surface vessels and floating marine structures.

When waves propagate from deep water to shoreline, the wave crest becomes shaper and wave trough becomes flatter, leading to a steeper and more asymmetric wave shape. Based on the second-order Stokes expansions for finite depth water, skewness and kurtosis of surface elevation increase as water depth decreases (Tuah and Hudspeth, 1985; Song et al., 2002).

When high-order nonlinearity is relevant, the (third-order) nonlinear wave interactions have a significant influence on the spectral evolution, nonlinear statistics, and particularly on the probability of large waves (Janssen, 2003; Socquet-Juglard et al.,

2005). For wavefields with narrow-banded spectrum and small directional spreading, modulational instability leads to significant spectral change and considerable non-Gaussian wave statistics. As the directional spreading angle increases, the importance of modulational instability reduces and the statistics are close to Gaussian in short-crested wavefields. The influence of modulational instability on spectral change, nonlinear wave statistics and occurrence probability of rogue waves in the context of deep water are discussed in detail in Chapter 3, Chapter 4, and Chapter 5 using direct simulations (SNOW).

Extension of the deep water results to finite depth is less addressed. The classic study suggests that, for unidirectional wavefields, the water depth effect on the wave spectrum evolution is insignificant as long as the water depth is not too shallow. According to classic theory, for the water depth h satisfies $\mu \equiv k_p h > 0.7$, where k_p is the peak wavenumber, the wave spectrum in finite depth can be obtained from deep water spectrum through a similarity transformation (Herterich and Hasselmann, 1980). However, a recent study, which is based on the Zakharov equation in finite depth, shows that a considerable reduction in the nonlinear energy-transfer rate among wave components in the spectrum occurs around μ=1.363, corresponding to a much deeper depth than that indicated in the classic study (Janssen and Onorato, 2007). As an special example, for unidirectional uniform stokes wave train, the Benjamin-Feir instability diminishes for small water depth satisfying $k_p h$ <1.363, therefore, we expect that the modulational instability due to one-dimensional perturbation (Benjamin-Feir type instability) may play a less important role in the generation of extreme waves in finite water depth. For water depth $k_p h$ <1.363, although the unidirectional stokes waves are stable to two-dimensional perturbations, they are unstable to three-dimensional perturbations (McLean, 1982). In the context of finite water depth, the instability due to three-dimensional perturbations becomes more important than that due to two-dimensional perturbations specially for steep waves. The influence of finite water depth on the nonlinear wave statistics for three-dimensional wavefields is investigated using HOS over relatively small computational domain in (Toffoli et al., 2009). They find, for wavefields with small spreading angle, finite depth in general

leads to a significant reduction in the kurtosis of surface evolution; for short-crested wavefields, the dependence of wave statistics on water depth is not significant. In this chapter, these conclusions are verified using SNOW simulations over domain size $\mathcal{L}/\lambda_p$, $\mathcal{T}/T_p = O(\varepsilon^{-2})$. Moreover, we investigate the influence of finite water depth on the wave breaking and occurrence probability of rogue waves.

In deep water, resonant triad wave-wave interactions are absent and four wave-wave interactions dominate the evolution of the spectrum. In very shallow water, triad wave-wave interactions transfer energy from lower frequencies to higher frequencies often resulting in lower and higher harmonics. The low-frequency energy generation by triad wave-wave interactions is general not considered in phase-averaged models (e.g. SWAN) (Booij et al., 1999). For intermediate water depth, triad and quartet nonlinear wave interactions coexist and their combined effect on the spectral evolution, nonlinear wave statistics and rogue wave probability over the spatial and temporal scale $\mathcal{L}/\lambda_p$, $\mathcal{T}/T_p = O(\varepsilon^{-2})$ is the topic of this chapter. We assume constant flat bottom and varying water depth involving shoaling process is not considered.

6.2 Initial finite-depth wavefield

6.2.1 Initial finite-depth wave spectrum

The frequency wave spectrum for finite depth $S(\omega, h)$ is given by multiplying the wave spectrum in deep water $S(\omega)$ by a depth factor $H(\omega_h)$:

$$S(\omega, h) = S(\omega)H(\omega_h). \tag{6.1}$$

where $\omega_h{=}\omega\sqrt{h/g}$ is the corresponding wave frequency in finite water depth. For $S(\omega)$, we use the JONSWAP spectrum

$$S(\omega) = \frac{\alpha g^2}{\omega^5}\exp\left[-\frac{5}{4}(\frac{\omega}{\omega_p})^{-4}\right]\gamma^{\exp\left[-\frac{(\omega-\omega_p)^2}{2\sigma_k^2\omega_p^2}\right]}, \tag{6.2}$$

where ω is the wave frequency, ω_p the peak wave frequency, α the Phillips parameter, γ the peak enhancement factor specifying the spectral bandwidth, and σ_k=0.07 for $\omega \leq \omega_p$; σ_k=0.09 for $\omega > \omega_p$. The depth factor has a form (Kitaigorodskii et al., 1975):

$$H(\omega_h) = \frac{1}{C_g(\omega, h)} \frac{\omega^5}{g^2 k^3}, \tag{6.3}$$

where C_g is the group velocity of the wave, k is related to ω by the dispersion relation, and g is the gravitational acceleration. For directional spreading, a cosine-square spreading function is employed. Figure 6-1 shows initial frequency spectra using same frequency JONSWAP spectrum but different water depths. With decreasing water depth, energy over short wave range increases considerably, suggesting an increasing wave steepness. Note that the representative wavefield steepness $\varepsilon = H_s k_p/2$ is slightly different for different water depths, because for given ω_p, k_p varies for different h. Here H_s and k_p are significant wave height and peak wave number.

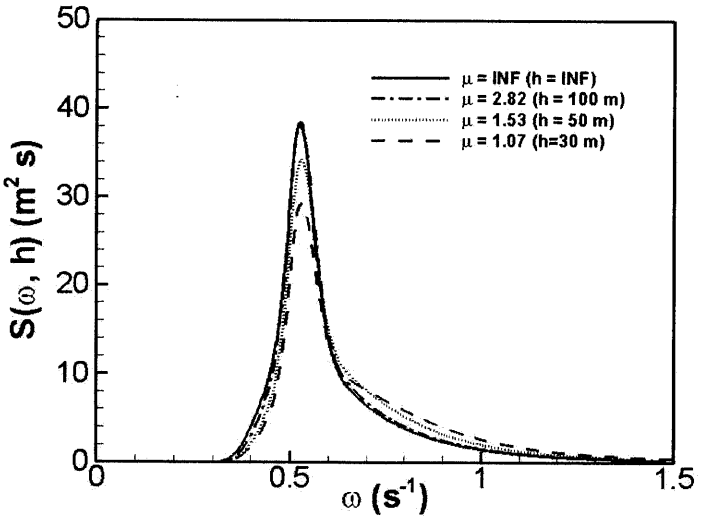

Figure 6-1: Initial frequency wave spectra for finite water wavefields $S(\omega, h)$, H_s=10 m, T_p=12 s, γ=3.3.

6.2.2 Physical and numerical parameters

To study the combined effects of finite water depth and directional spreading on wave evolution, we perform SNOW simulations for wavefields with a range of spreading angles and water depths. The scaled water depth $\mu = k_p h$ varies from ∞ (deep water) to 1.07, covering the theoretical stable to theoretical unstable range in water depth; Two different spreading angles are chosen, Θ=20° and Θ=80°, representing small and large spreading angles. The importance of wave nonlinearity relative to wave dispersion is measured by the dimensionless parameter *Ursell* number defined as $Ur=\varepsilon/(k_p h)^3$. In this chapter, we are interested in the cases with relatively small Ur ($Ur<1$). Under this assumption, the Stoke's expansion and the asymptotic expansions in HOS formulations (2.3) in Chapter 2 §2.2 converge for finite water depth.

We consider the computational domain $L_x \times L_y$ and evolution time T, with $L_x = L_y = 128\lambda_p$ and T/T_p=150. A uniform grid $N_x \times N_y = 4096 \times 4096$ is applied, which gives a spectral resolution of $\Delta k_x = \Delta k_y = k_p/32$. For the time integration, a constant time step of $\Delta t = T_p/64$ is used. In all SNOW computations, we use order of nonlinearity M=4 sufficient to capture the quartet and quintet nonlinear wave interactions including modulational instabilities over the space-time scales considered. At the initial stage of SNOW simulations, the free-surface boundary conditions are smoothly transitioned in time from linear to nonlinear for minimizing the numerical standing wave effect associated with the use of the linear initial conditions (Dommermuth, 2000).

6.3 Nonlinear statistics of waves in finite water depth

To study the effects of finite water depth on nonlinear wave statistics, we perform SNOW simulations of directional wavefields with H_s=10 m, T_p=12 s, γ=3.3 and a range of water depth and directional spreading angle. The normalized wave depth, $\mu = k_p h$=inf, 2.82, 1.53, and 1.07, varies from the values that are stable ($\mu > 1.363$) to

the values that are unstable ($\mu \leqslant 1.363$) to the unidirectional disturbances. Same topic has also been addressed in Toffoli et al. (2009) using relatively smaller computational domain.

6.3.1 Significant wave height in finite water

Figure 6-2 shows the evolution of the significant wave height (H_s=4σ) for wavefields with a range of water depth. For all the cases considered, H_s decreases with time due to non-ignorable wave breaking in directional finite depth wavefields. For given spreading angle, the reduction of H_s increases as water depth decreases, a clear indication of water depth dependent wave breaking. Comparing figure 6-2(a) and (b), we find the variational pattern and reduction amount of H_s are very similar between the two different spreading angles, although the energy dissipation in the case with broader spreading angle ($\Theta = 80°$) is slightly less than that in the case with narrow spreading angle ($\Theta = 20°$).

6.3.2 Skewness in finite water

In figure 6-3, we plot the temporal variation of skewness for wavefields with different water depths and spreading angles. For the wavefields with scaled water depth $\mu \gg 1.363$, the dependence of skewness on water depth is not significant for both spreading angles considered. For wavefields with scaled water depth $\mu \lesssim 1.363$, skewness increases as water depth decreases. Comparing figure 6-3(a) and (b), the variation patterns of skewness are similar between the cases with different spreading angles. The influence of water depth on the mean skewness over $0< t/T_p <150T_p$ is shown in figure 6-4. In the range of relatively shallow water depth, skewness increases significantly as water depth reduces. We find a sharp transition in the skewness from the shallow water to deep water. In the shallow water, skewness has a strong dependence on water depth and it is slightly greater in the case with broad spreading angle; while in the deep water, skewness is nearly independent of water depth and it is greater in the case with narrow spreading angle. These finds are consistent with

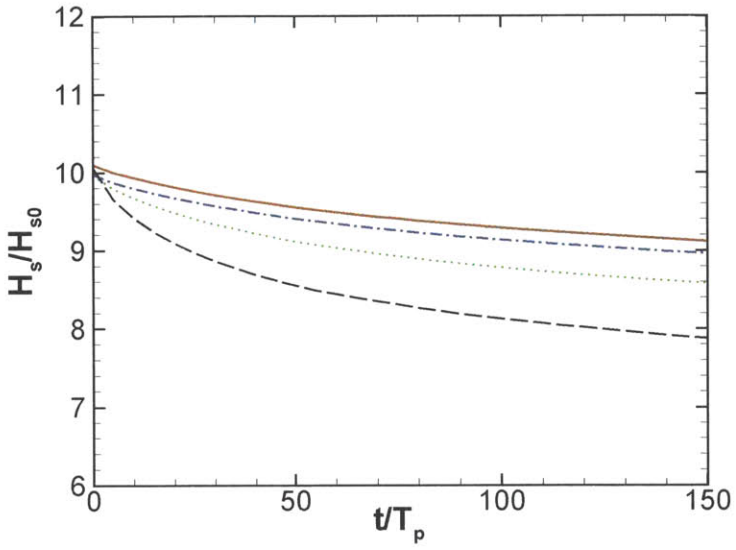

(a)

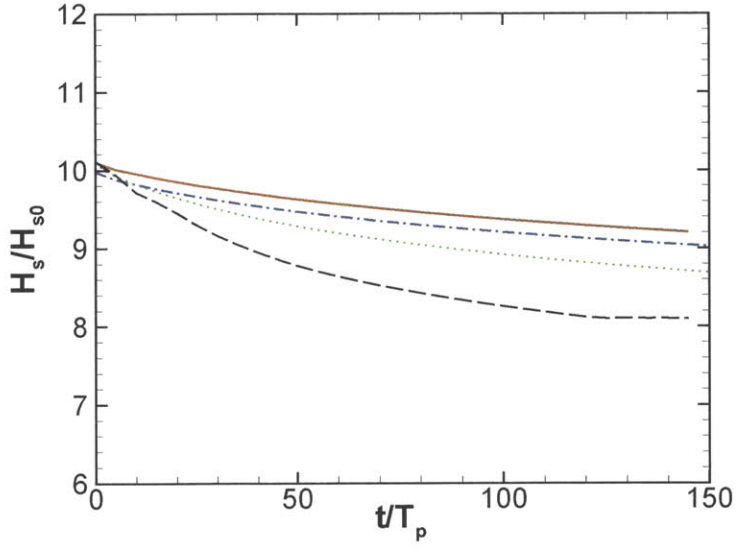

(b)

Figure 6-2: Temporal variation of the significant wave height in wavefields initialized by H_s=10 m, T_p=12 s, γ=3.3 with finite water depth. (a) Θ=20°; (b) Θ=80°. Deep water (—); $\mu = 2.82$, $h = 100$ m (– · –); $\mu = 1.53$, $h = 50$ m (· · ·); $\mu = 1.07$, $h = 30$ m (- - -).

what is observed in Toffoli et al. (2009). These results also agree qualitatively with the field measurements listed in Herbich (1990). The increasing skewness suggests more asymmetric wave shapes in shallower water depth, which is expected.

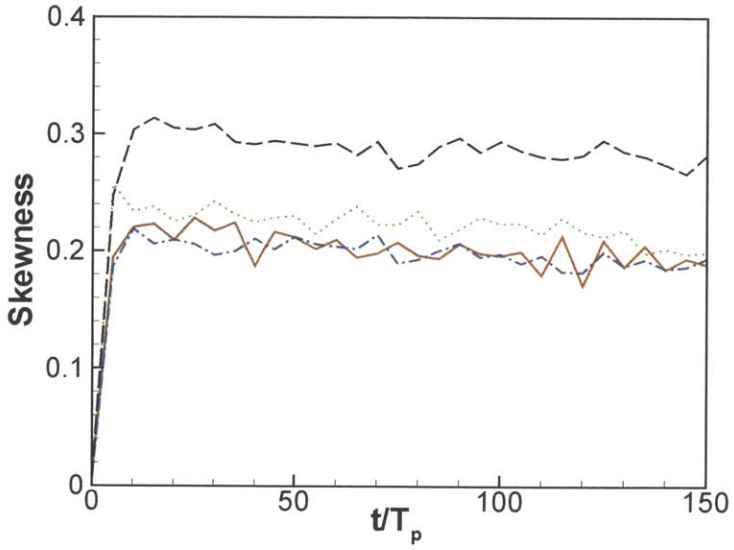

(a)

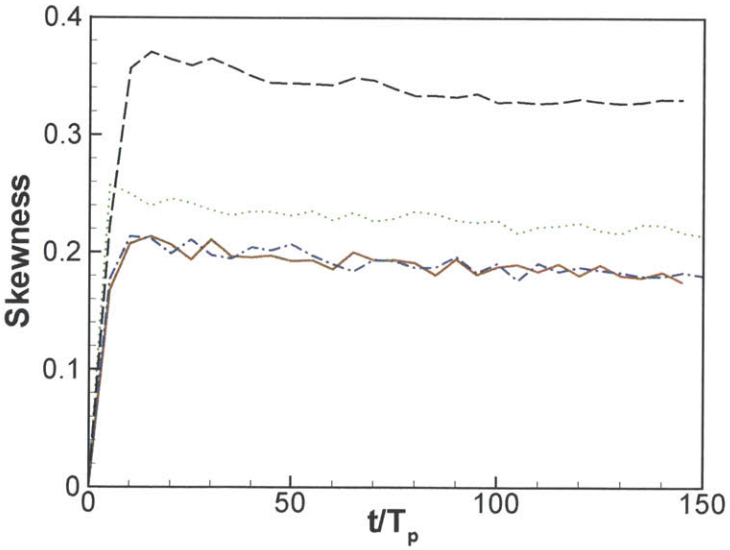

(b)

Figure 6-3: Temporal variation of the skewness for wavefields H_s=10 m, T_p=12 s, γ=3.3 with different water depths and angles of spreading. (a) $\Theta = 20°$; (b) $\Theta = 80°$. Deep water (—); $\mu = 2.82$, $h = 100$ m (– · –); $\mu = 1.53$, $h = 50$ m (· · ·); $\mu = 1.07$, $h = 30$ m (- - -).

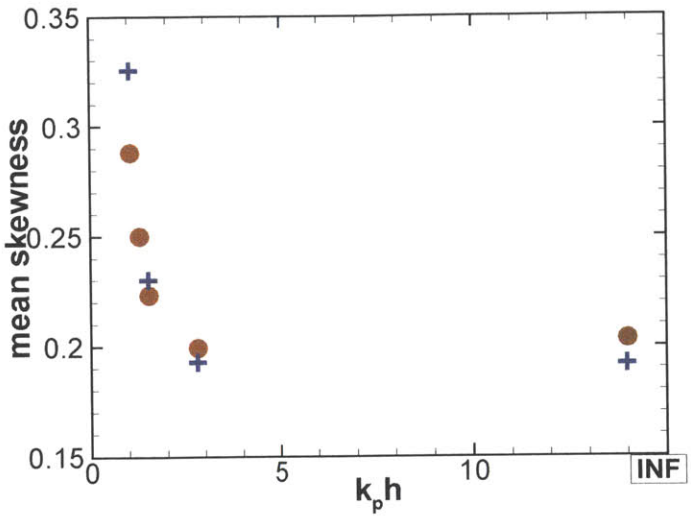

Figure 6-4: Mean skewness as a function of scaled water depth $\mu = k_p h$. $\Theta = 20°$ (•); $\Theta = 80°$ (+).

6.3.3 Kurtosis in finite water

Figure 6-5 shows the temporal variation of kurtosis for wavefields with a range of water depth. For the wavefields with small spreading angle ($\Theta = 20°$), the kurtosis decreases as water depth reduces. This is somewhat as expected since the kurtosis is largely influenced by the modulational instability that vanishes at shallow depth (with $\mu \leq 1.363$). For the case of $\Theta = 20°$ and μ=1.07 (h=30 m), in particular, the kurtosis even becomes less than the Gaussian value (3). This result is consistent with the predictions based on the Zakharov equation (Janssen and Onorato, 2007) and the KdV model (Pelinovsky and Sergeeva Kokorina, 2006). For the case with broad spreading angle, the dependence of kurtosis is less significant, although the decreasing trend with decreasing water depth remains. These results again are consistent with Toffoli et al. (2009).

Figure 6-6 shows the combined influence of finite water depth and the spreading angle on the maximum kurtosis over $0 \leqslant t/T_p \leqslant 150$, denoted by $\mathrm{Kur}^{\mathrm{max}}$. We find a strong dependence of $\mathrm{Kur}^{\mathrm{max}}$ on the water depth and spreading angle. For wavefields with small spreading angles, $\mathrm{Kur}^{\mathrm{max}}$ decreases as the water depth decreases. The

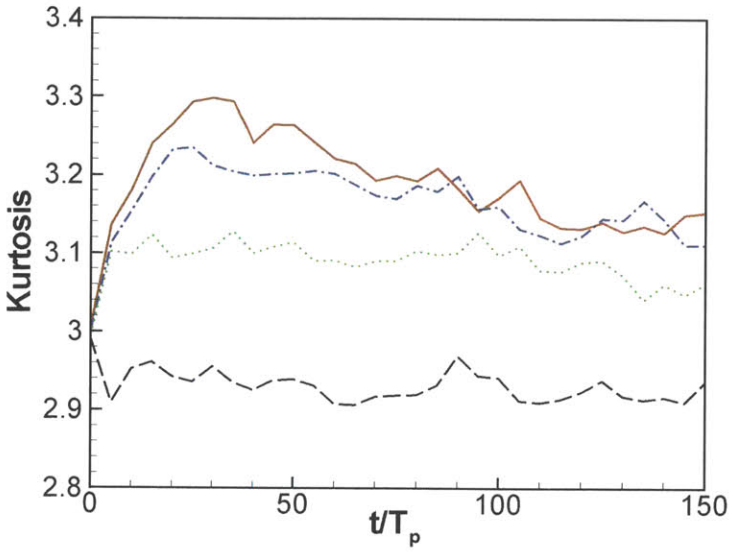

(a)

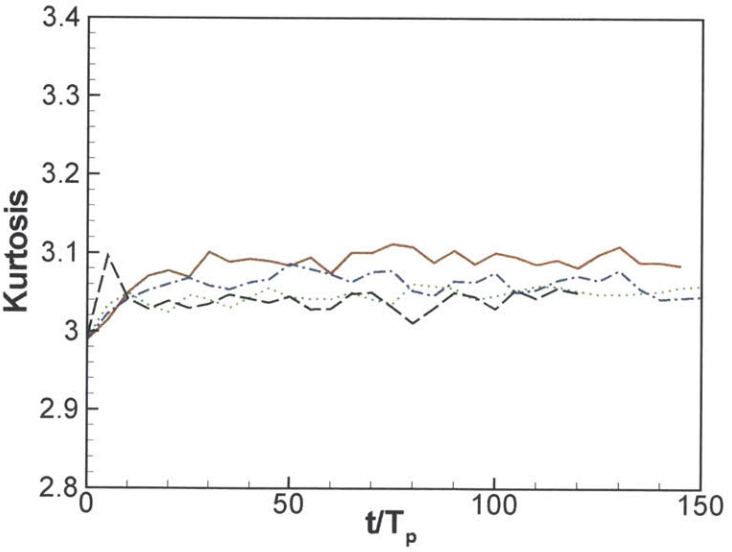

(b)

Figure 6-5: Time variation of the kurtosis in nonlinear wavefield evolution. (a) $\Theta = 20°$; (b) $\Theta = 80°$. Deep water (—); $\mu = 2.82$, $h = 100\,\mathrm{m}$ (– · –); $\mu = 1.53$, $h = 50\,\mathrm{m}$ (· · ·); $\mu = 1.07$, $h = 30\,\mathrm{m}$ (- - -).

reduction rate of $\mathrm{Kur}^{\max}$ with respect to water depth is greater in the shallow water depth range. For the case of large angle of spreading, the influence of water depth on kurtosis is greatly reduced and kurtosis is close to Gaussian and is nearly independent of water depth. In the shallow water region $\mu \lesssim 1.363$, for wavefields with small spreading angles, $\mathrm{Kur}^{\max} < 3$. The great reduction of kurtosis with decreasing water depth in the case of small angle of spreading suggests less likelihood of large wave occurrence.

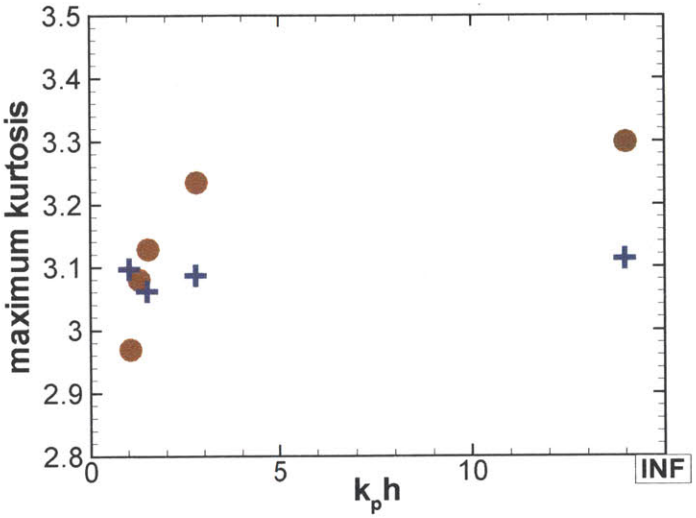

Figure 6-6: Maximum kurtosis as a function of scaled water depth. $\Theta = 20°$ (•); $\Theta = 80°$ (+).

6.3.4 Distributions of crests and troughs in finite water

In finite water depth, the wave becomes sharper and more asymmetric. The linear assumption of equal wave crest and trough is no longer valid. Figure 6-7 and 6-8 show the temporal variation of exceeding probabilities of crests for wavefields with different water depths and spreading angles. The the linear Rayleigh and second-order theories (Tayfun, 1980) are also shown as references. For the case with small angle of spreading ($\Theta = 20°$) the deviations from the Rayleigh and second-order predictions become significant, specially at the time $t = 30T_p$ when the kurtosis

is maximized in the case of deep water (figure 6-7). The deviations reduce a bit as wavefields evolve, but probability of large crests is still higher than second-order theory. This feature agrees with the experimental observations in the deep water wave basin (Onorato et al., 2009). As water depth decreases, the exceeding probability of crest is close to the second-order Tayfun prediction. The results suggest that the occurrence probability of large waves is reduced in the finite water depth. In the case of large angle of spreading, the exceeding probability of crests is very close to second-order prediction regardless of the water depth (figure 6-8). However, we notice that for the case of smallest water depth ($h = 30\,\mathrm{m}$), a slightly higher probability of crests is observed (figure 6-8b), which is also found in Toffoli et al. (2009). This might be related to the transverse (three-dimensional) instability. Exceeding probability of troughs are shown in figure 6-9 and 6-10. The exceeding probability of large troughs is greatly reduced in finite water depth for both spreading angles considered.

A very interesting phenomenon we find is that, unlike crest distributions which are well described by second-order theory in shallow water for both spreading angles, the trough distributions in shallow water are significantly underestimated by the second-order theory for both spreading angles. Moreover, in comparison with crest distribution, the trough distribution does not seem to vary with time as what is observed in crest distribution.

For finite water depth, the results suggest the wave profiles are more asymmetric for wavefields with small angles of spreading.

6.4 Spectral evolution in finite water depth

6.4.1 Omnidirectional wave spectrum

The omnidirectional spectrum $S(k)$, describing the energy distribution over wavenumber for all the directions, is defined as

$$S(k) = \int_{|\mathbf{k}|=k} \Psi(\mathbf{k})\, d\mathbf{k} = \int_{-\pi}^{\pi} \Psi(k,\theta) k\, d\theta. \tag{6.4}$$

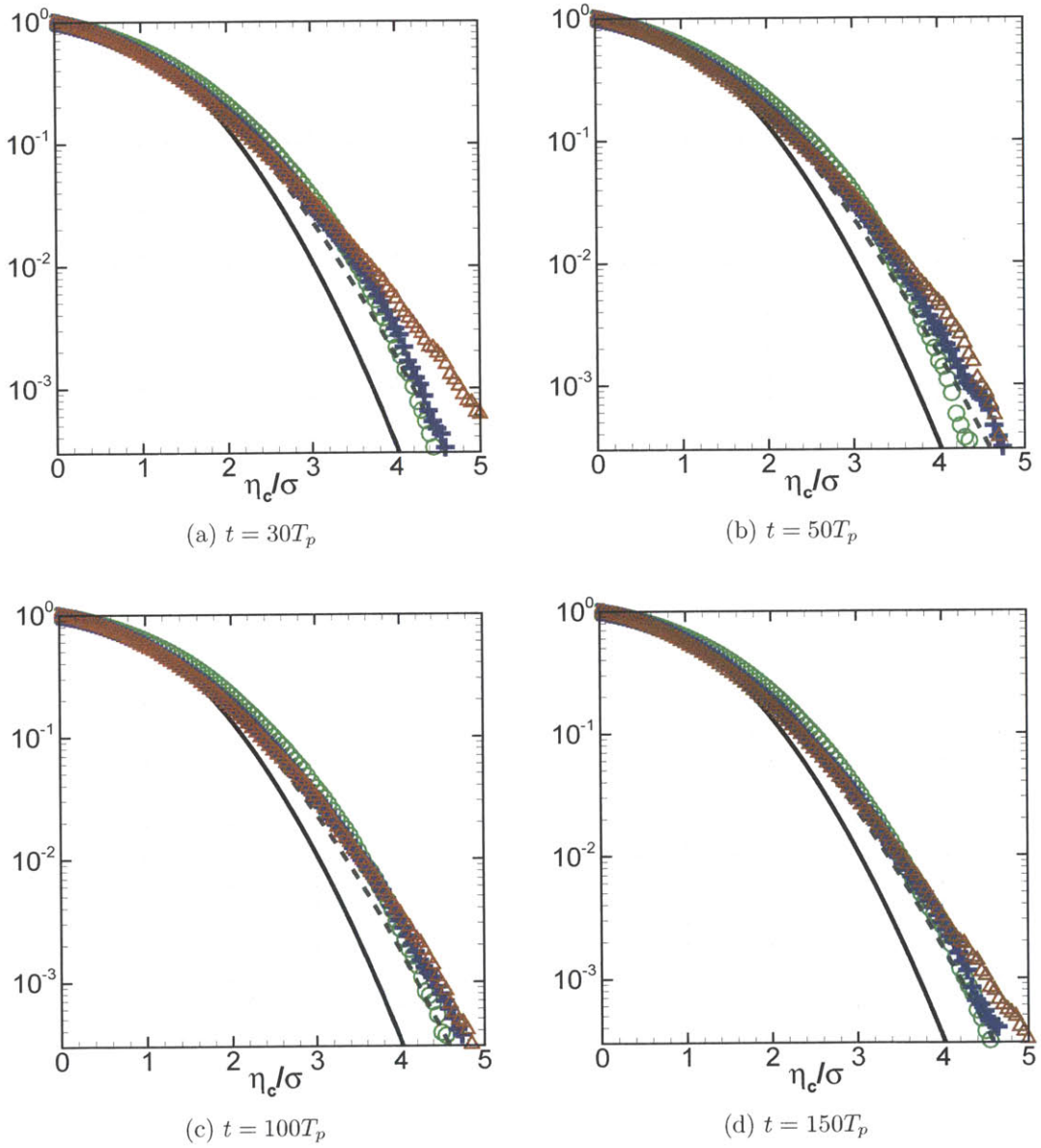

(a) $t = 30T_p$

(b) $t = 50T_p$

(c) $t = 100T_p$

(d) $t = 150T_p$

Figure 6-7: Exceeding probability of crests for wavefields $\Theta = 20°$ with different water depths. $\mu = \inf$ (△); $\mu = 1.53$, $h = 50\,\mathrm{m}$ (+); $\mu = 1.07$, $h = 30\,\mathrm{m}$ (◯). Rayleigh (—); Second-order theory (- - -).

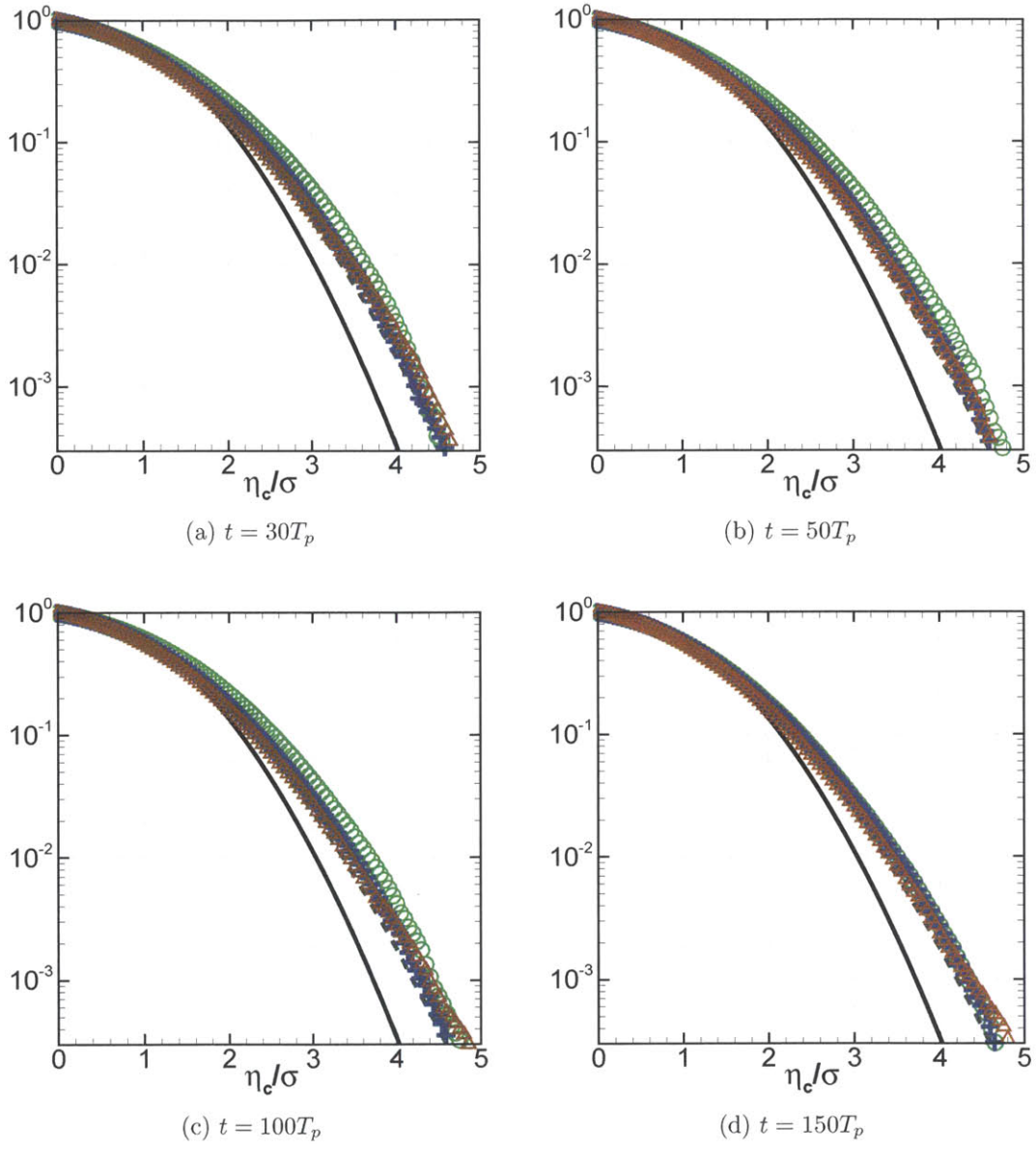

(a) $t = 30T_p$ (b) $t = 50T_p$

(c) $t = 100T_p$ (d) $t = 150T_p$

Figure 6-8: Exceeding probability of crests for wavefields $\Theta = 80°$ with different water depths. $\mu = \inf$ (△); $\mu = 1.53$, $h = 50\,\mathrm{m}$ (+); $\mu = 1.07$, $h = 30\,\mathrm{m}$ (◯). Rayleigh (—); Second-order theory (- - -).

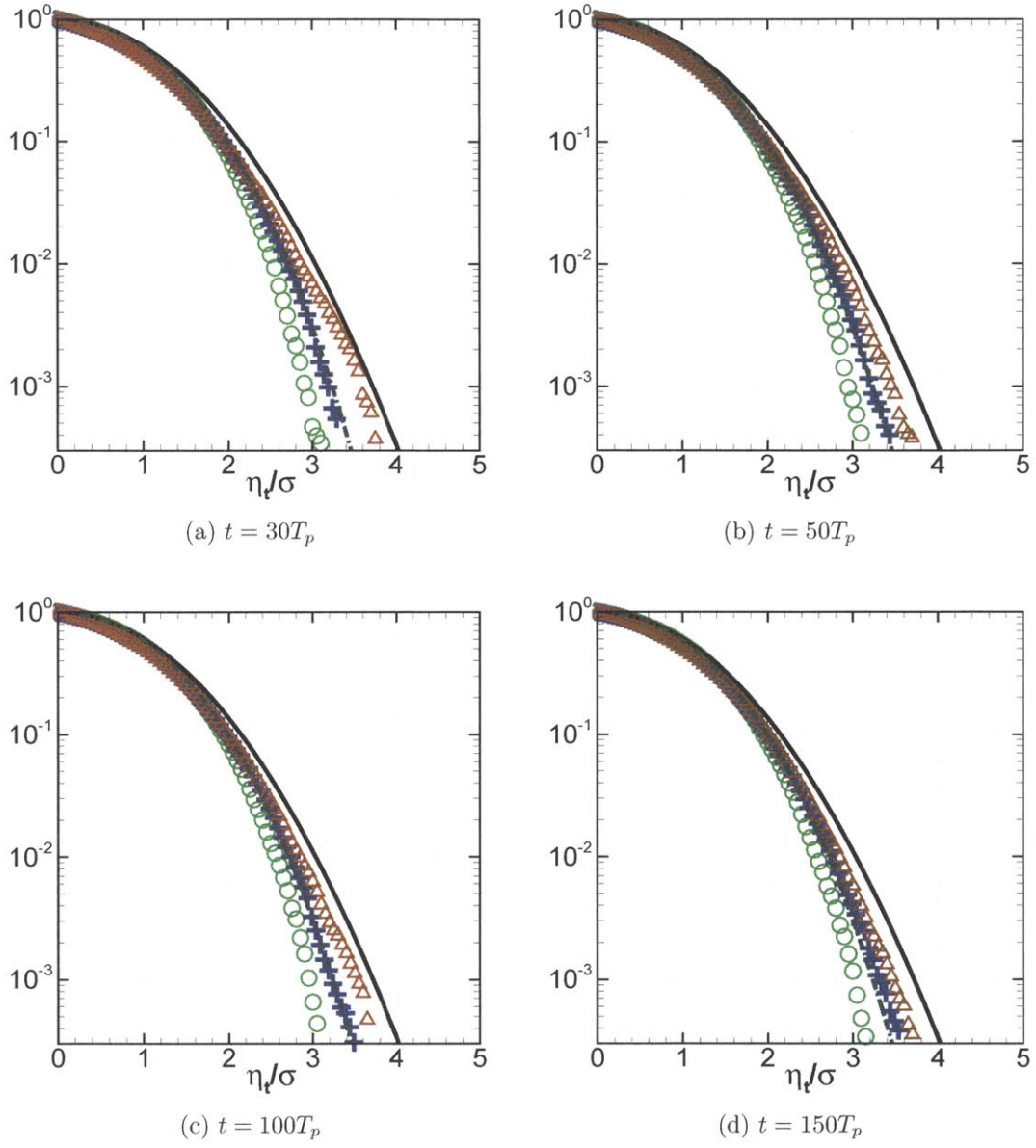

(a) $t = 30T_p$

(b) $t = 50T_p$

(c) $t = 100T_p$

(d) $t = 150T_p$

Figure 6-9: Exceeding probability of troughs for wavefields $\Theta = 20°$ with different water depths. $\mu = \text{inf}$ (△); $\mu = 1.53$, $h = 50\,\text{m}$ (+); $\mu = 1.07$, $h = 30\,\text{m}$ (◯). Rayleigh (—); Second-order theory (- - -).

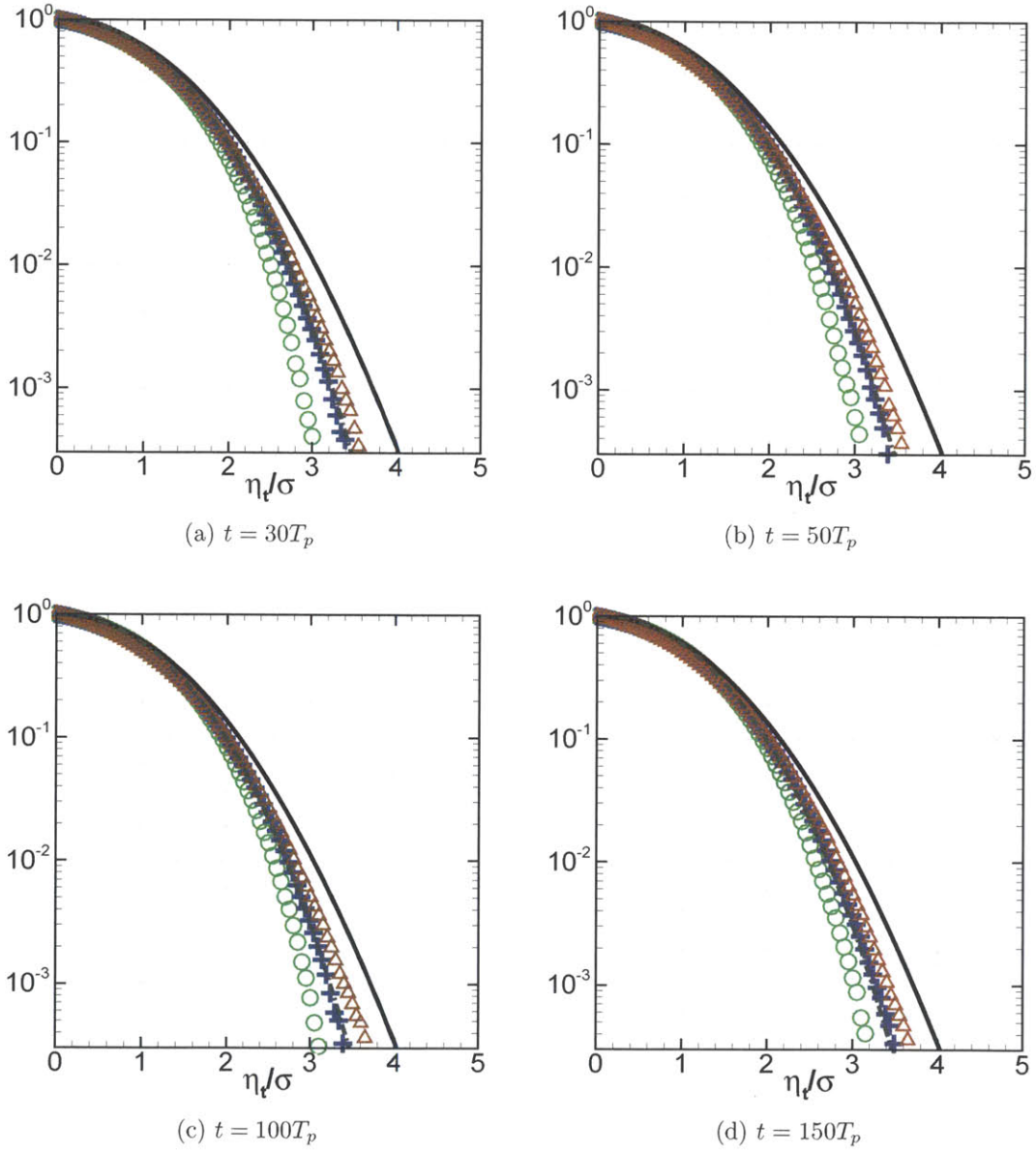

(a) $t = 30T_p$

(b) $t = 50T_p$

(c) $t = 100T_p$

(d) $t = 150T_p$

Figure 6-10: Exceeding probability of troughs for wavefields $\Theta = 80°$ with different water depths. $\mu = \inf$ (△); $\mu = 1.53$, $h = 50\,\mathrm{m}$ (+); $\mu = 1.07$, $h = 30\,\mathrm{m}$ (◯). Rayleigh (—); Second-order theory (- - -).

where $k = |\mathbf{k}|$ and Ψ is the wavenumber spectrum. Figure 6-11 shows the evolution of omnidirectional wave spectrum for wavefield $\Theta = 20°$. A significant downshifting of the spectral peak is observed in the case of deep water. As the water depth decreases, the spectral downshifting reduces, suggesting a reduction of nonlinear wave interactions among (dominant) energetic wave components. A considerable energy loss due to wave breaking is observed in the range of short waves, and it becomes more significant as the water becomes shallow, consistent with the results of decreasing significant wave heights discussed in §6.3.1. As water depth decreases, our results show the presence of a significant energy transfer to the low wavenumber region, leading to the generation of very long waves in nearshore areas. This is discussed in detail in §6.4.2. Figure 6-3b shows the evolution of omnidirectional spectra for wavefields with $\Theta = 80°$. We observe that the downshift of spectral peak and energy dissipation over short waves due to wave breaking are much weaker. The phenomenon of long wave generation however persists particularly in shallow depths.

The influence of water depth on the downshift of the spectral peak during evolution time $0 \sim 150T_p$ for the wavefields with $\Theta = 20°$ is shown in figure 6-13. A sudden and significant reduction in spectral peak downshift is observed as water depth becomes shallow.

6.4.2 Generation of long waves in finite water depth

As observed in figure 6-11 and 6-12, a significant energy is transferred to the low wavenumber region as the water depth decreases, leading to the generation of very long waves in nearshore areas. This is a result of second-order bound waves or triad wave-wave interactions, which are stronger with shallower depth. Proper prediction of such long waves is of particular importance in the designing of moorings of floating marine facilities in nearshore areas. The zoomed-in plots of the omnidirectional wave spectrum of long waves are shown in figure 6-14. The long waves are generated in wavefields as the water depth reduces. The energy transfer to long waves is more significant in the case $\Theta = 20°$ in comparison with the results observed in the case $\Theta = 80°$.

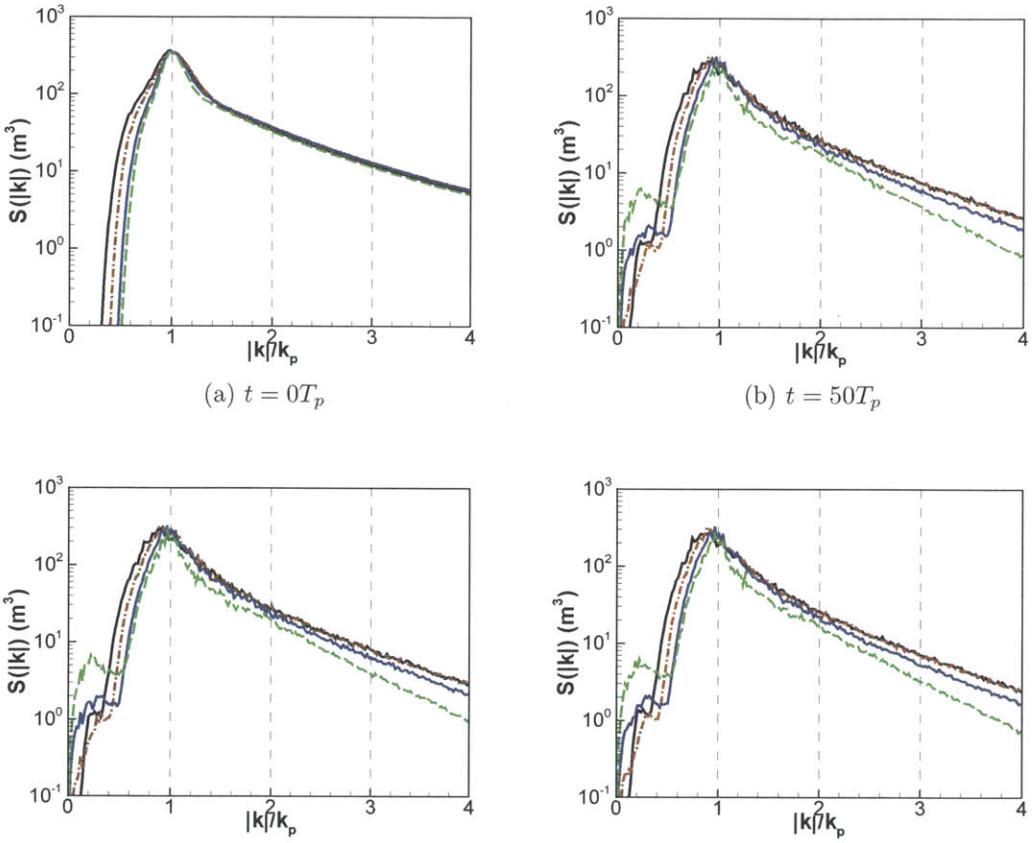

(a) $t = 0T_p$ (b) $t = 50T_p$

(c) $t = 100T_p$ (d) $t = 150T_p$

Figure 6-11: Evolution of omnidirectional spectra $S(\mathbf{k})$ of wavefields $\Theta = 20°$ with different water depths. $\mu = \inf$, Deep water (—); μ=2.82, h=100 m (– · –); μ=1.53, h=50 m (· · ·); μ=1.07, h=30 m (- - -).

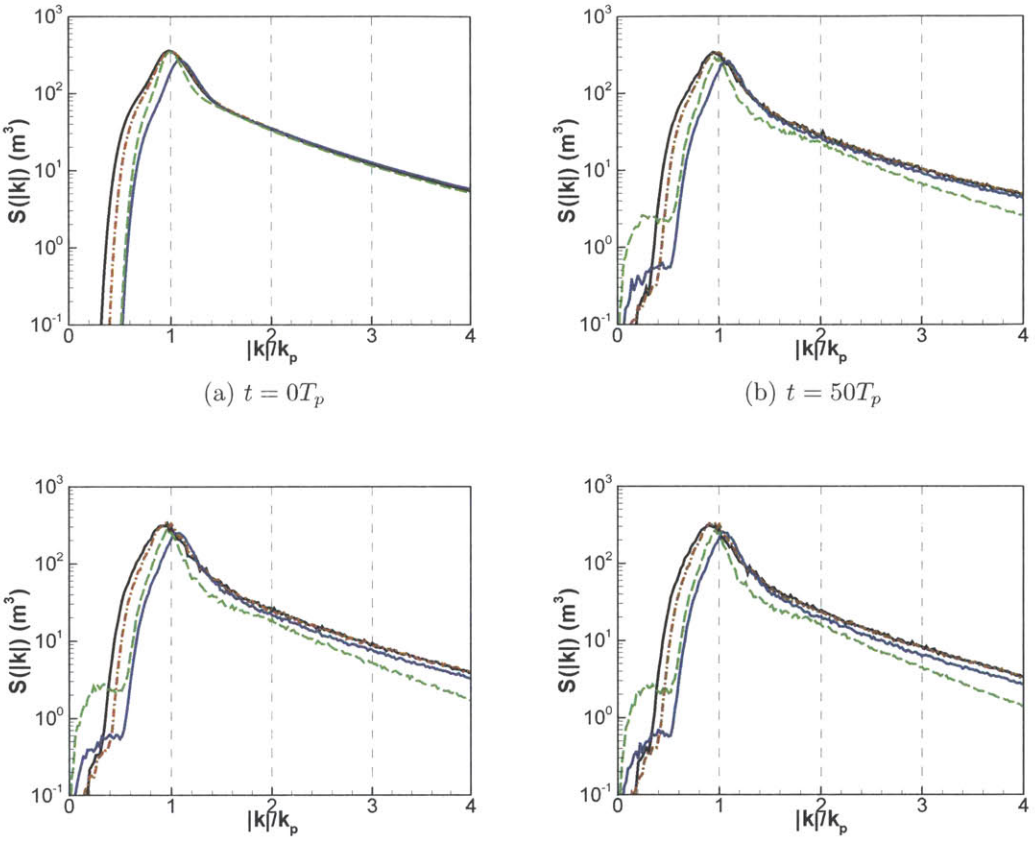

(a) $t = 0T_p$ (b) $t = 50T_p$

(c) $t = 100T_p$ (d) $t = 150T_p$

Figure 6-12: Evolution of omnidirectional spectra $S(\mathbf{k})$ of wavefields $\Theta = 80°$ with different water depths. μ = inf, Deep water (—); μ=2.82, h=100 m (– · –); μ=1.53, h=50 m (· · ·); μ=1.07, h=30 m (- - -).

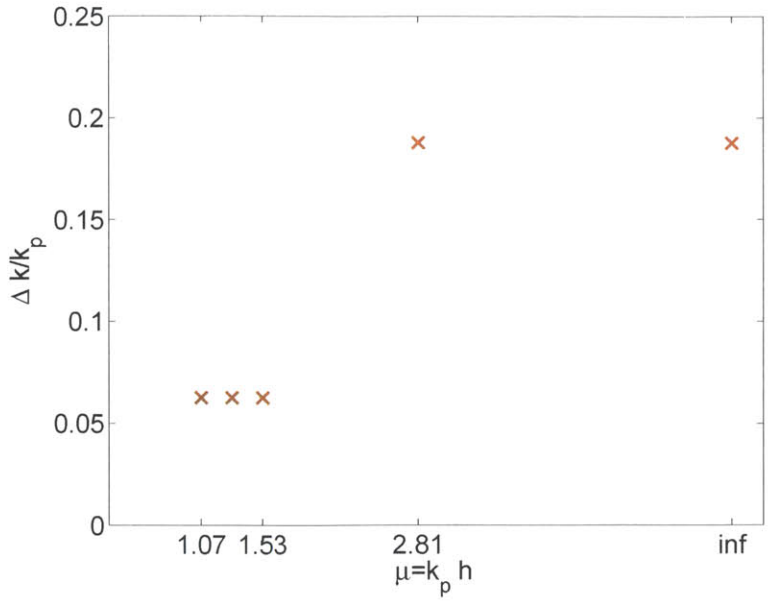

Figure 6-13: Downshift of the spectral peak as function of scaled water depth $\mu = k_p h$ for wavefields with $\Theta = 20°$.

6.5 Rogue waves in finite water depth

Figure 6-15 shows the temporal variation of number probability of rogue waves P_N defined in Chapter 5 for wavefields with a range of water depths. For both of the spreading angles considered, the occurrence probability of rogue waves decreases as water depth decreases. In small spreading angle case, for water depth $\mu \gtrsim 1.363$, the rogue wave occurrence is greatly enhanced in comparison with Rayleigh distribution, which is consistent with what we observe in the deep water case in Chapter 5. As water depth decrease, P_N reduces significantly due to the diminishment of modulational instability in shallow water. In shallow water depth, Rayleigh theory actually overestimates the occurrence of rogue waves. For large spreading, the dependence on water depth, although less considerable, remains. Figure 6-16 shows the temporal variation of area probability of rogue waves P_A for wavefields with different water depths. P_A has very similar variation trend with P_N expect that the magnitude of P_A is about five times of the magnitude of P_N. The influence of the water depth on the rogue wave probability is summarized in figure 6-17 for wavefields with $\Theta = 20°$. We find a sudden and significant reduction in number and area probabilities of rogue

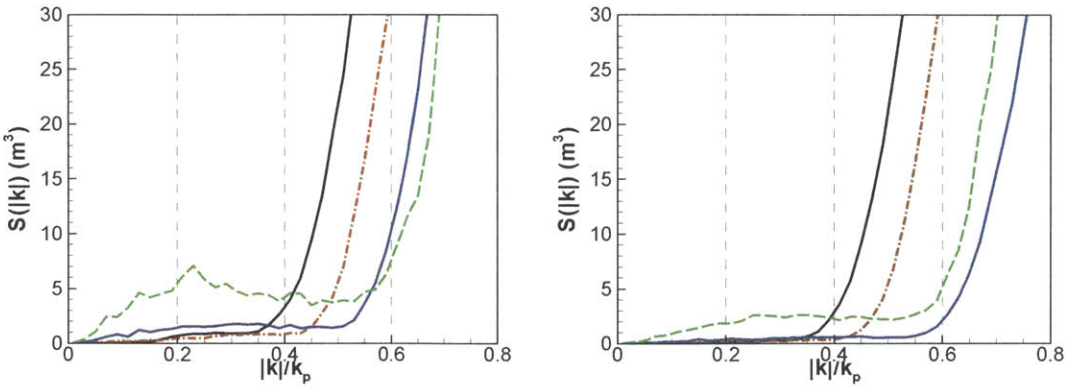

(a) $\Theta = 20°, t = 50T_p$ (b) $\Theta = 80°, t = 50T_p$

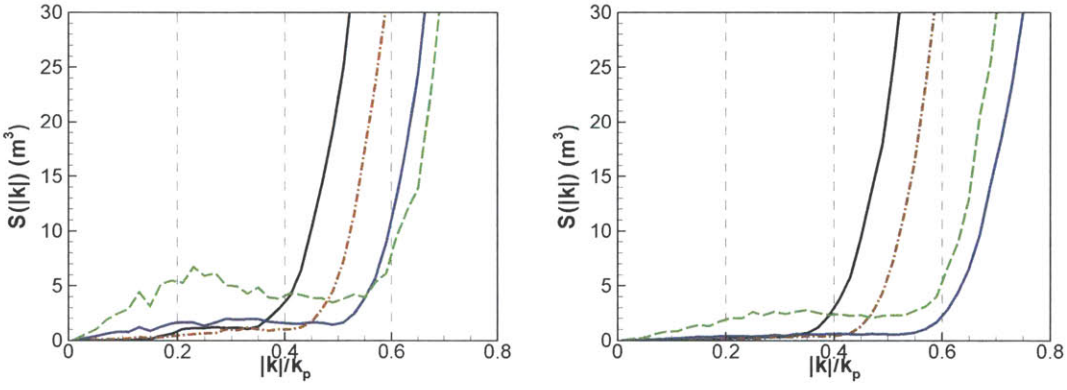

(c) $\Theta = 20°, t = 100T_p$ (d) $\Theta = 80°, t = 100T_p$

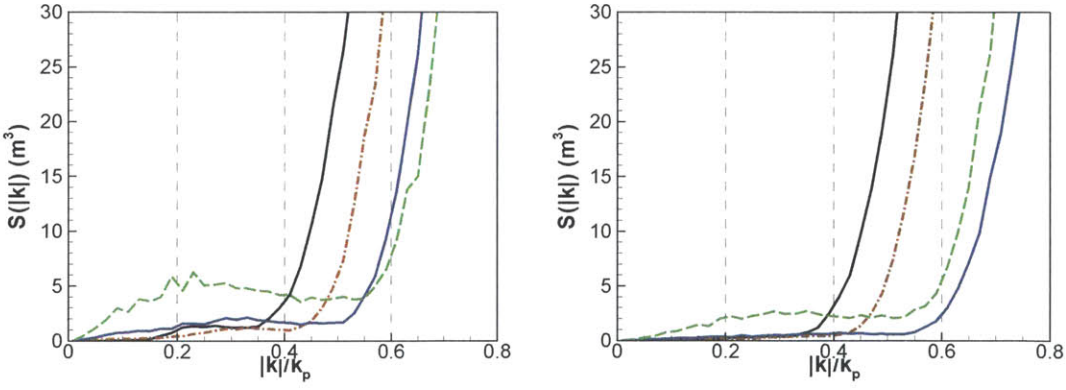

(e) $\Theta = 20°, t = 150T_p$ (f) $\Theta = 80°, t = 150T_p$

Figure 6-14: Wave spectra in the long wave region in different water depths with spreading angle $\Theta = 20°$ ((a), (c), (e)) and 80° ((b), (d), (f)). μ = inf, Deep water (—); μ=2.82, h=100 m (- · -); μ=1.53, h=50 m (···); μ=1.07, h=30 m (- - -).

waves as water depth reduces when $k_p h < 1.363$.

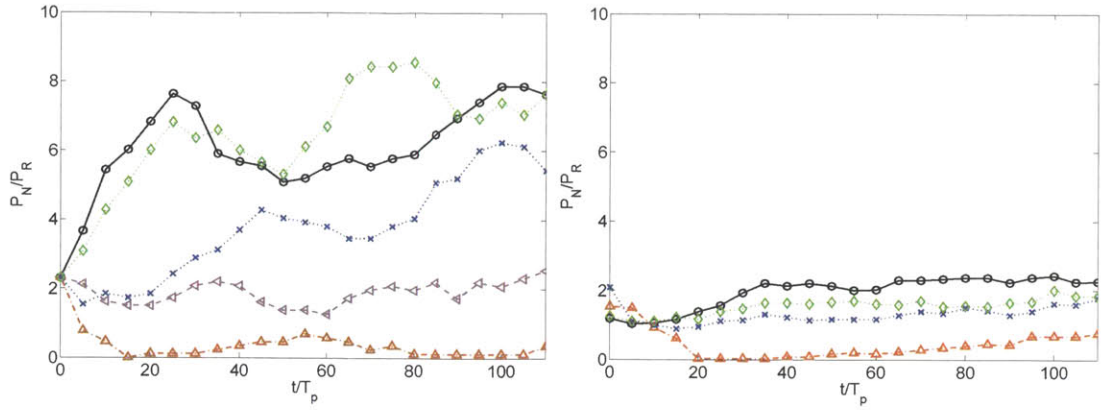

Figure 6-15: Variation of probability of rogue wave occurrence scaled by Rayleigh distribution P_N in wavefields with spreading angle $\Theta = 20°$. Deep water (◯); $\mu = 2.82$, $h = 100\,\text{m}$ (◇); $\mu = 1.53$, $h = 50\,\text{m}$ (+); $\mu = 1.30$, $h = 40\,\text{m}$ (◁); $\mu = 1.07$, $h = 30\,\text{m}$ (△). Results are scaled by the Rayleigh distribution P_R=3.35 × 10^{-4} for $H/H_s \geqslant \alpha$, α=2.

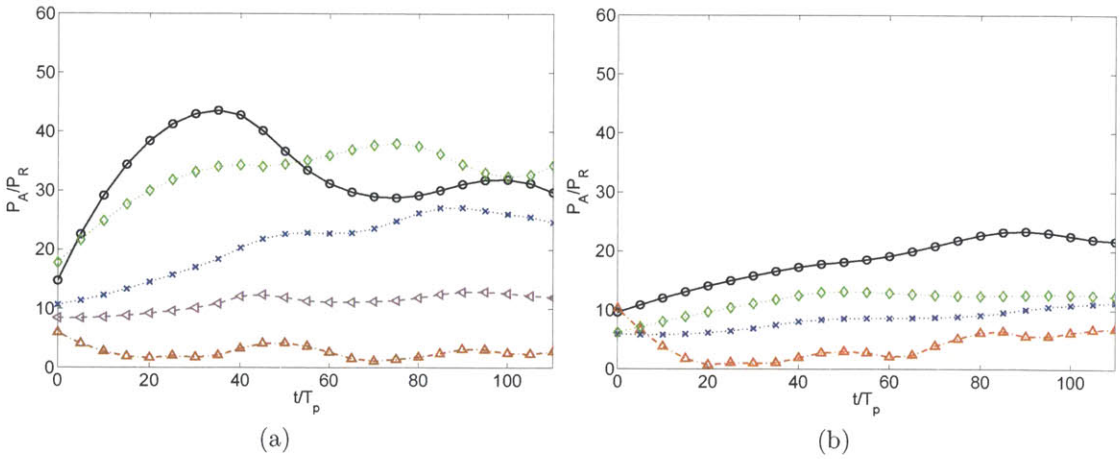

Figure 6-16: Variation of probability of rogue wave area P_A/P_N in wavefields with spreading angle $\Theta = 80°$. Deep water (◯); $\mu = 2.82$, $h = 100\,\text{m}$ (◇); $\mu = 1.53$, $h = 50\,\text{m}$ (+); $\mu = 1.30$, $h = 40\,\text{m}$ (◁); $\mu = 1.07$, $h = 30\text{m}$ (△). Results are scaled by the Rayleigh distribution P_R=3.35 × 10^{-4} for $H/H_s \geqslant \alpha$, α=2.

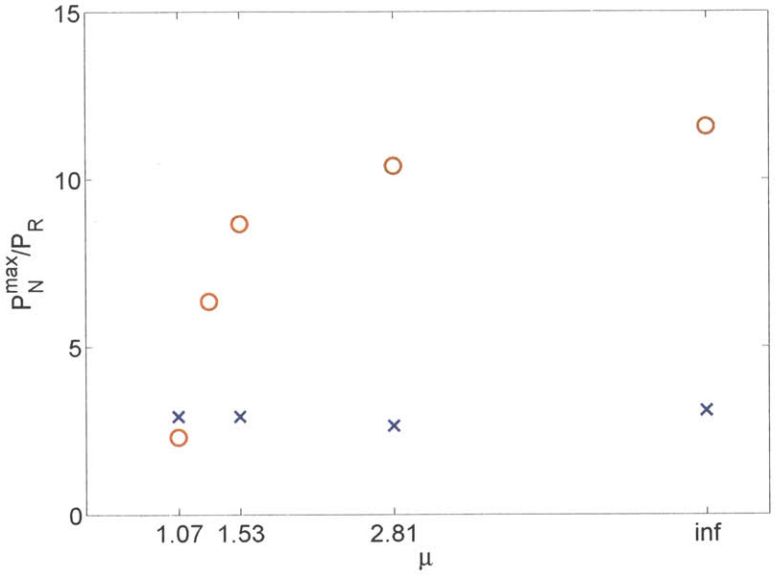

(a)

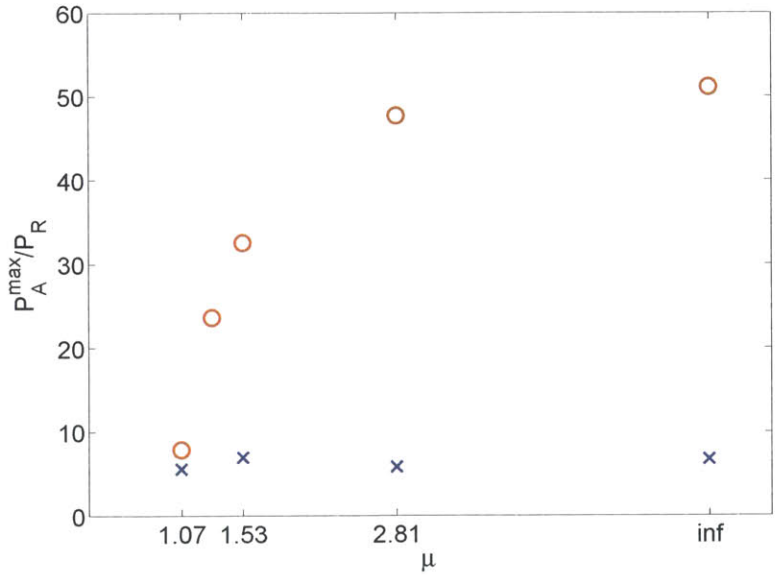

(b)

Figure 6-17: Dependence of (a) $P_N^{\max}/P_R$ and (b) $P_A^{\max}/P_R$ on the scaled water depth $\mu = k_p h$ for wavefields with $\Theta = 20°$. Results are scaled by the Rayleigh distribution P_R=3.35 $\times$ 10^{-4} for $H/H_s \geqslant \alpha$, α=2.

6.6 Summary and conclusions

We study the combined effects of finite water depth and directional spreading on the spectral evolution, nonlinear wave statistics, and probability of rogue waves using direct simulation approach SNOW. The results indicate considerable energy dissipation due to wave breaking for wavefields with shallow water depth. The finite water depth has a significant influence on skewness and kurtosis for wavefields with small spreading angle, specially for the scaled water depth $\mu \lesssim 1.363$. Skewness increases and kurtosis decreases as water depth reduces, which are consistent with Toffoli et al. (2009). This suggests the second-order nonlinearity associated with bound waves increases with water depth decreases, while the third-order nonlinearity dominated by modulational instability decreases as the water depth decreases. We find significant long waves are generated by second-order bound waves or triad wave-wave interactions in finite water depth. Compared to deep water, the occurrence probability of rogue waves is significantly reduced as the water becomes shallow. The threshold for instability at μ=1.363 has important consequences for wave modeling in intermediate depth. The effect of water depth on the wave statistics and rogue wave occurrence becomes less significant in wavefields with large directional spreading angle. In the relatively shallow water region $\mu \lesssim 1.363$, the kurtosis and occurrence probabilities of rogue waves are slightly greater in the cases with broader spreading angles.

It is important to point out that, for all the computations done in this chapter, the Ursell number, $\mathrm{Ur} = \varepsilon/(k_p h)^3$, is 0.006, 0.043 and 0.147 for $h = 100\,\mathrm{m}$, 50 m and 30 m, therefore the perturbation expansions in terms of the wave steepness in the mathematical formulations of HOS described in Chapter 2, are valid. We consider the case of flat bottom and shoaling process is not involved. If the water depth is slowly varying, the wave statistics and rogue wave probability may slowly adjust to different values in comparison with the ones obtained using the local depth assuming flat bottom. The varying bathymetry is not addressed in present study.

Chapter 7

Nonlinear wave statistics and rogue wave occurrence in bimodal wavefields

7.1 Introduction

The discussions in previous chapters are focused on the wave system with single spectral peak; however, wave spectra with multi-peaks are also measured in the ocean. Based on the data collected from the open North Sea, it is reported that the percentage of spectra with bimodal structure is about $20 \sim 25\%$ (Guedes Soares, 1991). Bimodal wavefield is described by a wave spectrum featuring two spectral peaks and it can form when a wind-sea and a swell coexist. A wind-sea, generated by the local wind, has relatively high peak frequency and is usually short-crested; a swell, generated from a storm far way, has relatively low peak frequency and is usually long-crested. A recent ship accident study found that a large percentage of ship accidents occur in bimodal seas (Toffoli et al., 2005).

In contrast to the wave statistics of single spectral peak wave system which are studied relatively intensively, the bimodal sea statistics have not been fully investigated. Unidirectional bimodal seas usually characterize in terms of relative significant

wave height ratio (HR) and peak period separation (PS) between the two systems:

$$HR = \frac{H_{ss}}{H_{sl}}, \qquad PS = \frac{T_l - T_s}{T_s + T_l}, \tag{7.1}$$

where H_{ss}*and* H_{sl} are significant wave heights of wind-sea and swell respectively, calculated as four times standard deviation of the surface elevation; T_s and T_l are peak periods of wind-sea and swell. The bimodal sea is called *wind-sea dominant* (or *swell dominant*) if $HR>1$ (or <1). Using second-order representations, Rodriguez et al. (2002) and Arena and Soares (2009) find that the presence of a second system can lead to an increased or decreased probability of large crests in comparison with linear Rayleigh theory, depending on whether the bimodal wavefield is wind-sea dominant or swell dominant.

To obtain a complete understanding on the statistics of bimodal seas is challenging, because the parameters in the bimodal system are double of the single system. Our intention here is not to do a complete quantification on the bimodal sea statistics as functions of spectral parameters, as we have done for the unimodal (single spectral peak) system in Chapter 5. Our focus in this chapter is a preliminary study on how a second swell-like system would affect the single wind sea system over the spatial temporal scales considered in Chapter 5. In particular, we study if an additional swell-like system will enhance the occurrence probability of large waves.

Several possible physical mechanisms responsible for enhanced occurrence probability of large waves in bimodal seas have been proposed. For unidirectional bimodal seas with $PS\approx 0$, that is, the two systems in bimodal sea have close periods and propagate in the same direction, energy can be transferred from wind-sea to swell due to resonance interactions (Masson, 1993). For directional bimodal seas with $PS\approx 0$, a second system with small oblique angle can result in an increase of the instability growth rates and enlargement of the instability region (Onorato et al., 2006). When the two systems have very different peak periods, $PS\approx 1$, energy transfer from swell to wind-sea due to nonlinear interactions occurs is expected to occur over large evolution time. Over small time scale, the presence of swell may, however, still change the wave

statistics through its modifications on the amplitudes and phases of wind sea. The influence of swell on a directional wind-sea is assessed using swell-modified nonlinear Schrödinger equation for $PS \approx 1$ (Gramstad and Trulsen, 2010). For short-crested wavefields, a second wave system can generally lead to a small increase (5%$\sim$10%) in probability of large crests except for the case in which the propagation direction of swell is orthogonal to the direction of wind-sea. For wavefields with small spreading angles, the influence of a second wave system is much less significant (Gramstad and Trulsen, 2010). To our knowledge, a comprehensive validation of the swell-modified nonlinear Schrödinger equation has not been performed by comparing with experiments or other numerical models.

In this preliminary study, we study the spectral evolution, nonlinear statistics and occurrence probability of rogue waves for swell-modulated wind-sea using direct simulations of nonlinear large-scale bimodal wavefields (SNOW). In particular, we are interested in the effect of swell on the modulational instability related to the wind-sea. We focus on the spatial and temporal scales relevant to the modulational instability of the wind-sea (or high-frequency) system: $\mathcal{L}/\lambda_s$, $\mathcal{T}/T_s = O(\varepsilon^{-2})$, where λ_s and T_s are wavelength and period of the wave at the spectral peak of wind-sea system. ε is the steepness of wind sea, $\varepsilon = H_{ss}k_s/2$, where $H_{ss} = 4\sigma_s$ (σ_s is the standard deviation of the surface elevation of wind sea) and k_s is the peak wavenumber of the wind sea.

7.2 Initial bimodal wavefield

7.2.1 Physical and numerical parameters

The physical parameters required to describe a bimodal wavefields are summarized in Table 7.1.

Although SNOW does not have restrictions on the specific shape of the bimodal spectrum, in this preliminary study, we study the cases in which the peak periods of the wind sea and swell are relatively close, that is, the peak period separation PS is relatively small. We investigate the influences of different aperture angles (β), the

Table 7.1: Input spectral parameters for the bimodal sea

Swell system	H_{sl} :	Significant wave height
	T_l :	Period
	k_l :	Peak wave number
	ω_l :	Peak wave frequency
	γ_l :	Peak enhancement parameter
	Θ_l :	Spreading angle of swell
Wind-sea system	H_{ss} :	Significant wave height
	T_s :	Period
	k_s :	Peak wave number
	ω_s :	Peak wave frequency
	γ_s :	Peak enhancement parameter
	Θ_s :	Spreading angle of swell
Bimodal	β	Bimodal aperture angle
	PS	$(T_l - T_s)/(T_s + T_l)$
	HR	H_{ss}/H_{sl}

relative significant wave height ratio HR, and the spreading angle of wind-sea Θ_s.

We consider the computational domain $L_x \times L_y$ and evolution time T, with $L_x = L_y = 128\lambda_p$ and T/T_p=150, leading to a physically domain 30 km in each direction for a typical spectral peak period T_p=10 s. A uniform grid $N_x \times N_y = 4096 \times 4096$ is applied, which gives a spatial resolution of $\Delta x = \Delta y \approx 7$ m for (T_p=10 s) and a spectral resolution of $\Delta k_x = \Delta k_y = k_p/32$. For the time integration, a constant time step of $\Delta t = T_p/32$ is used To capture nonlinear wave effects including quartet and quintet resonant interactions, we use the order of nonlinearity $M = 4$ in all SNOW computations. At the initial stage of the SNOW simulations, the free-surface boundary conditions are smoothly transitioned in time from linear to nonlinear for minimizing the numerical standing wave effect associated with the use of the linear initial conditions (Dommermuth, 2000).

7.2.2 Initial bimodal spectrum

The initial bimodal wavefield is composed of two JONSWAP spectra, one describes the high-frequency wind sea and the other describes the low-frequency swell. The

unimodal JONSWAP spectrum has a form

$$S(\omega) = \frac{\alpha_p g^2}{\omega^5} \exp\left[-\frac{5}{4}(\frac{\omega}{\omega_p})^{-4}\right] \gamma^{\exp\left[-\frac{(\omega-\omega_p)^2}{2\sigma_\omega^2 \omega_p^2}\right]}, \tag{7.2}$$

where ω is the wave frequency, ω_p is the peak wave frequency, α_p is the Phillips parameter, γ is the peak enhancement factor specifying the spectral bandwidth, and σ_ω=0.07 for $\omega \leq \omega_p$; σ_ω=0.09 for $\omega > \omega_p$.

The two-peak spectrum can be described by nine independent parameters, eight of which describe the significant wave height (H_s), peak period (T_p), peak enhancement parameter (γ) and spreading angle (Θ) of each wave system. The ninth parameter describes the aperture angle β between the propagation directions of the two wave systems. An example of bimodal spectrum $\Psi(k, \theta)$ and its relative one-dimensional omnidirectional spectrum are shown in figure 7-1.

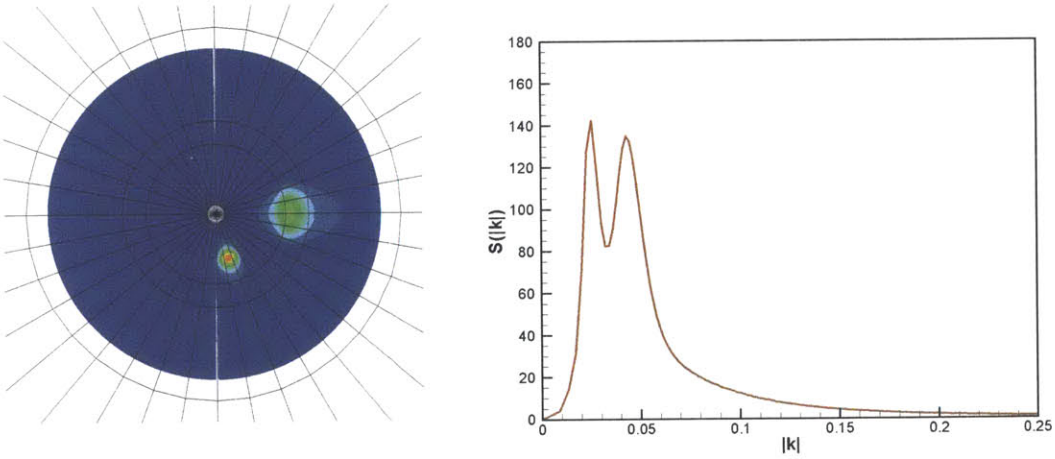

(a) (b)

Figure 7-1: (a) Example initial k-θ spectrum of a bimodal sea; (b) Omni-spectrum of the bimodal sea. Wind-sea (H_{ss}=5.5 m, T_s=9.5 s, γ_s=6, Θ_l=60°); Swell(H_{sl}=4 m, T_l=11.5 s, γ_l=10, Θ_l=20°) with aperture angle β=75°.

In this study, we focus on the influence of three bimodal spectral parameters on the spectral change, nonlinear statistics, and occurrence probabilities of rogue waves of the swell-modulated wind-sea. Our investigations are based on SNOW simulations of three scenarios:

Table 7.2: Parameter values for bimodal wavefield scenarios.

	H_s (m)	T_p (s)	γ	Θ (o)
Scenario A: effect of aperture angle				
swell	1.2	6	10	20
wind-sea	1.1	4	6	30
bimodal	β=20°, 40°, 60°, 80°, 90°, 100°			
Scenario B: effect of HR				
swell	1.2	6	10	20
wind-sea I	1.1	4	6	30
wind-sea II	1.5	4	6	30
bimodal	β=40°, 90°			
Scenario C: effect of Θ_s				
swell	1.2	6	10	20
wind-sea I	1.1	4	6	20
wind-sea II	1.1	4	6	30
wind-sea III	1.1	4	6	80
bimodal	β=40°			

Scenario A: Effect of aperture angle β;

Scenario B: Effect of relative significant wave height ratio HR;

Scenario C: Effect of spreading angle of wind sea Θ_s.

The initial input spectral parameters for these three scenarios are specified in Table 7.2.

7.3 Effect of the aperture angle between two wave systems

In this section, we study the influence of the aperture angle β, which is the angle between the dominant propagation directions of two wave systems, on the evolution of nonlinear bimodal wavefields. The input parameter values are described in scenario A in Table 7.2. The bimodal wavefields are composed of identical wind sea and

swell spectra with varying aperture angle β. The relative significant wave height ratio HR=0.92≈1 and the peak period separation PS=0.2. For unidirectional wavefields, a measure of the importance of modulational instability is the Benjamin-Feir index (BFI) (described in Chapter 5): BFI$\equiv\varepsilon/(\Delta k/k_p) > 1/\sqrt{2}$ (Janssen, 2003). The spectral bandwidth Δk is calculated as the half width at half maximum of the wavenumber spectrum. The corresponding values of BFI are equal to 0.93 and 0.52 for the wind sea and swell respectively.

7.3.1 Omnidirectional spectrum

Figure 7-2 shows the evolution of the omnidirectional spectra (described in Chapter 3 §3.3.2) of bimodal seas described in scenario A. For all the bimodal seas, we find considerable spectral peak downshift of the wind-sea system and energy loss in the large wavenumber region due to wave breaking. The peak downshift of wind-sea is calculated as $\Delta k/k_s$, where k_s is the initial peak wavenumber of the wind sea and $\Delta k = k_s - k_s(t)$ ($k_s(t)$ is the peak wavenumber at time t). Figure 7-3 shows the spectral downshift $\Delta k/k_s$ at time $t = 50T_s$ as a function of aperture angle β. For comparison, the results from unimodal wind sea is displayed. We find that a presence of swell in general leads to an enhanced spectral peak downshift of the wind sea. For small aperture angles, the spectral downshift is enhanced considerably. The downshift Δk decreases as the aperture angle β increases. For large aperture angles, the influence of swell on Δk is much less significant. The enhanced spectral peak downshift for small β is an indication of a more significant energy transfer around the spectral peak of the wind sea.

7.3.2 Skewness and kurtosis

Skewness, defined as Skew = $\langle\eta^3\rangle/\langle\eta^2\rangle^{3/2}$, measures the asymmetry of one distribution. Kurtosis, defined as Kur = $\langle\eta^4\rangle/\langle\eta^2\rangle^2$, describes the peakness of one distribution. Skewness and kurtosis of bimodal wavefields composed of a monochromatic swell and random short waves are studied in Gramstad and Trulsen (2010) with a

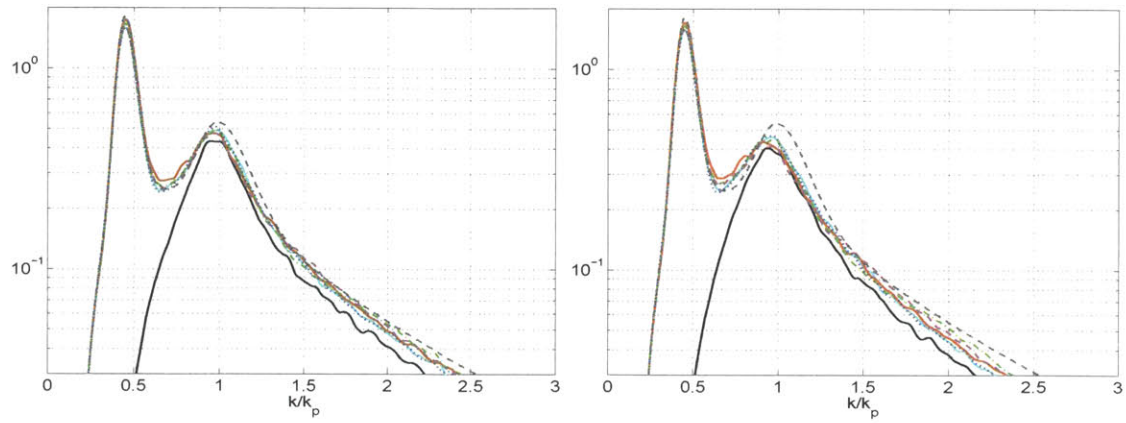

(a) $t = 30T_s$ (b) $t = 50T_s$

(c) $t = 70T_s$ (d) $t = 100T_s$

Figure 7-2: Evolution of omnidirectional spectrum of bimodal wavefields in scenario A. $\beta = 20°$ (—); 40° (- - -); 60° (- · -); 90° (· · ·); 100° (-··-); unimodal wind sea (—); initial bimodal spectrum (- - -).

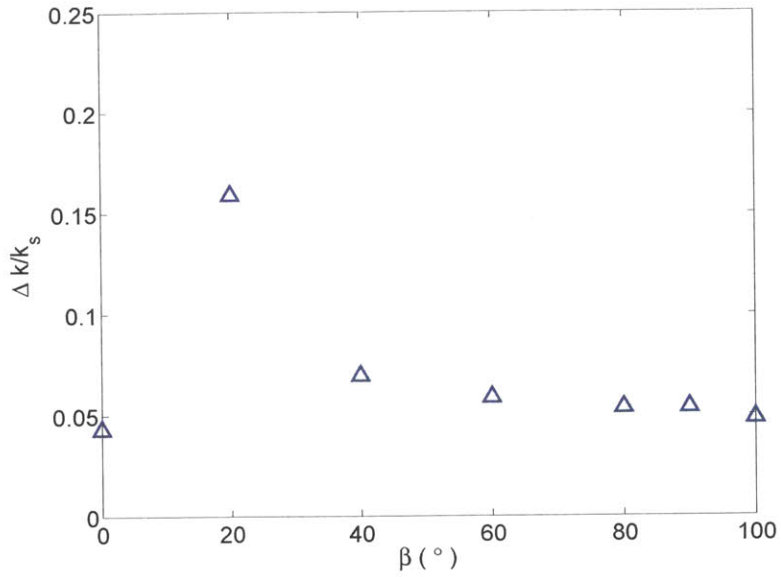

Figure 7-3: Influence of bimodal aperture angle β on the downshift of wind-sea spectral peak at time $t = 50T_s$. The unimodal wind sea is labeled as $\beta = 0°$.

peak period separation $HR{\approx}1$. Up to third-order wave nonlinearity, they find that the swell has no contribution to skewness and has only $O(\varepsilon^3)$ ($\varepsilon = k_s a_s$) contribution to kurtosis.

Figure 7-4 shows the temporal variation of skewness for bimodal wavefields with different aperture angles. For all the bimodal cases, skewness quickly increases from its initial value (Skew$\approx$0) to a quasi-steady value over a short time scale $t/T_s \sim (\varepsilon^{-1})$. Figure 7-5 shows the influence of β on the mean skewness, denoted as $\langle$skewness$\rangle$, which is defined as the mean of the skewness over time $0 \leqslant t/T_s \leqslant 100$. We find a presence of swell in general leads to a reduction in skewness in comparison with the mean skewness in uni-modal wind sea. This suggests that the wave profiles in bimodal wavefields in general are less skewed than the uni-modal wind-sea waves. The mean skewness increases as the aperture angle β decreases. The smallest value of $\langle$skewness$\rangle$ is found for β=90°.

Figure 7-6 shows the temporal variation of kurtosis for bimodal wavefields with different aperture angles. For short evolution time, kurtosis increases in a similar fashion with it does in uni-modal case and the value of kurtosis decreases as the aperture angle increases. This is because over short time, modulational instability plays

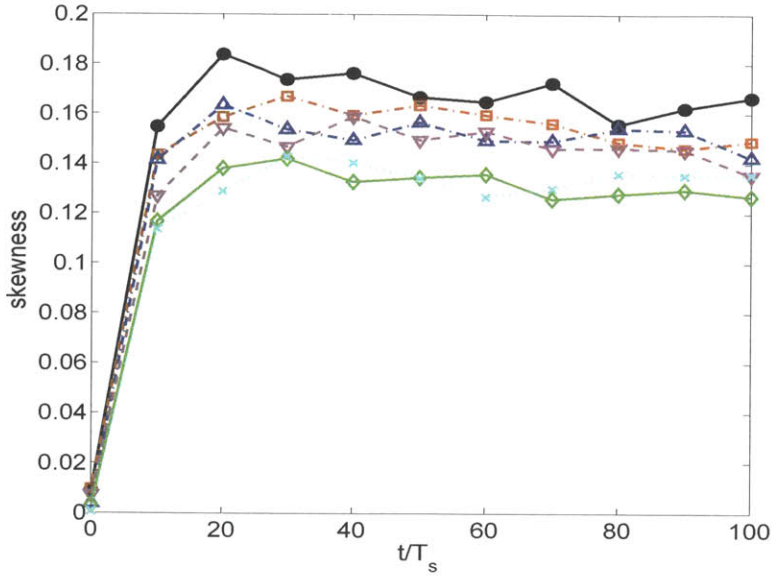

Figure 7-4: Temporal variation of skewness for bimodal wavefields in scenario A. $\beta = 20°$ (□); 40° (△); 60° (▽); 90° (◇); 100° (×); unimodal wind sea (•).

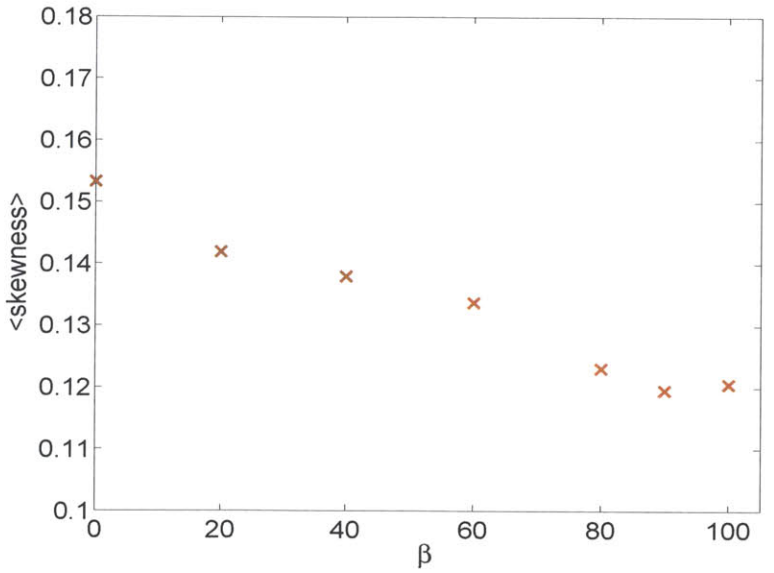

Figure 7-5: Influence of aperture angle β on the mean skewness $\langle$skewness$\rangle$ of bimodal wavefields in scenario A. The results of wind-sea only system is recorded as $\beta = 0°$.

a dominant role in wave dynamics and a presence swell leads to a broader effective directional spreading. For relatively longer time evolution, unlike the variation of kurtosis in uni-modal wind sea, kurtosis does not decrease after reaching its maximum value in bimodal wavefields, instead, it slowly increases to a quasi-stationary value.

We define the maximum kurtosis, attained during the entire SNOW simulation (up to t/T_p=100), as well as the average value of kurtosis, Kur^{+}, obtained over the quasi-steady phase of the SNOW evolution ($60 \leqslant t/T_p \leqslant 100$). Figure 7-7 shows $\mathrm{Kur}^{\max}$ and Kur^{+} as functions of aperture angle β. $\mathrm{Kur}^{\max}$ in bimodal seas is slightly smaller than its value in uni-modal wind sea except for the case with $\beta = 90°$, where a great reduction of $\mathrm{Kur}^{\max}$ is observed (figure 7-7(a)). Figure 7-7(b) shows Kur^{+} as a function of β. In contrast to $\mathrm{Kur}^{\max}$, Kur^{+} is greater in bimodal wavefields except for the case with $\beta = 90°$. A great reduction of Kur^{+} is found again for $\beta = 90°$.

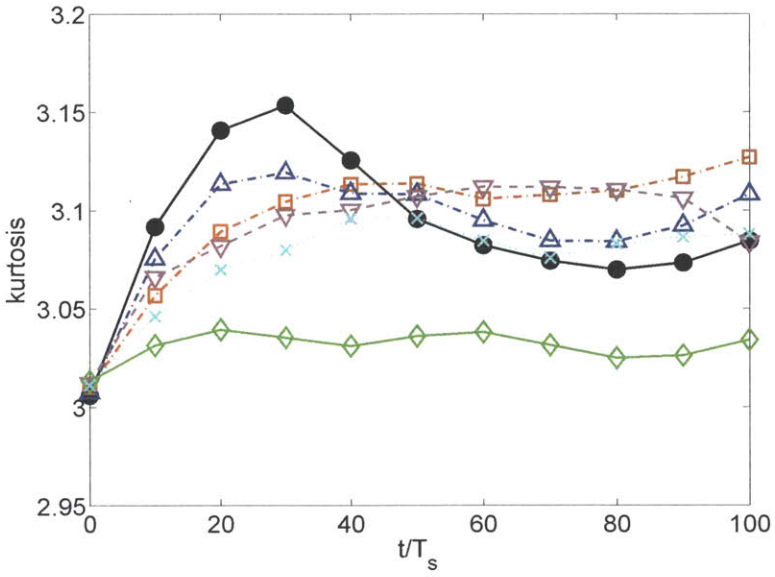

Figure 7-6: Temporal variation of kurtosis for bimodal wavefields in scenario A. $\beta =$ 20° (□); 40° (△); 60° (▽); 90° (◇); 100° (×); unimodal wind sea (•).

7.3.3 Exceeding probability of large crests

Figure 7-8 shows the exceeding probability of large crests for the bimodal seas in scenario A. The Rayleigh and second-order predictions are plotted for comparisons.

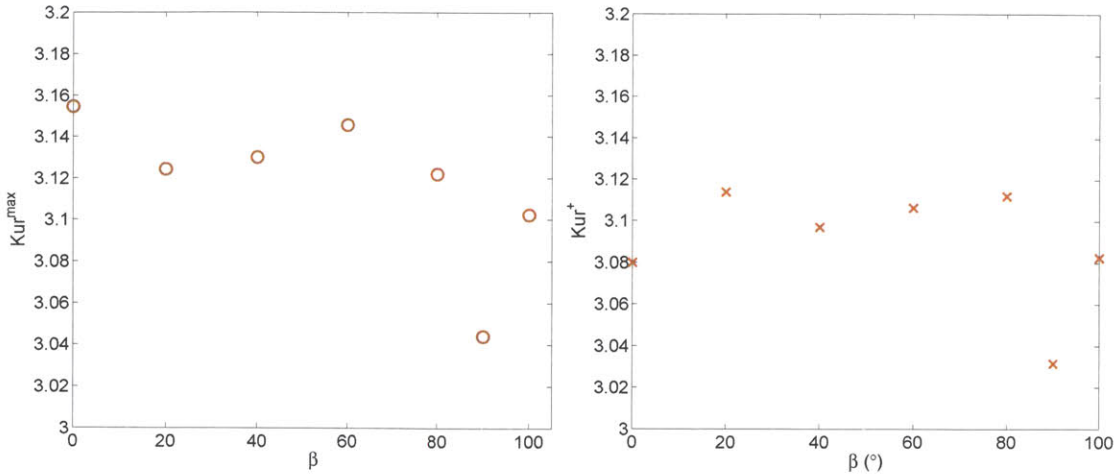

Figure 7-7: The influence of aperture angle β on (a) $\mathrm{Kur}^{\mathrm{max}}$ and (b) Kur^{+} for bimodal wavefields described in scenario A. The unimodal wind sea is labeled as $\beta = 0°$.

At short time scale ($t = 20T_s$), the probability of large crests in bimodal wavefields is smaller than the value in the unimodal wind sea (figure 7-8(a)). This might be because over short time the modulational instability is important and large crests are greatly enhanced in single wind sea. For larger time ($t > 20T_s$) when the modulational instability becomes less important, the probabilities of large crests in bimodal seas are higher than the large crest probability in single wind sea, except for the case with $\beta = 90°$. In the bimodal case with $\beta = 90°$, the exceeding probability of large crests is close to the one in unimodal wind sea. For all the cases considered, Rayleigh distribution underestimates the probability of large crests. For most of the bimodal seas considered, the second-order theory (Tayfun, 1980) underestimates the occurrence of large crests, except for the case $\beta = 90°$, where the crest distribution is found to be close to second-order theory.

Figure 7-9 plots the exceeding probability of large crests in bimodal seas, scaled by the corresponding value in unimodal wind sea, as a function of aperture angle β. We find that the influence of swell on the crest probability of wind sea is not monotonic. The probability of large crests can increase or decrease when a swell is present, but an inclusion of swell in general leads to an enhanced probability of large

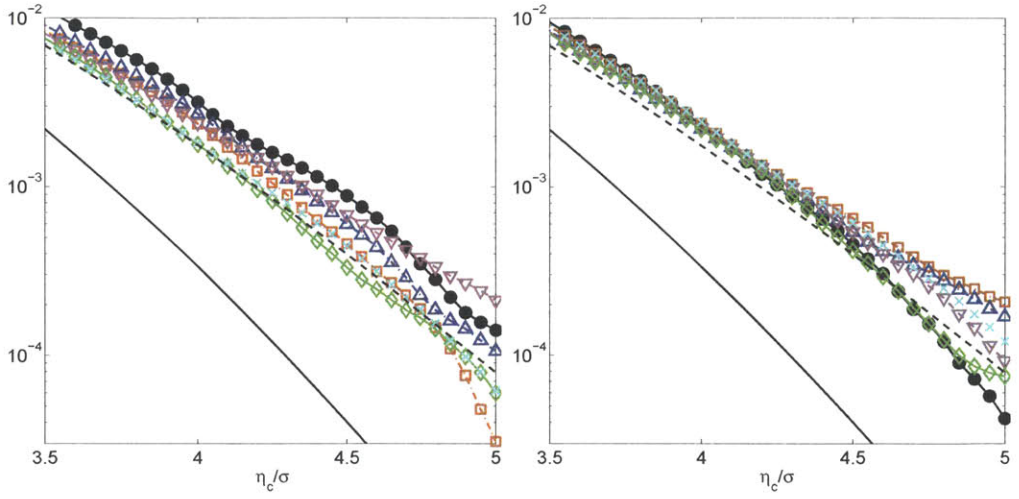

(a) $t = 20T_s$

(b) $t = 50T_s$

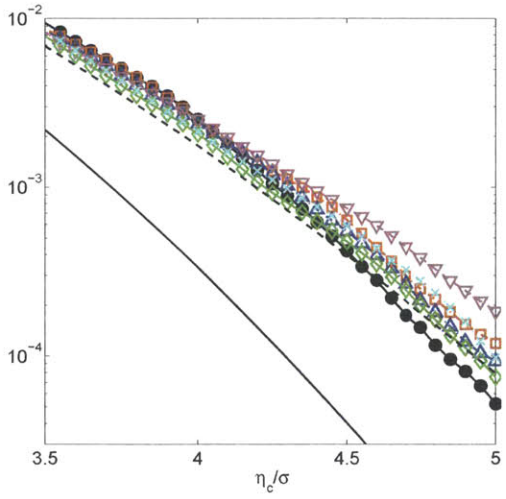

(c) $t = 70T_s$

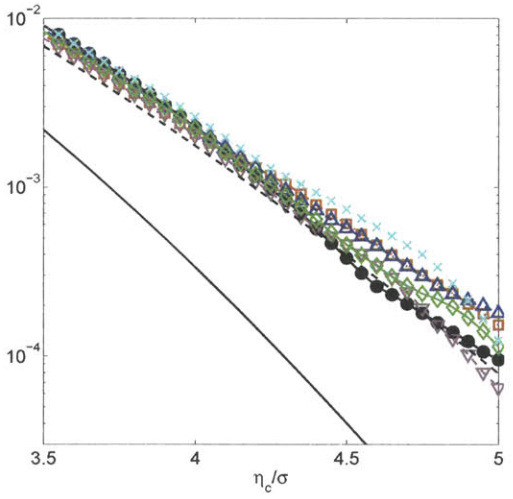

(d) $t = 100T_s$

Figure 7-8: Exceeding probability of large crests for bimodal wavefields in scenario A. $\beta = 20°$ (□); 40° (△); 60° (▽); 90° (◇); 100° (×); unimodal wind sea (•). Rayleigh theory (—); second-order theory (Tayfun, 1980) (- - -)

crests. The probability of large crests $\eta_c > 4.8\sigma$ is increased by 150% in bimodal wavefields (figure 7-9(b)). Consistent with previous findings, the probability of large crests is least enhanced for the bimodal wavefield with $\beta = 90°$.

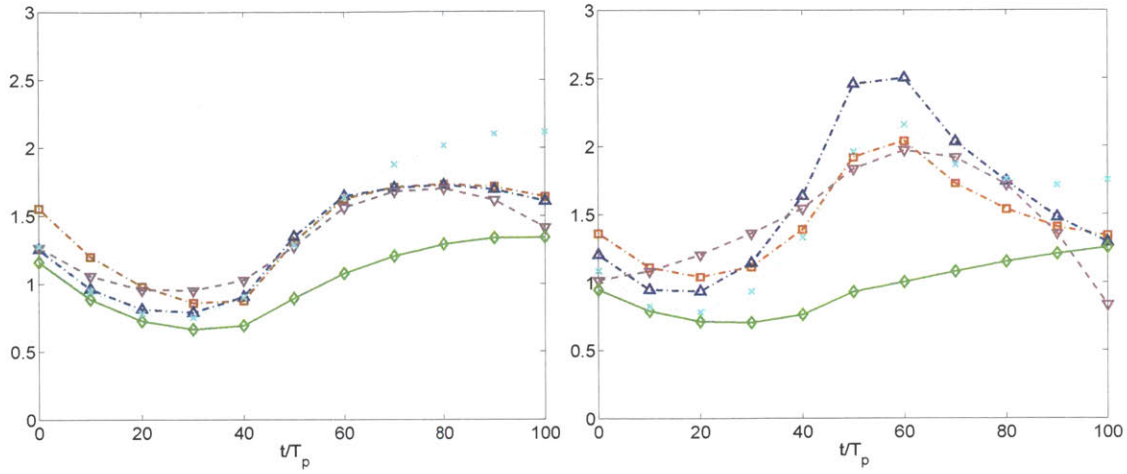

Figure 7-9: Temporal variation of exceeding probability of large crests in bimodal seas in scenario A, $P(\eta_c \geqslant \alpha\sigma)$, scaled by the values in unimodal wind sea. (a) α =4.6; (b) α =4.8. $\beta = 20°$ (□); 40° (△); 60° (▽); 90° (◇); 100° (×).

7.3.4 Area probability of rogue waves

In this subsection, we study here the occurrence probability of rogue waves in swell-modulated wind sea described in scenario A. We have discussed in Chapter 5 that the occurrence of rogue waves can be measured by the number probability (P_N) and area probability (P_A). For bimodal wavefields, it is unclear how to calculate the total number of waves, the area probability of rogue waves P_A, therefore, is particularly useful in this case. Figure 7-10 shows the area probability in bimodal seas is in general greater than its value in wind sea. The inclusion of a swell can lead to an increase of P_A up to 5 times comparing to P_A in unimodal wind sea. The area probability of rogue waves for bimodal seas with $\beta = 90°$ is close to the value in unimodal wind sea.

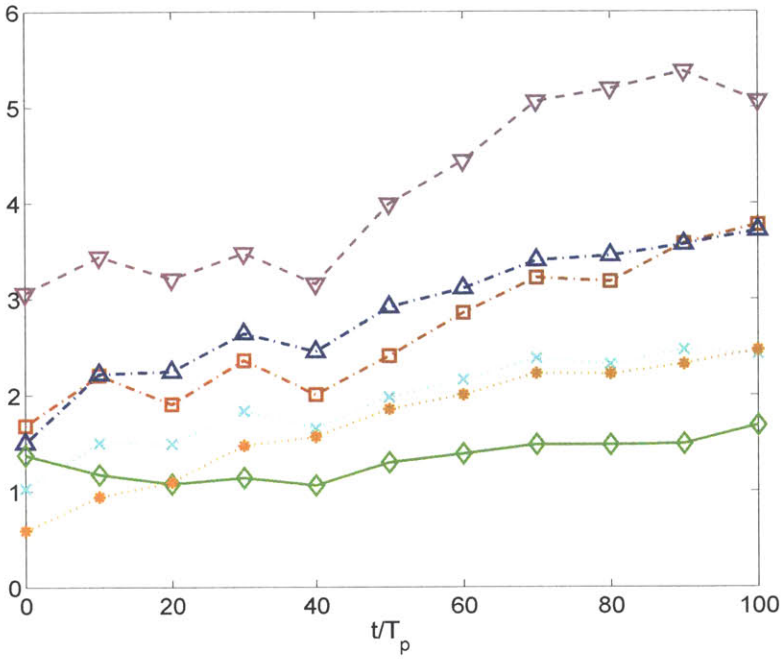

Figure 7-10: Evolution of area probability of rogue waves P_A scaled by the value in unimodal wind sea for bimodal wavefields in scenario A. β = 20° (□); 40° (△); 60° (▽); 80° (∗); 90° (◇); 100° (×).

7.4 Effect of relative significant wave height ratio

In this section, we study the effect of relative significant wave height ratio HR on the nonlinear evolution of bimodal wavefields described in Table 7.2 scenario B. The swell component in the bimodal wavefields considered in this section is identical. The peak period separation PS=0.2. The wind-sea components have two different significant wave heights H_{ss}. One bimodal wavefield is swell-dominant with HR=0.92<1; and one is wind-sea dominant HR=1.25>1. The values of BFI calculated from the wind seas are 0.93 and 1.26 for the swell-dominant and wind-sea dominant bimodal seas respectively.

7.4.1 Omnidirectional spectrum

Figure 7-11 shows the nonlinear evolution of the omnidirectional spectrum of bimodal wavefields described in scenario B. Considerable spectral peak downshifting is observed for all cases considered and it is more significant in the wind-sea dominant

($HR>$ 1) case. This is somewhat expected because the spectral peak downshift is caused by nonlinear wave interaction. For the same spreading angle Θ_s, a higher BFI value of the wind sea suggests a more significant wave nonlinearity of the wavefield. Figure 7-12 plots the peak wave downshift of the wind sea for the swell-dominant and wind-sea dominant bimodal wavefields with different aperture angles β. A more rapid downshift is observed in the wind-sea dominant case HR=1.25. In the wind-sea dominant case, after the rapid downshift, the omnidirectional spectra become quasi-stationary. For the swell-dominant bimodal wavefield, a slowly continuous spectral downshift is observed. For given HR, the spectral downshift is smaller for $\beta = 90°$, consistent with §7.3.1.

7.4.2 Skewness and kurtosis

Figure 7-13 shows the influence of HR on the skewness of bimodal wavefields. Consistent with the previous discussions, wave profiles are in general less skewed in bimodal wavefields. In comparison with the swell-dominant case, the influence of aperture angle is less significant in the wind-sea dominant bimodal sea. For both swell-dominant and wind-sea dominant cases, the skewness is minimized when $\beta = 90°$.

Figure 7-14 shows the variation of kurtosis for bimodal wavefields with different HR. For swell-dominant bimodal seas, as we discussed in §7.3.2, $\mathrm{Kur}^{\mathrm{max}}$ is smaller and Kur^{+} is greater in bimodal seas with β not equal to 90°. For wind-sea dominant bimodal wavefields, both $\mathrm{Kur}^{\mathrm{max}}$ and Kur^{+} are smaller in bimodal seas. For aperture angle $\beta = 90°$, a significant reduction of kurtosis is again observed for both values of HR.

7.4.3 Exceeding probability of large crests

Figure 7-15 shows the exceeding probability of large crests for bimodal wavefields in scenario B. The influence of swell on the probability of large crests are not monotonic. In the wind-sea dominant bimodal wavefields, the probability of large crests is in general smaller in bimodal wavefields than its value in wind sea. In this case, Tayfun

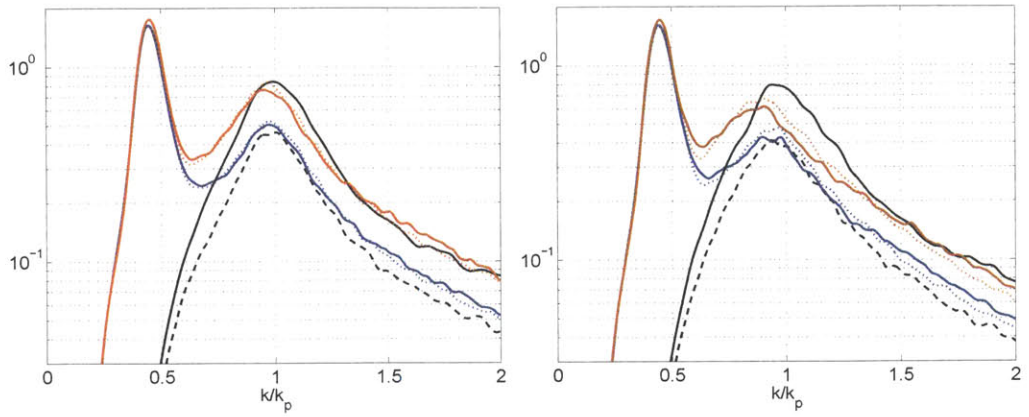

(a) $t = 30T_p$ (b) $t = 50T_p$

(c) $t = 70T_p$ (d) $t = 100T_p$

Figure 7-11: Evolution of omnidirectional spectra $S(k)$ of bimodal wavefields in scenario B. HR=1.25: β=40° (—), β=90° (· · ·) Wind sea (—); HR=0.92: β=40° (—), β=90° (· · ·). Wind sea (- - -).

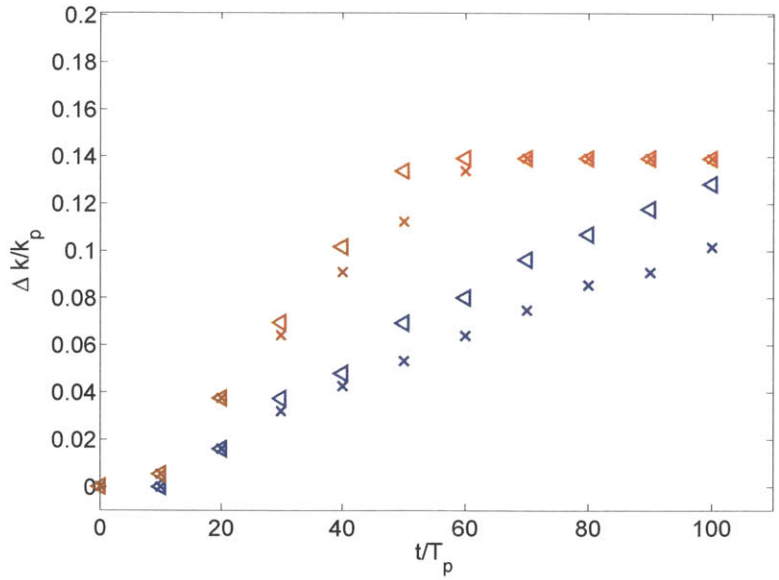

Figure 7-12: The spectral peak downshift $\Delta k/k_s$ for bimodal wavefields with different HR. HR=1.25> 1: $\Theta = 40°$ ($\triangleleft$), $\Theta = 90°$ ($\times$); HR=0.92< 1: $\Theta = 40°$ ($\triangleleft$), $\Theta = 90°$ ($\times$).

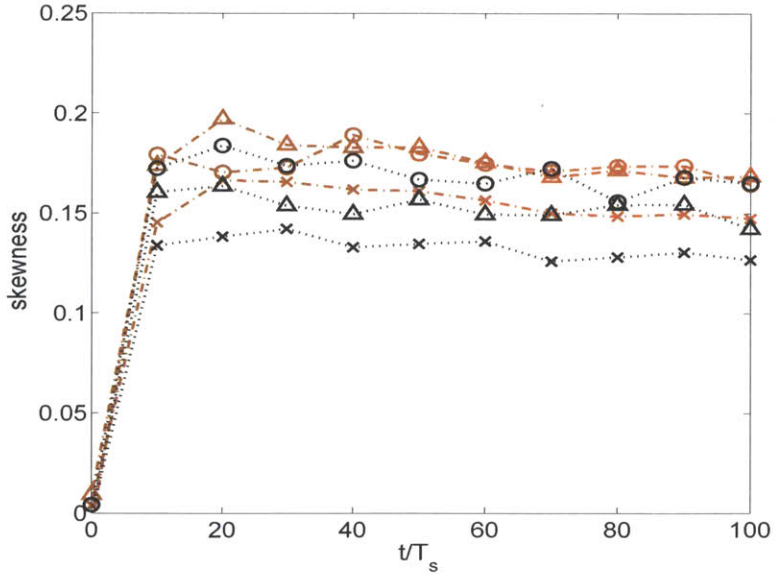

Figure 7-13: Influence of relative significant wave height HR on skewness for bimodal wavefields in scenario B. HR=1.25: Wind sea ($\bigcirc$) β=40° (Δ), β=90° ($\times$); HR=0.92: Wind sea ($\bigcirc$) β=40° (Δ), β=90° ($\times$).

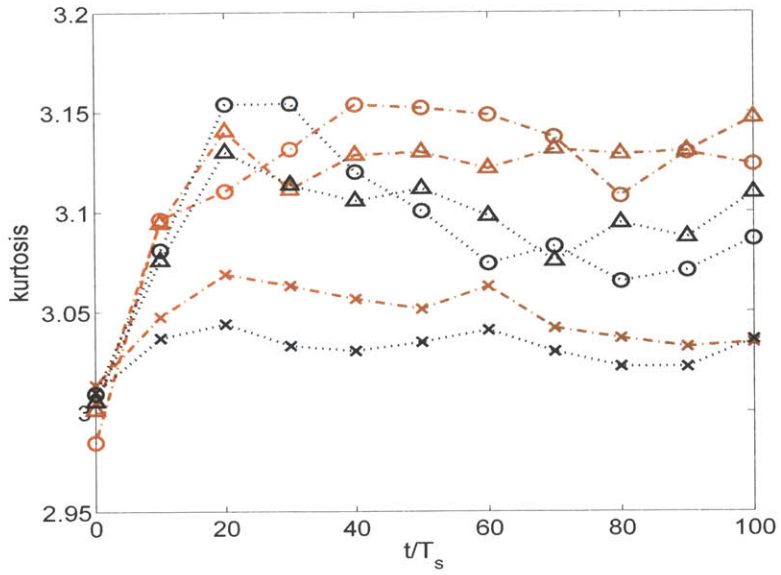

Figure 7-14: Influence of relative significant wave height HR on kurtosis for bimodal wavefields in scenario B. HR=1.25: Wind sea (◯) β=40° (△), β=90° (×); HR=0.92: Wind sea (◯) β=40° (△), β=90° (×).

second-order theory (Tayfun, 1980) underestimates the large crest probability in wind sea, but overestimates large crest probability in bimodal seas. This is because in the wind-dominant bimodal case considered, modulational instability plays a major role in the formation of large crests. The presence of swell leads to a broader effective spreading angle, leading to a similar or reduced probability of large crests. For the swell-dominant case, inclusion of a swell generally leads to an increase in large crest occurrence. This could be because the high-order nonlinearity is increased due to the inclusion of a strong swell (as seen in Figure 7-14). The influence of HR is seen more clearly in Figure 7-16, where the occurrence of large crests in bimodal seas scaled by the values in unimodal wind sea is plotted. A great reduction of large crest occurrence is observed for bimodal seas with $\beta = 90°$ regardless HR.

7.4.4 Area probability of rogue waves

Figure 7-17 shows the influence of relative significant wave height HR on the area probability of rogue waves. The area probability of large waves in bimodal seas, scaled by the value in unimodal wind sea, is plotted. For aperture angle $\beta = 40°$, for

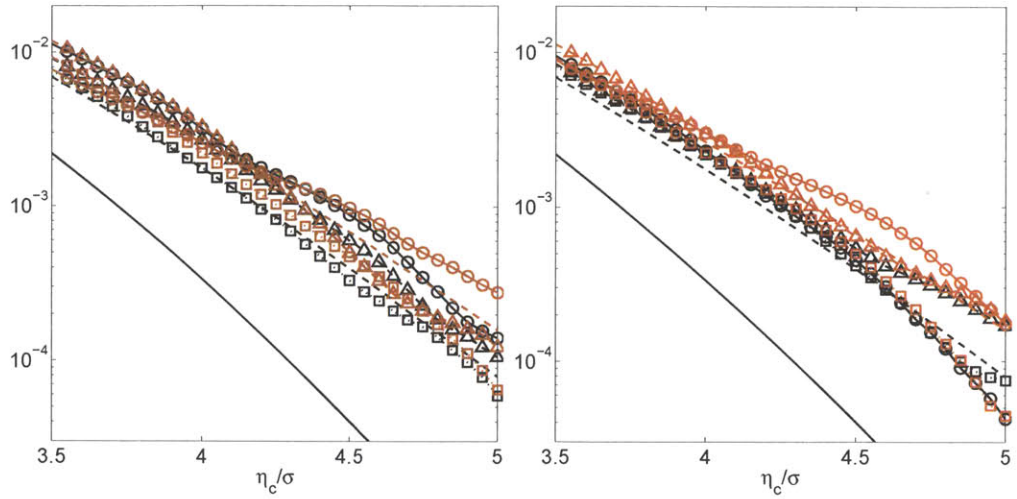

(a) $t = 20T_s$ (b) $t = 50T_s$

(c) $t = 70T_s$ (d) $t = 100T_s$

Figure 7-15: Exceeding probability of large crests of bimodal wavefields in scenario B. HR=1.25: β=40° (△), β=90° (□) Wind sea (○); Tayfun second-order theory (—) HR=0.92: β=40° (Δ), β=90° (□); unimodal wind sea (○). Linear Rayleigh theory (—), Tayfun second-order theory (- - -).

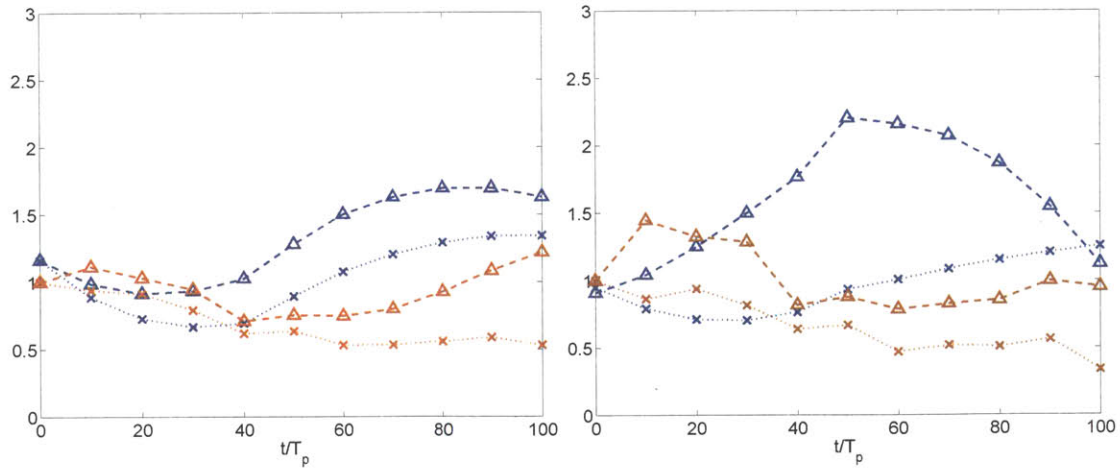

Figure 7-16: Temporal variation of exceeding probability of large crests in bimodal seas $P_\beta(\eta_c \geqslant \alpha\sigma)$ scaled by the values in unimodal wind sea $P(\eta_c \geqslant \alpha\sigma)$ for bimodal wavefields in scenario B. (a) α =4.6; (b) α =4.8. HR=1.25: β=40° (Δ), β=90° ($\times$); HR=0.92: β=40° (Δ), β=90° ($\times$).

wind-dominant bimodal sea (HR> 1), the area probability of rogue waves in bimodal seas is slightly enhanced relative to its value in unimodal wind sea; for swell-dominant bimodal sea (HR< 1), the area probability of rogue waves in bimodal seas is enhanced up to four times of its value in unimodal wind sea. For aperture angle $\beta = 90°$, the area probability of rogue waves are comparable to the value in unimodal wind sea in both swell-dominant and wind-sea dominant bimodal seas.

7.5 Effect of the spreading angle of wind sea

In this section, we study the influence of the spreading angle of wind sea Θ_s on the evolution of nonlinear bimodal wavefields described in Table 7.2 scenario C. The swell component of the bimodal seas is identical for all the cases. The wind-sea components in the bimodal seas have same frequency spectrum with varying spreading angle Θ_s. All the bimodal seas have relative significant wave height HR=0.92 and aperture angle $\beta = 40°$.

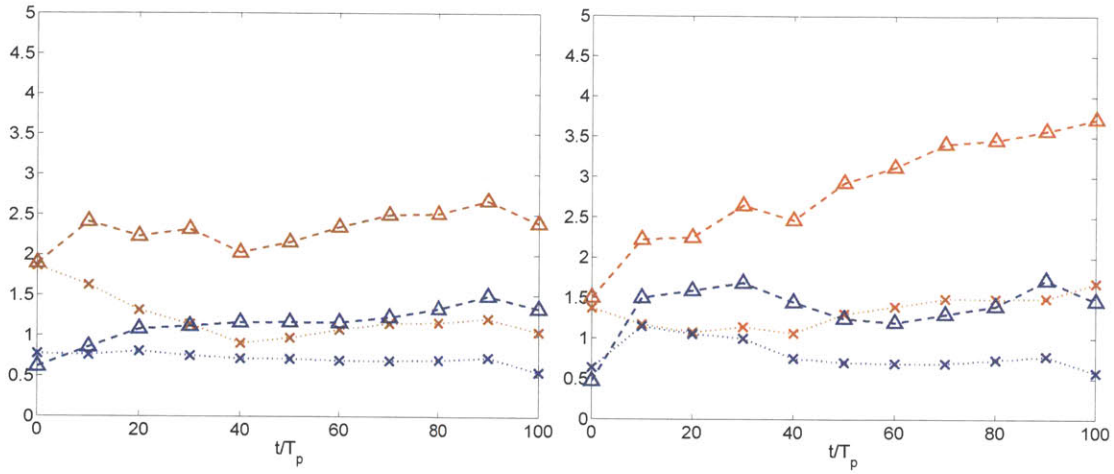

(a) (b)

Figure 7-17: Influence of relative significant wave height HR on area probability of rogue waves $H/H_s \geqslant \alpha$ for bimodal wavefields in scenario B. (a) $P_A(H/H_s \geqslant 1.9)$; (b) $P_A(H/H_s \geqslant 2.0)$ scaled by the values in relevant unimodal wind sea. HR=1.25: β=40° (Δ), β=90° ($\times$); HR=0.92: β=40° (Δ), β=90° ($\times$).

7.5.1 Omnidirectional spectrum

Figure 7-18 shows the evolution of omnidirectional spectrum of bimodal seas in scenario C. Considerable spectral peak downshift is again observed and the spectral downshift as a function of spreading angle of wind sea Θ_s is seen in figure 7-19. The downshift increases as Θ_s decreases, suggesting more significant nonlinear wave interactions in bimodal seas having small spreading wind-sea component, which is somewhat expected.

7.5.2 Skewness and kurtosis

Figure 7-20 shows the temporal variation of skewness for bimodal wavefields in scenario C. We observe that the value of skewness is nearly independent of Θ_s with slightly decreasing trend with increasing Θ_s. This is consistent with what we observe in unimodal wind sea (see figure 4-4 in Chapter 4).

Figure 7-21 shows the temporal variation of kurtosis for bimodal wavefields with different wind-sea spreading angles Θ_s. The variation pattern of kurtosis is similar for

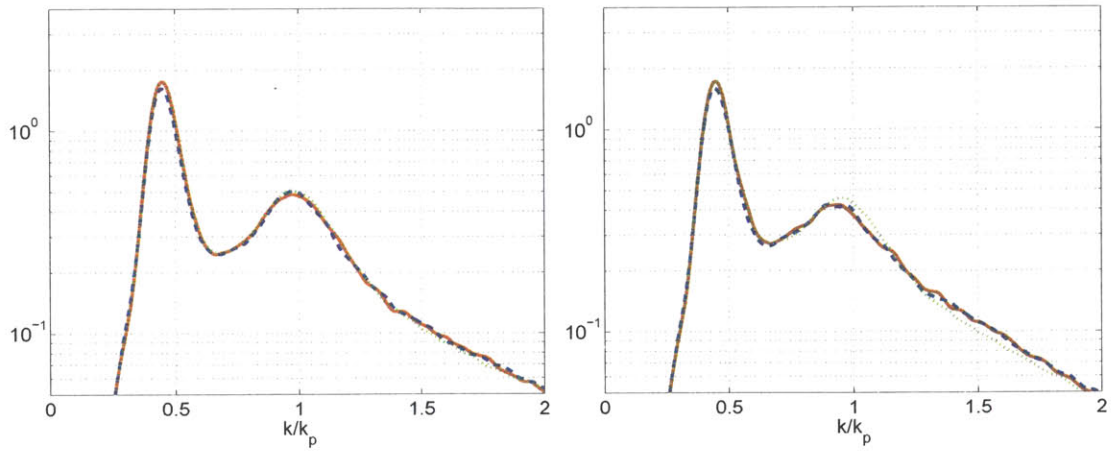

(a) $t = 20T_p$ (b) $t = 50T_p$

(c) $t = 70T_p$ (d) $t = 100T_p$

Figure 7-18: Evolution of omnidirectional spectra of bimodal wavefields in scenario B. Θ_s=20° (—), 30° (- - -) and 80° (· · ·).

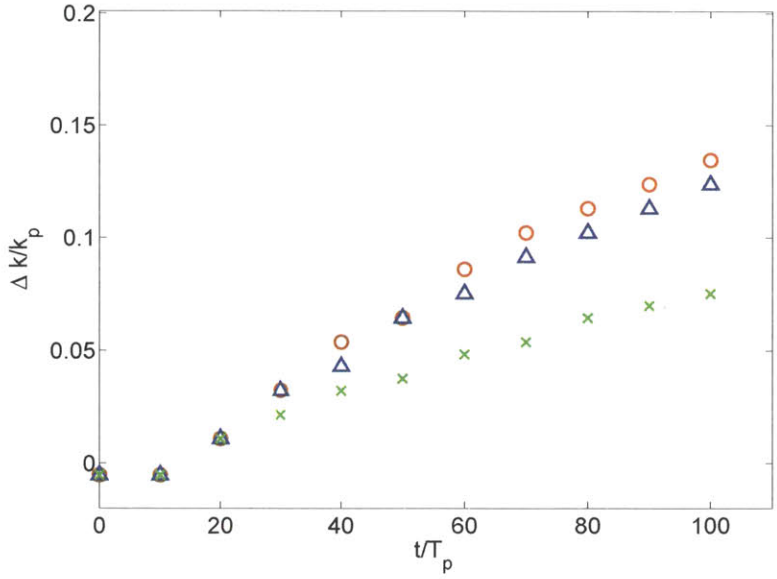

Figure 7-19: Influence of spreading angle of wind sea Θ_s on the spectral peak downshift. Θ_s=20° (◯), 30° (◁), 80° (×).

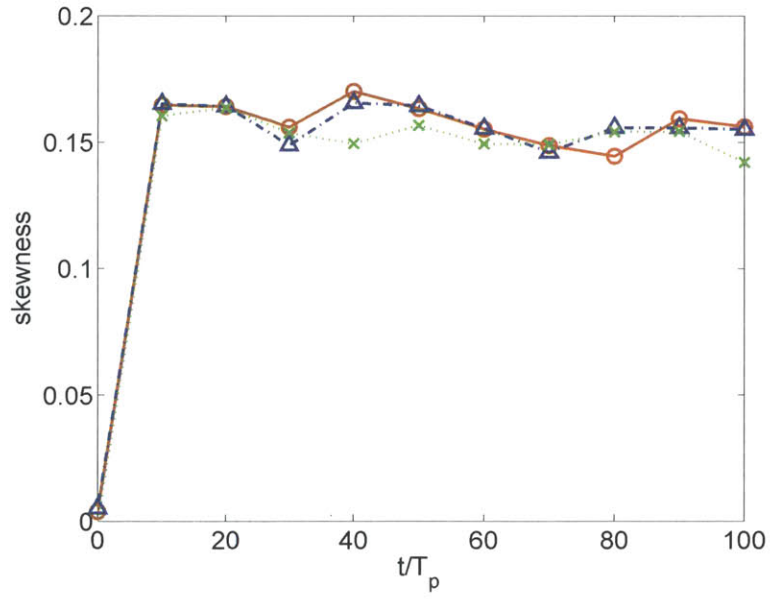

Figure 7-20: Temporal variation of skewness for bimodal wavefields in scenario B. Θ_s=20° (○), 30° (Δ), 80° (×).

different wind-sea spreading angle Θ_s. The value of kurtosis increases from its initial value Kur$\approx$3 to a quasi-stationary value Kur$^+$ and Kur$^+$ decreases with increasing Θ_s. This is not surprising because the value of kurtosis depends on the importance of modulational instability. The modulational instability diminishes in broad spreading seas, leading to a smaller value of kurtosis.

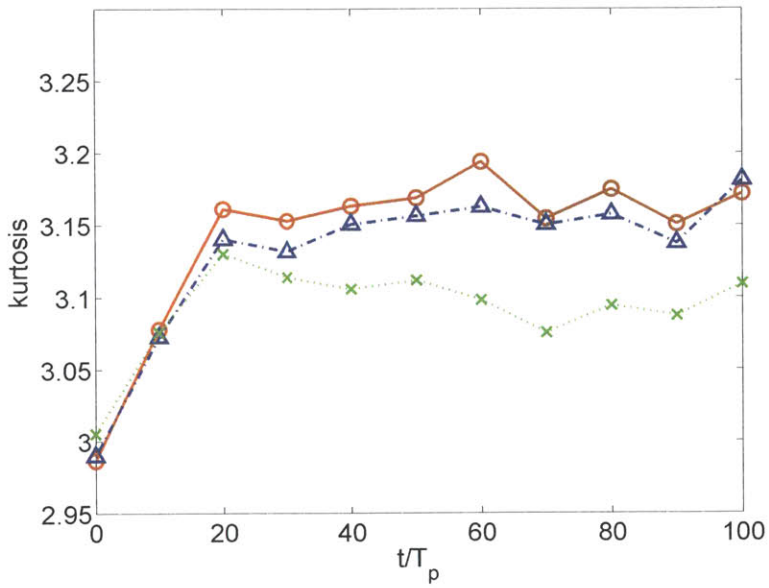

Figure 7-21: Temporal variation of kurtosis for bimodal wavefields in scenario B. $\Theta_s = 20°$ (◯); $30°$ (△); $80°$ (×).

7.5.3 Exceeding probability of crests

Figure 7-22 shows the effect of spreading angle of wind sea on the exceeding probability of large crests for bimodal seas described in scenario C. At the time scale when the modulational instability is relevant, the probability of large crests reduces with increasing Θ_s. The dependence on Θ_s, however, is less significant at large time. This is again consistent with the observations in unimodal wind sea.

7.5.4 Area probability of rogue waves

Figure 7-23 shows the effect of Θ_s on the area probability of rogue waves with $H/H_s \geqslant \alpha$, scaled by the Rayleigh distribution, in bimodal seas described in scenario C. A clear

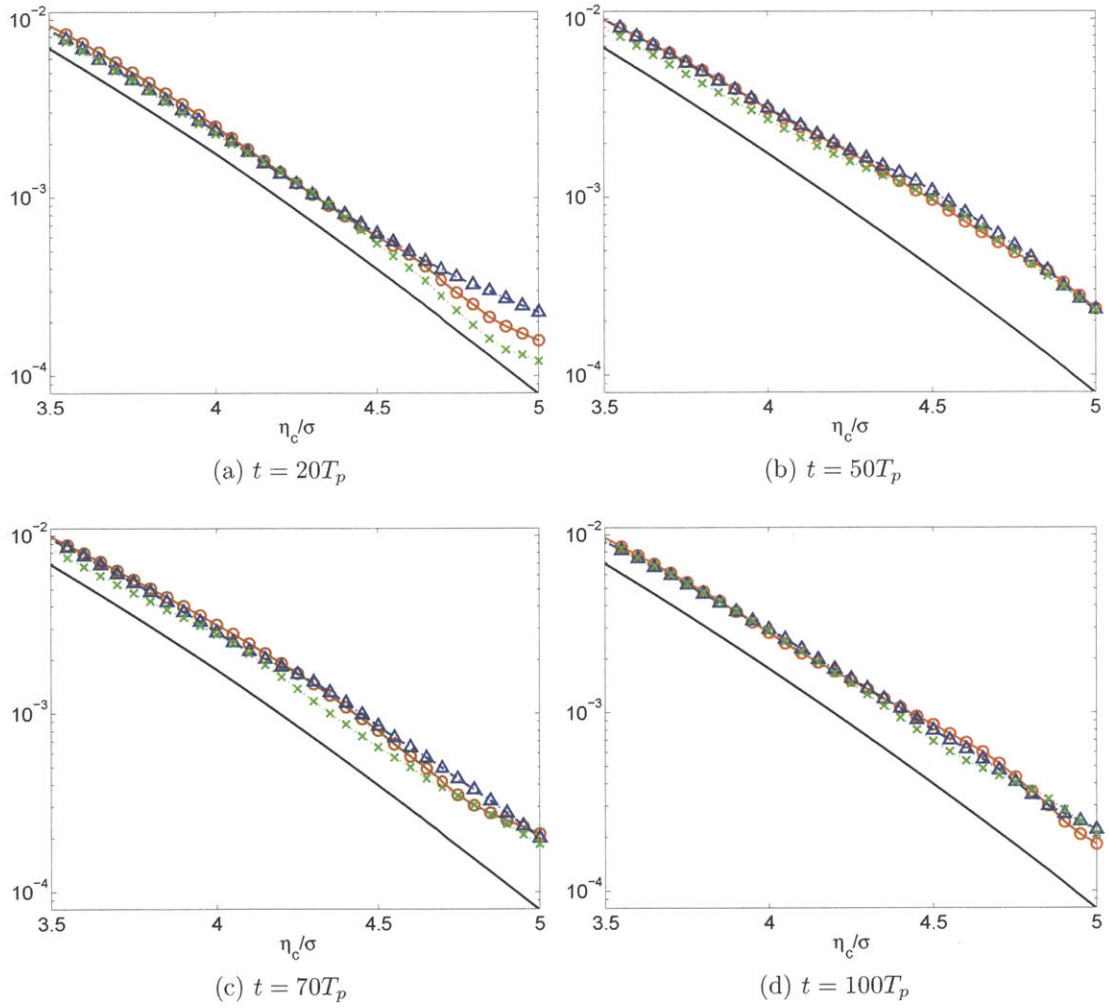

(a) $t = 20T_p$ (b) $t = 50T_p$

(c) $t = 70T_p$ (d) $t = 100T_p$

Figure 7-22: Exceeding probability of large crests for bimodal wavefields in scenario C. $\Theta_s = 20°$ (◯); $30°$ (Δ); $80°$ (×).

decreasing trend with increasing Θ_s is observed for both $\alpha = 1.9$ and $\alpha = 2.0$. This is because the modulational instability plays an important role in the formation of large waves. A smaller Θ_s leads a more significant modulational instability and thus higher occurrence probability of large waves.

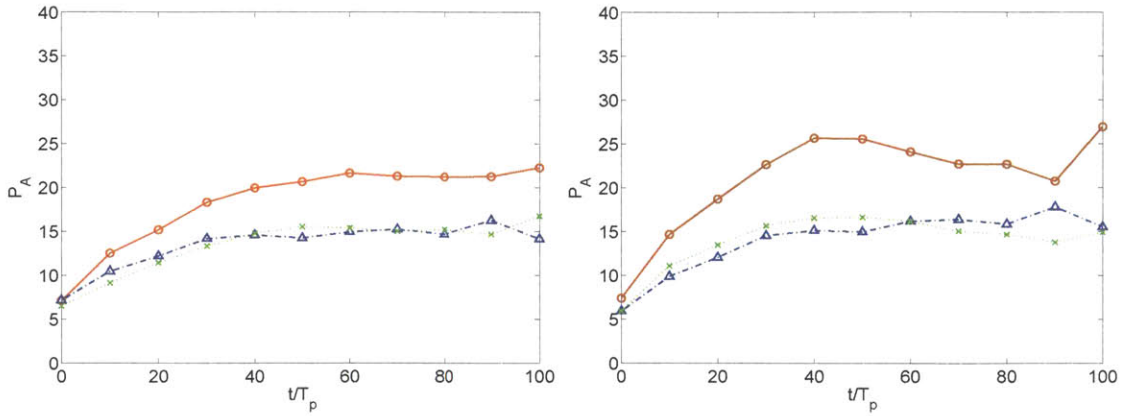

Figure 7-23: Temporal variation of $P_{A,\alpha}$ for bimodal wavefields in scenario B. (a) $P_{A,1.9}$ and (b) $P_{A,2.0}$ for bimodal wavefields $\Theta_s = 20°$ (∇); $30°$ ($\bigcirc$); $80°$ ($\times$).

7.6 Summary and conclusions

The nonlinear wave statistics and rogue wave occurrence of bimodal wavefields are studied using direct simulation approach over the space and time scale relevant to modulational instability, $\mathcal{L}/\lambda_p, \mathcal{T}/T_p = O(\varepsilon^{-2})$. This preliminary study is focused on the effects of aperture angle, relative significant wave height, and spreading angle of the wind sea. Our conclusions are summarized as following:

1. For bimodal seas composed of a swell and wind sea with comparable significant wave height (HR=0.92), an inclusion of swell in general leads to an enhanced occurrence probability of large waves, except for one special case where the aperture angle $\beta = 90°$. The area probability of rogue waves in bimodal seas can be enhanced up to five times of its value in unimodal wind seas. For bimodal wavefields with $\beta = 90°$, the swell system has a minimal influence on the occurrence of large waves.

2. The influence of the swell on the bimodal seas reduces as the relative significant wave height increases because the modulational instability related to the wind sea component plays a dominant role in the wavefield evolution for wind-sea dominant cases.
3. The deviation of nonlinear wave statistics from Gaussian statistics become less significant as the spreading angle of wind sea increases. Meanwhile, the area probability of large waves also reduces as wind-sea spreading angle increases.

In this preliminary study, we have chosen the bimodal cases in which the modulational instability related to the wind sea plays an important role in the nonlinear wavefield evolution. Our investigation reveals the possible influences of a presence of swell on the modulational instability. We find that the effect of swell is not monotonic. With a presence of swell, the nonlinear statistics and occurrence probability of rogue wave can either increase or decrease. At short evolution time when the modulational instability is relevant, the nonlinear statistics and large wave occurrence in bimodal seas decrease in comparison with their corresponding values in unimodal wind sea. At large evolution time when the modulational instability is less important, the swell in general leads to an enhanced nonlinear wave statistics and occurrence of rogue waves. To obtain comprehensive knowledge on the influence of swell on the bimodal wavefields, effect of other spectral parameters, including peak period separation PS, spectral bandwidths of wind sea and swell, to name a few, should be examined.

Chapter 8

Rogue wave shapes in deep water

8.1 Introduction

8.1.1 Observation of rogue waves of different shapes

An accurate description of the rogue wave shapes is essential for understanding the extreme loads and impacts of rogue waves on marine structures. Most of instrumental records of rogue waves are in time series obtained from buoys or other on-site wave gauges. In these measurements, a cross-cut of the rogue wave profile from certain direction can be obtained; however, the transverse information and three-dimensional structures of the large waves are missing. The three-dimensional records of rogue wave profiles are recently available from airborne spaceborne synthetic aperture radar (SAR) measurements (Lehner et al., 2002; Rosenthal et al., 2003); however, the measurement techniques have not been well validated. Arguments arises on the possibility of using SAR to obtain reliable measurements of waves, because both the wave motion and SAR imaging mechanism are strongly nonlinear Janssen and Alpers (2006).

Personal descriptions of experiencing unexpected large waves, which provide qualitatively information on the three-dimensional wave kinematics, are found useful. Many of these stories and photos can be found from review papers (Kharif and Pelinovsky, 2003; Dysthe et al., 2008) and internet. Rogue waves with different shapes

have been reported (Kharif et al., 2009). One of the most impressive kinds of rogue waves is a single extremely high wave with a long crest, usually referred as a *wall of water*. The cruise ship Queen Elizabeth II met such a wave with a height of 30 meter in the North Atlantic, in February 1995. The captain described it as "*a great wall of water, it looked as if we were going into the White Cliffs of Dover.*" (ESA, 2004). Rogue waves in the form of wave groups containing two or three successive large waves have also been documented (Moreau, 2004; Lawton, 2001). The different geometric characteristics of rogue waves may be reflections of different generation mechanisms and different underlying different environmental conditions. A visual classification of rogue wave shapes is proposed in Rosenthal and Lehner (2005):

1. Singular wave tower: very localized large wave;
2. Three sisters: a large wave group containing three successive large waves;
3. White wall: extreme wave group with a configuration similar to a ship wake.

8.1.2 Statistical model for extreme wave profile

The statistical description of average surface shape around an extreme crest for linear Gaussian wavefield is shown to be proportional to the auto-covariance function of the record (Lindgren, 1970; Boccotti, 1983):

$$\eta_L(\mathbf{x}) \propto \rho(\mathbf{x})/\rho(\mathbf{0}), \tag{8.1}$$

where $\rho(\mathbf{x})$ is the auto-covariance function of the wave elevation:

$$\rho(\mathbf{x}) = \int_{\mathbf{k}} \Psi(\mathbf{k}) \cos(\mathbf{k} \cdot \mathbf{x}) \, d\mathbf{k}, \tag{8.2}$$

for a wave spectrum $\Psi(\mathbf{k})$.

SNOW simulations obtain not only the probability of rogue waves, but also detailed information of the geometry and kinematics of such waves. Figure 8-1 shows average rogue wave profiles obtained from SNOW simulated wavefield and the relevant auto-covariance function. We observe that, in comparison with auto-covariance

function, the crest length of the average rogue wave is larger and the crest is also steeper.

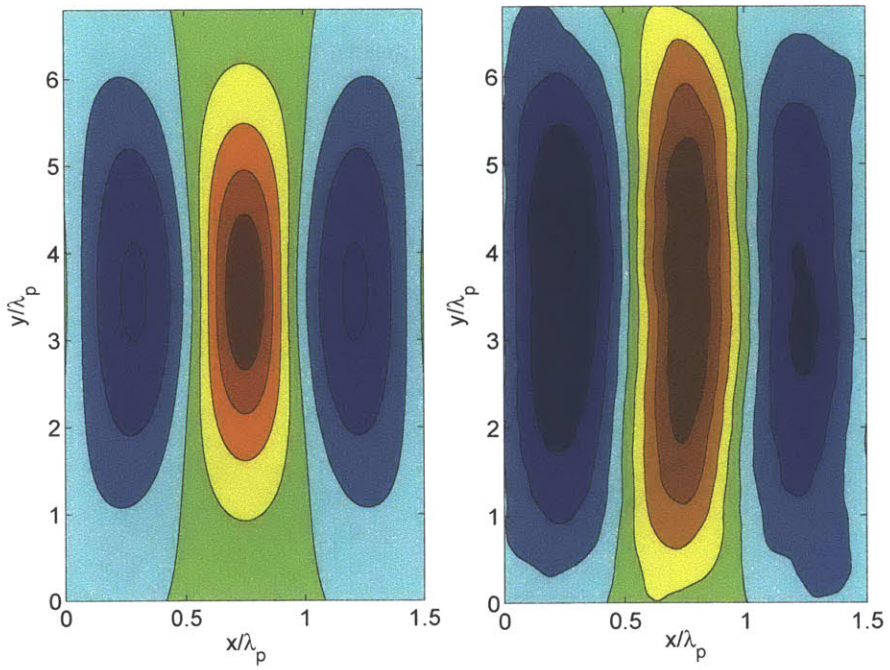

(a) (b)

Figure 8-1: (a) Auto-covariance function. (b) average profile of rogue waves $H/H_s \approx 2.0$ in wavefield H_s=12 m, T_p=12 s, $\gamma = 5$ and $\Theta = 30°$.

In this chapter, we use a large ensemble of rogue wave events obtained from MIT-Wave dataset to investigate their geometric features, including wave and crest length, area size and group structure, and their dependence on spectral parameters. We study the geometric structures and their dependence on spectral parameters using proper orthogonal decomposition (POD). For the rogue wave group containing only one wave, their profiles can be well represented using only a few POD modes.

8.2 Geometric characteristics of rogue waves

Rogue wave profiles reflect certain characteristics of the underlying wavefield. Figure 8-2 shows the geometric structures of typical rogue waves from wavefields with a range of initial spreading angles. As expected, the crest length of rogue waves decreases

as the initial spreading angle increases. The typical rogue wave from wavefield with small spreading angle ($\Theta = 16°$) has very similar geometric features with the *wall of water*.

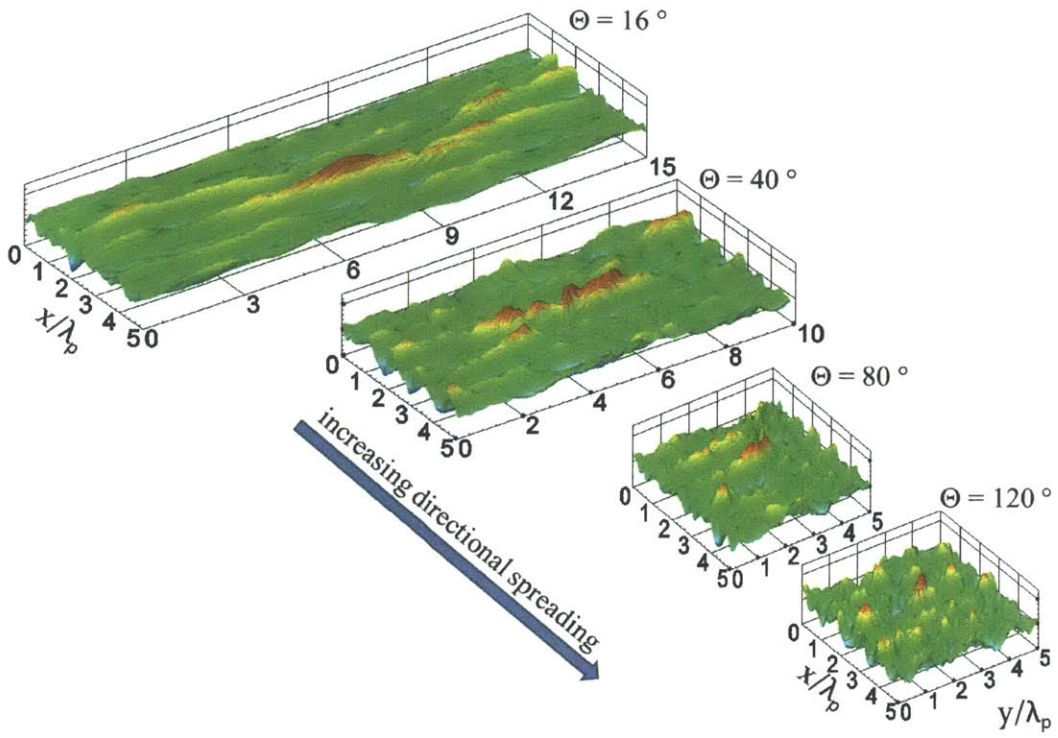

Figure 8-2: Rogue waves identified from simulated directional wavefields.

Once a rogue wave, in particular the crest and trough pair associated with $H(\geqslant \alpha H_s)$ (hereafter referred to as the "main" wave), is identified in a general directional wavefield, we define the wavelength of the rogue wave λ_{rogue} as the distance between the two adjacent zero up-crossing points along a line parallel to the dominant direction containing the crest point $\mathbf{x}_c$. Similarly a crest length C_{rogue} is defined as the distance between two adjacent zero crossing points along a line perpendicular to the dominant direction containing the crest point $\mathbf{x}_c$. To characterize the rogue wave groups, that is, the rogue wave is contained in a wave group of successive large waves, we repeat §5.4 (Chapter 5) but now use a new "group" threshold $H/H_s{=}\alpha_G(< \alpha$, typically), identifying all the $\mathcal{R} = \mathcal{R}_G$ for this threshold value. For given α and α_G, a rogue wave group is identified if any of the $\mathcal{R}_G$ overlaps and the union of the $\mathcal{R}_G$ contains a

main wave satisfying $H/H_s \geqslant \alpha$. In this case, we say that this is a rogue wave group of "n" waves (hereafter G_n) if "n" overlapping $\mathcal{R}_G$'s are involved. Note that this definition/procedure is general for arbitrary directionally spread wavefields, and the number "n" does not distinguish among the different configurations (or positions) of $\mathcal{R}_G$ in such groups.

8.2.1 Wave length of rogue waves

For the rogues waves identified in MIT-Wave (with α=2.0), figure 8-3 shows the average wave length of rogue waves over the evolution time $0 \leqslant t/T_p \leqslant 150$ as a function of spectral bandwidth (γ) for wavefields with a range of spreading angles. We observe for the broad range of spreading angles considered, λ_{rogue} is comparable to the peak wave length λ_p. This gives further support that the dominant mechanism is modulational instability around the peak wavenumber over slowly-varying space/time. For wavefields with broad band frequency spectrum (small γ), the average rogue wave length $\bar{\lambda}_{\text{rogue}}$ is slightly longer than λ_p, specially for small spreading angle where $\bar{\lambda}_{\text{rogue}} \approx 1.1\lambda_p$. With increasing spectral bandwidth, the standard deviation of λ_{rogue} increases. The dependence of λ_{rogue} on the spreading angle is rather subtle. There is a tendency that λ_{rogue} is slightly greater in wavefields with large spreading angles, although the difference is much smaller than the standard deviation.

8.2.2 Crest length of rogue waves

The dependence of crest length of rogue waves on the directional spreading of the underlying wavefield is visually obvious as seen in figure 8-2, where we observe the crest length of the rogue waves decreases as the spreading angle increases. To quantify the dependence of C_{rogue} on spectral parameters, in figure 8-4 we plot the average crest length of rogue waves $\bar{C}_{\text{rogue}}$ over the evolution time $0 \leqslant t/T_p \leqslant 150$ relative to the average crest length of the initial wavefield as a function of spreading angles. The

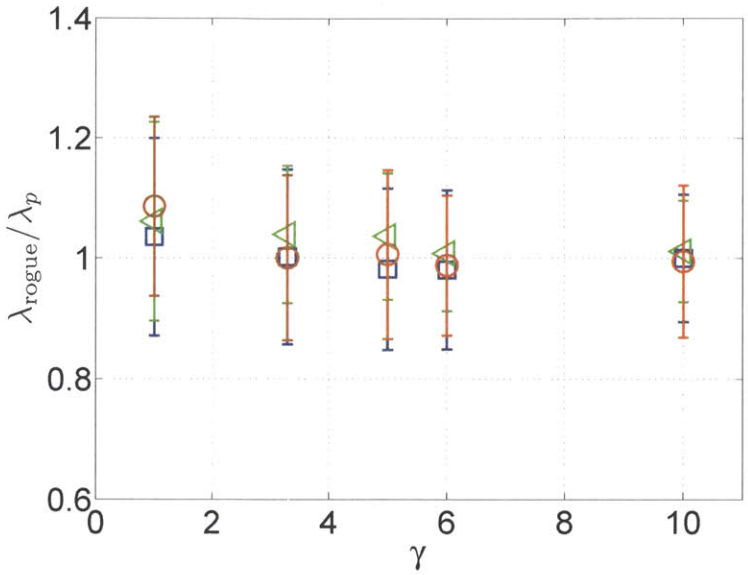

Figure 8-3: Average rogue wave length λ_{rogue} as function of spectral bandwidth for wavefields ε=0.14, $\Theta = 20°$ (◯), 40° (□), 80° (◁). The error bars indicate one standard deviation.

average crest length C_y of the wavefield is estimated as

$$C_y = \lambda_y/2, \tag{8.3}$$

where λ_y is the average wavelength in the y direction:

$$\lambda_y = 2\pi/\langle k_y^2\rangle^{1/2}, \text{ and } k_y^2\rangle = \int k_{x,y}^2 \Psi(\mathbf{k})\, d\mathbf{k} / \int \Psi(\mathbf{k})\, d\mathbf{k}. \tag{8.4}$$

In figure 8-4 we observe, for wavefields with small spreading angles, $\bar{C}_{\text{rogue}}/C_y$ increases with increasing Θ. As the spreading angle becomes large, $\bar{C}_{\text{rogue}}/C_y$ is nearly constant and independent of spreading angles. For a given spreading angle, $\bar{C}_{\text{rogue}}/C_y$ increases as spectral bandwidth increases. For short-crested wavefields with $\Theta \geqslant 60°$, the average crest length is considerably greater than the average crest length ($\bar{C}_{\text{rogue}}/C_y > 2$).

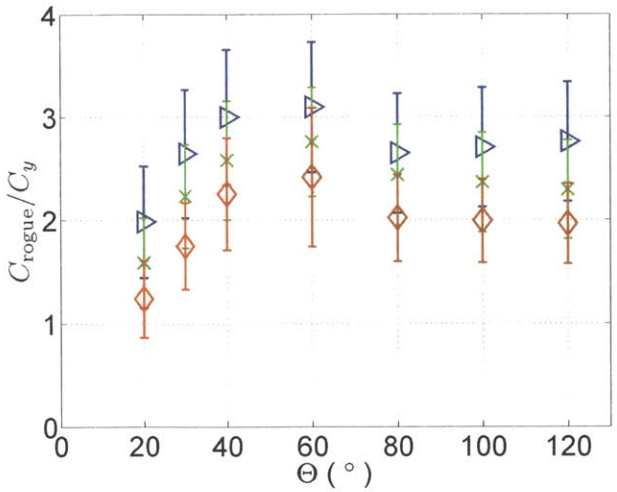

Figure 8-4: Average rogue wave crest length C_{rogue} relative to the average crest length C_y of the initial wavefield as function of spreading angle Θ for wavefields ε=0.14, γ=1 (▷); 5 (×); 10 (◇). Average crest length $C_y=\lambda_y/2=\pi/\langle k_y^2\rangle^{1/2}$. The error bars indicate one standard deviation.

8.2.3 Area size of rogue waves

Figure 8-5 shows the average size of rogue waves $\bar{a}_{\text{rogue}}$, scaled by the average wave size of the initial wavefield $\bar{a}_0$, as a function of spreading angle and spectral bandwidth. In the range of relatively small $\Theta <\sim 60°$, $\bar{a}_{\text{rogue}}/\bar{a}_0$ increases as Θ increases. For larger Θ, $\bar{a}_{\text{rogue}}/\bar{a}_0$ slowly decreases as Θ increases. For a given Θ, $\bar{a}_{\text{rogue}}/\bar{a}_0$ increases as the spectral bandwidth increases (γ decreases).

As wavefield evolves, the average size of waves $\bar{a}$ varies with time. Figure 8-6 shows $\bar{a}_{\text{rogue}}/\bar{a}$, which is the average of $a_{\text{rogue}}/\bar{a}(t)$ over time $0 \leqslant t \leqslant 150T_p$, as a function of Θ and γ. Comparing figure 8-5 and figure 8-6, $\bar{a}_{\text{rogue}}/\bar{a}$ behaves similarly to $\bar{a}_{\text{rogue}}/\bar{a}_0$ but with a larger value. The large standard deviation in the range of small Θ is associated with the significant change of the underlying spectrum due to the effect of modulational instability.

8.2.4 Grouping of rogue waves

For given $\alpha = 2$ and $\alpha_G = 1.8$, we catalogue the rogue wave groups G_n obtained from MIT-Wave. Figure 8-7 shows the percentages of G_2 and G_3 rogue wave groups,

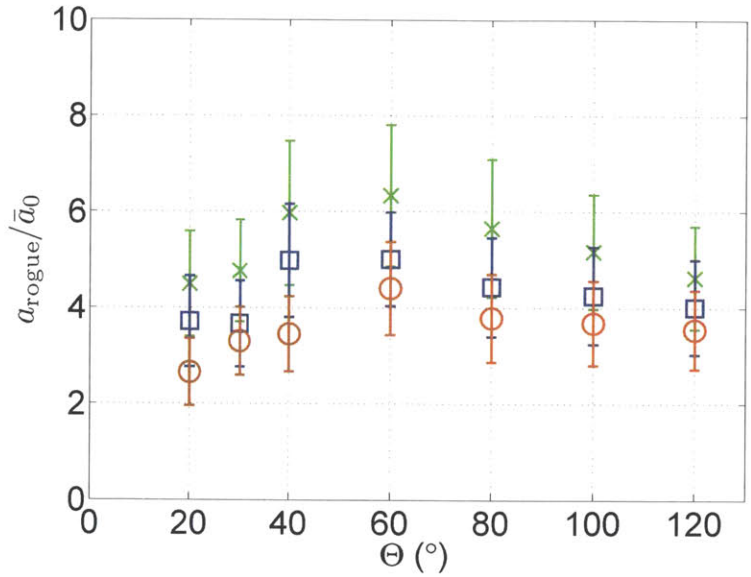

Figure 8-5: The average rogue wave area a_{rogue} scaled by the average area of initial wavefields $\bar{a}_0$ as a function of spreading angle, for directional wavefields with ε=0.14, γ=1 (×), 5 (□)) and 10 (○). $\bar{a} = \lambda_x \lambda_y / \sqrt{2\pi}$. The error bars indicate one standard deviation during the evolution time considered.

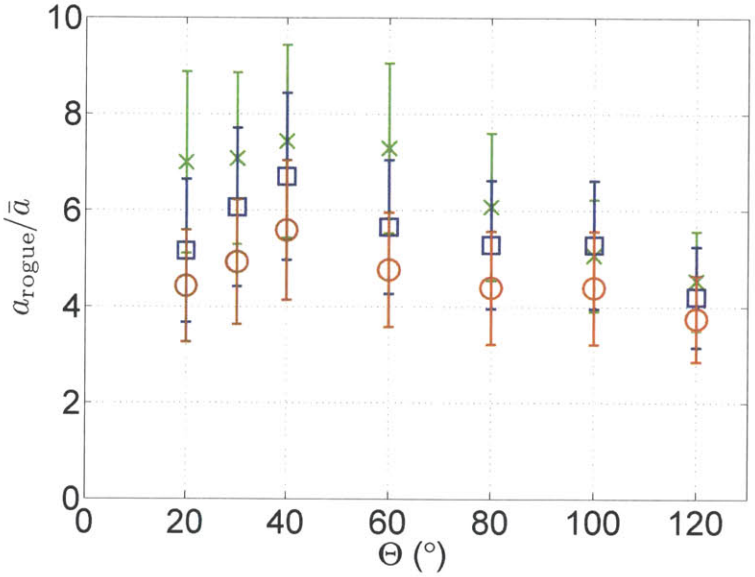

Figure 8-6: The average rogue wave area $\bar{a}_{\text{rogue}}$ relative to the average wave area of the wavefields as a function of spreading angle, for directional wavefields with ε=0.14, γ=1 (×), 5 (□)) and 10 (○). $\bar{a} = \lambda_x \lambda_y / \sqrt{2\pi}$. The error bars indicate one standard deviation during the evolution time considered.

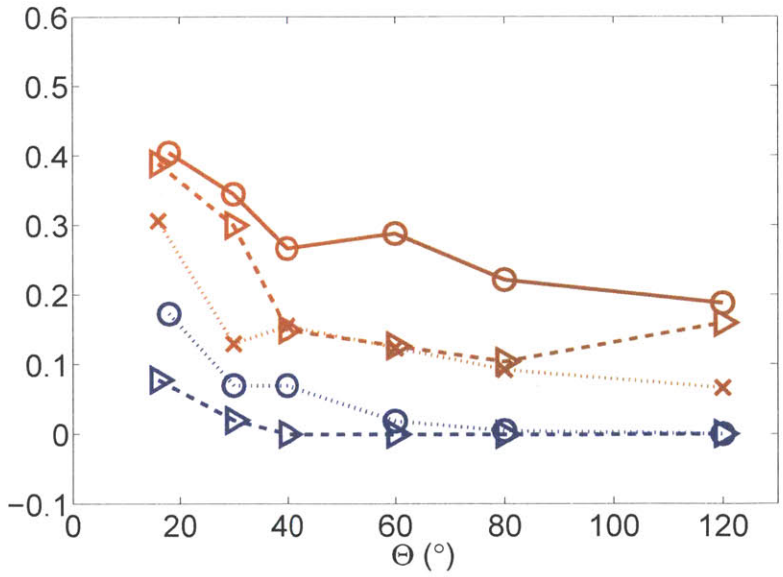

Figure 8-7: Percentage of rogue wave groups, $G_2\%$ and $G_3\%$ as functions of spreading angle for wavefields with steepness $\varepsilon = 0.14$, $\gamma = 1\,(\times)$, $5\,(\triangleright)$, $10\,(\bigcirc)$. G_2: (red); G_3: (blue). Results are obtained using α_G=1.8 and α=2.

denoted as $G_2\%$ and $G_3\%$, among the rogue wave populations. For a given spectral bandwidth, both $G_2\%$ and $G_3\%$ decrease with increasing Θ for $\Theta <\sim 60°$, while they are nearly independent of Θ for larger Θ. For a fixed Θ, both $G_2\%$ and $G_3\%$ increase as γ increases. These observations are consistent with the effect of modulational instability on rogue wave development.

For G_n rogue wave groups with general configurations, the length of the rogue wave group is not well-defined. For a special configuration when the crest points $\mathbf{x}_c$ of $\mathcal{R}_G$ forming the rogue wave group lining in the dominant propagation of the underlying wavefield, the group length Λ_{rogue} is defined as the distance between the zero up-crossing points of the last downwave and first upwave along a line parallel to the dominant direction containing the crest point $\mathbf{x}_c$. Figure 8-8 shows the distribution of the group lengths of this particular configuration. We find that the percentage of $\Lambda_{\text{rogue}} \approx 2$ or 3 increases as the spreading angle increases. Notice that this results are obtained for wave groups with a particular configuration.

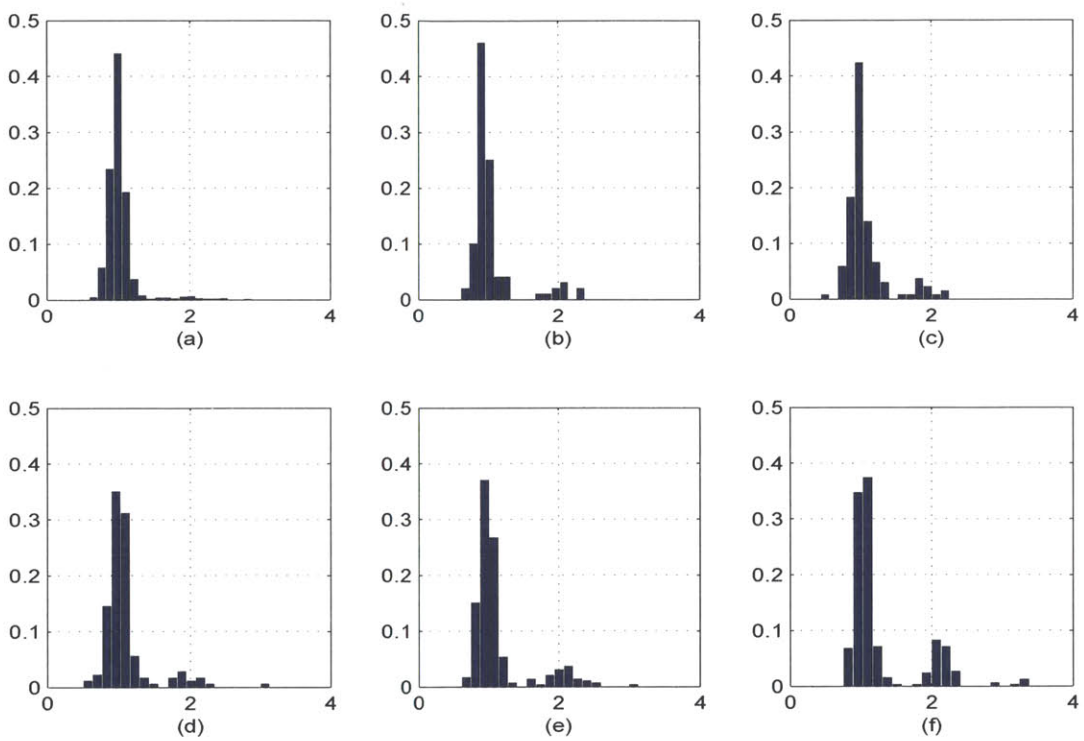

Figure 8-8: Distribution of group length of rogue wave groups with crests lining in the dominant direction of wavefields. (a) unidirectional; (b) $\Theta = 16°$; (c) $\Theta = 40°$; (d) $\Theta = 60°$; (e) $\Theta = 80°$; (f) $\Theta = 120°$.

8.3 Analysis of rogue wave shapes using proper orthogonal decomposition (POD)

8.3.1 POD of rogue wave shapes in unidirectional wavefields

A large number of rogue waves obtained for broad range of spectral parameters are found to have surprisingly similar geometric features. To identify these salient features and to see if these can be represented by relatively small number of parameters, we analyze rogue wave surface profiles in MIT-Wave by applying the proper orthogonal decomposition (POD), which provides a statistical method to obtain a compact representation of the data to extract the dominant structures.

The general analysis of rogue wave groups which contain large "n" waves involving different possible configurations is complex. As a preliminary investigation, we focus on the relatively simple case of G_1, i.e., a single large (3D) wave satisfying $H \geqslant \alpha H_s$.

We first consider unidirectional waves and write the POD expansion of the rogue wave:

$$\eta_{\text{rogue}}(\hat{x})/H_s = \eta_{\text{POD}}(\hat{x}) = \sum_{m=1}^{M_x} C_m U_m(\hat{x};\varepsilon,\gamma), \qquad 0 \leq \hat{x} \leq 1, \tag{8.5}$$

where $\hat{x}=x/\Lambda_r$, and Λ_r is the length of the rogue wave defined as the distance between the down crossing of the upwave trough and the up crossing of the downwave trough around the rogue wave crest. In (8.5), $U_m(\hat{x};\varepsilon,\gamma)$ is the mth POD mode for wavefields with spectral parameters ε and γ; C_m is the coefficient of the mth POD mode, and M_x the total mode number. U_m, m=1, 2, ..., form orthogonal basis vectors that characterize the ensemble of rogue wave shapes. The rogue wave profiles are selected from SNOW simulations with time interval $\Delta T=10T_p$. To compute U_m, we typically use $O(1000)$ rogue wave profiles from MIT-Wave (the difference in U_m obtained using a larger ensemble is less than 1%). Note that unlike the rogue wave probability, POD shapes are not invariant if crest and trough are interchanged in above procedure. For uniqueness of POD shapes, we have chosen to describe rogue waves in 'crest-centered'

profile. To obtain POD shapes of rogue waves described in 'trough-centered' profile, similar approaches can be applied.

Figure 8-9(a) shows the leading POD mode U_1 of G_1 rogue waves for unidirectional wavefields with different spectral steepness ε. We observe U_1 has a sharp crest and two shallow troughs, indicating the nonlinearity of the wave. U_1 is asymmetric with respect to the crest and the crest is skewed to the upwave trough (i.e., right trough in the figure with wave propagation to right). The downwave trough is slightly deeper than upwave trough, which suggests more rogue waves may be identified if up-crossing approach is used in analyzing time series. This is consistent with the observations in Pinho et al. (2004). With increasing steepness, U_1 becomes more asymmetric and skewed, suggesting more significant nonlinearity of the rogue waves. This mode profile can be contrasted to the average profile around a local extreme crest for linear Gaussian waves, which is proportional to the autocovariance function, $\rho(x)=\int_k \cos(kx)\Psi(k)\ dk/\int_k \Psi(k)\ dk$, where $\Psi(k)$ is the wavenumber spectrum (Lindgren, 1970; Boccotti, 1983). In comparison with $\rho(x)$, U_1 has shallower upwave trough and deeper downwave trough, while $\rho(x)$ is symmetric with respect to the wave crest. Figure 8-9(b) plots the profile of the higher order POD modes U_m, m=2, 3, 4. U_m describe the perturbations of rogue wave profiles around the leading mode U_1. Higher POD modes are more oscillatory, describing perturbations with successively shorter scales.

It is more interesting to distinguish the rogue waves with crest greater/less than trough ("wall of water"/"deep hole") and name them as crest-dominant/trough-dominant rogue waves. We find that crest-dominant rogue waves generally occur more frequently than trough-dominant rogue waves. The first POD modes of crest/trough-dominant rogue waves are shown in figure 8-10. For the trough-dominant rogue waves, a trough-center profile is used. Similarly to figure 8-9(a), U_1 becomes more asymmetric and skewed for both crest and trough-dominant rogue waves as the wave steepness increases.

Figure 8-11(a) shows the coefficients of POD modes C_m for wavefields with a range of spectral bandwidths. The magnitudes of the coefficients decrease rapidly and only

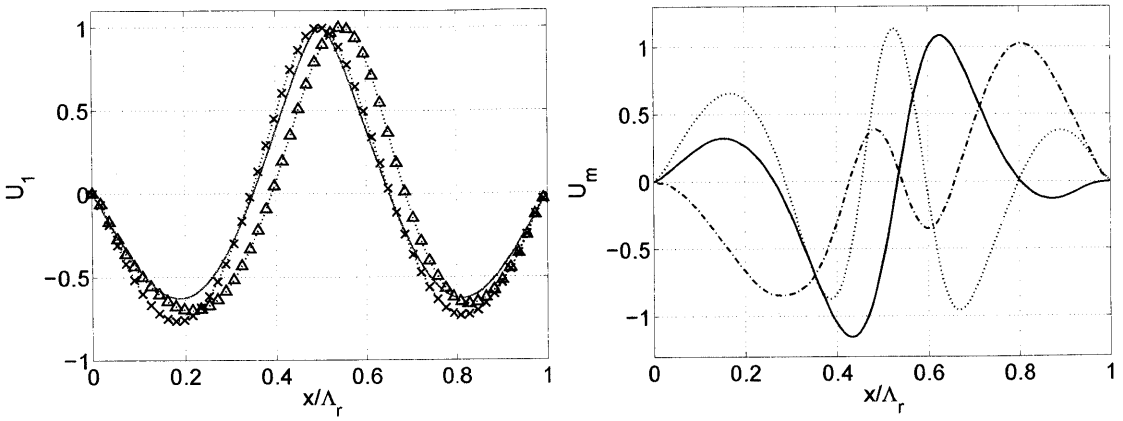

(a) (b)

Figure 8-9: (a) $U_1(x)$ for unidirectional wavefields γ=6, ε=0.07 ($\cdot \times \cdot$); ε=0.14 ($\cdot \ \Delta \ \cdot$). Autocovariance function $\rho(x)$ (—). (b) U_m for unidirectional wavefields ε=0.14, γ=6. m=2 (—), m=3 (- - -), m=4 ($\cdots$). Waves propagate from left to right.

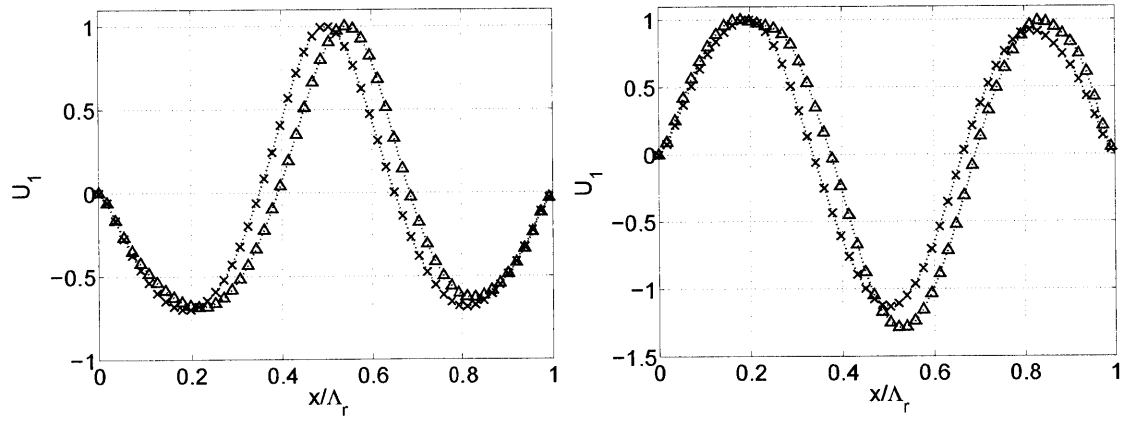

(a) (b)

Figure 8-10: Leading POD mode $U_1(x)$ for (a) crest-dominant rogue waves; (b) trough-dominant rogue waves. Unidirectional wavefields γ=6, ε=0.07 ($\cdot \times \cdot$, 710 crest-dominant and 290 trough-dominant rogue waves); ε=0.14 ($\cdot \ \Delta \ \cdot$, 914 crest-dominant and 86 trough-dominant rogue waves). Waves propagate from left to right.

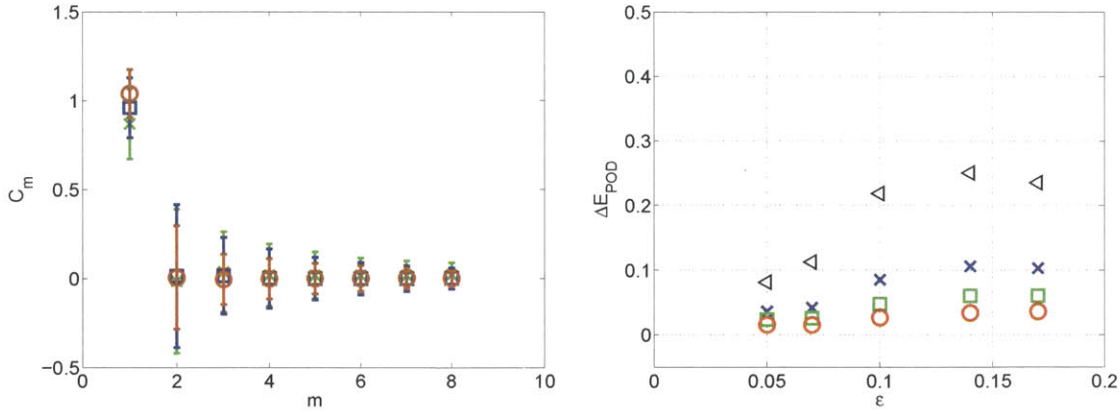

(a) (b)

Figure 8-11: (a) Coefficients of POD modes C_m, $m = 1 \cdots 8$, for unidirectional wavefields with γ=5, ε=0.07 (○), 0.1 (□), 0.14 (×). The error bars indicate one standard deviation. (b) The average error of POD approximations ΔE_{POD} using M_x POD modes. M_x=1 (◁); 2 (×); 3 (□), 4 (○).

the first mode has a non-zero mean. The standard deviation of the coefficients decreases for the higher modes. This suggests that the dominant geometry of the rogue wave profile η/H_s can be reasonably approximated using only U_1. The representation error of POD is defined as $\Delta E_{\text{POD}}=|E_{\text{POD}} - E_R|/E_R$, where $E_{R,\text{POD}}=\int \dot{\eta}^2_{\text{rogue,POD}}\, dx$. Figure 8-11(b) shows the average representation error of POD modes for wavefields with a broad range of steepnesses. For relatively small steepness ε <0.1, the errors are within 20% using only U_1. For wavefields with greater steepness, more POD modes are needed to achieve a satisfied accuracy. The error decreases as more POD modes are used. For a broad range of wavefield steepness, when M_x=4 POD modes are used, the mean representation error ΔE_{POD} is less than 5%. Using similar approach, the POD modes of rogue wave groups containing two large waves (G_2) in unidirectional wavefields can be obtained (shown in figure 8-12).

Examples of rogue wave groups, G_1 and G_2, and their POD representations are shown in figure 8-13. We find that the rogue wave profiles can be approximated well with only three POD modes.

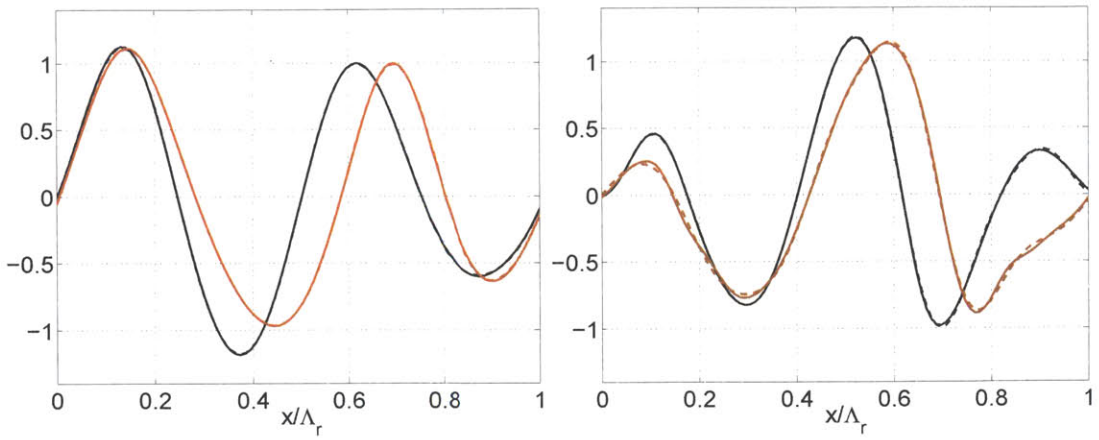

Figure 8-12: Leading POD modes of rogue waves of type G_2 for unidirectional wavefields $\gamma = 6$. (a) $U_1(x)$; (b) $U_2(x)$. ε=0.07 (—); ε=0.14 (—).

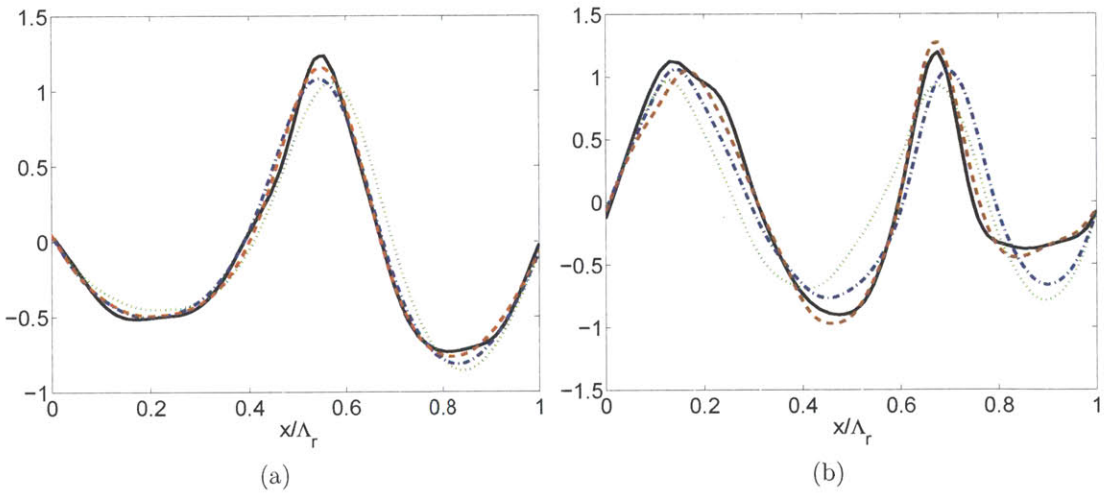

Figure 8-13: Examples of (a) single rogue wave (G_1); (b) rogue wave group containing two large waves (G_2). Rogue wave (group) profile (—); POD approximations using number of modes M_x=1 (···); M_x=2 (-·-); M_x=3 (—).

8.3.2 POD of rogue wave shapes in directional wavefields

For directional wavefields, the POD representations of rogue waves η_{rogue} are written in the form

$$\eta_{\text{rogue}}(\hat{x},\hat{y})/H_s = \eta_{\text{POD}}(\hat{x},\hat{y}) = \sum_{n}^{M_y}\sum_{m}^{M_x} C_{mn}V_{x,m}(\hat{x})V_{y,n}(\hat{y}), \tag{8.6}$$

where $\hat{x} = x/\Lambda_r$ and $\hat{y} = y/C_{\text{rogue}}$; $V_{x,m}(\hat{x})$, $V_{y,n}(\hat{y})$ are the POD modes in x and y directions; and M_x and M_y are the number of POD modes in the two horizontal directions.

There are several ways to calculate $V_{x,m}$ and $V_{y,n}$ in (8.6). One approach is to assume that $V_{x,m}(\hat{x})$ in (8.6) is given by (8.5), and focus on the transverse modulations $V_{y,n}(\hat{y})$. Another approach is to assume $V_{y,0}$=**1**, and apply inner product both sides of (8.6) by $V_{y,0}$:

$$\eta_{\text{POD}} \cdot V_{y,0} = \sum_{m}\left(C_{mn}\sum_{n} V_{y,n}\cdot \mathbf{1}\right)V_{x,m}. \tag{8.7}$$

Then $V_{x,m}$ can be obtained by applying 1D POD on (8.7). We use $U_m(\hat{x})$ to denote the 1D POD calculated using the former method and $V_{x,m}(\hat{x})$ to denote the 1D POD using the latter method. Figure 8-14 shows the 1D POD modes $V_{x,m}$ in (8.7) calculated from two approaches. The two approaches lead to 1D POD modes with qualitatively similar structures. We observe the leading order of $V_{x,m}$ calculated from second approach is considerably less asymmetric than the 1D POD modes from unidirectional wavefields shown in figure 8-14(a). $V_{x,1}(\hat{x})$ has deeper upwave trough and shallower downwave trough, and the crest is less skewed in comparison with $U_1(\hat{x})$. This suggests rogue waves in the directional wavefields are less nonlinear than the unidirectional rogue waves, which is consistent with the effect of directional spreading on the modulational instability. Similar features are observed for the second mode as seen in figure 8-14(b).

The POD modes in the y direction, $V_{y,n}$, n =1, 2, 3, and 4 obtained from $O(200)$ 3D rogue waves are shown in figure 8-15 using the two approaches described above. We observe the two approaches lead to very similar profiles for the longitudinal modulations. $V_{y,1}$, the leading order along-crest modulation (scaled by C_{rogue}), is positive

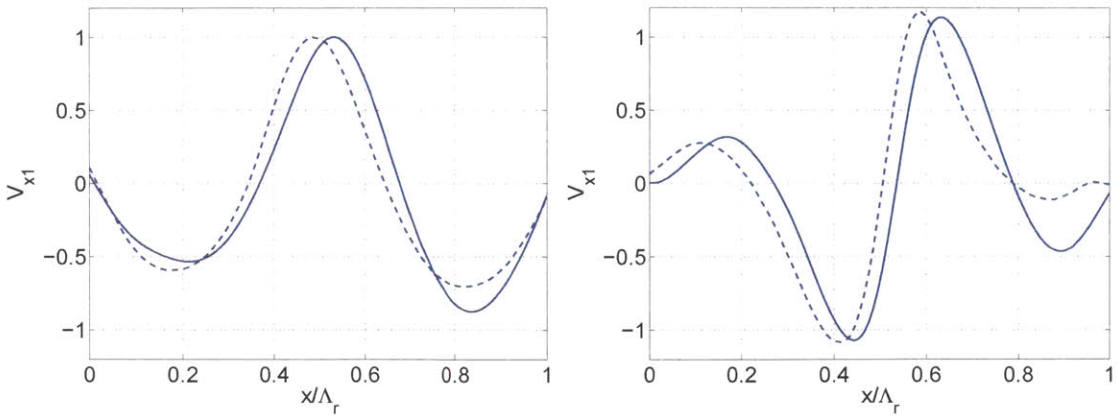

Figure 8-14: 1D POD modes using two approaches. (a) first mode $U_1(\hat{x})$ (—); $V_{x,1}(\hat{x})$ (- - -). (b) second mode. $U_2(\hat{x})$ (—); $V_{x,2}(\hat{x})$ (- - -) for wavefields H_s=12 m, T_p=13 sec, γ=5, and Θ=60°.

definite and approximately symmetric with respect to y_c. The higher order transverse POD modes $V_{y,n}$ ($n \geqslant 2$) describe successively shorter modulations with both positive and negative values and are generally not symmetric (relative to y_c).

To assess the assumptions inherent in (8.6), we can alternatively represent η_{rogue} using 2D POD modes:

$$\eta_{\text{rogue}}(\hat{x},\hat{y})/H_s = \eta_{POD}(\hat{x},\hat{y}) = \sum_{m=1}^{M_{xy}} C_m W_m(\hat{x},\hat{y};\ \varepsilon,\gamma,\Theta), \tag{8.8}$$

where M_{xy} is the number of 2D POD modes and $W_m(\hat{x},\hat{y};\ \varepsilon,\gamma,\Theta)$ is the mth 2D POD mode for directional wavefields specified by ε, γ and Θ. Figure 8-17 plots the contours of $W_m(\hat{x},\hat{y})$, m=1, 2, and 3.

Figure 8-17 plots the contours of $W_1(\hat{x},\hat{y})$ as compared to $U_1(\hat{x})V_1(\hat{y})$ from (8.6) and (8.8) respectively. Qualitatively, W_1 and U_1V_1 are very similar; however W_1 is less asymmetric than U_1V_1 in both the longitudinal and transverse directions. The quantitative differences between W_1 and U_1V_1 (figure 8-17(c)) are mainly in the shallower upwave and downwave troughs of U_1V_1 relative to W_1, which are consistent with the reduction effect of directional spreading on the nonlinearity of wavefields.

Figure 8-18 shows the coefficients of the leading POD modes in (8.8). Similar

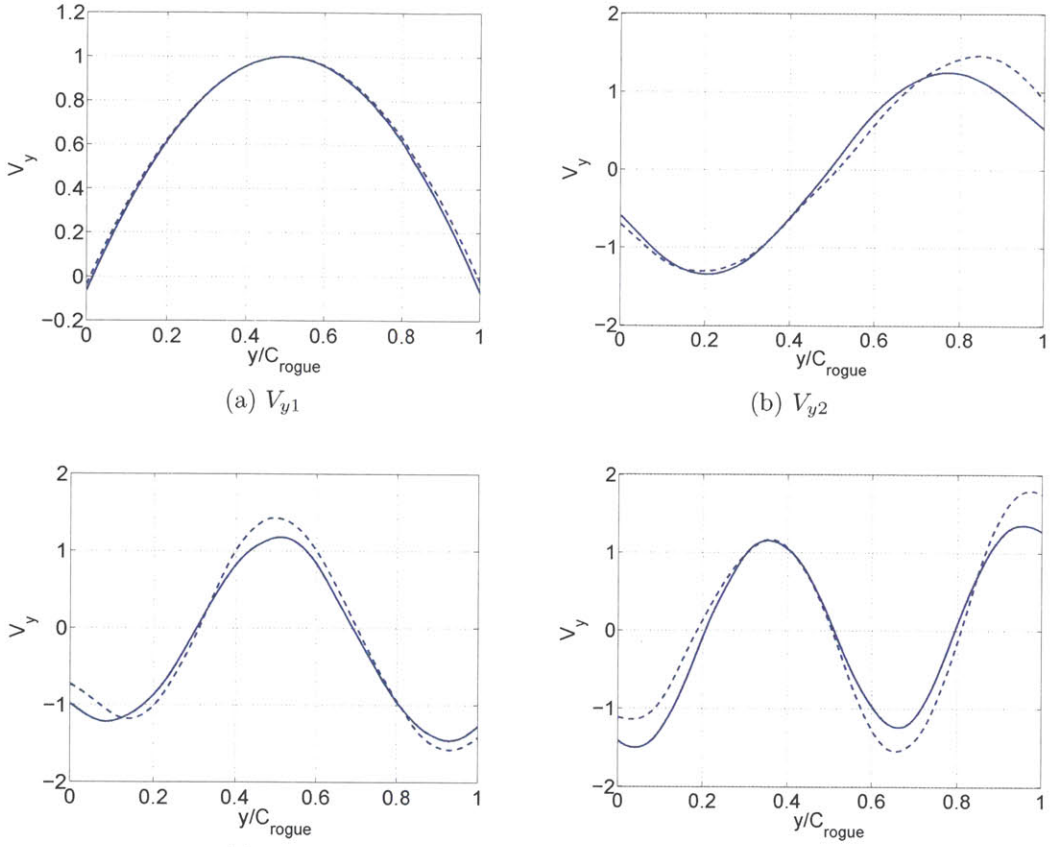

(a) V_{y1} (b) V_{y2}

(c) V_{y3} (d) V_{y4}

Figure 8-15: POD modes in y direction. (a) $V_{y,1}(\hat{y})$; (b) $V_{y,2}(\hat{y})$; (c) $V_{y,3}(\hat{y})$; (d) $V_{y,4}(\hat{y})$. Approach one (- - -); approach two (—).

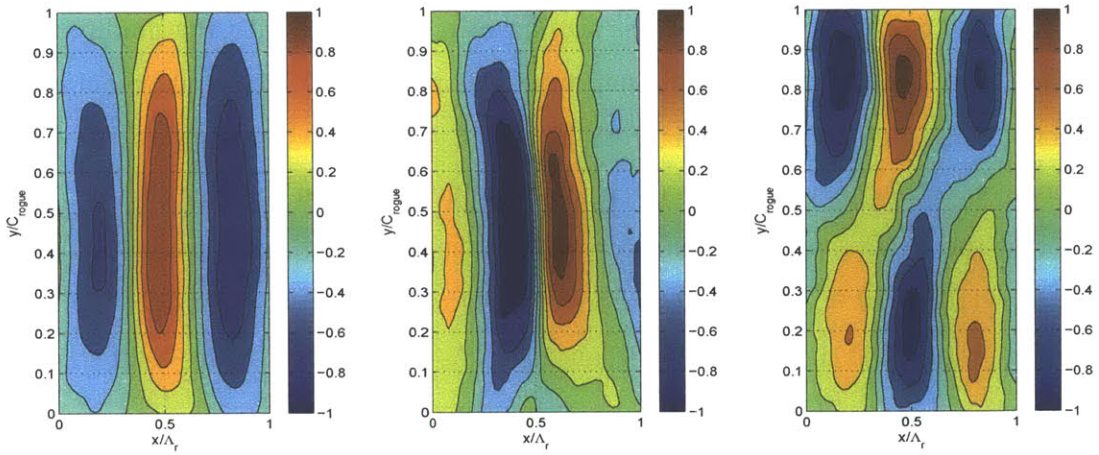

(a) $W_1(\hat{x}, \hat{y})$ (b) $W_2(\hat{x}, \hat{y})$ (c) $W_3(\hat{x}, \hat{y})$

Figure 8-16: POD modes of rogue wave profiles of type G_1 in the directional wavefield $\varepsilon = 0.1$, $\gamma = 5$ and $\Theta = 60°$ based on 200 samples. (a) $W_1(\hat{x}, \hat{y})$; (b) $W_2(\hat{x}, \hat{y})$; (c) $W_3(\hat{x}, \hat{y})$.

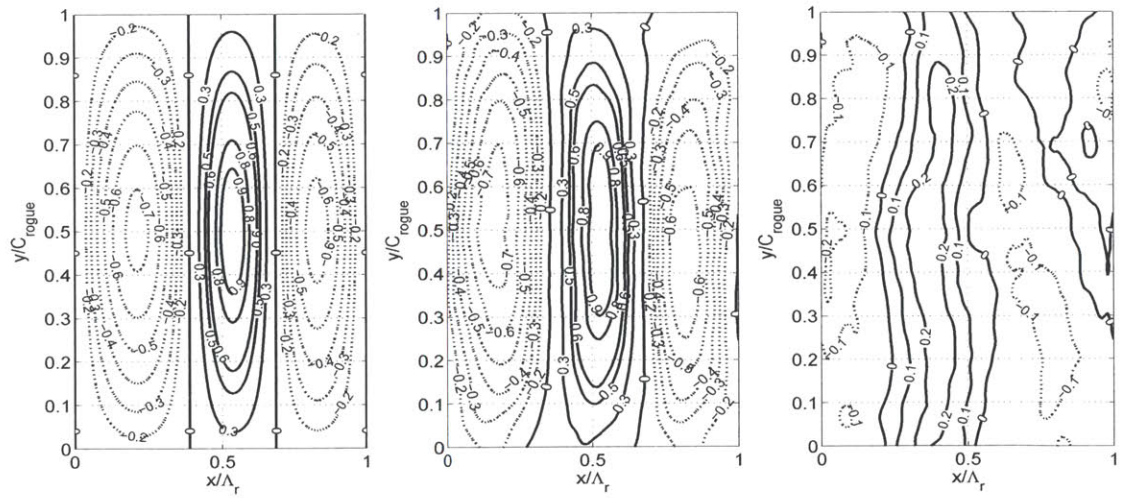

(a) (b) (c)

Figure 8-17: (a) Leading POD mode $U_1(\hat{x})V_1(\hat{y})$ in (8.6); (b) $W_1(\hat{x}, \hat{y})$ in (8.8); (c) $W_1(\hat{x}, \hat{y})$-$U_1(\hat{x})V_1(\hat{y})$ for rogue waves in the directional wavefield ε=0.1, γ=5 and $\Theta = 60°$. The POD modes are obtained based on a sample size of 200. Waves propagate from left to right.

to the case of unidirectional wavefields (figure 8-11(a)), the coefficient C_m decreases rapidly and only the leading mode has a non-zero mean. Comparing with figure 8-11(a), the coefficients decrease less significantly comparing with the unidirectional case, which suggests for directional wavefields more POD modes are required to archive a satisfied accuracy. Figure 8-19 shows the average accuracy of the POD expressions of rogue waves for wavefields with different initial spreading angles. The error of the POD representation decreases as the spreading angle increases. Over the broad range of Θ, the average errors of POD representation using only the three leading-order POD modes are less than 20%. As an example, figure 8-20 shows a rogue wave and its POD representation using three POD modes.

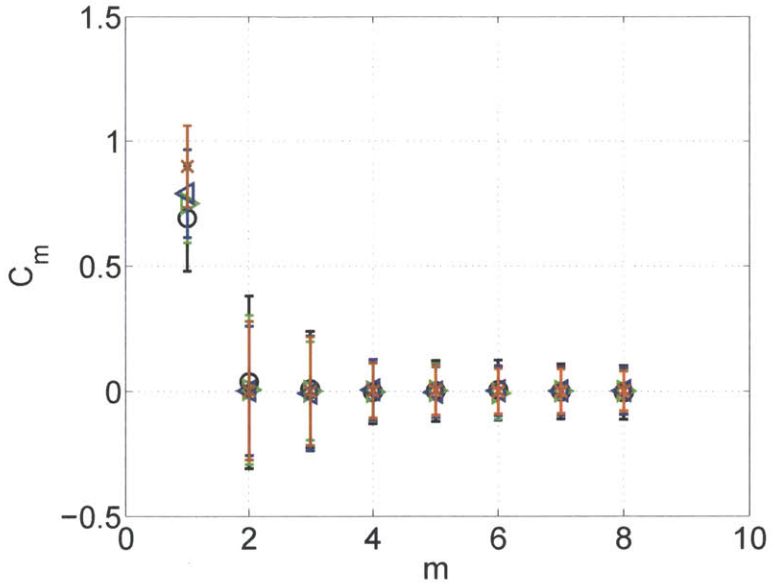

Figure 8-18: Coefficients C_m of leading POD modes of rogue waves in directional wavefields characterized by $\varepsilon = 0.14$ and $\gamma = 5$. $\Theta = 16°$ (◯), $40°$ (▷), $80°$ (◁) and $120°$ (×). The error bar indicates one standard deviation of the values.

8.4 Summary

In this section, we investigate the geometrical characteristics of rogue waves and their dependence on spectral parameters. We find the wave length of the rogue waves is comparable to the peak wave length. The crest length of rogue waves is generally

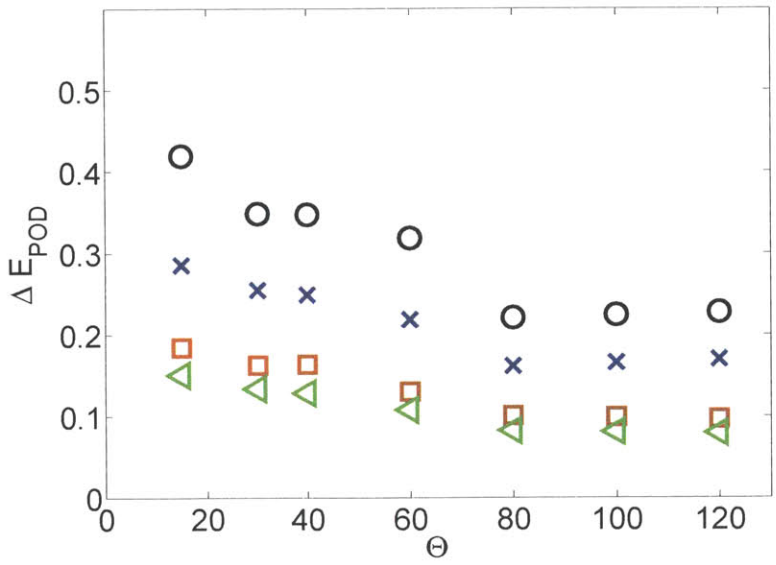

Figure 8-19: Average error of POD representations ΔE_{POD} using M_{xy}=1 (◯); M_{xy}=2 (×); M_x=3 (□).

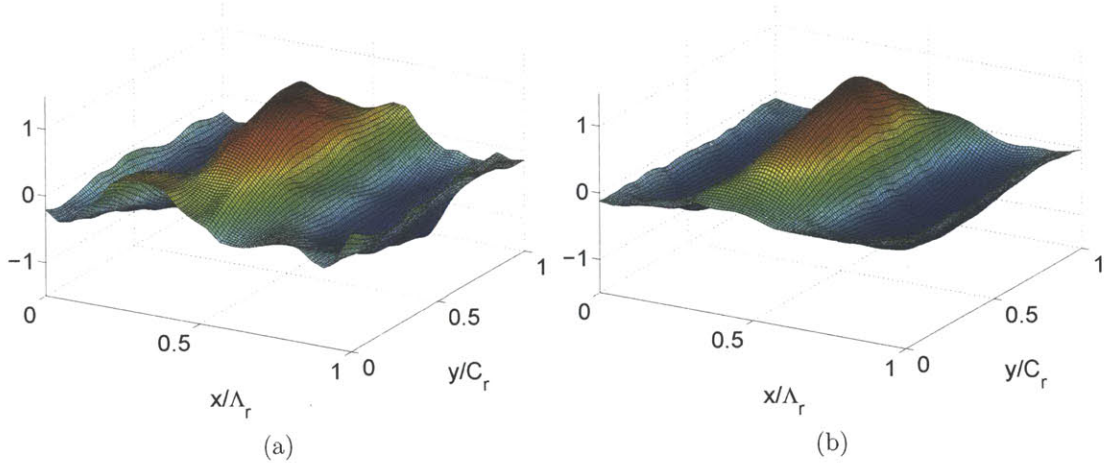

Figure 8-20: Example of rogue wave from directional wavefield ε=0.12, γ=6 and $\Theta = 60°$. (a) rogue wave profile $\eta_{\text{rogue}}(\hat{x}, \hat{y})$; (b) POD representation using leading three POD modes.

longer than the average crest length of the wavefield, resulting in a rogue wave area much larger than the average wave area. Rogue wave groups containing several large waves are also studied and we find the percentage of rogue wave groups among the total rogue wave populations decreases as spreading angle decreases. The structure of the rogue waves is analyzed using proper orthogonal decomposition (POD). For 2D and 3D rogue waves, we find the rogue wave profiles can generally be represented using a few leading POD modes.

Chapter 9

Phase-resolved prediction of nonlinear wavefield and rogue wave occurrence based on wave measurements

9.1 Introduction

The discussions in the previous chapters focus on the statistical aspects of the wavefield predictions. Unlike classic wave forecast models such as WAM and SWAN which can only provide statistical properties of the wavefield, SNOW simulations provide phase-resolved deterministic information of the wavefield. Recent advanced technology in radar sensing obtains high-resolution marine radar image, from which the surface elevation can be estimated by applying an inversion algorithm described in Nieto Borge et al. (2004). The radar inversion surface has high-resolution over a large domain and allows for individual wave detection in continuous time. The relatively large-scale, high-resolution measurements of wave surface give a description of present sea that could be used as initial conditions for wave forecast models. Phase-resolved deterministic forecast of the wavefields can, therefore, be obtained by assimilating the

measured data into wave evolution models.

A phase-resolved and reliable description of the ocean wave surface is crucial to improve maneuverability and active control of ship motion and to increase operational envelop and survivability of marine structures in severe seas. For example, the deterministic near real-time predictions of the surrounding surface profile could be used to find operational windows for side boat launch and recovery, or to obtain deterministic predictions of rogue wave occurrence.

The project High Resolution Air-Sea Interaction DRI (Hi-Res), carried out in June 2010 and funded by the Office of Naval Research, aims to obtain reliable deterministic predictions of nonlinear wavefields in moderate to high sea states using phase-resolved direct wave simulations (SNOW) with field measurement from ship-based radars. Assimilating radar measured high-resolution information of wave surface provided by WaMos®II, our nonlinear phase-resolved wave model (SNOW) provides improved predictions of realistic wavefields, from which the nonlinear wave statistics and occurrence probability of large waves are obtained. For more information on the project see `http://airsea.ucsd.edu/hires/`.

The main objective of this chapter is to develop and evaluate a simulation-based capability of phase-resolved reconstruction and (short-time) forecasting of realistic ocean wavefield evolution based on marine radar measured wave surface in Hi-Res (WaMos®II) . Special interests and focus are the incorporation and assimilation of radar measurements in the SNOW-simulation-based reconstruction and forecasting of the wavefield. The wave model predictions are directly compared with field measurements. The nonlinear statistics and occurrence of large waves are investigated based on the SNOW reconstructed and forecasted realistic wavefields. Equally important, forecast of the wavefield can be used for the validation, interpretation and improvement of the radar measured wave data.

9.2 Predictability based on instantaneous and continuous radar images

For a given wave measurement, there exists a spatial-temporal zone in which the wave elevation can be predicted deterministically. The predicable zone using on-site buoy measurements is derived theoretically and is discussed extensively in Wu (2004). In this section, we follow the similar procedure in Wu (2004) to derive the predicable zone of directional wavefields based on instantaneous and continuous radar measured surface elevations.

9.2.1 Predictability based on one radar image

. We assume the radar measured wave surface is accurate, and further assume that the spectral bandwidths of the wavefield are finite in both x and y directions. We derive the spatial-temporal predicable zone based on radar measured wave surface at time $t = t_0$, $\xi(\mathbf{x})$ with $\mathbf{x} \equiv (x, y) \in \mathcal{M}$, where $\mathcal{M}$ is the region of radar measurement.

The wave elevation is described as

$$\eta(\mathbf{x}, t) = \int_{k_x^{\min}}^{k_x^{\max}} \int_{k_y^{\min}}^{k_y^{\max}} A(\mathbf{k}) e^{i(\mathbf{k}\cdot\mathbf{x} - \omega t)} \, dk_x dk_y \tag{9.1}$$

Therefore, at $t = t_1$

$$\xi(x, y) = \eta(x, y, t_1) \int_{k_x^{\min}}^{k_x^{\max}} \int_{k_y^{\min}}^{k_y^{\max}} A(\mathbf{k}) e^{i(\mathbf{k}\cdot\mathbf{x} - \omega t_1)} \, dk_x dk_y, \tag{9.2}$$

where $(x, y) \in \mathcal{M}$. To apply fourier transform, we extend $\xi(x, y)$ to unbounded domain and still note it as $\xi(x, y)$. The inverse two-dimensional fourier transform of $\xi(x, y)$ gives

$$\xi(x, y) = \frac{1}{4\pi^2} \int_{-\infty}^{\infty} \int_{-\infty}^{\infty} B(\mathbf{k}) e^{i(\mathbf{k}\cdot\mathbf{x})} \, dk_x dk_y, \tag{9.3}$$

where

$$B(\mathbf{k}) = \int_{-\infty}^{\infty}\int_{-\infty}^{\infty} \xi(x', y') e^{-i(\mathbf{k}\cdot\mathbf{x}')}\, dx' dy'. \tag{9.4}$$

Together equation 9.2 and 9.3 gives

$$A(\mathbf{k}) = \frac{1}{4\pi^2} e^{i\omega t_1} B(\mathbf{k}) = \frac{1}{4\pi^2} e^{i\omega t_1} \int_{-\infty}^{\infty}\int_{-\infty}^{\infty} \xi(x', y') e^{-i\mathbf{k}\cdot\mathbf{x}'}\, dx' dy'. \tag{9.5}$$

The wavenumber domain is discretized into

$$k_x^m = k_x^{min} + (m - 1/2)\Delta k_x^{min} \tag{9.6}$$

$$k_x^n = k_y^{min} + (n - 1/2)\Delta k_y^{min}, \tag{9.7}$$

where $\Delta k_x = (k_x^{\max} - k_x^{\min})/N_{k_x}$, $\Delta k_y = (k_y^{\max} - k_y^{\min})/N_{k_y}$ and $N_{k_x} \times N_{k_y}$ are the number of the discrete wave modes. We thus have

$$\xi(x, y) = \sum_{m=1}^{N_{k_x}} \sum_{n=1}^{N_{k_y}} \xi_{mn}(x, y), \tag{9.8}$$

where

$$\xi_{mn} = \frac{1}{4\pi^2} \int_{k_y^n - \Delta k_y/2}^{k_y^n + \Delta k_y/2} \int_{k_x^m - \Delta k_x/2}^{k_x^m + \Delta k_x/2} A(\mathbf{k}) e^{i(\mathbf{k}\cdot\mathbf{x} - \omega t_1)}\, dk_x dk_y. \tag{9.9}$$

The frequency ω and wavenumber $\mathbf{k}$ is related through dispersion relation. The Taylor expansion of ω is

$$\omega(k_x, k_y) = \omega_{mn} + \frac{C_g^{mn}}{k_{mn}} [\vec{k}_{mn} \cdot (\mathbf{k} - \mathbf{k}_{mn})] + O(\frac{\partial^2 \omega}{\partial k_x^2}(\Delta k_x)^2, \frac{\partial^2 \omega}{\partial k_y^2}(\Delta k_y)^2), \tag{9.10}$$

where C_g^{mn} is the group velocity of the wave with frequency ω_{mn}. Comparing (9.1)

and (9.8), and using (9.10), the surface elevation is then:

$$\eta(\mathbf{x},t)=\sum_{m=1}^{N_{kx}}\sum_{n=1}^{N_{ky}}e^{i[C_g^{mn}k_{mn}-\omega_{mn}](t-t_1)}\xi_{mn}(\mathbf{x}-\frac{C_{mn}(t-t_1)}{k_{mn}}\mathbf{k}_{mn})[1+O(\epsilon_{mn}^x,\epsilon_{mn}^y)], \tag{9.11}$$

where $\epsilon_{mn}^x=|\frac{\partial^2\omega}{\partial k_{x,mn}^2}(\Delta k_x)^2(t-t_1)|$ and $\epsilon_{mn}^y=|\frac{\partial^2\omega}{\partial k_{y,mn}^2}(\Delta k_y)^2(t-t_1)|$.

$\eta(\mathbf{x},t)$ is predictable if

$$\mathbf{x}-\frac{C_{mn}(t-t_1)}{k_{mn}}\mathbf{k}_{mn}\in\mathcal{M},\quad \text{for all } m,\ n. \tag{9.12}$$

Equation 9.12 is the predicable zone based on the radar inversion surface in $\mathcal{M}$ at time $t=t_0$. At the future time $t=t^*$ $(t^*>t_1)$, the predicable range in space is

$$\vec{x}-\frac{C_{mn}(t^*-t_1)}{k_{mn}}\vec{k}_{mn}\in\mathcal{M},\quad \text{for all } m,\ n. \tag{9.13}$$

For a rectangular measurement domain $(x,y)\in[0,L_x]\times[0,L_y]$ at time $t=t^*$, and for wavefields with $c_{g,\min}\le c_g\le c_{g,\max}$ and spreading angle $(-\theta_w,\theta_w)$, the predicable zone is:

$$c_{g,\max}t^*\le x_p\le L_x+c_{g,\min}\cos\theta_w t^*; \tag{9.14a}$$

$$c_{g,\max}\sin\theta_w t^*\le y_p\le L_x-c_{g,\max}\sin\theta_w t^*. \tag{9.14b}$$

Figure 9-1 shows the evolution of predicable region based on radar measured surface at one time instant. We find the predicable zone decreases with time.

9.2.2 Predictability based on series radar images

The predicable zone of the image series is the combination of the predication zones based on each radar image. The predicable zone at $t=t_1$ in space based on radar measurement at $t=t_0$ $(t_0<t_1)$ is

$$\mathcal{P}_1=\{\mathbf{x}|\mathbf{x}-\frac{C_{mn}(t_1-t_0)}{k_{mn}}\mathbf{k}_{mn}\in\mathcal{M}\}. \tag{9.15}$$

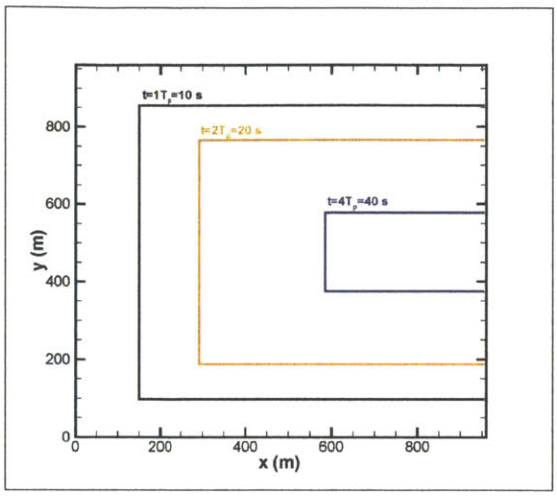

Figure 9-1: Variation of predicable zone based on wave data in a rectangle region for wavefields with $0.423\,\mathrm{s}^{-1} \leqslant f \leqslant 0.83\,\mathrm{s}^{-1}$, -30° $\leqslant \theta \leqslant$30°.

The effective radar measurement at $t = t_1$ is therefore expanded to

$$\mathcal{M}_1 = \mathcal{M} \bigcup \mathcal{P}_1. \tag{9.16}$$

The predicable region at $t = t_2$=$t_1 + \Delta t$ based on $\mathcal{M}_1$ is, therefore,

$$\mathcal{P}_2 = \{\mathbf{x} | \mathbf{x} - \frac{C_{mn}(t_2 - t_1)}{k_{mn}} \mathbf{k}_{mn} \in \mathcal{M}_1\}. \tag{9.17}$$

The predicable zone (x_p, y_p, t^*) based on N radar images $t = n\Delta t, t = 0 \cdots N$ is

$$c_{g,\max}(t^* - N\Delta t) \leq x_p \leq L_x + c_{g,\min} \cos\theta_w t^* \tag{9.18a}$$

$$c_{g,\max} \sin\theta_w (t^* - N\Delta t) \leq y_p \leq L_x - c_{g,\max} \sin\theta_w (t^* - N\Delta t). \tag{9.18b}$$

Comparing (9.18) with (9.14), the predicable zone with relative elapsed time τ=$t^* - N\Delta t$ is expanded by $c_{g,\min} \cos\theta_w N\Delta t$ in x-direction and the expansion is not significant if $c_{g,\min} \cos\theta_w$ is small.

9.3 Phase-resolved reconstruction of the wavefield using wave measurements

9.3.1 Mathematical formulations

The linear random wave-field can be written as suppositions of sinusoidal waves with different frequencies and propagation directions:

$$\eta(x,y,t)=\sum_{j=1}^{M_{k_y}}\sum_{i=1}^{M_{k_x}} a_{ij}\cos(k_{x,i}x+k_{y,j}y-\omega_{ij}t+\theta_{ij}), \tag{9.19}$$

where $(k_{x,i},k_{y,j})$ is the wavenumber vector, ω_{ij} is the frequency, which is related with the magnitude of the wavenumber $k_{ij}=\sqrt{k_{x,i}^2+k_{x,i}^2}$ by the linear dispersion relation $\omega_{ij}=\sqrt{gk_{ij}}$, a_{ij} and θ_{ij} are the amplitude and phase of the wave respectively.

Given the wave measurements, denoted by $\widetilde{\eta}(\mathbf{x}_p,t)$ at grid points of the radar image $\mathbf{x}_p=(x_p,y_p)$ $(p=1,\cdots,N_p)$ and successive instants $t=n_T\Delta t$, $n_T=0,\cdots,\alpha_T$, the reconstruction problem is to construct a wavefield $\eta(\mathbf{x},t)$ in a domain, denoted by $R(\mathbf{x},t)$, such that

$$\eta(\mathbf{x}_p,n_T\Delta t)=\widetilde{\eta}(\mathbf{x}_p,n_T\Delta t),\quad p=1,\cdots,N_p,\ n_T=0,\cdots,\alpha_T. \tag{9.20}$$

The forecasted wavefield for $t>\alpha_T\Delta t$ is obtained by evolving the reconstructed wavefield using wave forecasting model SNOW.

9.3.2 Optimization schemes

Considering (9.19) and (9.20), we have

$$\eta(\mathbf{x}_p,t)=\sum_{j=1}^{M_{k_y}}\sum_{i=1}^{M_{k_x}} a_{ij}\cos(k_{x,i}x_p+k_{y,j}y_p+\theta_{ij}), \tag{9.21}$$

For given measurements, for simplicity, the wavenumber is chosen as $k_{x,i}=k_{x,\min}+(i-1)\Delta k_x$, $i=1,\cdots,M_{k_x}$, $k_{y,j}=k_{y,\min}+(j-1)\Delta k_y$, $j=1,\cdots,M_{k_y}$. The wave

amplitude and phase, a_{ij} and θ_{ij}, are the variables to be optimized.

(9.21) can be written in another form:

$$\eta(\mathbf{x}_p, t) = \sum_{j=1}^{M_{k_y}} \sum_{i=1}^{M_{k_x}} a_{1,ij} \cos(k_{x,i} x_p + k_{k_y,j} y_p - \omega_{ij} t) - a_{2,ij} \sin(k_{x,i} x_p + k_{k_y,j} y_p - \omega_{ij} t) \tag{9.22}$$

where

$$a_{1,ij} = a_{ij} \cos(\theta_{ij}), \quad \text{and} \quad a_{2,ij} = a_{ij} \sin(\theta_{ij}). \tag{9.23}$$

Equation (9.22) is in the standard form of linear model $\mathbf{Ax} = \mathbf{b}$, where $\mathbf{A}$ is a $N_p \times 2M_{k_x}M_{k_y}$ matrix. Matrix $\mathbf{A}$ is usually not a square matrix, and in most cases $N_p > 2M_{k_x}M_{k_y}$. The equation (9.22), therefore, is an over-constrained problem without an exact solution. We instead solve the corresponding least square problem:

$$\min_x \|\mathbf{Ax} - \mathbf{b}\|^2, \tag{9.24}$$

which is equivalent to the problem

$$\mathbf{A}^T\mathbf{Ax} = \mathbf{A}^T\mathbf{b}. \tag{9.25}$$

$\mathbf{A}^T\mathbf{A}$ is symmetric and positive definite. Note that $\mathbf{A}^T\mathbf{A}$ is a sparse matrix because the plane monochromatic waves are orthogonal to each other. $\mathbf{A}^T\mathbf{A}$ has size of $2M_{k_x}M_{k_y} \times 2M_{k_x}M_{k_y}$. For a typical ocean wavefield, it requires $M_{k_x} = M_{k_y} = 20$ to obtain a satisfied representation. The matrix $\mathbf{A}^T\mathbf{A}$ therefore has a size of 800×800. A large linear system like (9.25) can be solved by many standard iterative methods including Gauss-Seidal method, or its improvement form, method of Successive Over-Relaxation, and Conjugate Gradient Method. In this study, we apply the conjugate gradient method to solve (9.25) and it converges in at most n iterations, for a linear system with a matrix size of $n \times n$.

9.4 Radar inversion data vs. SNOW reconstruction and forecast

9.4.1 Comparison metrics

The *point-by-point* error map is defined as

$$\mathrm{Err}(x,y) = \frac{|\eta_{\mathrm{model}}(x,y) - \eta_{\mathrm{radar}}(x,y)|}{4\sigma}, \tag{9.26}$$

where $\eta_{\mathrm{radar}}(x,y)$ is the (radar) wave measurements, $\eta_{\mathrm{model}}(x,y)$ is the model (SNOW) reconstructed and forecasted wavefield, and σ is the standard deviation of the surface elevation.

The cross correlation with zero-shift between η_{model} and η_{radar} is defined by

$$Corr = \frac{\iint \eta_{\mathrm{model}}(x,y)\eta_{\mathrm{radar}}(x,y)\ dxdy}{\sqrt{\iint \eta^2_{\mathrm{model}}(x,y)\ dxdy}\sqrt{\iint \eta^2_{\mathrm{radar}}(x,y)\ dxdy}}. \tag{9.27}$$

9.4.2 Reconstruction and forecast of wavefields based on radar inversion data

High-resolution wave measurements were obtained during the Hi-Res project by applying the WaMos®II radar inversion algorithm on the surface image from ship-based marine radars. Using the reconstruction algorithm described above, phase-resolved wavefields are reconstructed based on the WaMos®II radar inversion data. Figure 9-2 shows an example of a comparison between radar inversion data and SNOW reconstructed wave surface. The comparison is very satisfactory.

The forecasted wavefield is obtained by evolving the reconstructed wavefield using SNOW. Figure 9-3 shows comparisons of surface elevation between radar inversion data and SNOW forecast at different time for wave data shown in figure 9-2. The theoretical predicable zone is also shown as a reference. We observe the comparisons are reasonably well in the predicable domain over a short-time evolution, while the comparisons are less satisfied outside the predicable zone. This can be seen quantita-

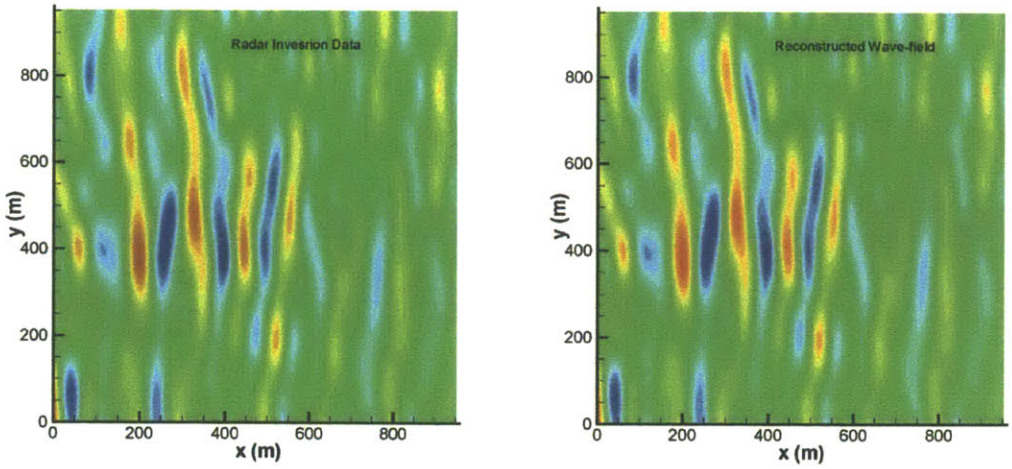

(a) $\eta_{\text{radar}}(x, y)$ (b) $\eta_{\text{model}}(x, y)$

Figure 9-2: (a) radar inversion data; (b) SNOW reconstructed wave-field using $M_{k_x} = M_{k_y} = 20$.

tively from the point-by-point error maps in Figure 9-4. In the predicable region, the forecasted wavefields agree reasonably well with the radar inversion data; however, significant discrepancy is observed around the boundary areas.

The correlations between radar inversion data and model prediction in entire domain and in predicable region are shown in Figure 9-5. We find that, for the entire computational domain, the correlation decreases with time as the waves outside the domain propagate into the domain as observed in figure 9-4. In the theoretical predicable zone, the correlation does not decrease with time and the prediction is almost certain (with correlation close to unity).

To assess the predicability outside the measurement domain, we only use a sub-domain of the radar inversion data, denoted by $\mathcal{S}_{\text{sub}}$, to reconstruct a wavefield. The forecasted wavefield is then compared with the entire radar inversion data. We present two examples of reconstructed and forecasted wavefields using radar data obtained on two different days during the Hi-Res project. One wavefield has relatively small spreading angle and the other has broader spreading angle. The amplitude maps of the reconstructed wavefields, $a(k_x, k_y)$, are shown in figure 9-6(a) for small spreading

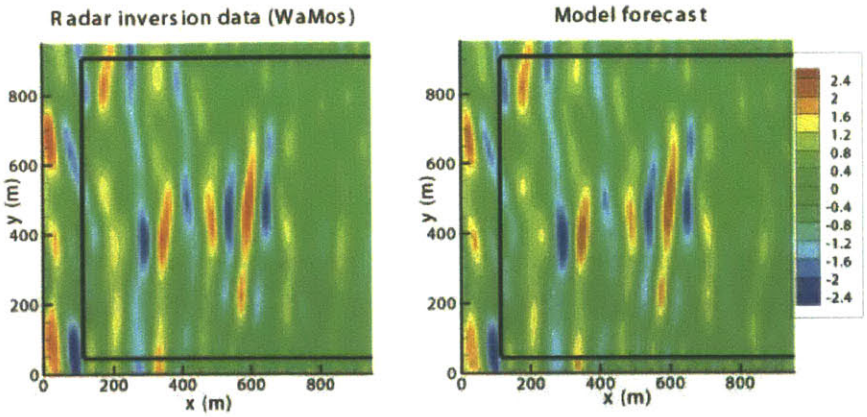

(a) Radar vs. SNOW $t = 1T_p$

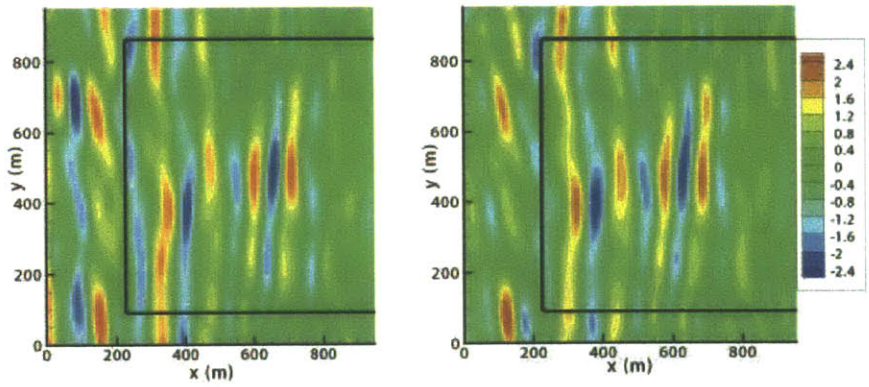

(b) Radar vs. SNOW $t = 2T_p$

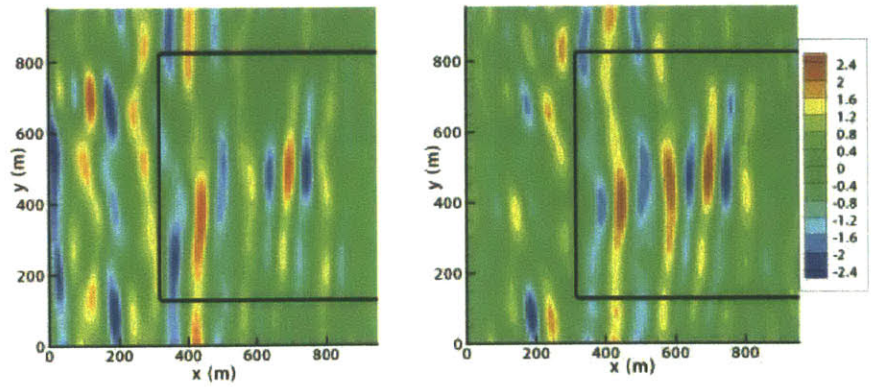

(c) Radar vs. SNOW $t = 3T_p$

Figure 9-3: Comparison between radar inversion data (WaMos) and SNOW forecast at (a) $t = 1T_p$; (b) $t = 2T_p$; (c) $t = 3T_p$. The unit of the legend is meter. T_p=10 sec. The black box shows the theoretical predicable zone.

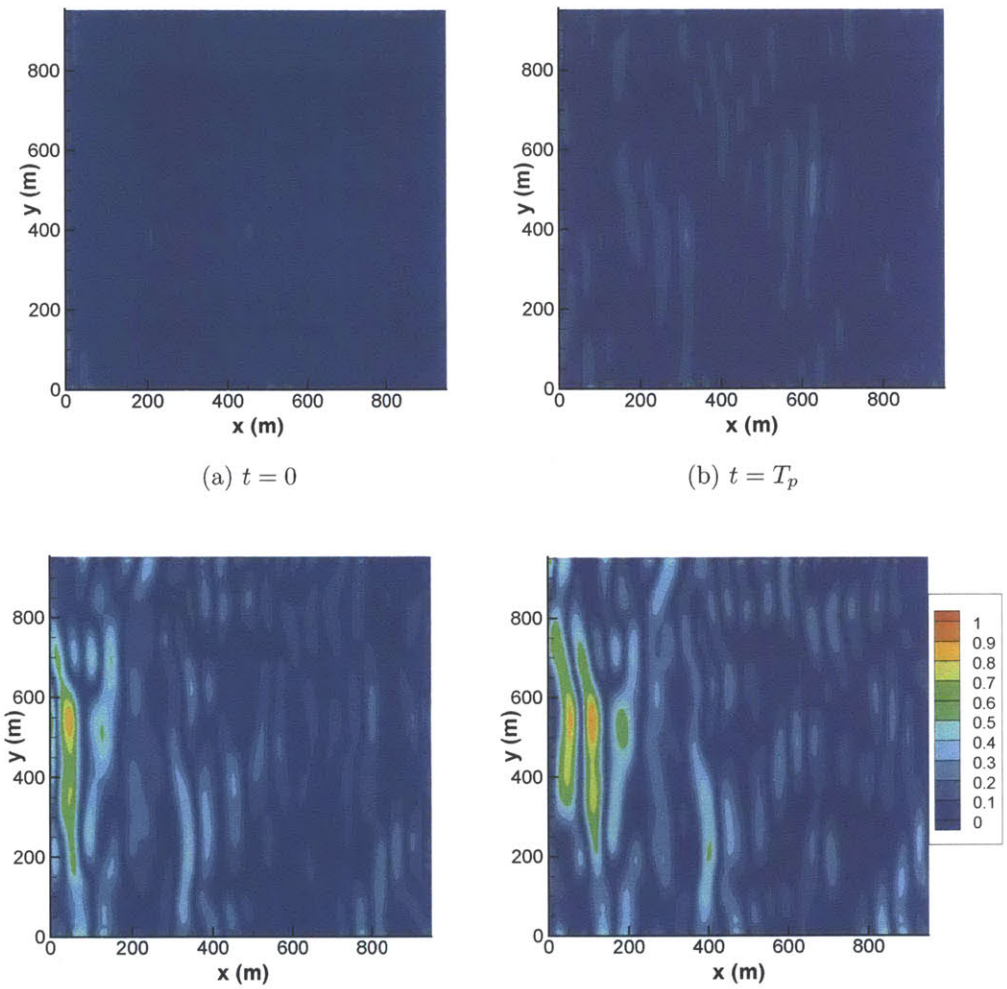

(a) $t = 0$

(b) $t = T_p$

(c) $t = 3T_p$

(d) $t = 4T_p$

Figure 9-4: Point-by-point err between radar inversion data and model forecasted wavefields at (a) $t = 0$; (b) $t = T_p$; (c) $t = 3T_p$; (d) $t = 4T_p$. The legend unit is meter.

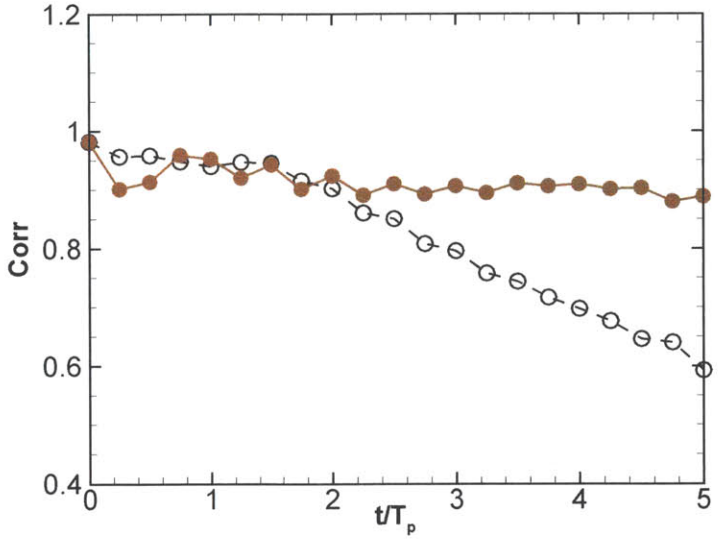

Figure 9-5: The correlation with zero shift Corr $= C(0,0)$ between radar inversion data and SNOW predicted wavefield in entire computational domain (–o–) and predicable region (–•–). T_p=10 sec.

case and figure 9-6(b) for broad spreading case.

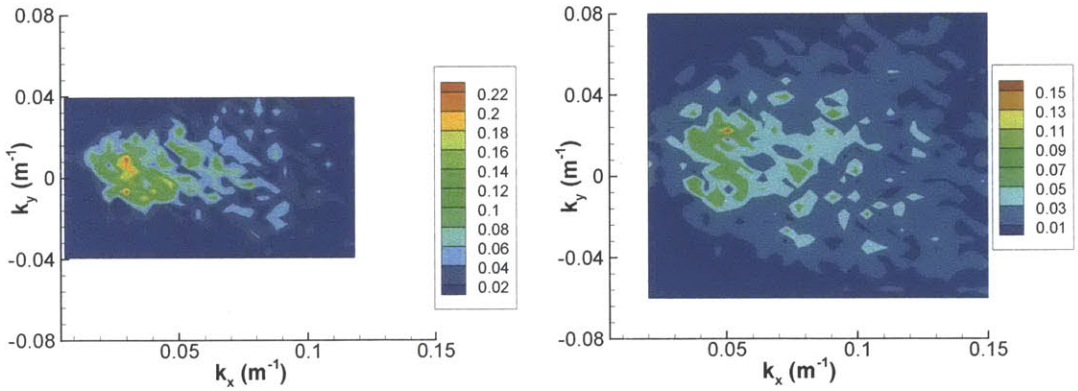

(a) (b)

Figure 9-6: Reconstructed amplitude $a(k_x, k_y)$. (a) wavefield with small spreading angle; (b) wavefield with broad spreading angle. The unit is in meter.

Figure 9-7 shows the comparisons between radar inversion data and SNOW forecast for the wavefield with small spreading angle. For a short time t/T_p=10, S-NOW forecast agrees reasonably well with radar inversion data in the region $\mathcal{S}_{\text{sub}}$

($0 \leq x \leq 2000$ m and $0 \leq y \leq 2000$ m). At later time $t = 20T_p$, SNOW gives a reasonable prediction outside $\mathcal{S}_{\text{sub}}$ ($2000 \leq x \leq 3000$ m). The point-by-point error maps at different time are shown in figure 9-8. We observe that, at short time, the point-by-point error in $\mathcal{S}_{\text{sub}}$ is small, while considerable error is observed in the region outside $\mathcal{S}_{\text{sub}}$. For longer time, the theoretical predicable zone moves as waves propagate through the region $\mathcal{S}_{\text{sub}}$ leading to a better comparison outside $\mathcal{S}_{\text{sub}}$ but worse comparison inside $\mathcal{S}_{\text{sub}}$.

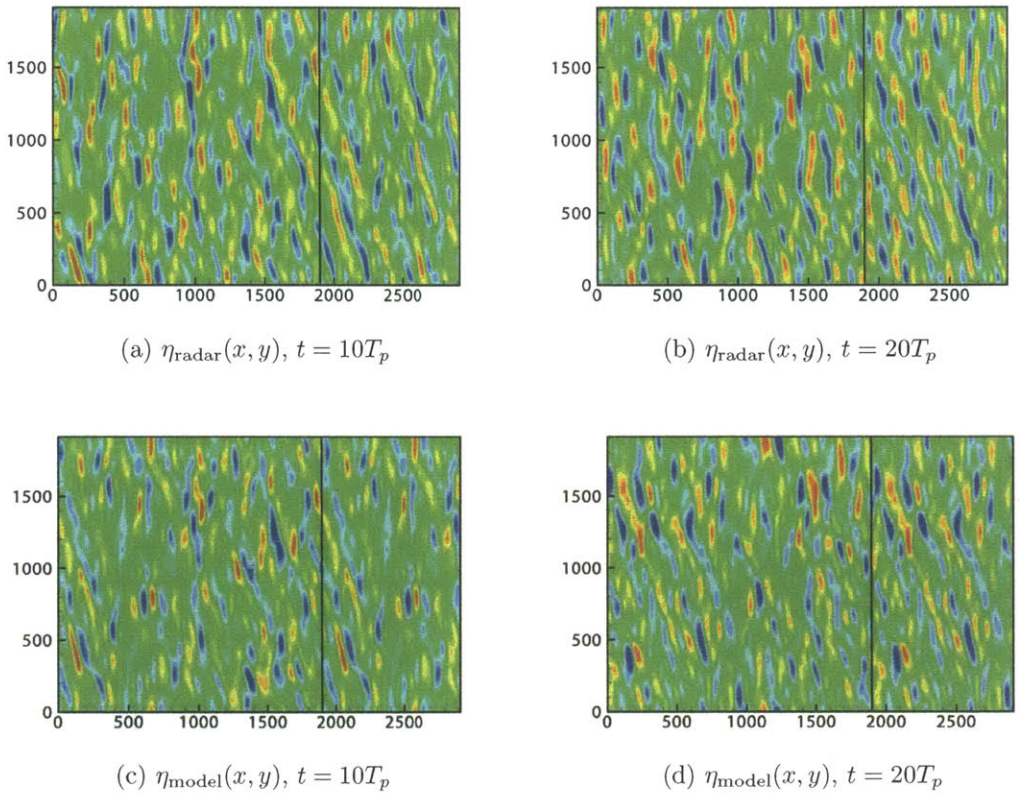

(a) $\eta_{\text{radar}}(x, y)$, $t = 10T_p$

(b) $\eta_{\text{radar}}(x, y)$, $t = 20T_p$

(c) $\eta_{\text{model}}(x, y)$, $t = 10T_p$

(d) $\eta_{\text{model}}(x, y)$, $t = 20T_p$

Figure 9-7: The comparisons between radar inversion data and model forecast. The radar measurement region used for reconstruction $\mathcal{S}_{\text{sub}}$ is $0 \leq x \leq 2000$m and $0 \leq y \leq 2000$m. Radar measurement (WaMos): (a) t/T_p=10, (b) t/T_p=20; SNOW: (c) t/T_p=10, (d) t/T_p=20.$H_s \approx$5.3 m, T_p=6 s.

Figure 9-9 shows the radar inversion data and the point-by-point error map of the SNOW reconstructed and forecast wavefields for the case with broad spreading angle. At a short time t/T_p=4, SNOW forecast agrees reasonably well with radar inversion

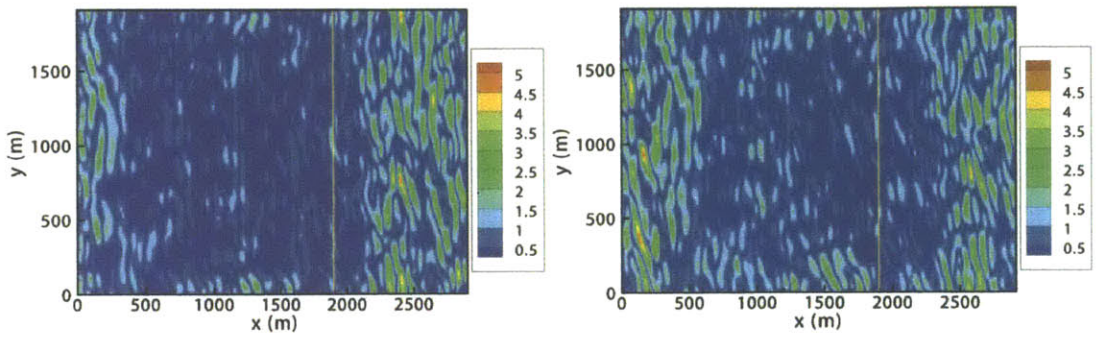

(a) $t = 5T_p$

(b) $t = 10T_p$

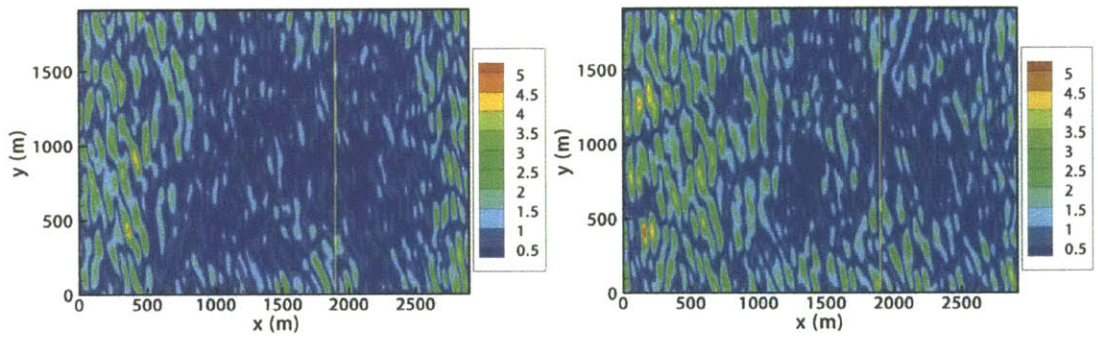

(c) $t = 15T_p$

(d) $t = 20T_p$

Figure 9-8: The point-by-point error between radar inversion data and model prediction. The radar measurement region is $0 \leq x \leq 2000$m and $0 \leq y \leq 2000$m. The unit is in meter.

data in the region $\mathcal{S}_{\text{sub}}$ ($0 \leq x \leq 2000\,\text{m}$ and $0 \leq y \leq 2000\,\text{m}$). As waves evolve, SNOW gives a reasonable prediction outside $\mathcal{S}_{\text{sub}}$ ($2000 \leq x \leq 3000\,\text{m}$). We observe that at earlier time, the point-by-point in $\mathcal{S}_{\text{sub}}$ is small, while considerable error is observed in the region outside $\mathcal{S}_{\text{sub}}$. For longer time, good comparison outside $\mathcal{S}_{\text{sub}}$ but worse comparison inside $\mathcal{S}_{\text{sub}}$ are observed . The overall agreement between radar inversion data and SNOW forecast in this case is less satisfactory comparing the case with small spreading angle shown in figure 9-8. This is because the theoretical predicable zone based on (9.14) decreases faster with time for wavefields with large spreading angle.

9.5 Dependence of model performance on spectral resolution

The reconstructed wavefields based on the radar inversion surface data using different spectral resolutions (M_{k_x}, M_{k_y}) with fixed incremental wavenumber, Δk_x and Δk_y, for a given radar measurement are shown in figure 9-10. The spectral band coverage increases with the number of wave modes used in the wavefield reconstruction and forecasting. Waves with shorter length scales could be resolved using higher spectral resolutions (M_{k_x}, M_{k_y}).

The forecasted wavefields with different spectral resolutions are compared with on-site buoy record. Figure 9-11 shows the wave frequency spectra calculated from buoy time series and model forecast for different spectral resolutions. With increasing spectral resolution, waves with high frequencies are reconstructed, leading to wavefields containing shorter wave scales. The frequency spectrum from forecasted wavefield with sufficient number of wave modes $M_{k_x} \times M_{k_y}$=34×26 is very close to the frequency spectrum measured from buoy.

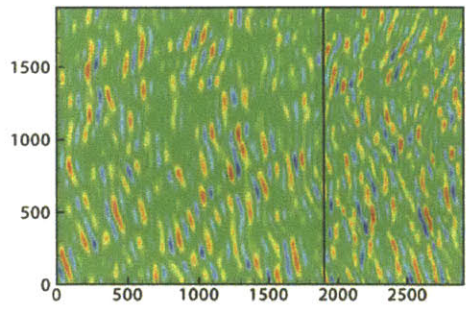

(a) $\eta_{\text{radar}}(x, y)$, $t = 0T_p$

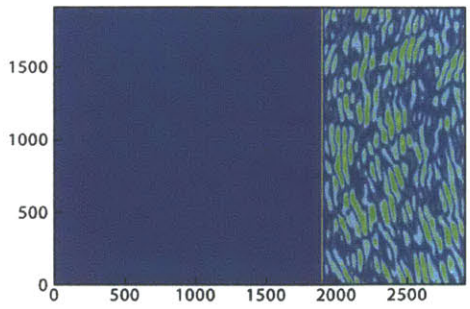

(b) $\text{Err}(x, y)$, $t = 0T_p$

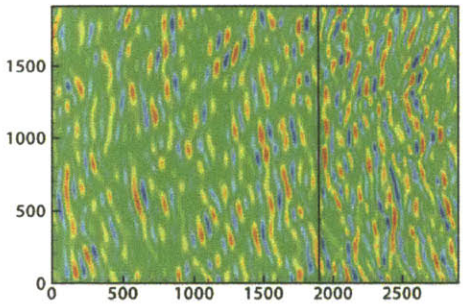

(c) $\eta_{\text{radar}}(x, y)$, $t = 4T_p$

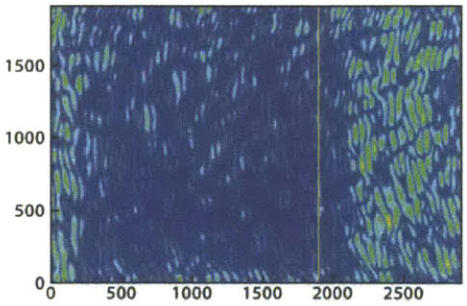

(d) $\text{Err}(x, y)$, $t = 4T_p$

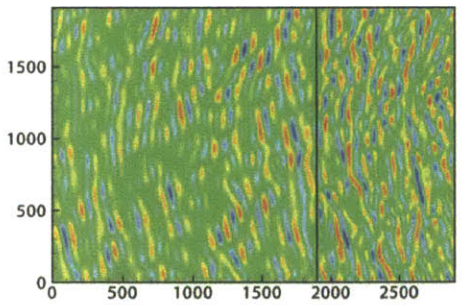

(e) Radar $t = 7T_p$

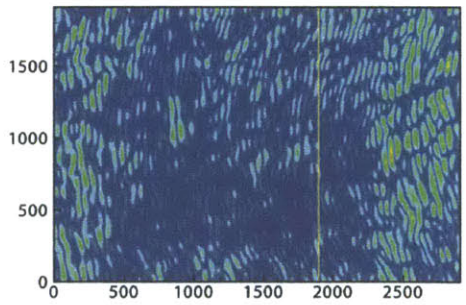

(f) Error $t = 7T_p$

Figure 9-9: The point-by-point error between radar inversion data and model prediction. The radar measurement region is $0 \leq x \leq 2000$m and $0 \leq y \leq 2000$m. H_s=3.6 m, T_p=8.3 sec.

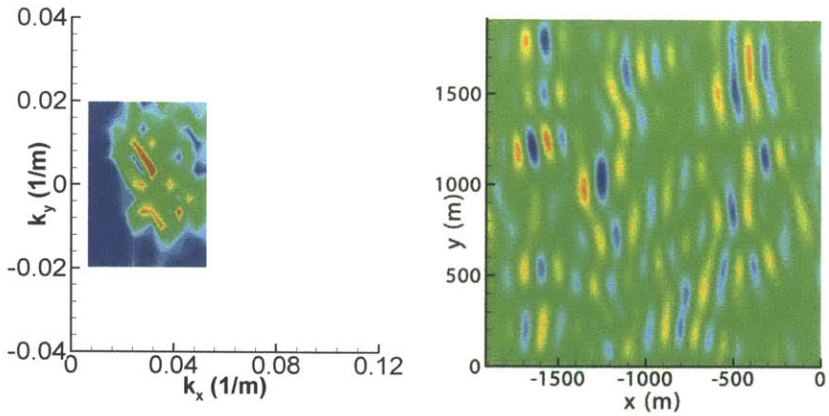

(a) M_{k_x}=14, M_{k_y}=13 (b) M_{k_x}=14, M_{k_y}=13

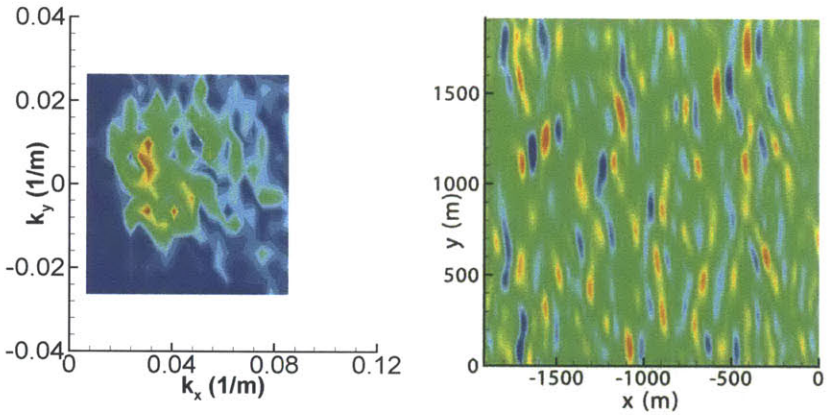

(c) M_{k_x}=24, M_{k_y}=17 (d) M_{k_x}=24, M_{k_y}=17

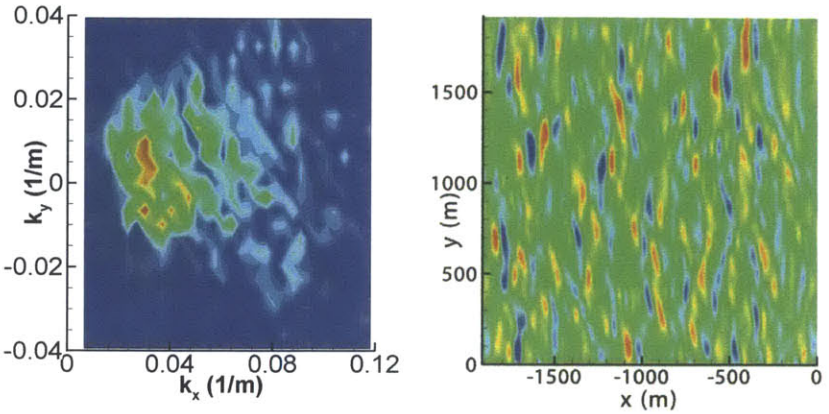

(e) M_{k_x}=34, M_{k_y}=25 (f) M_{k_x}=34, M_{k_y}=25

Figure 9-10: Amplitude $a(k_x, k_y)$ ((a), (c), (e)), and reconstructed wavefield $\eta_R(x, y)$ ((b), (d), (f)), obtained using different spectral resolutions (M_{k_x}, M_{k_y}) for given radar measurement at one time instant. M_{k_x}=14, M_{k_y}=13 ((a), (b)); M_{k_x}=24, M_{k_y}=17: (c), (d); M_{k_x}=34, M_{k_y}=25: (e), (f).

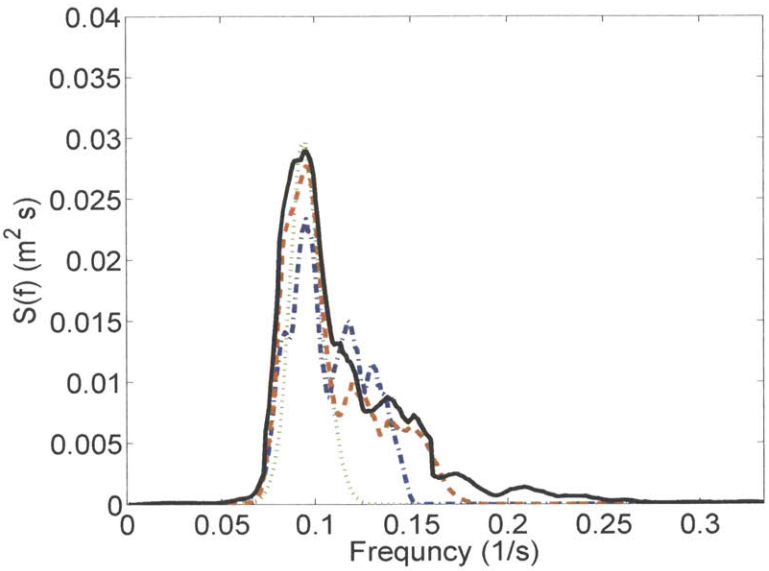

Figure 9-11: The wave frequency spectra calculated from buoy time series and model prediction at the buoy location. $(M_{k_x}, M_{k_y}) = (14 \times 13)$ (···); (24×17) (-·-); (34×26) (- - -). Buoy record (—).

9.6 Effect of shear current on the reconstruction and forecast of wavefields

An accurate and reliable estimation on the current profile is very important for phase-resolved wavefield prediction. In the radar inversion surface data, the background current is estimated as the constant current which gives the optimal fit to the measurement using linear dispersion relation with constant current (Nieto Borge et al., 2004).

The current may also be obtained by finding the current profile in SNOW that produces the maximum correlation between the radar inversion data and model forecast. This is considered to be a better approach because the possible nonlinear interactions between current and waves are considered. More importantly, the current in SNOW can be space-dependent. Figure 9-12 shows two simple cases where constant current is considered. We find the correlation between the radar inversion data and model prediction with and without consideration of background current for two different radar data sets. It shows that the agreement between the radar data and model

prediction is improved considerably by including the background current.

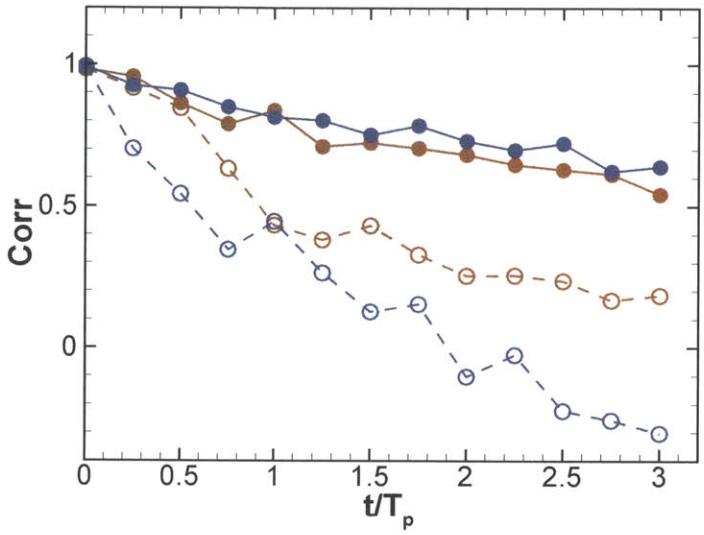

Figure 9-12: The correlation between radar inversion data and model forecast. Model forecast with optimal current: data set one (—•—) and data set two (—•—); model forecast without current: data set one (- -o- -) and data set two (- -o- -).

For the current with weak vorticity, the flow including the current can still be treated as potential flow. The interaction between such current and irregular wavefield is studied in Wu (2004). We here implement depth-dependent shear current using the concept of equivalent current. The equivalent uniform current for given wave mode is defined as the constant current which leads to the same wave phase velocity observed in stationary coordinates as the shear current for the wave mode.

Kirby and Chen (1989) derived an approximate dispersion relation for weak current with $\max(U(z))/c_0 = O(\varepsilon)$, where c_0 is the wave phase speed and ε is a small parameter. For water with finite depth, the equivalent current $\tilde{U}$ is

$$\tilde{U} = \frac{2k}{\sinh 2kh} \int_{-h}^{0} U(z) \cosh 2k(h+z)\, dz, \tag{9.28}$$

and for deep water, it is

$$\tilde{U} = 2k \int_{-h}^{0} U(z) \exp(2kz)\, dz. \tag{9.29}$$

For a special shear current profile

$$U(z) = U_s(1 + \alpha z/h) = U_s + \Omega z, \tag{9.30}$$

the exact absolute velocity is

$$c_a = \sqrt{g/k}\sqrt{1 + \Omega^2/4gk} + U_s - \Omega/2k. \tag{9.31}$$

The equivalent velocity can be calculated by substituting (9.28) into (9.29) which gives

$$\tilde{U}(k) = U_s - \Omega/2k. \tag{9.32}$$

The difference between the estimated absolute velocity and the exact solution is $O(\Omega^2)$. The discussion on the action flux conservation using the equivalent current can be found in Kirby and Chen (1989).

The effect of shear current on the wave propagation is counted in the leading order using the equivalent current. The implementation of the shear current vector is done in the wavenumber space. The project current, in the direction of wavenumber $\mathbf{k} = (k_x, k_y)$, denoted by $U'(z)$, is $U'(z) = \vec{U}(z) \cdot \vec{k}/k$. The equivalent current of the shear current $\vec{U}(z) = U(z)(\cos\beta_U, \sin\beta_U)$, where β_U is the direction of shear current, is $\vec{U}(\mathbf{k}) = \hat{U}(\mathbf{k})(\cos\theta_k, \sin\theta_k)$, where $\cos\theta_k = k_x/k$, $\sin\theta_k = k_y/k$ and

$$\hat{U}(k) = 2k \int_{-\infty}^{0} U'(z) e^{2kz}\, dz, \tag{9.33}$$

where $k = \sqrt{k_x^2 + k_y^2}$ and $U'(z)$ is the projected velocity of $\vec{U}(z)$ in the direction of

$\vec{k} = (k_x, k_y)$:

$$U'(z) = \vec{U}(z) \cdot \vec{k}/k = U(z)(\cos\beta_u \cos\theta_k + \sin\beta_u \sin\theta_k). \tag{9.34}$$

The shear current is considered in the leading order of SNOW in the form:

$$\hat{\eta}_t = \hat{\phi}_z - \hat{U}(\mathbf{k}) \cos\theta_k \hat{\eta}_x + \hat{U}(\mathbf{k}) \sin\theta_k \hat{\eta}_y; \tag{9.35a}$$

$$\hat{\phi^s}_t = -\hat{\eta} - \hat{U}(\mathbf{k}) \cos\theta_k \hat{\phi^s}_x + \hat{U}(\mathbf{k}) \sin\theta_k \hat{\phi^s}_y. \tag{9.35b}$$

We simulate a nonlinear directional wavefields with a background shear current:

$$U(z) = [a \exp(\kappa z), 0], \tag{9.36}$$

where a is the current magnitude and κ is the current parameter. Figure 9-13(a) shows the profile of the shear current. The current decreases exponentially with depth and is mainly penetrated in a thin layer close to the surface. A subdomain of the simulated wavefield is used as synthetic radar inversion data. Two wavefields are reconstructed. one uses uniform current and the other uses wavenumber dependent current described in (9.35). Figure 9-13(b) shows the correlation between the synthetic radar surface and the forecasted wavefields with and without considering current. In the case in which the current is not considered, the correlation between synthetic radar data and model forecast decreases rapidly with time. The correlation is improved significantly when the current is considered, specially in the case in which the wavenumber-dependent current is used (9.33). For an accurate phase-resolved reconstruction and forecast, it is important to consider background current properly.

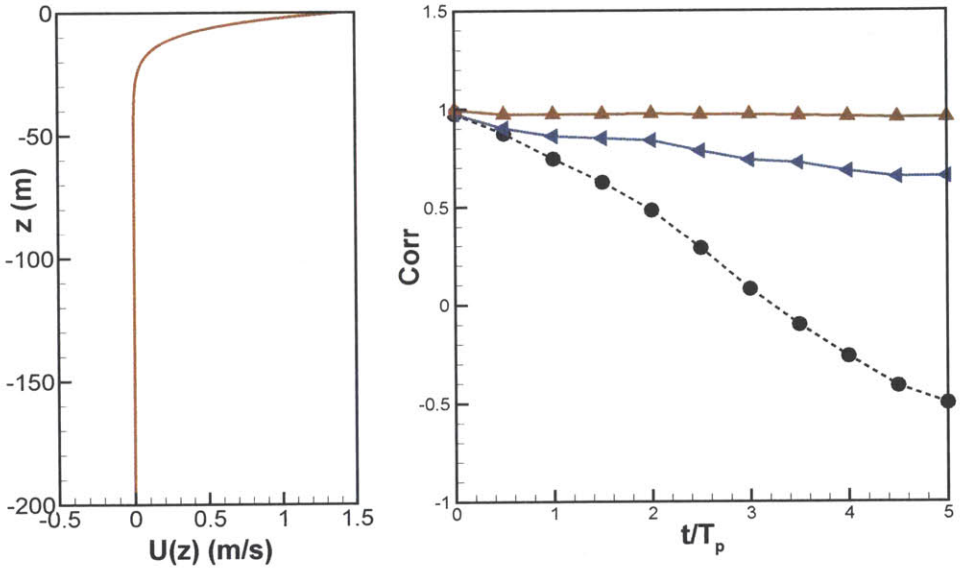

(a) (b)

Figure 9-13: (a) Profile of depth dependent shear current (9.36) with a=1.5 and $kappa$=$2k_p$. (b) Correlation wavenumber dependent current $\hat{U}(k)$(—▲—); constant current U_0 (· ◀ ·); no current (- -●- -) for JONSWAP directional wavefield H_s=10 m, T_p=10 s, γ=3.3 and Θ=80°.

9.7 Interpretation of radar measurement errors

9.7.1 Spatial-dependent modulations

In Radar image, the intensity of backscattering related to the wave tilt modulations depends on the distance of the local surface patch from the radar antenna, and the orientation of the local surface patch relative to the antenna (Nieto Borge et al., 2004). These modulations usually show as low-wavenumber and time-independent signal in the 2D spectrum of the radar image, therefore they can be removed by filtering. It is not straightforward to remove more complex space-dependent modulations. The spatial dependent modulations lead spatial-dependent error in the induced radar inversion data. The radar inversion surface data with spatial-dependent error may be approximated as

$$\zeta_{\text{radar}}(x, y, t) = M(X, Y)\eta_{\text{radar}}(x, y, t) \tag{9.37}$$

where ζ_{radar} is the radar inversion data with spatial-dependent error, η_{radar} is the corrected radar inversion data, and $M(X, Y)$ is slowing varying function describing the spatial-dependent error. $M(X, Y)$ can be approximated using (chebyshev) polynomials with unknown coefficients. The original wavefield may therefore be retrieved from η_{radar} using iterative nonlinear optimal algorithm. An example of the calibration process is shown in figure 9-14. figure 9-14(a) and (c) are the original radar inversion data. The radar antenna is located on the right of the domain. Considerable spatial-dependent modulations are observed with the intensity of radar image decreases as the distance from the antenna increases. The calibrated surfaces are shown in Figure 9-14(b) and (d). The spatial-dependent modulations are removed and the wave energy distributes more evenly over space.

9.7.2 Dependence on radar looking angle

The accuracy of radar inversion wave data depend on the angle between dominant direction of wavefield and radar looking angle, denoted as α. To asses dependence

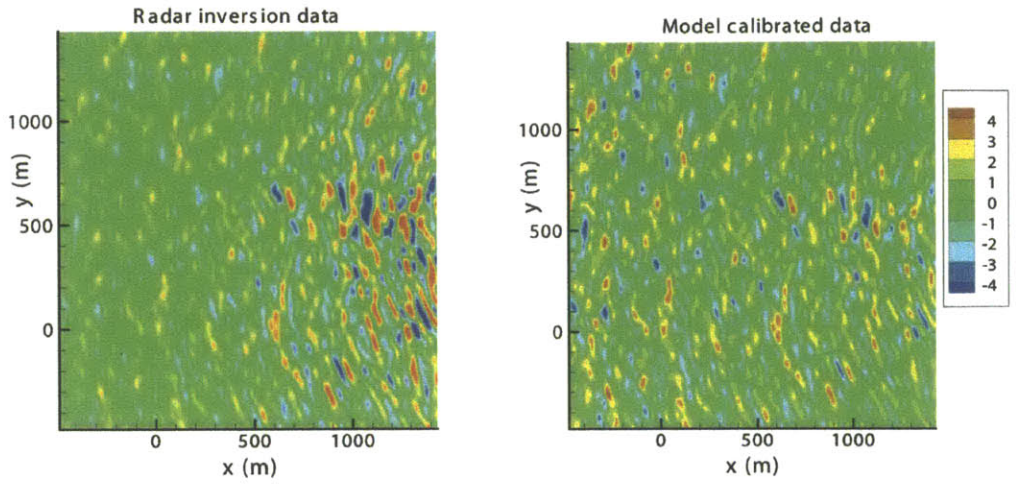

(a) η_{radar}, t=0 (b) η_{model}, $t = 0$

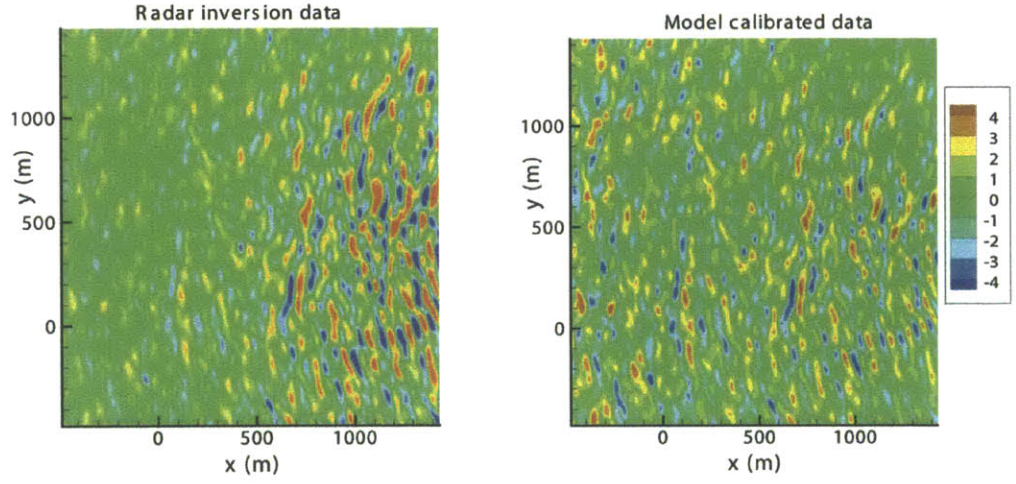

(c) η_{radar}, $t = 1T_p$ (d) η_{model}, $t = 1T_p$

Figure 9-14: Radar inversion data vs. model calibrated surface. Radar inversion data at (a) $t = 0T_p$; (c) $t = 1T_p$; Model calibrated surface at (b) $t = 0T_p$; (d) $t = 1T_p$.

of the radar inversion data accuracy on α, we choose the four sub-domains in the radar image located in different radar looking directions shown in figure 9-15(a). The correlations between the radar inversion data and SNOW forecasted wavefields for each subdomain at time $t = 2T_p$ as functions of radar looking angles are shown in figure 9-15b for different radar inversion data sets. For the three sets of radar inversion data, the maximum correlation is observed for α=180°. The agreement between the radar inversion data and model prediction is satisfactory when the wave propagation direction is parallel to the radar looking direction (β=0° and 180°). The minimum correlations are observed at α=90° and 180°, when the propagation direction of the wavefield is perpendicular to the radar looking angle. This is because the radar backscatter is minimally effected when the wave crests are aligned in the direction of the radar looking direction.

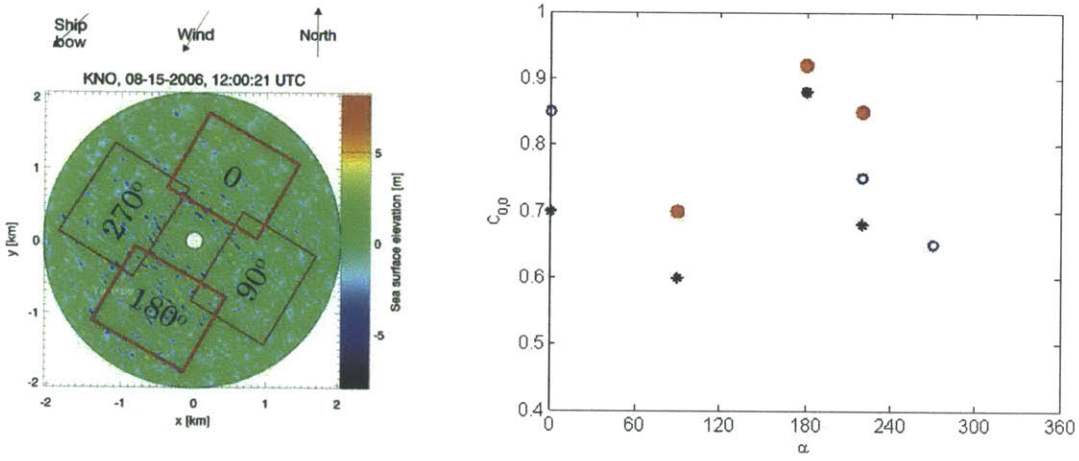

(a) (b)

Figure 9-15: (a) Sub-domain of radar inversion data. The number marked in the rectangle is the radar looking angle for that domain. (b) Sub-domain of radar inversion data. The number marked in the rectangle is the radar looking angle for that domain. Different symbols are used to represent different data sets of radar inversion data.

9.8 Nonlinear wave statistics and occurrence of large waves in phase-resolved forecasted realistic wavefields

9.8.1 Reconstruction and forecast in a large domain size using multiple measurements

Using multiple radar measurements, a wavefield with large domain size could be reconstructed by extending (9.19) to a large domain. Figure 9-16(a) shows an example of a reconstructed large wavefield with size of $15\times15\,\mathrm{km}^2$ using two collocated radar inversion data (for each radar, two subdomain images in upwind and downwind are shown) obtained from the Hi-Res project. The reconstructed amplitude map $a(k_x, k_y)$ of the free waves is shown in Figure 9-16(b). The wavefield has an estimated significant wave height H_s=5.3 m and T_p=11.58 sec. The large-scale wavefield is forecasted by evolving the reconstructed initial wavefield using SNOW simulations.

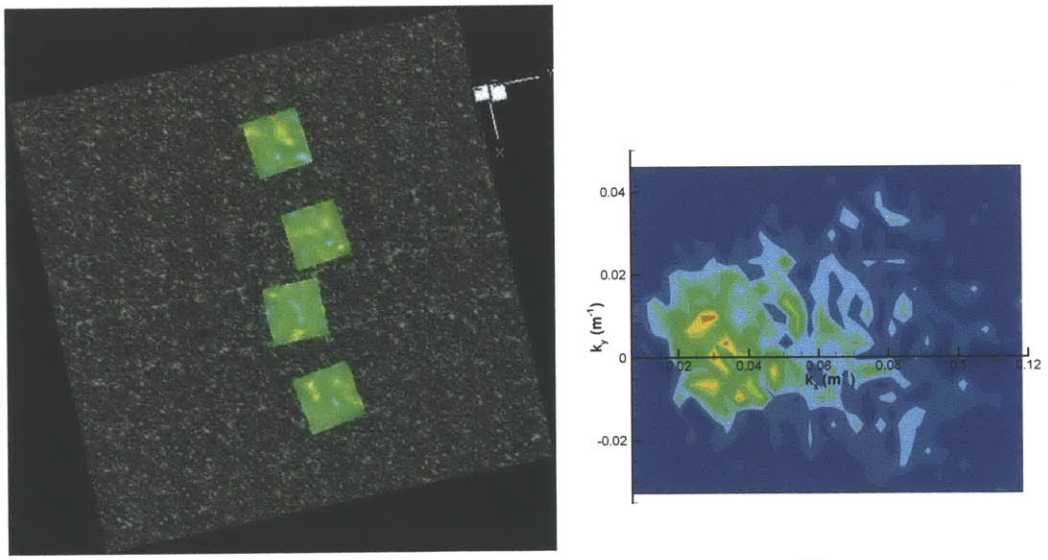

(a) (b)

Figure 9-16: (a) Reconstructed large-scale wavefield with a domain size of $15\times15\,\mathrm{km}^2$ using two radar measurements. For each radar, two subdomain images in upwind and downwind directions are shown. (b) Amplitude $a(k_x, k_y)$ of the free waves of the reconstructed wavefield using two radar measurements.

The one-dimensional omnidirectional spectrum $S(k)$ and integral directional distribution function $D(\theta)$ are defined as

$$S(k) = \int_{\theta} k\Psi(k,\theta)\, d\theta, \quad \text{and} \quad D(\theta) = \int_{k} k\Psi(k,\theta) dk. \tag{9.38}$$

Figure 9-17 shows the omnidirectional spectrum and the integral directional distribution function for the reconstructed wavefield. Local smoothing has been applied on the spectra. The estimated spectral bandwidth $\Delta k/k_p \approx 0.26$ (Δk is calculated as half width at half maximum of the spectrum). The estimated directional spreading angle $\Theta \approx 42.75°$ (Θ is calculated as the width at half maximum of the directional distribution function $D(\theta)$). The Benjamin-Feir index and modified BFI introduced in Chapter 5 § are BFI=0.31 and MBFI=0.23 respectively. We use the forecasted wavefield to demonstrate the importance of using nonlinear simulation in phase-resolved prediction of wavefield evolution. The initial wavefield is evolved using SNOW simulations with orders of nonlinearity M=1 and M=4, from which the nonlinear wave statistics and occurrence probability of large waves can be calculated and the results obtained from linear and nonlinear simulations are compared.

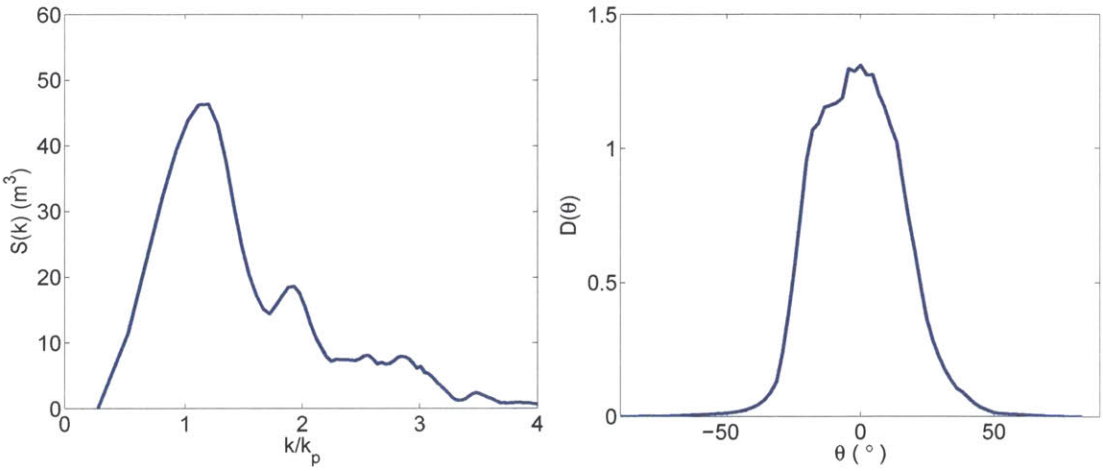

Figure 9-17: (a) One-dimensional omnidirectional spectrum $S(k)$. (b) Integral directional distribution function $D(\theta)$ of the initial spectrum of the reconstructed wavefield.

9.8.2 Skewness and kurtosis

Figure 9-18 shows the evolution of skewness and kurtosis of the forecasted large domain wavefield shown in Figure 9-16(a). The SNOW simulations are applied using M=1 (linear) and M=4 to assess the importance of using nonlinear wave prediction model to capture the nonlinear wave statistics. Linear model gives a value of skewness close to zero, while in nonlinear model (M=4), the value of skewness quickly evolves from its initial value to a quasi-stationary value 0.125. The wavefield has a estimated significant wave height H_s=5.3 m and peak period T_p=11.58 s. Based on the second-order theory, Skew $= 3k_p\sigma \approx 3.12$, which is very close to SNOW prediction. For kurtosis, second-order theory gives an estimation Kur=$3 + 24(k_p\sigma)^2$ ≈3.04. Figure 9-18(b) shows the predictions of kurtosis using linear (M=1) and nonlinear model (M=4). The value of kurtosis obtained from nonlinear model is slightly greater than the second-order prediction.

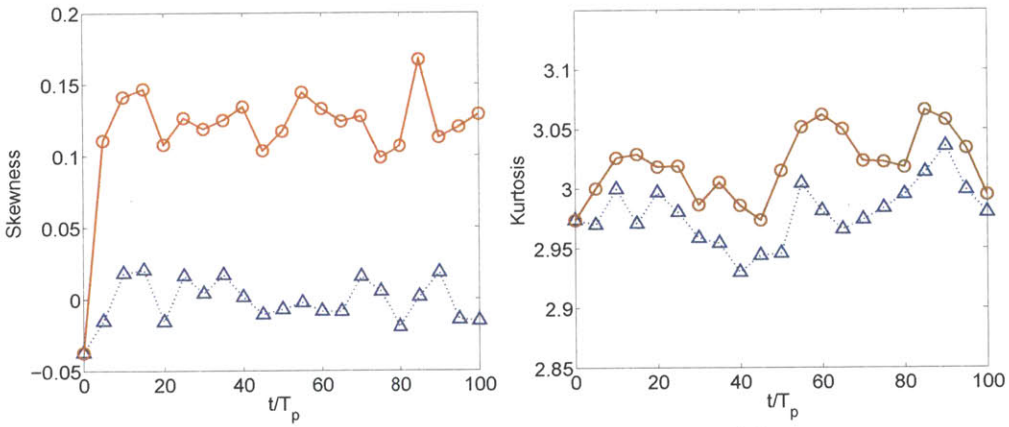

(a) (b)

Figure 9-18: Evolution of (a) skewness and (b) kurtosis for the forecasted large domain wavefield reconstructed using two radar measurements using SNOW simulations with M=1 (△); M=4 (◯).

9.8.3 Exceeding probability of crests

Figure 9-19 shows the exceeding probability of crests obtained from SNOW simulations using $M = 1$ and $M = 4$. For comparison, linear Rayleigh and second-order

predictions are also plotted. We find the crest distribution from $M = 1$ is very close to Rayleigh distribution. Comparing the prediction from $M = 1$ with that from $M = 4$, for crests with small to intermediate crest height $\eta_c \lesssim 2.5$, linear and nonlinear theories give similar predictions. For large crests, linear theory and linear simulations underestimate the probability of large crests significantly comparing the prediction from nonlinear ($M = 4$) simulation. The second-order theory gives a better prediction than linear theory, although it still underestimates the occurrence of large crests relative to SNOW nonlinear simulations.

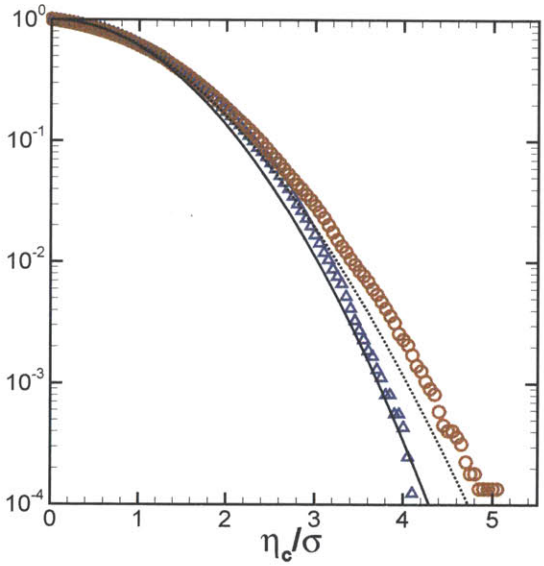

Figure 9-19: Exceeding probability of wave crests at $t = 60T_p$ (T_p=11.58 sec). M =1 (△); M =4 (○). Rayleigh (—), second-order theory (Tayfun, 1980) (- - -).

9.8.4 Occurrence probability of large waves

In Chapter 5, we have shown that it is important to include nonlinearity to predict correctly the occurrence probability of rogue waves. The linear theory underestimates the occurrence of rogue waves significantly, especially for wavefields with narrow-band spectra and small spreading angle. Linear and nonlinear simulations result in not only different large wave statistics but also different phase-resolved information of

large waves, including the occurrence locations and geometric shapes of such large waves. Figure 9-21 shows the crest locations of large waves satisfying $H/H_s \geqslant \alpha$, α=2.0, identified from SNOW forecasted wavefields using $M = 1$ and $M = 4$ during evolution time $0 \leqslant t/T_p \leqslant 100$. We find linear and nonlinear SNOW simulations give different predictions on the location of rogue wave occurrences. The large waves can either be missed or over counted if linear simulations are used. For proper predictions of large (rogue) waves, it is essential to consider high-order nonlinearity. Moreover, large waves are often steep waves, having sharp crest and flat trough. Figure 9-21(a) and 9-21(b) show the rogue wave profiles obtained from SNOW using M=1 and M=4 respectively. The cross profile along x coordinate through the crest point from linear and nonlinear simulations are shown in Figure 9-21(c). The rogue wave profile obtained from nonlinear simulation has longer crest length and shorter wave length than the one obtained from linear simulation. The crest is also sharper and higher in nonlinear simulations.

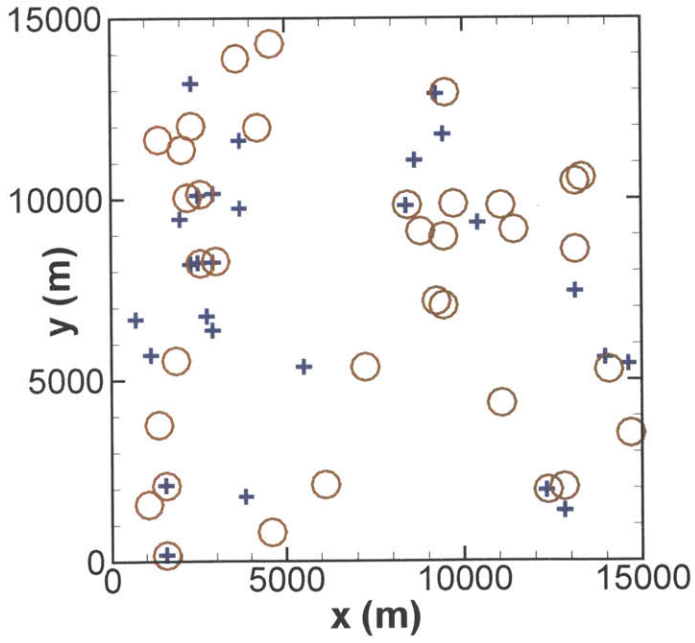

Figure 9-20: Crest locations of the large waves satisfying $H/H_s \geqslant \alpha$ (α=2.0) identified from SNOW forecasted wavefields over evolution time $0 \leqslant t/T_p \leqslant 100$. M =1 (+); M =4 (○).

Figure 9-22 shows evolution of number (P_N) and area (P_A) probabilities of large waves satisfying $H/H_s \geqslant \alpha$, α=1.8. For short time evolutions ($t \lesssim 40T_p$), we find linear and nonlinear SNOW simulations give similar predictions on P_N and P_A. For longer time evolutions ($t \gtrsim 40T_p$), nonlinear simulations in general give a greater prediction (up to 50%) on the occurrence of large waves in comparison with linear simulations. We apply the relationship between P_N, P_A and $\mathrm{Kur}^{\max}$ in §5.7 (Chapter 5), and it gives

$$P_N^{\max}/P_R = 1 + 18.64 \times (\mathrm{Kur}^{\max} - 3) = 2.23, \tag{9.39a}$$

$$P_A^{\max}/P_R = 5.06 + 90.30 \times (\mathrm{Kur}^{\max} - 3) = 11.02, \tag{9.39b}$$

using $\mathrm{Kur}^{\max}$=3.066. These estimations agree reasonably well with what is observed in figure 9-22, although (9.39) are derived for large waves $H/H_s \geqslant$2.0. The empirical relation (5.20) derived in §9.8.1 for large waves with $H/H_s \geqslant \alpha$ (α=2.0), using the estimated modified Benjamin-Feir index, MBFI=0.23, gives:

$$P_N^{\max}/P_R = 1.51 + 9.80 \times \mathrm{MBFI}^2 = 2.03, \tag{9.40a}$$

$$P_A^{\max}/P_R = 8.60 + 43.88 \times \mathrm{MBFI}^2 = 10.92. \tag{9.40b}$$

9.9 Conclusions and discussions

We develop a simulation-based capability of phase-resolved reconstruction and (short-time) forecast of realistic ocean wavefield based on radar inversion surface data. Within this capability, a phase-resolved wavefield is reconstructed and forecasted. The correlation between the radar inversion wave data and forecasted wavefield is close to unity in the theoretical predicable region. A large-scale wavefield is reconstructed and forecasted using multiple radar measurements. We study the nonlinear statistics and occurrence probability of large waves of the forecasted realistic wavefield. The comparison between the linear and nonlinear simulations shows the nonlinearity is

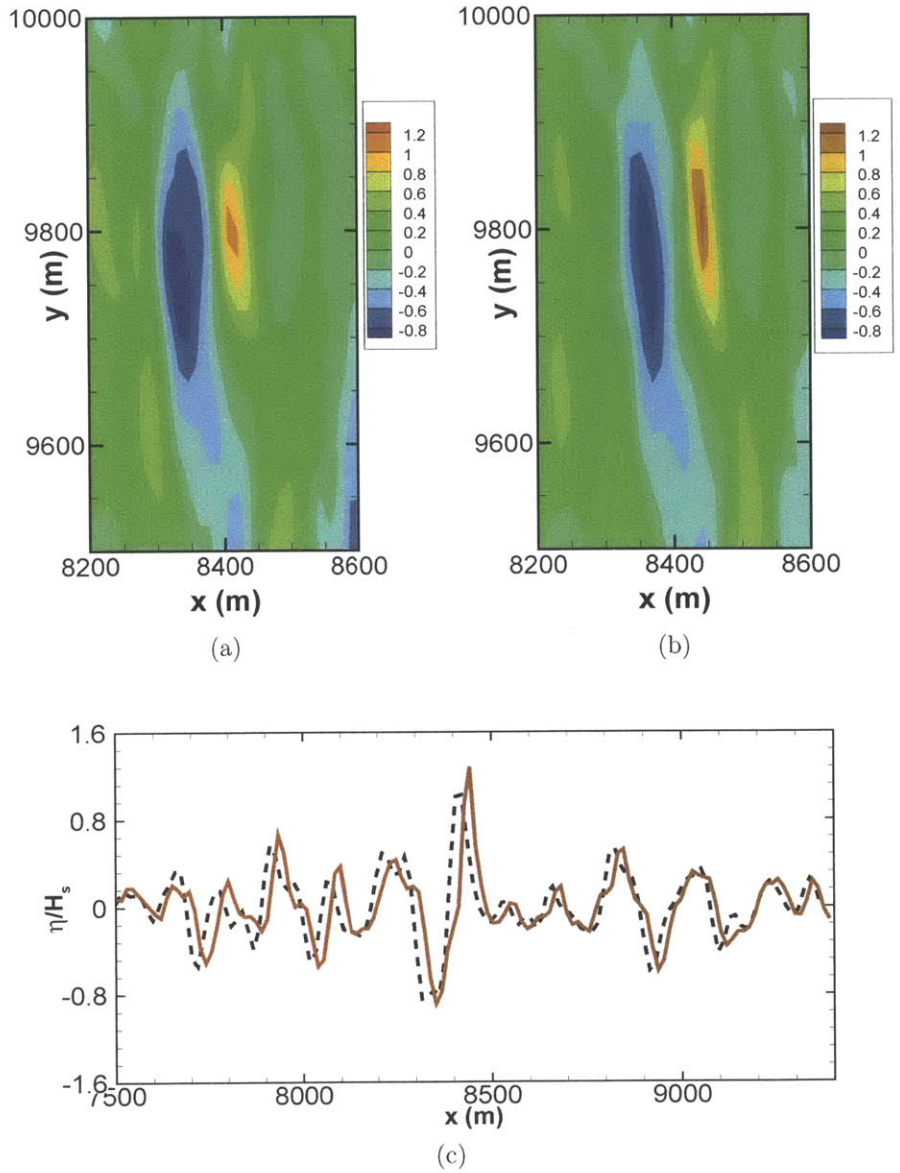

Figure 9-21: Rogue wave profiles obtained from SNOW forecasted wavefields. (a) M=1; (b) M=4. (c) Cross profile along x coordinate. M=1 (- - -); M=4 (—).

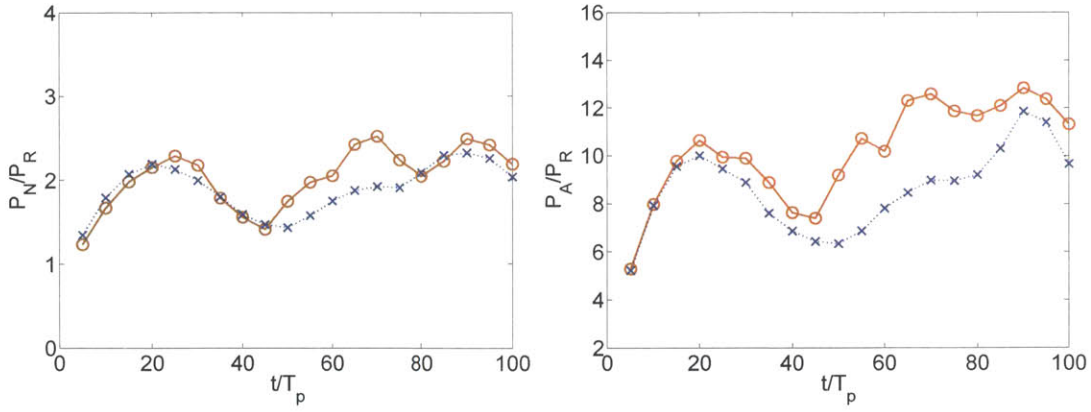

(a) (b)

Figure 9-22: Evolution of (a) number probability P_N/P_R, and (b) area probability of large waves $H/H_s \geqslant \alpha$, α=1.8. Rayleigh distribution $P_R = P(H/H_s \geqslant 1.8)$=$1.53\times10^{-3}$.

essential to obtain accurate predictions of nonlinear wave statistics and rogue wave probability. Moreover, nonlinear simulations are crucial to obtain reliable phase-resolved (large) wave characteristics.

Chapter 10

Conclusions and future work

10.1 Summary of conclusions

We develop and apply a direct large-scale nonlinear phase-resolved wavefield simulation tool, named as SNOW (**s**imulation of **n**onlinear **o**cean **w**avefields), to study the evolutions of directional ocean waves with a primary focus on rogue waves. Commensurate with quartet wave-wave interactions including modulational instability, we consider spatial domains $\mathcal{L} \times \mathcal{L}$ and evolution times $\mathcal{T}$ with $\mathcal{L}/\lambda_p$, $\mathcal{T}/T_p \sim O(\varepsilon^{-2})$, where λ_p and T_p are the wavelength and period of the peak wave and ε is the wavefield steepness, for our simulations.

We elucidate the importance of modulational instability in the evolution of directional wavefields using NLS-type and SNOW simulations. For wavefields with small spreading angles, modulational instability leads to significant spectral broadening and strongly non-Gaussian wave statistics over a relatively short time scale in both SNOW and NLS-type simulations. Over longer time, for initially narrow-banded and narrow-spreading wavefields, SNOW obtains statistically quasi-stationary nonlinear non-Gaussian states and this is not predicted by NLS-type models in which energy spreads continuously to short waves and the wave statistics are close to Gaussian. For wavefields with large spreading angles, the spectral change is much slower and wave statistics are close to Gaussian in both NLS-type and SNOW simulations. Comparing the nonlinear wave statistics from the two simulations with wave basin experiments,

SNOW obtain an overall better comparisons with experiments comparing with NLS-type models.

The relevance of modulational instability to the formation of rogue waves is investigated using SNOW simulations. A large number $O(200)$ of three-dimensional nonlinear SNOW wavefields (MIT-Wave dataset) are generated using initial (JONSWAP) spectra with a broad range of spectral parameters. For small spreading seas, modulational instability leads to strongly non-Gaussian wave statistics and enhanced probability of rogue waves over short time. For longer time, the rogue wave probability reaches a quasi-stationary value still considerably higher than the Rayleigh distribution. For broad-spreading seas, the modulational instability diminishes and the rogue wave probability is close to the Rayleigh theoretical prediction. Comparing with SNOW, NLS-type models generally underpredict the occurrence of rogue waves at longer time. We introduce area probability (P_A) as a better and convergence quantity to measure the likelihood of rogue wave occurrence. We confirm the general correlation between P_N, P_A and kurtosis. For broad spreading wavefield, kurtosis and occurrence probabilities depend on both the Benjamin-Feir index (BFI) and spreading angle. We propose a modified Benjamin-Feir index (MBFI) which accounts for directional spreading for predicting rogue wave occurrence. We show that P_N, P_A and kurtosis are well predicted by MBFI over a broad range of spectral nonlinearity, frequency bandwidth and directional spreading. Based on a large catalogue of rogue waves found from SNOW simulations, the geometric shapes of rogue waves are analyzed using proper orthogonal decomposition (POD). It is found that rogue wave profiles can generally be described by a small number of POD modes.

The influence of other environmental factors, including the finite water depth and bimodal seas, are also examined. In finite water depth, for small spreading angles, we find the occurrence probability of rogue waves as well as wave kurtosis reduces as the water becomes shallow and significant reductions occur for scaled water depth $\mu \lesssim 1.363$. For large spreading angles, the influence of water depth on wave statistics becomes less significant. In bimodal seas, the influence of swell on the wave statistics is not monotonic. The occurrence probability of rogue waves can either increase

or decrease depending on the bimodal spectrum shape. We find the rogue wave probability and wave kurtosis are minimized when the propagation directions of swell and wind sea are orthogonal.

Advanced remote sensing technology allows for high-resolution measurement of surface wave elevation. By assimilating hi-resolution wave measurements into SNOW, we develop a capability of phase-resolved reconstruction and forecasting of wavefield. The usefulness of this capability in the understanding of rogue wave dynamics and in the practical marine operation and safety is demonstrated.

This thesis describes a new-generation wave forecasting model that is capable of providing heretofore unavailable large-scale phase-resolved information on the ocean waves. In this work, we show a first attempt to apply this model to study the evolution of ocean waves and understand the essential generation mechanisms of rogue waves for a broad range of sea states.

10.2 Future work

10.2.1 Wind input

The input from wind forcing is not considered in present study due to the relatively small space-time scale considered. At greater scales, effects from wind (at even moderate speeds) could also play appreciable roles (Abdalla and Cavaleri, 2002; Lavrenov, 1998; Dysthe et al., 2003; Kharif et al., 2007) . In particular, the effect of wind forcing on the occurrence of rogue waves is studied experimentally and numerically in Kharif et al. (2007), in which it is found an inclusion of wind force may lead an longer duration time of the rogue waves. The effects of wind input on the occurrence probability of rogue waves and the characteristics of local wave profile deserve a further study.

10.2.2 Nonlinear wave statistics and rogue waves in bimodal wavefields

In Chapter 7, the effect of a presence of swell on the nonlinear wave statistics and occurrence probability of rogue waves is studied for the bimodal wavefields in which the peak periods of swell and wind sea are relatively close. Different wave dynamics are expected to be involved in the bimodal wavefields with different values of peak period separation (PS). Most existing studies of bimodal wavefields are derived for specified range of PS (Onorato et al., 2006; Gramstad and Trulsen, 2010). To better understand the dynamics in bimodal wavefields, SNOW can be applied to study the evolution of bimodal wavefields described by different bimodal spectral parameters (different values of significant wave height ratio, peak period separation, MBFI of each wave system, etc. .).

Recently, Wright et al. (2001) measured the directional wave spectrum in all quadrants of Hurricane Bonnie in open water using airborne topographic mapper (ATM) and wavefields with bimodal or multi-modal spectra were recorded at many locations in the hurricane. Assimilating ATM measurements into SNOW, bimodal or multi-modal wavefields could be reconstructed and forecasted to understand the nonlinear wave statistics and rogue wave occurrence in a realistic hurricane environment.

10.2.3 Effect of bottom bathymetry

In Chapter 6, the nonlinear wave statistics and occurrence probability of rogue waves are studied for constant water depth. As the water depth decrease, the Benjamin-Feir type modulational instability becomes less important, however, the transverse (three-dimensional) modulational instability caused by five-wave interactions becomes dominant. Moreover, as water depth becomes shallow, trial resonant wave interactions start playing a role. The role of each nonlinear wave process plays in determining ocean wave evolutions and occurrence of rogue waves requires a further investigation. During the wave evolution in the finite water, a generation of long waves is observed. The influence of these long waves on the wave evolution is also not clear.

In this thesis, we only examined the influence of constant water depth and varying bathymetry involving shoaling process is not considered. A recent study by Zeng and Trulsen (2012) show a slowly varying bathymetry could result in different nonlinear wave statistics . The nonlinear wave statistics and occurrence of rogue waves in varying bathymetry deserves a further study.

10.2.4 Effect of weak current

In the region where a strong current is present, rogue waves could form due to wave-current interactions and this has been well studied, for example, in Lavrenov (1998) and Lavrenov and Porubov (2006). For realistic wavefields, a weak current $\sim 0.5\,\mathrm{m/s}$ is usually present. The wave statistics in wave-basin-generated random wavefield traveling obliquely over an ambient current are studied by Toffoli et al. (2011) and an increase occurrence probability of rogue waves is observed. The influence of weak current on the nonlinear wave statistics and occurrence probability of rogue waves needs to be carefully investigated.

10.2.5 Bimodal directional spreading function of short waves

In Chapter 3, we observed the directional spreading functions of short waves develop into an interesting bimodal feature over time $0 \leqslant t/T_p \leqslant 150$. We find this bimodal feature only exists in wavefields with relatively broad spreading angle. Moreover, the dependence of angle width (the angle between the two peaks) on the wavenumber becomes nearly independent of initial spreading angle for wavefields with broad initial spreading angle $\Theta \geqslant 60°$. The wave dynamics responsible for the formation of bimodal directional spreading functions have not been carefully studied. We expect that the bimodal directional spreading function of short waves is formed due to quartet wave (quasi) resonance. Whether this is the case requires a further study.

10.2.6 Long time evolution

In this thesis, we have been focused on the role of Benjamin-Feir type modulational instability in the nonlinear wavefield evolution, therefore, the spatial-temporal scales used in present study is $\mathcal{L}/\lambda_p$, $\mathcal{T}=O(T_p\varepsilon^{-2})$ (Table 1.1). We find, over these scales, for wavefields with small spreading angles, nonlinear wave statistics and occurrence probability of rogue waves reach to a quasi-stationary non-Gaussian state; for wavefields with broad spreading angles, the occurrence probability of rogue waves slowly increases. For deep water waves, the quartet wave interaction is the lowest nonlinear order over which the wave resonant interactions could occur. Although a few attempts have been made (Dyachenko et al., 1995; Kalmykov, 1998; Mori and Yasuda, 2001), the influence of high-order resonance wave-wave interactions on the wavefield evolutions remains unclear.

To study the effect of high-order nonlinearity on the wavefield evolution, according to Table 1.1 evolutions over larger space and longer time are required. For example, to study the influence of quartet and quintet resonant interactions on the wavefield change, a spatial-temporal scale $\mathcal{T}/T_p$, $\mathcal{L}/\lambda_p=O(\varepsilon^{-4})$ should be considered. For these larger scales, some of the approximations made in present study, including ignorable wind input and viscous damping, may become inappropriate and these factors should be addressed in the further study.

Appendix A

Convergence tests of SNOW simulations

A.1 Number of realizations

Due to the large computational effort required for each large-scale SNOW simulation, for most of the wave spectra considered in MIT-Wave, only one realization is performed. The wavefield considered in this thesis normally contains number of waves $N_w = 10^4 \sim 10^5$ at any instant time depending on the spreading angle. For the large number of waves, the moments of surface wave elevation obtained using only one realizations are expected to be reliable. To verify this, we here investigate the variations of nonlinear statistics calculated from different realizations.

Figure A-1 shows the evolution of skewness and kurtosis calculated from different realizations. It is observed that the variational trends of skewness and kurtosis are very similar among different realizations although small variations over different realizations are still noticeable. Figure A-2 shows the ensemble average of average skewness ($\langle$Skewness$\rangle$) and maximum kurtosis $\mathrm{Kur}^{\mathrm{max}}$ over the evolution time, $0 \leqslant t/T_p \leqslant 150$, as a function of number of realizations. We find the variation of $\langle$Skewness$\rangle$ and $\mathrm{Kur}^{\mathrm{max}}$ are less than 5% over the number of realizations.

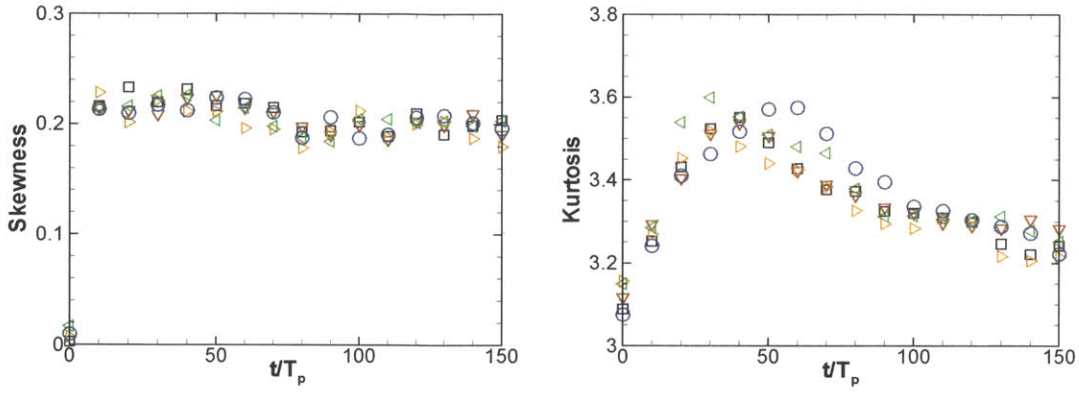

(a) (b)

Figure A-1: Nonlinear wave statistics calculated from different realizations of wavefield H_s=12 m, T_p=13 sec, γ=6, and Θ=20°: (a) skewness; (b) kurtosis.

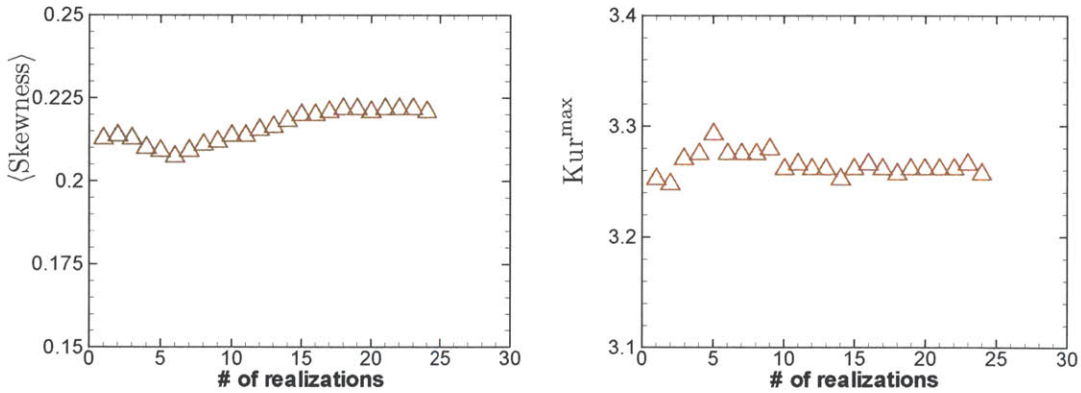

(a) (b)

Figure A-2: (a) Average skewness $\overline{\text{Skew}}$; (b) maximum kurtosis Kur_{max} as functions of number of realizations for wavefield H_s=12 m, T_p=13 sec, γ=6, and Θ=30°.

A.2 Order of wave nonlinearity

In this thesis, our focus is the influence of modulational instability on the wavefield evolutions, therefore order of nonlinearity M=4 is chosen which is sufficient to account for third-order nonlinearity. The nonlinear statistics, skewness and kurtosis, obtained using identical initial wavefields but different orders of nonlinearity (M) in SNOW simulations are shown in Figure A-3. We find using different orders of nonlinearity leads to a variation of skewness less than 5%, and a slightly greater value of skewness is obtained if a greater M is used (Figure A-3(a)). We find the differences between the evolutions of kurtosis using M=3 and M=4 are negligible. A variation around 5% is noticed in maximum value of kurtosis $\mathrm{Kur}^{\mathrm{max}}$ if a value of M greater than 5 is used. We find the quasi-stationary value of kurtosis Kur^{+} keeps invariant for $M \geqslant 3$. These results suggest for the space-time scale used, M =3 is sufficient to include the key nonlinear wave dynamics. The greater $\mathrm{Kur}^{\mathrm{max}}$ obtained at short time could be due to steeper waves are resolved using greater value of M.

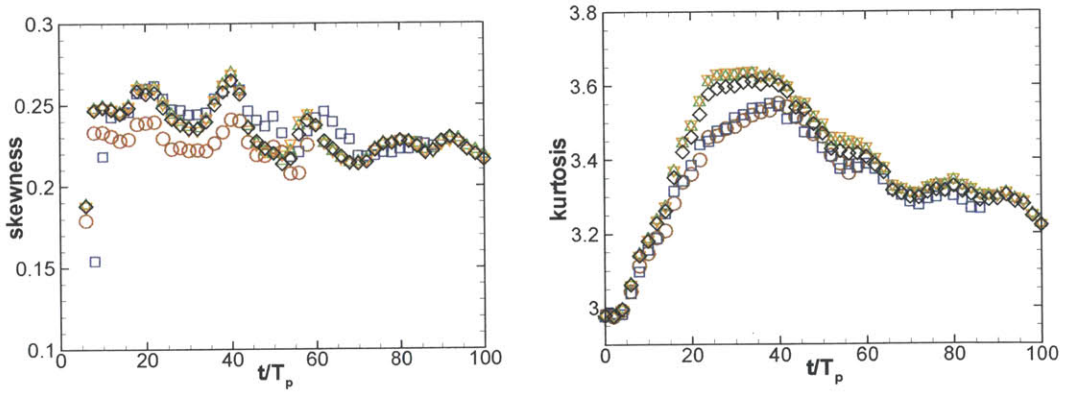

(a) (b)

Figure A-3: Nonlinear statistics calculated from SNOW simulated wavefield H_s=12 m, T_p=13 sec, γ=6, and Θ=20° using different orders of nonlinearity (M). M=3 (○); 4 (□); 5 (△); 6 (▽); 7 (◇). (a) skewness; (b) kurtosis.

A.3 Grid size

To identify the grid size sufficient for the calculations of nonlinear wave statistics, we simulate wavefields using different grid sizes (N_x=N_y=N) while keeping the spatial resolution unchanged. In this case, varying the grid size is equivalent to varying number of wave modes and wavefield domain size. Figure A-4 shows the mean skewness $\langle \text{Skewness} \rangle$ and maximum kurtosis Kur^{max} as functions of grid size. Values of $\langle \text{Skewness} \rangle$ and Kur^{max} oscillate significantly for grid size $N \leqslant 1024$. The dependence of nonlinear statistics on grid size becomes much less significant for grid size $N > 1024$. In this thesis, most of simulations are performed using N=4096, which is sufficient to obtain reliable nonlinear wave statistics. To obtain statistics of rare events like large crests and rogue waves, a larger grid size or more realizations may be needed.

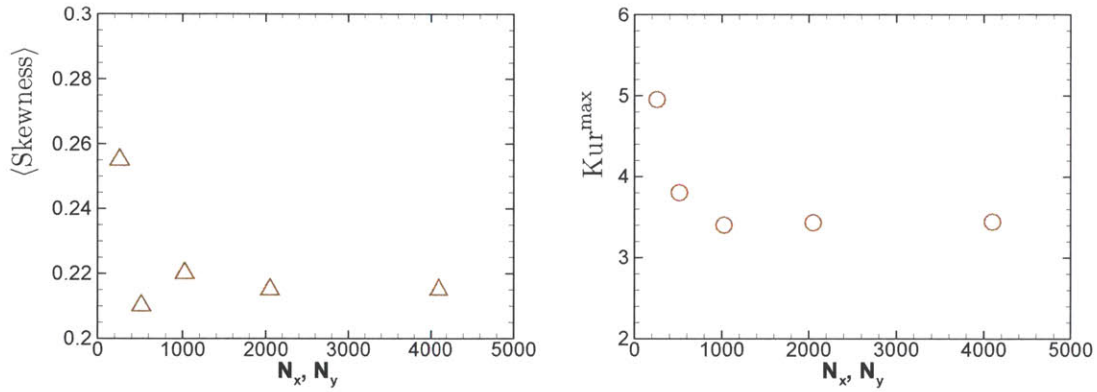

Figure A-4: (a) average skewness; (b) maximum kurtosis over time $0 \leqslant t/T_p \leqslant 100$ as functions of grid number N_x, N_y.

Appendix B

On the calculation of occurrence probabilities of rogue waves

B.1 Identification algorithm of rogue waves

In short-crested wavefields, the precise definition of the extent of the rogue wave event (within which $H \geq \alpha H_s$ obtains) is not unique, the rogue wave events obtained using a different way may be slightly different. In the procedures to identify rogue waves (Chapter 5 §5.4), a rectangular region $\mathcal{R}$ centered on $\mathbf{x}_c$ (5.4) is used to define the relevant trough $\mathbf{x}_t$ and thus the relevant crest-to-trough wave height H of the wave. One rogue wave is identified if the crest-to-trough wave height satisfies $H/H_s \geqslant \alpha$, α=2. To assess the effect of using $\mathcal{R}$ of a different size on the resulting rogue wave probability, we calculate P_N and P_A using $\mathcal{R}$ of three different sizes:

$$\mathcal{R}_1 = \{(x,y)||x-x_c| \leqslant \lambda_p, |y-y_c| \leqslant C_y\}, \tag{B.1a}$$

$$\mathcal{R}_2 = \{(x,y)||x-x_c| \leqslant \lambda_p, |y-y_c| \leqslant C_y/2\}, \tag{B.1b}$$

$$\mathcal{R}_3 = \{(x,y)||x-x_c| \leqslant \lambda_p, |y-y_c| \leqslant C_y/4\}, \tag{B.1c}$$

where $\mathcal{R}_1$ is the standard $\mathcal{R}$ used in this thesis and $\mathcal{R}_2$, $\mathcal{R}_3$ are modified search regions with successively smaller range in the y direction.

Figure B-1 shows P_N and P_A calculated using different sizes of $\mathcal{R}$ specified in (B.1). We find that the evolutions of P_N and P_A obtained using different $\mathcal{R}$ have very similar variation trend. Moreover, although the size of $\mathcal{R}$ is increased four times in the y direction, we find both P_N and P_A decrease only slightly. Therefore, using different $\mathcal{R}$ in the rogue wave identification algorithm, the general conclusions are expected to be similar. Moreover, these results also support the assumption that large (rogue) waves are usually isolated from ambient small waves.

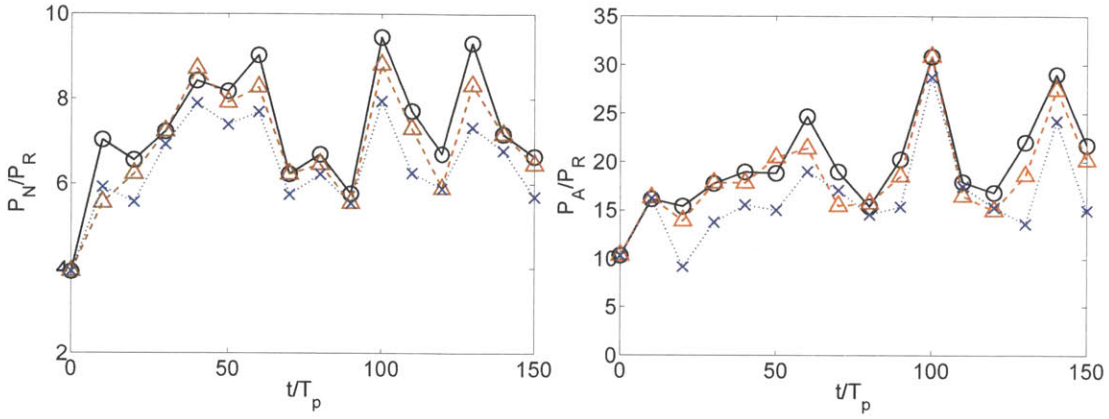

(a) (b)

Figure B-1: Evolution of P_N/P_R using searching range $\mathcal{R}$ of different sizes for JONSWAP wavefield H_s=12 m, T_p=13 s, γ=5, Θ=30°. $\mathcal{R}_1$ (◯), $\mathcal{R}_2$ (△), $\mathcal{R}_3$ (×).

B.2 Threshold value of large waves

The calculations and discussions on rogue waves in this thesis are based on the large waves satisfying $H/H_s \geqslant \alpha$, α=2.0. To assess how sensitive the conclusions are to different (but still relatively large) threshold values α, we calculate P_N and P_A using different values of α.

The evolutions of P_N and P_A using different values of α and $\mathcal{R}$ are shown in Figure B-2 and Figure B-3. We find the magnitudes of P_N/P_R and P_A/P_R increases as α increases. This suggests that the underestimation of Rayleigh distribution becomes more serious for greater values of α. Comparing the variation trend of P_N and P_A using different size of $\mathcal{R}$, similar features are observed for different values of α.

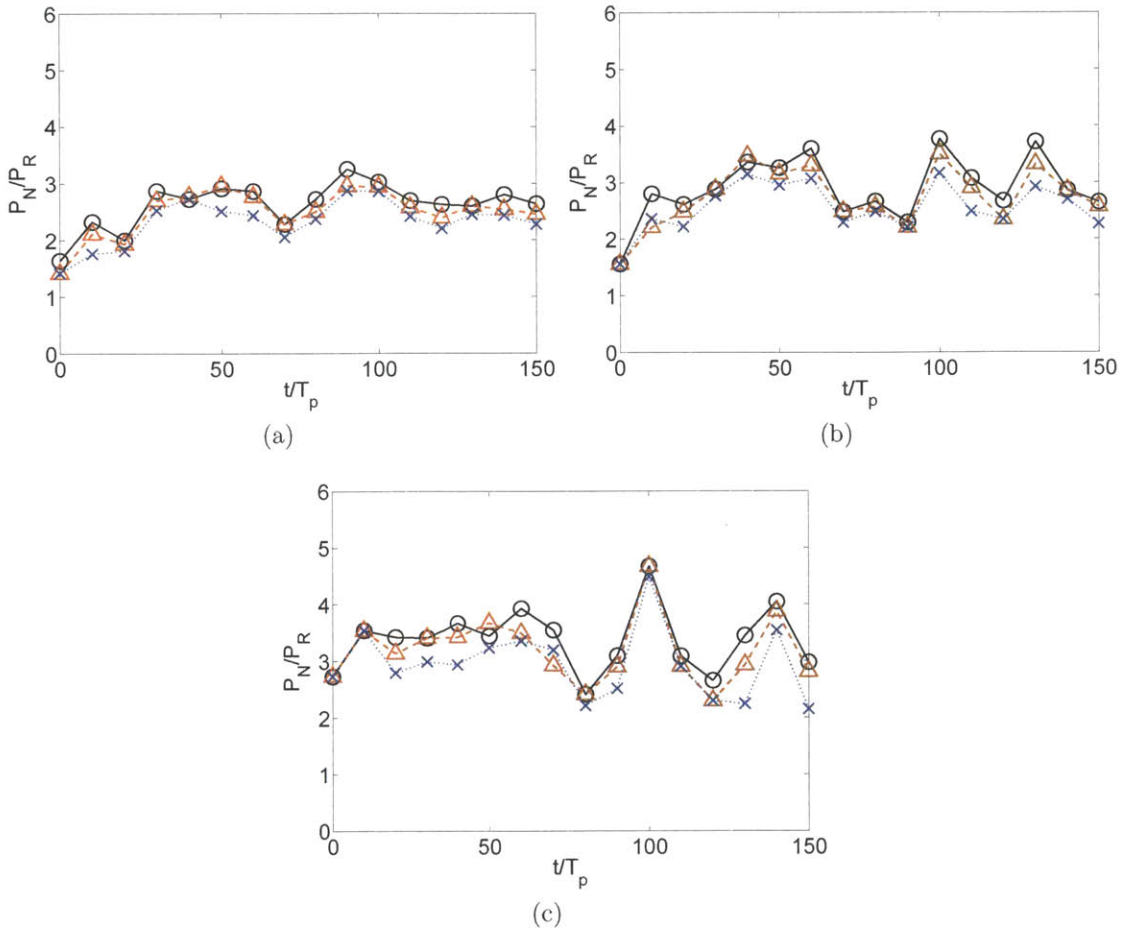

(a) (b) (c)

Figure B-2: Evolution of P_N/P_R for large waves with $H/H_s \geqslant \alpha$ for JONSWAP wavefield H_s=12 m, T_p=13 s, γ=5, Θ=30°. (a) α=1.8, (b) α=1.9, (c) α=2.0. $\mathcal{R}_1$ (◯), $\mathcal{R}_2$ (△), $\mathcal{R}_3$ (×).

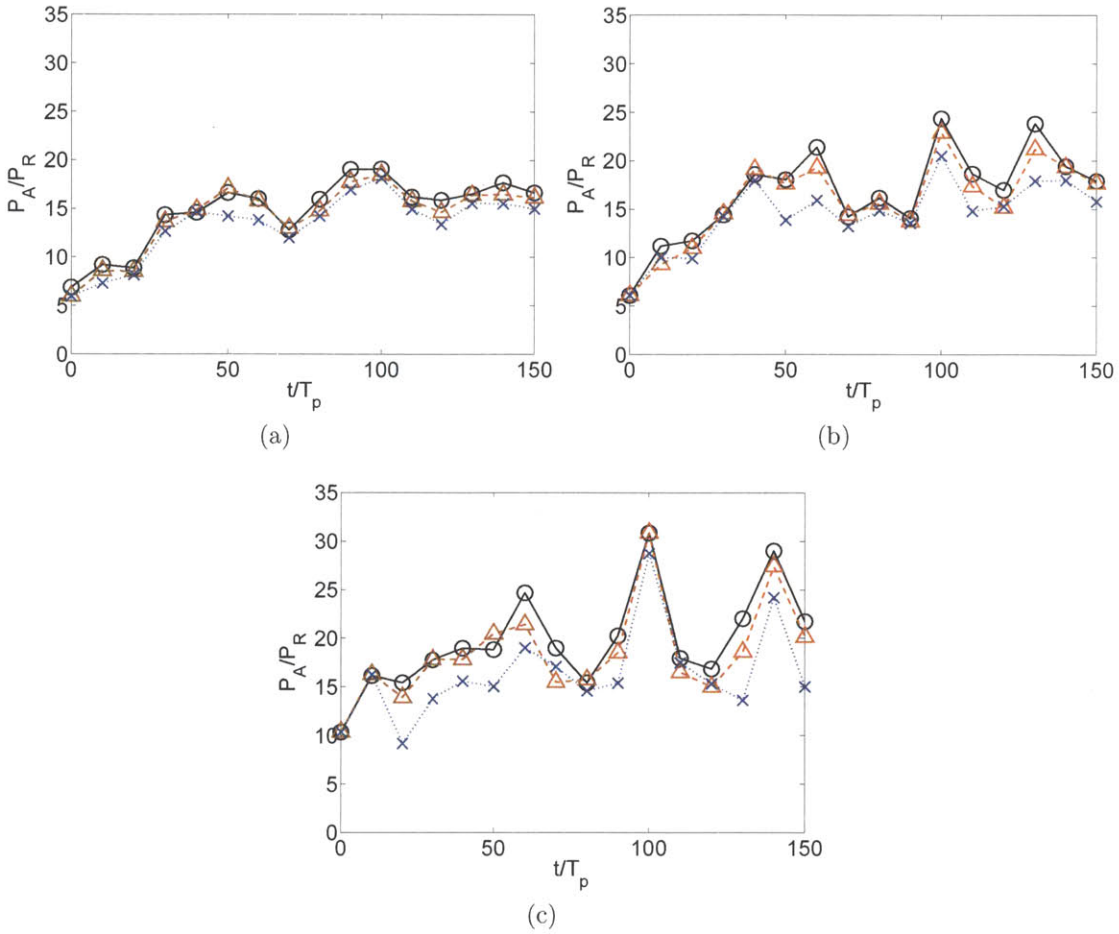

Figure B-3: Evolution of P_N/P_R for large waves with $H/H_s \geqslant \alpha$ for JONSWAP wavefield H_s=12 m, T_p=13 s, γ=5, Θ=30°. (a) α=1.8, (b) α=1.9, (c) α=2.0. $\mathcal{R}_1$ (◯), $\mathcal{R}_2$ △, $\mathcal{R}_3$ ×.

Bibliography

S. Abdalla and L. Cavaleri. Effect of wind variability and variable air density on wave modeling. *J. Geo. Res.*, 107(C7):3080, 2002.

I. E. Alber. The effects of randomness on the stability of two-dimensional surface wavetrains. *Proc. R. Soc. Lond. A.*, 363:525–546, 1978.

F. Arena and C. G. Soares. Nonlinear crest, trough, and wave height distributions in sea states with double-peaked spectra. *J. Offshore Mech. Arctic Eng.*, 131:041105, 2009.

M. L. Banner and W. L. Peirson. Wave breaking onset and strength for two-dimensional deep-water wave groups. *J. Fluid Mech.*, 585(1):93–115, 2007.

T. P. Barnett and J. C. Wilkerson. On the generation of ocean wind waves as inferred from airborne radar measurements of fetch-limited spectra. *J. Mar. Res.*, 25(3): 292–328, 1967.

W. J. D Bateman, C. Swan, and P. H. Taylor. On the efficient numerical simulation of directionally spread surface water waves. *J. Comput. Phys.*, 174(1):277–305, 2001.

T. B. Benjamin and J. E. Feir. The disintegration of wave trains in deep water. Part 1. Theory. *J. Fluid Mech.*, 27(3):417–430, 1967.

P. Boccotti. Some new results on statistical properties of wind waves. *Appl. Ocean Res.*, 5(3):134–140, 1983.

N. Booij, R. C. Ris, and L. H. Holthuijsen. A third-generation wave model for coastal regions. 1. model description and validation. *J. Geophys. Res.*, 104(C4):7649–7666, 1999.

E. A. Caponi, P. G. Saffman, and H. C. Yuen. Instability and confined chaos in a nonlinear dispersive wave system. *Phys. Fluids*, 25:2159, 1982.

D. Chalikov. Freak waves: Their occurrence and probability. *Phys. Fluids*, 21:076602, 2009.

A. D. D. Craik. The origins of water wave theory. *Annu. Rev. Fluid Mech.*, 36:1–28, 2004.

A. D. D. Craik. George gabriel stokes on water wave theory. *Annu. Rev. Fluid Mech.*, 37:23–42, 2005.

O. Darrigol. The spirited horse, the engineer, and the mathematician: Water waves in nineteenth-century hydrodynamics. *Arch. Hist. Exact. Sci.*, 58(1):21–95, 2003.

F. W. Dobson, S. D. Smith, and R. J. Anderson. Measuring the relationship between wind stress and sea state in the open ocean in the presence of swell. *Atmos.-Ocean*, 32(1):237–256, 1994.

D. Dommermuth. The initialization of nonlinear waves using an adjustment scheme. *Wave Motion*, 32(4):307–317, 2000.

D. Dommermuth and D. K. P. Yue. A higher-order spectral method for the study of nonlinear gravity waves. *J. Fluid Mech.*, 184:267–288, 1987. ISSN 0022-1120.

D. Dommermuth and D. K. P. Yue. The nonlinear three-dimensional waves generated by a moving surface disturbance. In *Proc. of 17th Symp. on naval hydro.*, Hague, Netherlands, 1988.

M. A Donelan, J. Hamilton, W. H. Hui, MA Donelan, J. Hamilton, and W. H. Hui. Directional spectra of wind-generated waves. *Phil. Trans. R. Soc. Lond. A*, 315 (1534):509–562, 1985.

M. A. Donelan, W. M. Drennan, and K. B. Katsaros. The air-sea momentum flux in conditions of wind sea and swell. *J. Phys. Oceano.*, 27(10):2087–2099, 1997.

J. H. Duncan. An experimental investigation of breaking waves produced by a towed hydrofoil. *Proc. R. Soc. London*, 377(1770):331–348, 1981.

A. I. Dyachenko, Y. V. Lvov, and V. E. Zakharov. Five-wave interaction on the surface of deep fluid. *Phys. D Non. Pheno.*, 87(1):233–261, 1995.

K. B. Dysthe. Note on a modification to the nonlinear schrdinger equation for application to deep water waves. *Proc. R. Soc. Lond. A*, 369(1736):105–114, 1979.

K. B. Dysthe, K. Trulsen, H. E. Krogstad, and H. Socquet-Juglard. Evolution of a narrow-band spectrum of random surface gravity waves. *J. Fluid Mech.*, 478:1–10, 2003.

K. B. Dysthe, H. E. Krogstad, and P. Muller. Oceanic rogue waves. *Annu. Rev. Fluid Mech.*, 40:287–310, 2008.

ESA. Ship-sinking monster waves revealed by ESA satellites. European Space Agency., July 2004. URL `http://www.esa.int/esaCP/SEMOKQL26WD_index_0.html`.

K. C. Ewans. Observations of the directional spectrum of fetch-limited waves. *J. Phys. Oceanogr.*, 28(3):495–512, 1998.

G. Z. Forristall. Wave crest distributions : Observations and second-order theory. *J. Phys. Oceanogr.*, 30(8):1931–1943, 2000.

G. Z. Forristall. Understanding rogue waves: Are new physics really necessary? In *Rogue Waves: Proc. 14th Aha Hulikoa Hawaii. Winter Workshop*, pages 29–35, Honolulu, HI, 2005.

J. R. Gemmrich and D. M. Farmer. Observations of the scale and occurrence of breaking surface waves. *J. Phys. Oceanogr.*, 29(10):2595–2606, 1999.

Y. GODA. A comparative review on the functional forms of directional wave spectrum. *Coast. Eng. J.*, 41(01):1–20, 1999.

O. Gramstad and K. Trulsen. Influence of crest and group length on the occurrence of freak waves. *J. Fluid Mech.*, 582:463–472, 2007.

O. Gramstad and K. Trulsen. Can swell increase the number of freak waves in a wind sea? *J. Fluid Mech.*, 650:57–79, 2010.

The WAMDI Group. The wam model-a third generation ocean wave prediction model. *J. Phys. Oceanogr.*, 18(12):1775–1810, 1988.

C. Guedes Soares. On the occurence of double peaked wave spectra. *J. Ocean Eng.*, 18(1-3):167–171, 1991.

J. L. Hammack and D. M. Henderson. Resonant interactions among surface water waves. *Ann. Rev. Fluid Mech.*, 25(1):55–97, 1993.

K Hasselmann. On the non-linear energy transfer in a gravity-wave spectrum part 1. general theory. *J. Fluid Mech.*, 12(4):481–500, 1962.

K. Hasselmann. Feynman diagrams and interaction rules of wave-wave scattering processes. *Rev. Geophys.*, 4(1):1–32, 1966.

K. Hasselmann. On the spectral dissipation of ocean waves due to white capping. *Bound.-Layer Meteor.*, 6(1):107–127, 1974.

K. Hasselmann, T. P. Barnett, E. Bouws, H. Carlson, D. E. Cartwright, K. Enke, J. A. Ewing, H. Gienapp, D. E. Hasselmann, P. Kruseman, et al. Measurements of wind-wave growth and swell decay during the joint north sea wave project (jonswap). *D. Hydrogr. Z.*, 8(12), 1973.

J. B. Herbich. *Handbook of coastal and ocean engineering. Wave Phenomena and Coastal Structure. Chapter 4, Random Waves and Spectra (by Y. Goda), vol. 1.* Gulf Publishing Company, Houston, TX, 1990.

K. Herterich and K. Hasselmann. A similarity relation for the nonlinear energy transfer in a fhite-depth gravity-wave spectrum. *J. Fluid Mech.*, 97(part 1):215–224, 1980.

D. S. A. Hughes. Directional wave spectra using cosine-squared and cosine 2s spreading functions. *Coastal Engineering Technical Note. Coastal Engineering Research Center, Coastal and hydraulics Laboratary*, 1985.

P. A. Hwang, D. W. Wang, E. J. Walsh, W. B. Krabill, and R. N. Swift. Airborne measurements of the wavenumber spectra of ocean surface waves. Part II: Directional distribution. *J. Phys. Oceanogr.*, 30(11):2768–2787, 2000.

P. A. E. M. Janssen. Nonlinear four-wave interactions and freak waves. *J. Phys. Oceanogr.*, 33(4):863–884, 2003.

P. A. E. M. Janssen. Progress in ocean wave forecasting. *J. Comp. Phys.*, 227(7): 3572–3594, 2008.

P. A. E. M. Janssen and W. Alpers. Why sar wave mode data of ers and envisat are inadequate for giving the probability of occurrence of freak waves. In *Proceedings of the SEASAR 2006 workshop. ESA/ESRIN*, 2006.

P. A. E. M. Janssen and M. Onorato. The intermediate water depth limit of the zakharov equation and consequences for wave prediction. *J. Phys. Oceanogr.*, 37 (10):2389–2400, 2007.

V. A. Kalmykov. Waves by resonance five wave-wave interactions. In *Nonlinear Waves and Weak Turbulence*, page 83. American Mathematical Society Translations Series 2, 1998.

C. Kharif and E. Pelinovsky. Physical mechanisms of the rogue wave phenomenon. *Eur. J. Mech. B/Fluids*, 22(6):603–634, 2003.

C. Kharif, J. P. Giovanangeli, J. Touboul, L. Grare, and E. Pelinovsky. Influence of wind on extreme wave events: experimental and numerical approaches. *J. Fluid Mech.*, 594:209–247, 2007.

C. Kharif, E. Pelinovsky, and A. Slunyaev. *Rogue waves in the ocean.* Springer, 2009.

C. Kharif, R. A. Kraenkel, M. A. Manna, and R. Thomas. The modulational instability in deep water under the action of wind and dissipation. *J. Fluid Mech.*, 664 (1):138–149, 2010.

B. Kinsman. *Wind waves: their generation and propagation on the ocean surface.* Courier Dover Publications, 1965.

J. T. Kirby and T Chen. Surface waves on vertically sheared flows: approximate dispersion relations. *J. Geo. Res.*, 94:1013–1027, 1989.

S. A. Kitaigorodskii, V. P. Krasitskii, and M. M. Zaslavskii. On phillips' theory of equilibrium range in the spectra of wind-generated gravity waves. *J. Phys. Oceanogr*, 5(7):410–420, 1975.

G. J. Komen, S. Hasselmann, and K. Hasselmann. On the existence of a fully developed wind-sea spectrum. *J. Phys. Oceanogr.*, 14(8):1271–1285, 1984.

G. J. Komen, L. Cavaleri, M. Donelan, K. Hasselmann, K. Hasselmann, and P. A. E. M. Janssen. *Dynamics and Modelling of Ocean Waves.* Cambridge University Press, 1994.

P. K. Kundu and I. M. Cohen. *Fluid Mechanics.* Elsevier, Boston, 2004.

B. M. Lake, H. C. Yuen, H. Rungaldier, and W. E. Ferguson. Nonlinear deep-water waves: theory and experiment. part 2. evolution of a continuous wave train. *J. Fluid Mech*, 83(1):49–74, 1977.

I. V. Lavrenov. The wave energy concentration at the Agulhas current off South Africa. *Natural Hazards*, 17(2):117–127, 1998.

I. V. Lavrenov and A. V. Porubov. Three reasons for freak wave generation in the non-uniform current. *Eur. J. Mech. B Fluids*, 25(5):574–585, 2006. ISSN 0997-7546.

G. Lawton. Monsters of the deep (The perfect wave). *New Scientist*, 170(2297):28–32, 2001.

S. Lehner, J. Schulz-Stellenfleth, and A. Niedermeier. Detection of extreme waves using synthetic aperture radar images. In *Geoscience and Remote Sensing Symposium, 2002. IGARSS '02. 2002 IEEE International*, volume 3, pages 1893 –1895. IEEE, 2002.

G. Lindgren. Some properties of a normal process near a local maximum. *Ann. Math. Statist.*, 41(6):1870–1883, 1970.

Y. Liu and D. K. P. Yue. On generalized Bragg scattering of surface waves by bottom ripples. *J. Fluid Mech.*, 356:297–326, 1998.

Y. Liu and D. K. P. Yue. Large scale phase-resolved simulations of ocean surface waves. In *oceanography in 2025: Proceedings of a workshop*, 2009.

E. Lo and C. C. Mei. A numerical study of water-wave modulation based on a higher-order nonlinear schrödinger equation. *J. Fluid Mech.*, 150:395–416, 1985.

M. S. Longuet-Higgins. On the statistical distribution of the heights of sea waves. *J. Mar. Res.*, 11(3):245–266, 1952.

M. S. Longuet-Higgins. The effect of non-linearities on statistical distribution in the theory of sea waves. *J. Fluid Mech.*, 17:459–480, 1963.

M. S. Longuet-Higgins. On the joint distribution of the periods and amplitudes of sea waves. *J. Geo. Res.*, 80(18):2688–2694, 1975.

D. Masson. On the nonlinear coupling between swell and wind waves. *J. Phys. Oceanogr.*, 23(6):1249–1258, 1993.

J. W. McLean. Instabilities of finite-amplitude gravity waves on water of finite depth. *J. Fluid Mech.*, 114:331–341, 1982.

J. W. McLean, Y. C. Ma, D. U. Martin, P. G. Saffman, and H. C. Yuen. Three-dimensional instability of finite-amplitude water waves. *Phys. Rev. Lett.*, 46(13): 817–820, 1981.

C. C. Mei, M. Stiassnie, and D. K. P. Yue. *Theory and applications of ocean surface waves. Part 1: linear aspects*, volume 23. World Scientific, 2005a.

C. C. Mei, M. Stiassnie, and D. K. P. Yue. *Theory and applications of ocean surface waves. Part 2: nonlinear aspects*, volume 23. World Scientific, 2005b.

J. W. Miles. On the generation of surface waves by shear flows. *J. Fluid Mech.*, 3: 185–204, 1957.

H. Mitsuyasu. On the growth of the spectrum of wind-generated waves. 1. *Rep. Res. Inst. Appl. Mech., Kyushu Univ.*, 16:459–482, 1968.

H. Mitsuyasu. On the growth of the spectrum of wind-generated waves. 2. *Rep. Res. Inst. Appl. Mech., Kyushu Univ.*, 17:235–243, 1969.

H. Mitsuyasu. A historical note on the study of ocean surface waves. *J. Oceano.*, 58 (1):109–120, 2002.

H. Mitsuyasu and Y. Yoshida. The effect of swell on the growth of wind waves. *Elsevier oceanography series*, 54:381–392, 1991.

F. Moreau. Ship-sinking monster waves revealed by esa satellites, 2004. URL `http://www.ifremer.fr/web-com/stw2004/rw/fullpapers/glorious.pdf`. Translated by Olagnon M. and Chase G. A.

N. Mori and P. A. E. M. Janssen. On kurtosis and occurrence probability of freak waves. *J. Phys. Oceanogr.*, 36(7):1471–1483, 2006.

N. Mori and T. Yasuda. E?ects of high-order nonlinear interactions on gravity waves. In *Proc. Rogue Waves 2000 (ed. M. Olagnon and G. Athanassoulis)*, 2001.

N. Mori and T. Yasuda. A weakly non-gaussian model of wave height distribution for random wave train. *Ocean Eng.*, 29(10):1219–1231, 2002a.

N. Mori and T. Yasuda. Effects of high-order nonlinear interactions on unidirectional wave trains. *Ocean Eng.*, 29(10):1233–1245, 2002b.

N. Mori, P. A. E. M. Janssen, and M. Onorato. Freak wave prediction from spectra. In *10th Int. workshop on wave hindcasting and forecasting coastal hazard symposium*, 2007.

N. Mori, M. Onorato, and P. A. E. M. Janssen. On the estimation of the kurtosis in directional sea states for freak wave forecasting. *J. Phys. Oceanogr.*, 41(8): 1484–1497, 2011.

J. C. Nieto Borge, G.R.Í. RodrÍguez, K. Hessner, and P. I. González. Inversion of marine radar images for surface wave analysis. *J. Atmos. Oceanic Technol.*, 21(8): 1291–1300, 2004.

M. K. Ochi. *Ocean waves: the stochastic approach*, volume 6. Cambridge University Press, 2005.

M. Onorato, A. R. Osborne, M. Serio, and S. Bertone. Freak waves in random oceanic sea states. *Phys. Rev. Lett.*, 86(25):5831–5834, 2001.

M. Onorato, A. R. Osborne, M. Serio, L. Cavaleri, C. Brandini, and C. T. Stansberg. Observation of strongly non-gaussian statistics for random sea surface gravity waves in wave flume experiments. *Phys. Rev. E*, 70(6):67302–67305, 2004.

M. Onorato, A. R. Osborne, and M. Serio. On deviations from gaussian statistics for surface gravity waves. In *14th Aha Hulikoa Hawaiian Winter Workshop on Rouge Waves.*, 2005.

M. Onorato, A. R. Osborne, and M. Serio. Modulational instability in crossing sea states: A possible mechanism for the formation of freak waves. *Phys. Rev. Lett.*, 96(1):14503, 2006.

M. Onorato, L. Cavaleri, O. Gramstad, P. A. E. M. Janssen, J. Monbaliu, A. R. Osborne, M. Serio, C. T. Stansberg, A. Toffoli, and Trulsen K. Statistical properties of mechanically generated surface gravity waves: a laboratory experiment in a 3d wave basin. In *Rogue Waves 2008*, Brest France, October 2008.

M. Onorato, L. Cavaleri, S. Fouques, O. Gramstad, P. A. E. M. Janssen, J. Monbaliu, A. R. Osborne, C. Pakozdi, M Serio, C. T. Stansberg, A. Toffoli, and K. Trulsen. Statistical properties of mechanically generated surface gravity waves: a laboratory experiment in a three-dimensional wave basin. *J. Fluid Mech.*, 627:235–257, 2009.

M. H. Patel. *Dynamics of offshore structures.* Stoneham, MA (USA); Butterworth Publishers, 1989.

E. Pelinovsky and A. Sergeeva Kokorina. Numerical modeling of the kdv random wave field. *Eur. J. Mech. B Fluid.*, 25(4):425–434, 2006.

O. M. Phillips. On the generation of waves by turbulent wind. *J. Fluid Mech.*, 2(5): 417–445, 1957.

O. M. Phillips. On the dynamics of unsteady gravity waves of finite amplitude part 1. the elementary interactions. *J. Fluid Mech.*, 9:193–217, 1960.

O. M. Phillips. Spectral and statistical properties of the equilibrium range in wind-generated gravity waves. *J. Fluid Mech.*, 156(1):505–531, 1985.

W. J. Pierson, G. Neumann, and R. W. James. Practical methods for observing and forecasting ocean waves by means of wave spectra and statistics. In *Us Navy Hydorgraphic Office, Washington, DC, No.603 284p*, 1955.

U. F. Pinho, P. C. Liu, and C. E. P. Ribeira. Freak waves at campos basin, brazil. *Geofizika*, 21:53–66, 2004.

V. I. Piterbarg. *Asymptotic Methods in the Theory of Gaussian Processes and Fields.* Translations of Mathematical Monographs. American Mathematical Soc., 1996. ISBN 9780821804230.

R. J. Rapp and W. K. Melville. Laboratory measurements of deep-water breaking waves. *Phil. Trans. R. Soc. Lond. A*, 331(1622):735–800, 1990.

R. C. Ris, L. H. Holthuijsen, and N. Booij. A third-generation wave model for coastal regions: 2. verification. *J. Geophys. Res.*, 104(C4):7667–7681, 1999.

G. Rodriguez, C. G. Soares, M. Pacheco, and E. Prez-Martell. Wave height distribution in mixed sea states. *J. Offshore Mech. Arctic Eng.*, 124(1):34–40, 2002.

W. Rosenthal and S. Lehner. Results of the maxwave project. In *Proceedings of the 14 th'Aha Huliko'a Hawaiian Winter Workshop*, pages 1–7, 2005.

W. Rosenthal, S. Lehner, H. Dankert, H. Guenther, K. Hessner, J. Horstmann, A. Niedermeier, J. C. Nieto-Borge, J. Schulz-Stellenfleth, and K. Reichert. Detection of extreme single waves and wave statistics. In *Proceedings of MAXWAVE Final Meeting*, 2003.

V. P. Ruban. Enhanced rise of rogue waves in slant wave groups. *JETP Lett.*, 94(3): 177–181, 2011.

H. Segur, D. Henderson, J. Carter, J. Hammack, C-M. Li, D. Pheiff, and K. Socha. Stabilizing the Benjamin-Feir instability. *J. Fluid Mech.*, 539:229–271, 2005. ISSN 0022-1120.

H. Segur, DM Henderson, and JL Hammack. Can the benjamin-feir instability spawn a rogue wave. In *Proceedings of the Aha Hulikoía Hawaiian Winter Workshop, University of Hawaii, Retrieved August*, volume 5, 2008.

J. Skourup, N. E. O. Hansen, and K. K. Andreasen. Non-gaussian extreme waves in the central north sea. *J. Offshore Mech. Arct. Eng.*, 119(3):146–150, 1997.

A. Slunyaev, I. Didenkulova, and E. Pelinovsky. Rogue waters. *Contemp. Phys.*, 52 (6):571–590, 2011.

A. V. Slunyaev and A. V. Sergeeva. Stochastic simulation of unidirectional intense waves in deep water applied to rogue waves. *JETP Lett.*, 94(10):779–786, 2011.

F. E. Snodgrass, G. W. Groves, K. F. Hasselmann, G. R. Miller, W. H. Munk, and W. H. Powers. Propagation of ocean swell across the pacific. *Phil. Trans. Royal Soc. London. Series A, Math. Phys. Sci.*, pages 431–497, 1966.

R. L. Snyder and C. S. Cox. A field study of the wind generation of ocean waves. *J. Mar. Res.*, 24:141–178, 1966.

R. L. Snyder, F. W. Dobson, J. A. Elliott, and R. B. Long. Array measurements of atmospheric pressure fluctuations above surface gravity waves. *J. Fluid Mech.*, 102:1–59, 1981.

H. Socquet-Juglard, K. Dysthe, K. Trulsen, H. E. Krogstad, and J. Liu. Probability distributions of surface gravity waves during spectral changes. *J. Fluid Mech.*, 542: 195–216, 2005.

J. B. Song, Y. J. Hou, Y. J. He, Y. H. Wu, and B. S. Yin. Statistical distribution of wave-surface elevation for second-order random directional ocean waves in finite water depth. *Coastal eng.*, 46(1):51–60, 2002.

P. Stansell. Distributions of extreme wave, crest and trough heights measured in the north sea. *Ocean Eng.*, 32(8-9):1015–1036, 2005.

M. Stiassnie and L. Shemer. On modifications of the zakharov equation for surface gravity waves. *J. Fluid Mech.*, 143:47–67, 1984.

M. Stiassnie and L. Shemer. Energy computations for evolution of class I and II instabilities of stokes waves. *J. Fluid Mech.*, 174(1):299–312, 1987.

G. G. Stokes. On the theory of oscillatory waves. *Trans. Cambridge Philos. Soc.*, 8: 441–473, 1847.

M. Y. Su. Evolution of groups of gravity waves with moderate to high steepness. *Phys. Fluids*, 25(12):2167 – 2174, 1982a.

M. Y. Su. Three-dimensional deep-water waves. part 1. experimental measurement of skew and symmetric wave patterns. *J. Fluid Mech*, 124:73 – 108, 1982b.

H. U. Sverdrup and W. H. Munk. Wind, sea, and swell: theory of relations for forecasting. In *Us Navy Hydorgraphic Office, Washington, DC, No.601 44p*, 1947.

M. A. Tayfun. Narrow-band nonlinear sea waves. *J. Geophys. Res.*, 85(C3):1548–1552, 1980.

A. Toffoli, J. M. Lefevre, E. Bitner-Gregersen, and J. Monbaliu. Towards the identification of warning criteria: analysis of a ship accident database. *Appl. Ocean Res.*, 27(6):281–291, 2005.

A. Toffoli, M. Benoit, M. Onorato, and E. M. Bitner-Gregersen. The effect of third-order nonlinearity on statistical properties of random directional waves in finite depth. *Nonlin. Processes Geophys*, 16:131–139, 2009.

A. Toffoli, O. Gramstad, K. Trulsen, J. Monbaliu, and E. Bitner-gregersen. Evolution of weakly nonlinear random directional waves: laboratory experiments and numerical simulations. *J. Fluid Mech.*, 664:313–336, 2010.

A. Toffoli, L. Cavaleri, A. V. Babanin, M. Benoit, E. M. Bitner-Gregersen, J. Monbaliu, M. Onorato, A. R. Osborne, and C. T. Stansberg. Occurrence of extreme waves in three-dimensional mechanically generated wave fields propagating over an oblique current. *Nat. Hazards Earth Syst. Sci*, 11:895–903, 2011.

H. L. Tolman. A third-generation model for wind waves on slowly varying, unsteady, and inhomogeneous depths and currents. *J. Phys. Ocean.*, 21(6):782–797, 1991.

K. Trulsen and K. B. Dysthe. A modified nonlinear schrödinger equation for broader bandwidth gravity waves on deep water. *Wave Motion*, 24:281–289, 1996.

K. Trulsen, I. Kliakhandler, K. B. Dysthe, and M. G. Velarde. On weakly nonlinear modulation of waves on deep water. *Phys. Fluids*, 12:2432–2437, 2000.

H. Tuah and R. T. Hudspeth. Finite water depth effects on nonlinear waves. *J. Waterway, Port, Coastal*, 111:401–415, 1985.

M. P. Tulin and T. Waseda. Laboratory observations of wave group evolution, including breaking effects. *J. Fluid Mech.*, 378:197–232, 1999.

T. Waseda, T. Kinoshita, and H. Tamura. Evolution of a random directional wave and freak wave occurrence. *J. Phys. Oceanogr.*, 39(3):621–639, 2009.

B. J. West, K. A. Brueckner, R. S. Janda, D. M. Milder, and R. L. Milton. A new numerical method for surface hydrodynamics. *J. Geohpys. Res.*, 92(C11):11803–11824, 1987.

G. B. Whitham. *Linear and nonlinear waves*, volume 42. Wiley-interscience, 2011.

C. W. Wright, E. J. Walsh, D. Vandemark, W. B. Krabill, A. W. Garcia, S. H. Houston, M. D. Powell, P. G. Black, and F. D. Marks. Hurricane directional wave spectrum spatial variation in the open ocean. *J. Phys. Oceanogr.*, 31(8):2472–2488, 2001.

G. Wu. *Direct simulation and deterministic prediction of large-scale nonlinear ocean wave-field.* PhD thesis, Massachusetts Institute of Technology, Cambridge, MA, 2004.

G. Wu, Y. Liu, and D. K. P. Yue. A note on stabilizing the Benjamin-Feir instability. *J. Fluid Mech.*, 556:45–54, 2006.

G. Wu, W. Xiao, Y. Liu, and D. K. P. Yue. Direct phase-resolved simulations of nonlinear ocean wavefield evolution. *in process*, 2012.

M. Xue, H. Xu, Y. Liu, and D. K. P. Yue. Computations of fully nonlinear three-dimensional wave-wave and wave-body interactions. part 1. dynamics of steep three-dimensional waves. *J. Fluid Mech.*, 438:11–39, 2001.

H. C. Yuen and B. M. Lake. Instabilities of waves on deep water. *Ann. Rev. Fluid Mech.*, 12(1):303–334, 1980.

V. E. Zakharov, A. I. Dyachenko, and O. A. Vasilyev. New method for numerical simulation of a nonstationary potential flow of incompressible fluid with a free surface. *Eur. J. Mech. B/Fluids*, 21(3):283–291, 2002.

H. Zeng and K. Trulsen. Evolution of skewness and kurtosis of weakly nonlinear unidirectional waves over a sloping bottom. *Nat. Hazards Earth Syst. Sci*, 12: 631–638, 2012.